# A Study on the Design of Receiver Optics and Waveguide Components Towards High-Performance (Sub)Millimeter Wave Multibeam Receivers

*Submitted in partial fulfillment of the requirements for the degree of*

## Doctor of Philosophy

*by*

**Takaho Masai**


Department of Astronomical Science
The Graduate University for Advanced Studies, SOKENDAI

**January, 2024**

## ABSTRACT

Millimeter/Submillimeter wave radio astronomy is a crucial tool for probing the universe. Observations of key spectral lines can provide invaluable information such as star formation activities and many other characteristics in the form of physical, chemical, and spatial information. The detector of choice at (sub)millimeter wavelengths are heterodyne receivers, especially because they have high-spectral resolution, high-sensitivity, and can be used in interferometers to achieve high-angluar resolution. There has been a big push in recent years to accelerate the scientific output from heterodyne receivers by upgrading key aspects of the detector. One notable upgrade is from a single-beam receiver to a multibeam receiver which has a larger field-of-view (FoV) on the sky wide-field studies.

Multibeam heterodyne receivers are often developed for a large single-dish telescope with sufficient room or for a dedicated cryostat in an antenna. One unique development plan is that of the Atacama Large Millimeter/Submillimeter Array (ALMA) development roadmap. Here, the replacement of the current single-beam receivers to multibeam receivers has been a highlight as the next mid to long term upgrade. The antennas are designed for single-beam receivers and thus impose a uniquely challenging setting for considering a multibeam receiver, as the antenna was originally meant for single-beam receivers. In this situation, the number of pixels that can be integrated on the receiver will be limited by the antenna itself, and only a modest number of pixels may be implemented. It is inevitable to design the individual pixels to have as high of performance as possible to cover for the limited number of pixels. However, the design of the receiver front-end components; the receiver tertiary optics, feed horns, and waveguide block, have not had sufficient considerations.

In this thesis, several topics concerning the design and integration of multibeam heterodyne receiver front-ends under the setting of replacing a single-beam receiver in a radio telescope are discussed.

One critical aspect of the receiver optics is the effect of aberrations. Aberrations are the errors introduced by an optical system which causes degradation in optical efficiency. For a radio telescope, the effect of aberrations will lower its aperture efficiency. In a multibeam receiver, each pixel is located at a different position in the focal plane of the telescope meaning they all see different amounts of aberrations. A comprehensive understanding of aberrations is crucial towards aiming for high-efficiency receiver optics. This thesis presents the development of software code to rapidly calculate the aperture efficiency affected by aberrations. The code is

based on the latest theories of the effect of aberrations on aperture efficiency.

This thesis investigates the detailed design of the receiver tertiary optics to obtain frequency independent designs (FID). FID has been well established in single-beam receivers, although the expansion of the design to multibeam has not been discussed much. FID comes with the very attractive merit of constant aperture efficiency within the frequency band. However, the demerit is more complex optical designs that require more consideration. This thesis looks at the design and analysis of individual pixels in a multibeam receiver and solves the conditions to obtain frequency independent illumination at the sub-reflector utilizing ray tracing and physical optics simulations. A few pixel multibeam receiver was designed. The optics were able to achieve a high aperture efficiency of $\eta_{\mathrm{A}} \geq 0.8$ on the sky. Critical design constraints such as the cryostat were also identified.

This thesis also looks at the design of re-imaging optics for overcoming the strong constraint introduced by a cryostat window. Cryogenically cooled receivers are put in a cryostat to lower its physical temperature which imposes strong constraints on the design of the receiver optics. Here, re-imaging optics were used to redirect receiver beams from a multibeam receiver to pass through a small 35 mm diameter aperture, and to obtain the frequency independent condition for each receiver beam. A design consisting of two dielectric lenses and a two-beam multibeam receiver is presented. The optics were successfully able to pass both beams through a small 35 mm window. The optics were also able to create a relatively frequency independent illumination with an aperture efficiency difference of less than 1% at the 385 and 500 GHz. Trade-offs including truncation at the window, additional thermal load to the cryostat, and dielectric loss from the lenses were also identified and considered.

Finally, a novel wideband waveguide-based Magic Tee junction was developed for tackling potential issues for the waveguide block and Local Oscillator distribution circuits. The Magic Tee is a 4-port junction that has exceptional port-to-port isolation, which is a crucial trait for key waveguide components. Here, a wideband waveguide based Magic Tee was designed to replace the conventional E-plane T/Y-junctions used in current split-block receivers waveguide blocks. The Designed Magic Tee was able to obtain high performance of return loss higher than 20 dB and isolation higher than 20 dB with a fractional bandwidth of 47.9 %.

## ACKNOWLEDGEMENT

This thesis could not have been possible without the mountain of support I have received throughout the preparation and completion of this study, it is a pleasure to thank those who made it a possibility.

It is with immense pleasure and deep sense of gratitude, I wish to express my sincere thanks to **Professor Alvaro Gonzalez**. Alvaro-san has provided me the chance to study and work on radio receivers. His guidance and encouragement has continuously reassured me to aim for the finish line time after time.

I am deeply indebted to **Dr. Hiroaki Imada**, as he has taught me almost everything I know about optics and optics software. Imada-san's expertise has inspired me countless times and his generosity knows no bounds.

I express my sincere thanks to **Dr. Takafumi Kojima**, for taking over as primary supervisor during the hectic period towards the end of the program.

I am grateful to my dissertation committee members, Prof. Satoru Iguchi, Dr. Masahiro Sugimoto, Dr. Saeko Hayashi, Dr. Hiroyuki Maezawa, and Dr. Frederick Takayuki Matsuda for providing suggestions which have significantly improved this thesis.

I would like to express my appreciation to Doug Henke for the fruitful collaboration, and I thank Dr. Lewis Knee and the Millimetre Instrumentation Group at the Herzberg Astronomy and Astrophysics Research Centre, National Research Council of Canada, for the many discussions, seminars, and experiences gained from accepting me as a visitor.

I would like to thank Keiko Kaneko and Ryo Sakai at the Advanced Technolohy Center at the National Astronomical Observatory of Japan. Kaneko-san has helped tremendously with the design of the waveguide components and with the procurement. Sakai-san has helped with setting up and teaching me how to use the measurement systems. I also thank the fabrication team at ATC for the fabrication of the metal 3D printed components. I appreciate the entire receiver development team at ATC for including me in their monthly meetings.

Thank you to the SOKENDAI student affairs office and secretaries for their tireless work. I am also grateful to Prof. Takashi Sekii for the consultations when I ran into troubles during the program.

I deeply appreciate the ALMA secretaries for making stressful transactions and travel related work extremely streamlined. Many thanks to Dr. Toshiki Saito, Dr. Shun Ishii, and Dr. Tetsuhiro Minamidani for the many wonderful discussions.

I am grateful to Dr. Shinya Komugi and Dr. Takayuki Muto and the physics lab at

Kogakuin University for the holding many seminars for the graduate students.

I thank Kang Haoran for providing his support and discussions during the weekly meetings. I appreciate Dr. Kosuke Namekata and Dr. Takafumi Tsukui for their emotional support and generosity in the ALMA building.

I could not have undertaken this journey without the support from my fellow peers and friends in SOKENDAI and the University of Tokyo. Some lasting memories were made with Ikki Mitsuhashi, Jin Beniyama, Raiga Kashiwagi, Shinichi Kinoshita, and Yui Kasagi. They have also reassured me that I was not, in fact, completely insane.

My lab mates from undergrad, Ayumi Takahashi, Kiyoto Maeyama, and Yuto Sato have kept each other in check after going to different schools, which I truly value. My personal friends Hikaru Koyanagi, Hiroyuki Kinoshita, Koki Mikami, and Ryoya Fukunaga, have given me many breaths of fresh air away from research which has helped keep myself motivated.

Finally, I wish to extend my profound sense of gratitude to my family, especially to my parents **Yuko and Satoru Masai** for raising me to this point and for all the sacrifices they made. They provided unconditional love and support throughout my life. I thank my brother Mizuho for looking after me growing up and giving me his very nice used clothes (including suits) as I could not afford my own.

Last but not least, I thank the most adorable creature to ever exist, my dog Coco (Fig. 1). Her mere presence during COVID was enough to keep my head up high, and her *surprisingly accurate* biological clock for breakfast forced to regulate my sleep schedule, at the time. Rest easy buddy, you will be missed.

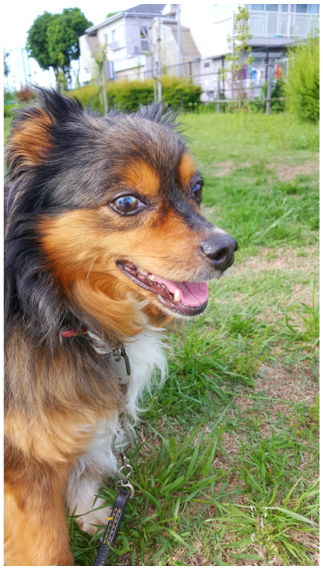

**Fig. 1** A miniature Australian shepherd named Coco (2005.7 - 2023.03)

This work was supported in part by The Graduate University for Advanced Studies, SOKENDAI. The 3D printed components were fabricated by the Advanced Technology Center at the National Astronomical Observatory of Japan.

Place: Tokyo, Japan

Date: 07/01/2024 **Takaho Masai**

# CONTENTS

# List of Figures

# List of Tables

# CHAPTER 1

# Introduction

## 1.1 Millimeter/Submillimeter Wave Astronomy

Radio astronomy has evolved from the discovery of astronomical radio waves by Karl G, Jansky (Jansky, 1982) to detecting the first signals from the earliest galaxies in the universe (Hashimoto et al., 2018). In recent years, radio observations have become an integral and necessary component to modern astronomy. The complements supplied by radio observations to other wavelength observations have drastically accelerated our understanding of several key branches in astronomy and astrophysics (Rohlfs and Wilson, 2000). Of these branches, there are still many unanswered fundamental questions. These include:

- **How do galaxies form and evolve?**
- **How do stars and planets form?**
- **Does organic life exist outside of Earth?**

To answer the many remaining questions, we require conducting observations at key wavelengths in the electromagnetic spectrum. A particularly important wavelength range is the millimeter and submillimeter band. Millimeter/Submillimeter waves are the electromagnetic waves which have wavelengths spanning from $\lambda = 0.3$ mm to 30 mm, or frequencies of $\nu = 10$ GHz to 1000 GHz. This frequency range is the home to some extremely important spectral lines that provide invaluable data to probe celestial objects such as galaxies and molecular clouds.

A key spectral line is the Carbon monoxide (CO) $J = 1 - 0$ transition line which can be observed at 115.27 GHz for nearby targets. Another crucial spectral line is the Neutral carbon line [CI] observable at 492.16 GHz. These spectral lines can provide information concerning chemical composition and physical properties of interstellar medium. These properties are crucial towards understanding.

Neutral carbon can be observed along side CO to better estimate the amount of molecular gas and dust from regions near active galactic nuclei (AGN) (Saito et al., 2022). The neutral carbon line has particular importance in regions of high density photo dissociated carbon monoxide, where observing only CO would otherwise lead to apparently less molecular gas.

The examples listed here, along with a diverse spectrum of science cases, can be conducted more efficiently by using radio telescopes and detectors with higher sensitivity.

## 1.2 Millimeter/Submillimeter Wave Radio Receivers

### 1.2.1 Coherent Detectors

**Fig. 1.1** ALMA receiver cartridges. Left: Band 4 (125-163GHz), Center: Band 8 (385-500GHz), Right: Band 10 (787-950GHz). Photo credit: ALMA(ESO/NAOJ/NRAO). https://www.nao.ac.jp/en/gallery/weekly/2014/20140701-alma-receivers.html

Coherent detectors in millimeter wave astronomy mainly consist of Heterodyne receivers. Heterodyne receivers are radio receivers that take an input radio signal with frequency $f_{\mathrm{RF}}$, and mix it with a synthetically generated Local Oscillator (LO) signal with a constant frequency of $f_{\mathrm{LO}}$ that is close to $f_{\mathrm{RF}}$. The output intermediate frequency signal at $f_{\mathrm{IF}}$ is a signal with a frequency given by the difference of the RF and LO signals $f_{\mathrm{IF}} = |f_{\mathrm{RF}} - f_{\mathrm{LO}}|$. Examples of heterodyne receivers are the Atacama Large Millimeter/Submillimeter Array (ALMA) receivers shown in Fig. 1.1. This frequency down-conversion is necessary due to the limit of analog signal sampling speed of IF digitizers and readout electronics. High-speed ADC sampling receivers are being developed and have been demonstrated in Kojima, T. et al. (2020). Proposals towards next generation correlators for radio interferometer backend are described in Quertier et al. (2021).

The noise temperature of a heterodyne receiver will be given by the cascaded sum of noise temperature $T$ and gain $G$ contributions from each section. The receiver noise temperature can be represented using the Fris formula (Pozar, 2011),

$$T_{\mathrm{RX}} = T_{\mathrm{OPTICS}} + \frac{T_{\mathrm{LO}}}{G_{\mathrm{OPTICS}}} + \frac{T_{\mathrm{MIXER}}}{G_{\mathrm{OPTICS}} G_{\mathrm{LO}}} + \frac{T_{\mathrm{AMP}}}{G_{\mathrm{OPTICS}} G_{\mathrm{LO}} G_{\mathrm{MIXER}}} + \cdots \tag{1.2.1}$$

The gain from a component may be above unity to indicate a gain in power, unity to indicate no gain, and less than unity to indicate a loss of power $L$ ($L = 1 - 1/G$ when $G < 1$). Is is evident from Eq.(1.2.1), having low noise temperatures and high gain from each component

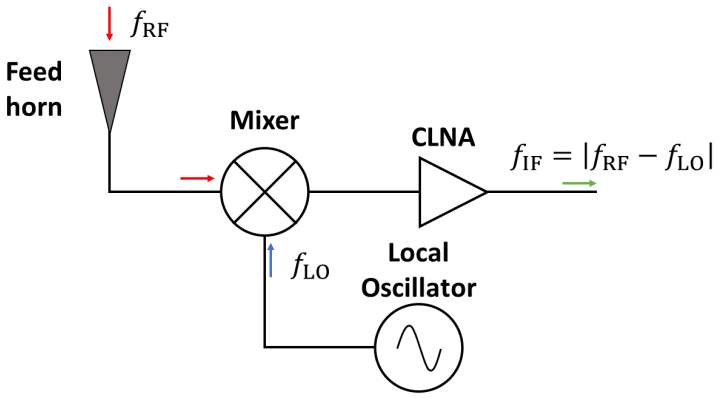


**Fig. 1.2** Simple block diagram of a heterodyne receiver.

contributes to lower receiver noise temperature. Passive components may have their physical temperature cooled down to limit the total thermal noise. Components with gain may also be introduced towards the first stages of the components chain. Thus, adding the Cooled Low-Noise Amplifiers (CLNA) in the first stages contributes to reduce the receiver noise considerably since CLNAs typically have very high gain of a few tens of dB (White et al., 2019). Frequencies above roughly 120 GHz require down-conversion before amplification due to the lack of available high-performance CLNAs at submillimeter frequencies.

Coherent detectors are able to retain the information of both the amplitude and phase of the RF signal. As a result, Heterodyne receivers are capable of obtaining high-spectral resolution by controlling the LO frequency, which is crucial for the aforementioned spectral line observations. They are also used in radio interferometers (Thompson et al., 2018) such as the Atacama Large Millimeter/Submillimeter Array when more spacial resolution is required.

Some common detectors used in radio receivers are introduced below.

**High-Electron-Mobility Transistors** : High-Electron-Mobility Transistors (HEMT) utilize the field-effect modulation of the high-mobility two-dimensional electron gas in semi-conductors (Mimura, 2005). At millimeter wave frequencies up to around 120 GHz, low noise amplifiers such as Microwave Monolithic Integrated Circuits (MMIC) (White et al., 2019) can be used for pre-amplification before mixing and low-noise HEMT based receivers can be utilized.

**Superconducter-Insulator-Superconductor Mixers** : The superior choice for the mixer at submillimeter wave frequencies is the Superconductor-Insulator-Superconductor mixer (SIS). SIS mixers have detection sensitivities near the physical quantum limit at (sub)millimeter wave frequencies (Graf et al., 2015). SIS mixers utilize the non-linear response of the SIS tunneling junction for the detection (Phillips and Dolan, 1982). SIS mixers can be used up to around 1.2 THz limited by the material properties of the superconductor (Winkler and Claeson, 1987).

**Hot Electron Bolometers** : At very high frequencies above 1 THz, Hot Electron Bolometer

(HEB) detectors are used (Zhang et al., 2022). HEBs utilize the creation of hot electrons when the superconductivity of a thin superconductor is broken introducing some resistance. The HEB is operated in a regime where the resistance is highly dependent on temperature. A local oscillator can be used to introduce a bias at a point where a small change in temperature results in a large change in resistance which can be use for the detection (Shurakov et al., 2016).

### 1.2.2 New Requirements for Radio Telescopes

Radio telescopes are requiring even greater sensitivities and resolving power along with accelerated data output. It was emphasized in Graf et al. (2015) that this can be either done by increasing the output bandwidth covering more of the RF spectrum, or by increasing the total physical number of detectors to acquire a wider Field-of-View (FoV) on the sky.

A radio telescope is usually built as a "single-pixel" instrument meaning the FoV of the telescope is limited to a singular point on the sky per pointing given by its beam size. An area spanning over a large distance must be mapped point-by-point to scan the whole patch of sky (Fig. 1.3, top left).

An increase in the number of detectors insists on the use of a multibeam receiver. Multibeam receivers are radio receivers with multiple input feed channels which all act as independent pixels. Each pixel observes a slightly different area of sky which all combine to give the radio telescope a larger FoV. The total time to map a source will generally decrease proportionally by the number of pixels $N$.

A wider FoV is beneficial especially for a few key wide-field observation cases:

1. **Wide-field mapping of extended sources**
2. **Wide-field sky surveys**

Wide-field studies are necessary for targets that have a large angular footprint on the sky such as nearby galaxies and molecular clouds. These targets may span over a few tens or hundreds of arcseconds on the sky.

Wide-field observations also include blind sky surveys. Here, a region of the sky is scanned to to find potential targets of interest (Zavala et al., 2021).

Promoting more wide-field observations requires the continued development of the state-of-the-art receiver technologies and development of multibeam receivers are necessary.

## 1.3 Development Projects for Radio Telescopes

### 1.3.1 Multibeam Heterodyne Receivers

A Multibeam heterodyne receiver is an array of heterodyne receivers integrated as one a single instrument (Fig. 1.4). The design and implementation of a multibeam receiver will depend on many factors including the scientific motivation behind the instrument and the telescope it is

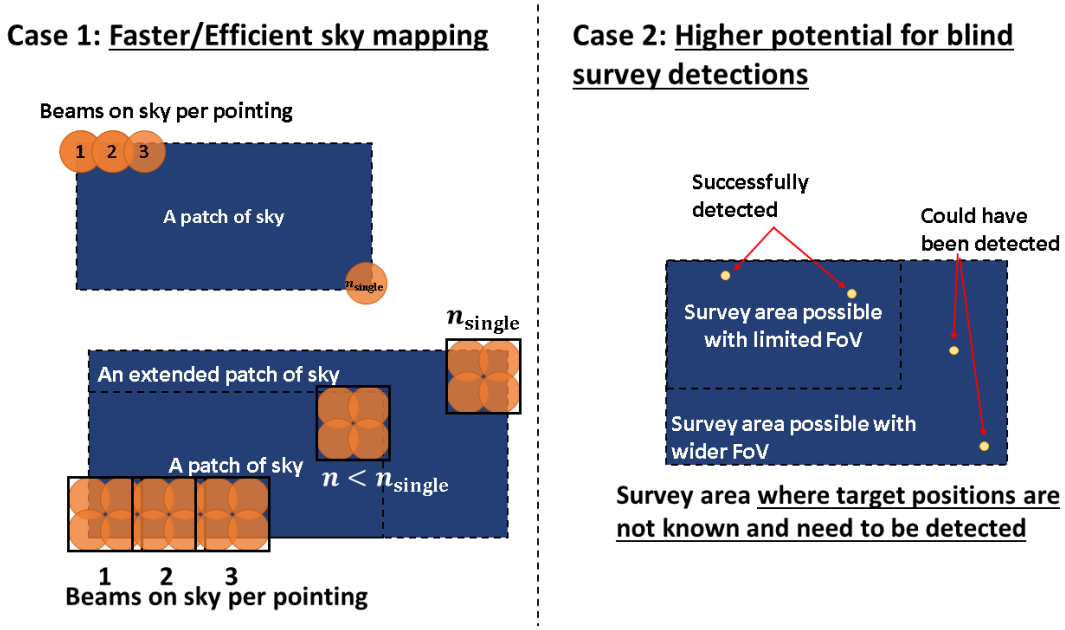


**Fig. 1.3** Diagram depicting the two key science cases for wide-field studies.

designed for. Consequently, there is no universal design that can work for every radio telescope and each receiver must be developed with careful consideration. The FoV of a radio telescope will be given by ratio between the wavelength $\lambda$ and diameter of the antenna $D$ times the number of pixels on the receiver $N$.

For an observation that requires $P$ number of pointings, an increase of $N$ pixels will reduce the total number to $P/N$. The total time required to observe the target will depend on the sensitivity of the radio telescope and the required signal-to-noise ratio.

If a set signal-to-noise ratio is required, a single-beam receiver with sensitivity $\eta$ will require some integration time $\tau$. The integration time will be inversely proportional to the square to of the efficiency and will follow $\tau \propto 1/\eta^2$. To conduct $P$ number of pointings, the total observation time $t$ will ideally follow the relation,

$$t \propto \frac{P\tau}{N}. \tag{1.3.1}$$

### 1.3.2 Radio Telescopes with Multibeam Receivers

There has been a number of new projects aiming for state-of-the-art multibeam receivers housed in a large single-dish telescope.

These telescopes use or are currently developing incoherent detectors such as bolometer cameras with thousands of pixels in a large format array utilizing Microwave Kinetic Inductance Detectors (MKIDs) and Transition Edge Sensors (TES). These cameras are extremely broadband and are best suited for wide-field continuum observations. A notable development project is CCAT-Prime (Parshley et al., 2018). CCAT-Prime is planned 6-m large single dish project planning to be constructed at the Atacama desert in Chile. However, incoherent detectors only readout the total power and do not preserve the phase information. Thus, these detectors generally are not the best choice for spectroscopic observations because their spectral resolution is limited by the frequency resolution of microwave filters.

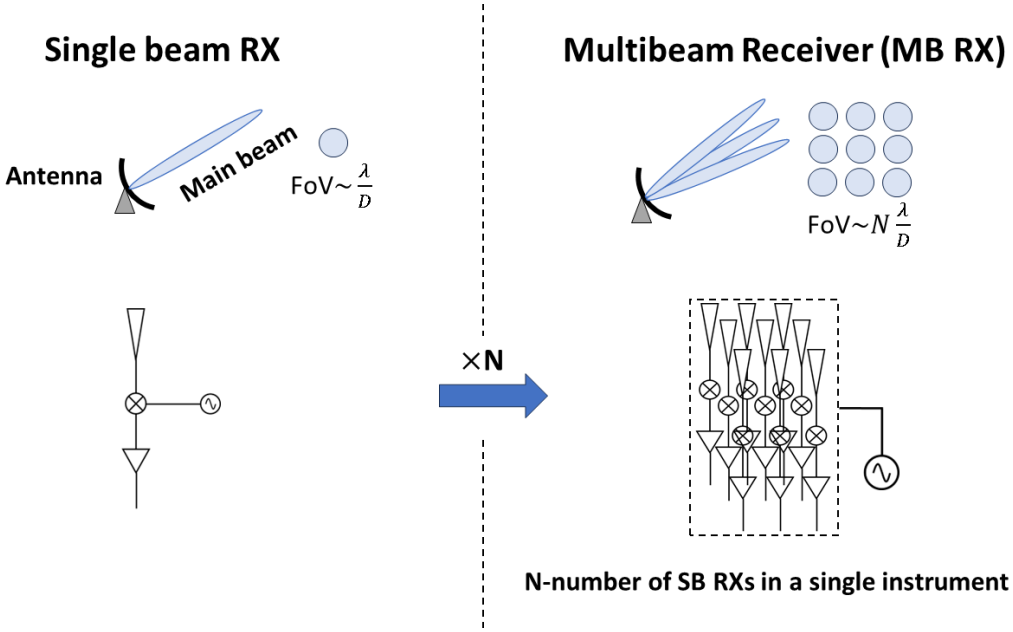


**Fig. 1.4** Diagram of a multibeam heterodyne receiver.

In the domain of multibeam heterodyne receivers, there are a few notable examples. The IRAM 30 m telescope has developed a $3\times3$ SIS heterodyne array (HERA) described in Schuster et al. (2004). The James Clerk Maxwell telescope has developed a $4 \times 4$ SIS heterodyne array receiver HARP-b (Smith et al., 2003). SuperCam is a $8\times8$ pixel array operating on the Heinrich Hertz Telescope (Kloosterman et al., 2014).

A list of radio telescopes currently utilizing or developing multibeam heterodyne receivers are summarized in Table. 1.1.

**Table 1.1** Summary of radio telescopes with multibeam heterodyne receivers

| Observatory | Primary diameter | Receiver | Detector type | No. PX | Frequency |
|---|---|---|---|---|---|
| CCAT-Prime | 6 m | CHAI | SIS | 64, 64 | 460 - 500 GHz, 780 - 820 GHz |
| IRAM | 30 m | HERA | SIS | 9 | 210 - 240 GHz |
| JCMT | 15 m | HARP | SIS | 16 | 325 - 375 GHZ |
| KOSMA | 3 m | CHARM | SIS | 9 | 330 - 360 GHz |
| SMTO | 10 m | SuperCAM | SIS | 64 | 345 GHz |

## 1.4 Challenges Towards Multibeam Heterodyne Receivers

The general development of a multibeam heterodyne receiver will be faced with many technical obstacles. A telescope will face one technical challenge while a different telescope will face another, there is no standard best answer for development. Common issues to overcome, in no particular order, are:

- Compact design.
- Efficient LO power distribution.

- Fabrication and mass production.
- Cooling capacity of the cryostat.
- Design of optics.

As a result, there has been several big pushes towards compact and high-efficiency components for the various stages of the receiver. Examples include, a novel low-noise amplifier based on SIS up and down conversion demonstrated in Kojima et al. (2023) and a compact planar SIS mixer demonstrated in Shan et al. (2018).

This thesis is mainly concerned with the challenges associated with the front-end components of heterodyne receivers; the waveguide block, feed horns, and receiver (tertiary) optics (Fig. 1.5).

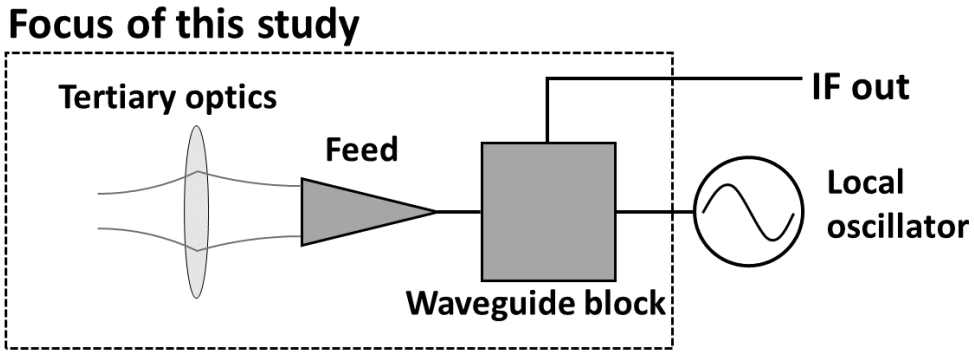


**Fig. 1.5** Diagram showing focus of interest in this thesis.

## 1.5 Replacing Existing Single-Beam Receivers

### 1.5.1 ALMA Development Roadmap

One significant development case is the development roadmap indicated for the Atacama Large Millimeter/Submillimeter Array (ALMA) (Carpenter et al., 2018. Fig. 1.6). ALMA is a millimeter/submillimeter wave radio interferometer operating at the Atacama desert in Chile. The array consists of fifty 12-m Cassegrain antennas, twelve 7-m Cassegrain antennas, and four 12-m Cassegrain antennas for supplemental single-dish total power data. ALMA conducts observations from 35 GHz up to 950 GHz split up into 10 frequency bands. Each antenna is expected to house 10 different single-beam receivers for each frequency band.

The ALMA development roadmap specifies key performance upgrades for ALMA such as extended baselines for higher spatial resolution, wider bandwidths for higher sensitivity, multi-beam receivers for wider field-of-view, and a large single dish telescope for observation synergy. One of the proposed near-term upgrades targeting the increase in bandwidth has been recently ignited as the ALMA 2030 wideband sensitivity upgrade (WSU) in Carpenter et al. (2023). This thesis is concerned with one of the highlighted upgrades for the medium to long term with

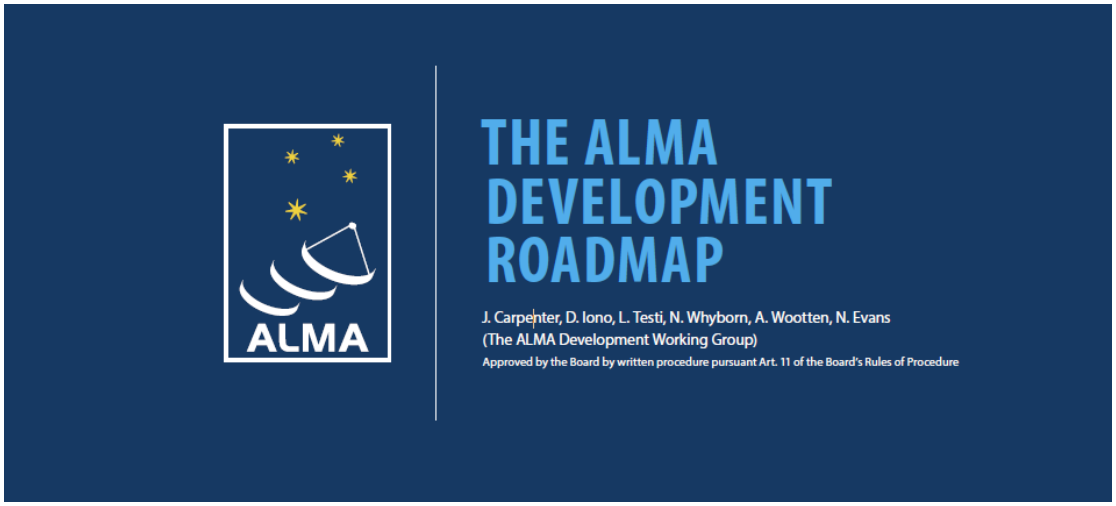


**Fig. 1.6** The ALMA development roadmap. Credit: ALMA (NRAO/ESO/-NAOJ, https://www.almaobservatory.org/wp-content/uploads/2018/07/20180712-alma-development-roadmap.pdf)

the development of multibeam receivers to increase the field-of-view towards improving survey speeds for efficient wide-field observations.

The ALMA development roadmap presents a challenging case where the current single-beam receiver is to be replaced with a multibeam receiver. Telescopes looking to replace single-beam receivers with multibeam receivers will generally face more challenges trying to implement large format arrays. An existing antenna system will require major modifications for a large format array because they are tailored for the single-beam system.

Under this setting, some critical limitations for a large format array are the following:

- Limited space in a receiver cabin and cryostat.
- Cooling capacity of the cryostat.
- Distribution of the scarce LO power.

These points will physically limit the maximum number of pixels in a multibeam heterodyne receiver. Thus, these telescopes are mostly limited to small format arrays with a modest number of pixels upwards of around ten pixels. As a direct result, the field-of-view will at most, only increase by a few factors. To make up for the smaller field-of-view compared to large format arrays, the individual pixels in the small format array will need to prioritize high-performance to maintain efficient surveying speeds for the telescope and to justify the development of such a complex instrument (Graf et al., 2015).

However, even when considering small format arrays, the existing antenna systems meant for single-beam receivers will act as a major hurdle. This setting considering the replacement of a single-beam receiver with a multibeam receiver has not been discussed much because multi-beam receivers are often times developed in parallel with new radio telescope projects with dedicated cryostats, or because they are being designed in a large single-dish telescope.

As a result, the development setting of replacing a single-beam receiver with a multibeam receiver presents its own unique challenges and constraints.

For the particular case of ALMA, the state-of-the-art performance of its current receivers must be preserved to not interfere with current observation capabilities. Not only does ALMA currently conduct a variety of extremely high-sensitivity observations, it does so across a relatively wide bandwidth. Thus, each pixel in a multibeam receiver for ALMA should have the nearly the same high-performance comparable to its current receivers.

## 1.6 Issues to be Discussed

The setting of replacing an existing single-beam heterodyne receiver and replacing it with a high-performance multibeam heterodyne receiver in the same antenna will present unique challenges which need to be addressed.

### 1.6.1 Receiver Optics

Almost all multibeam heterodyne receivers that have been developed or are being developed (e.g. CCAT-prime) utilize so-called Focal Plane Arrays (FPA). The main priority for these arrays were to achieve very high-pixel counts with a compact design, and to have close beams on the sky for efficient mapping.

Focal plane arrays have their receiver inputs distributed along the focal plane of the telescope where they either directly illuminate the sub-reflector (Fig. 1.7), or utilize re-imaging optics to change the effective F-number (Fig. 1.8). These re-imaging optics takes the fields at the focal plane, and create its image at a different position. A special case for re-imaging optics is having a set of optical elements separated by the sum of their focal lengths. This is called a *Gaussian Beam Telescope* (GBT). The feed horn array is then placed at the final focus of the GBT. The feeds are often designed to be parallel to each other for a compact and scalable design. They may also be slightly tilted to reduce the asymmetric illumination at the sub-reflector. Focal plane arrays have the distinct advantage of being able to achieve densely packed feed horn arrays to increase the total number of pixels. Closely packed feed horn arrays also have the advantage of having very close beams on the sky for efficient mapping of sources.

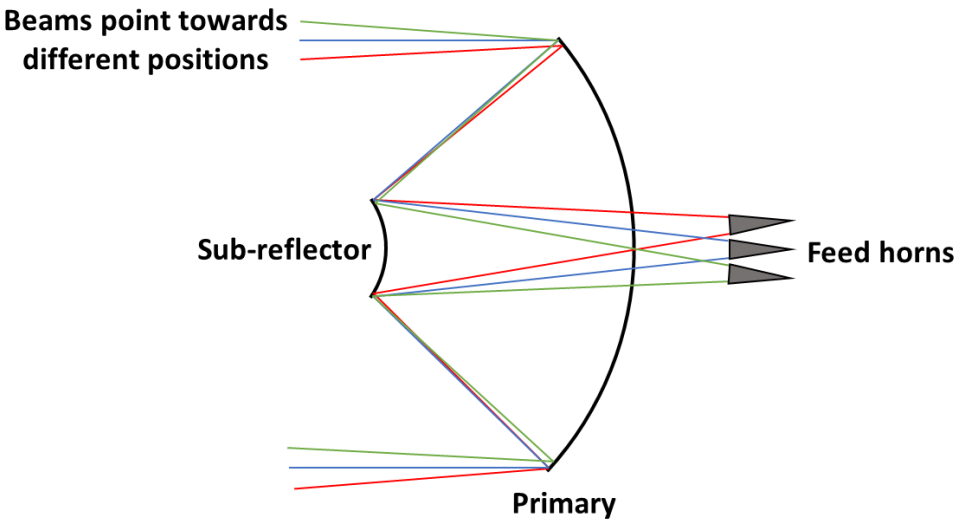


**Fig. 1.7** Diagram of a direct illumination focal plane array.

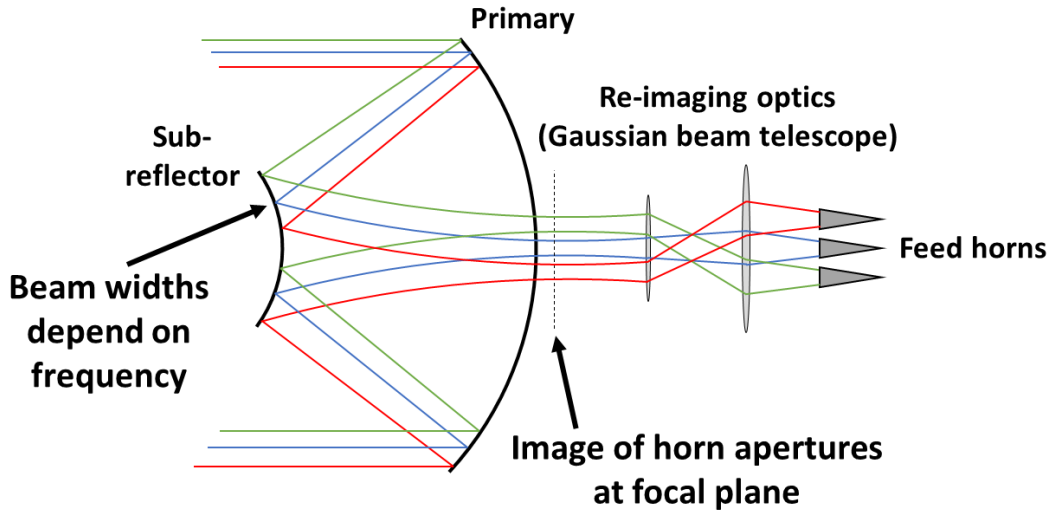


**Fig. 1.8** Diagram of a focal plane array with Gaussian beam telescope re-imgaging optics.

However, FPAs have a disadvantage of generally having degraded optical efficiency (Graf et al. 2015). This is due to them having asymmetrical illumination for the off-axis pixels which increases the beam spill-over (Padman, 1995). Another aspect is their frequency dependent beam size at the sub-reflector and effect of aberrations.

The sensitivity of the receiver, and in extension the telescope, will be directly proportional to the efficiency of the receiver optics. As a result, degraded optical efficiency will increase the required total observation time as indicated in Eq. (1.3.1). The minimum integration time will be dictated by the lowest sensitivity pixel in the array. Thus, striving for very high optical efficiency from each individual pixel is especially crucial when considering a small number of pixels (Fig. 1.9).

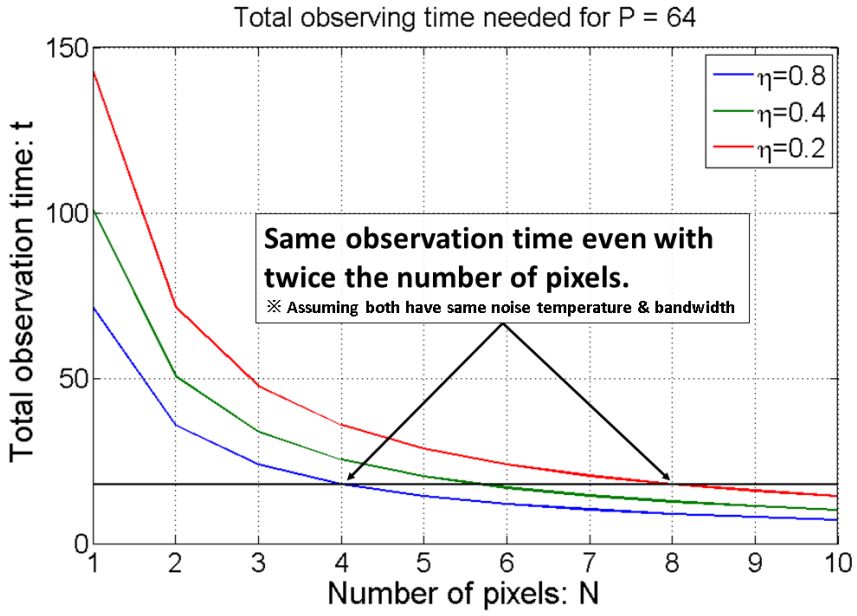


**Fig. 1.9** Comparison between total observation times $t$ for a multibeam receiver with different efficiencies $\eta$ and pixel numbers $N$ for a $P = 64$ observation.

The optical design of single-beam receivers is well established and has been applied to design high-efficiency optics. The optical efficiency is determined by many factors. However, one of the most important figures-of-merit for high-performance optics is having high-aperture efficiency.

Single-beam receiver optics utilize the frequency independent imaging condition (Chu, 1983) to produce a constant beam width on the sub-reflector as shown in Fig. 1.10. A focusing element (such as a lens or mirror), or a combination of focusing elements, are used to create an image of the horn aperture at the sub-reflector. The frequency independent fields at a feed horn aperture are directly imaged at the sub-reflector which results in a constant illumination of the sub-reflector from the feed. This constant illumination translates to ideally constant and high aperture efficiency across the whole frequency band.

If the aim is to achieve high-efficiency optics for each pixel in a multibeam receiver, we should consider each pixel and its optics individually. Naturally, it is reasonable to assume and consider each pixel in a small format array as individual single-beam receiver and conduct the

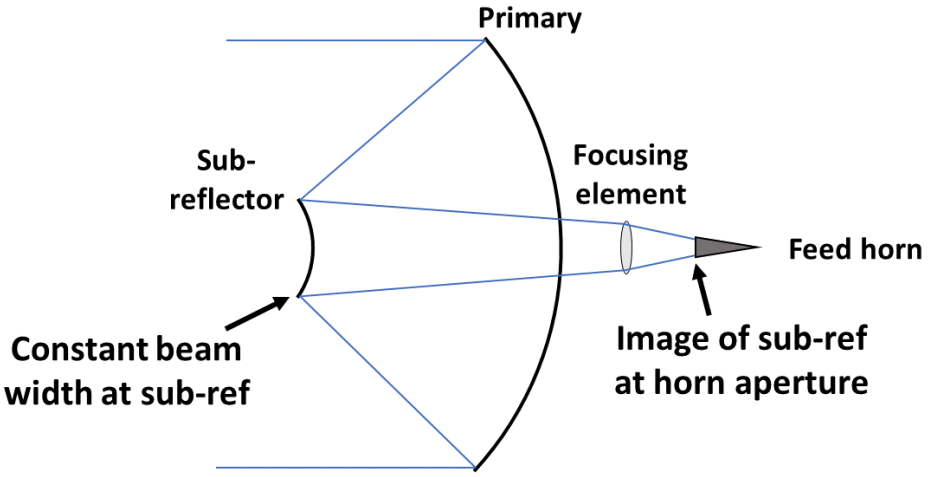


**Fig. 1.10** Diagram of single-beam receiver optics and the imaging of the horn aperture beam to produce a frequency independent illumination at the sub-reflector.

analysis and design based on the previous methods for single-beam. This can be done for a small format array because we are focused on a small number of pixels. Symmetrical designs may further decrease the required effective number of unique designs.

The extension the single-beam optics design for multibeam, especially the principle of frequency independent optics, has not had sufficient discussion. The concept of frequency independent optics in multibeam receivers is one strong driver in this study. Estimations of performance, design pros and cons, constraints and limitations, and trade-offs are key topics of discussion.

### 1.6.2 LO Distribution

Efficient distribution of the LO must be considered, especially at the higher frequencies since frequency multipliers must be used to generate an LO frequency close to the RF. Frequency multipliers generally introduces some loss which introduces some limitations for the power distribution (Chattopadhyay, 2011). For a multibeam receiver, the LO power will be divided between all pixels in the array. As a result, distributing the LO power efficiently is crucial, not only to maintain sufficient LO power for each mixer in a multibeam heterodyne receiver, but also to maintain the signal purity of the LO minimizing the LO noise.

LO injection methods for heterodyne receivers can be broadly categorized into quasioptical coupling and waveguide based coupling. Both methods have their strengths and limitations depending on the application.

**Quasioptical coupling** : Quasioptical LO coupling utilizes free-space propagation to inject an LO signal to a receiver feed. The LO beam is transmitted by a LO horn and propagated towards a horn on the mixer block. The propagated LO beam is received by the LO horn on the mixer block and finally coupled to the RF. The advantage of quasioptical coupling

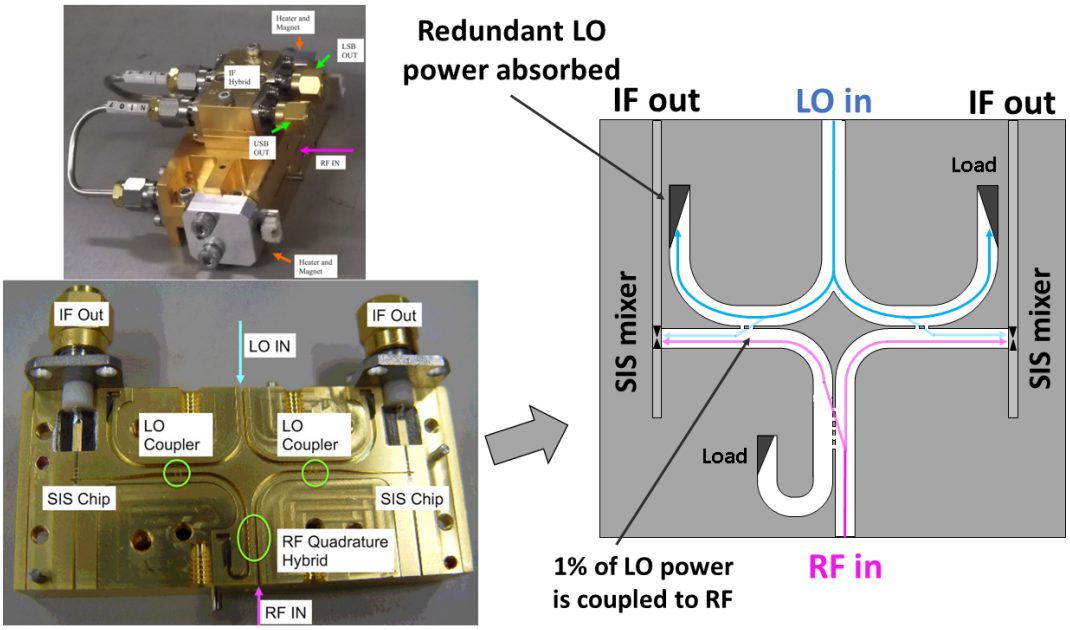


**Fig. 1.11** Top Left: Photo of ALMA band 4 2SB mixer block from Asayama et al. (2014). Bottom left: bottom half of block showing waveguide circuits. Right: diagram showing the RF and LO paths in the mixer block.

is minimal loss of LO power at high frequencies roughly greater than 500 GHz. However, their disadvantage is requiring sufficient space for the LO optics. The LO optics will require their own optics and clearance to propagate the LO beam.

**Waveguide coupling** : Waveguide based LO coupling utilizes low-loss waveguide components (such as oversized wavegudies) to guide the LO signal to a mixer. The LO can be coupled to the RF with waveguide couplers or power combiners. The advantage of waveguide based LO injection is the ability to integrate the LO coupling network and the mixers in a compact waveguide block. The disadvantage of waveguide based LO coupling is the attenuation from conductor loss in a waveguide which become significant at high frequencies.

The LO distribution network will require some considerations for small format arrays. A singular LO will be required to keep the LO phase error as low as possible. This entails using power dividers to distribute LO power.

If current sideband separating mixers are to be used, we run into the issue of standing waves caused by the poor return loss of SIS mixers. Consider a sideband separating mixer (2SB) such as the 2SB waveguide block in the ALMA band 4 receiver (125 - 163 GHz) shown in Fig. 1.11 (Asayama et al., 2014). An LO signal is injected into the waveguide block and a -3 dB in-phase power divider is used to split half the LO power towards both mixers. A -17 dB coupler is used to combine the LO and RF before entering into the SIS junction. Here, only -17 dB of the input LO power is being coupled to the RF, the redundant LO power is terminated with an absorber. If the LO is divided using a typical power divider such as a T/Y-junction, there will be no output isolation between the two SIS mixers. This will cause issues with stable LO power distribution

as SIS mixers are generally optimized for low-noise performance and have poor return loss which reflects a large amount of the incident power. The poor return loss causes standing waves to form inside the LO distribution network which causes ripples in the frequency response or may excite resonant frequencies.

Another critical aspect is maintaining sufficient LO power to pump into each SIS mixer since LO power tends to become scarce at higher frequencies. Less LO power is required to drive a SIS mixer at submm-wave frequencies compared to mm-wave frequencies (D'Addario et al., 2001). However, the available LO power also tends to decrease at the higher frequencies and sources of loss, such as waveguide attenuation, become significant.

Here, we can broadly divide the problem into three categories: LO source power, high-isolation components, efficient design of distribution network. There are a few angles of approach to tackle each issue of LO power distribution. Development of LO power sources are out of the scope of this thesis. Here, the isolation between pixels stands out as an initial topic and is one point of interest towards developing efficient ways to distribute the LO to each pixel in a multibeam receiver.

## 1.7 Goal of this Thesis

This thesis discusses several topics towards the development of high-performance multibeam heterodyne receiver front-ends under the setting of replacing a single-beam receiver in an existing radio telescope.

There are three main questions to be discussed in this thesis:

**Question 1:** How can high-efficiency optics be designed for individual pixels in a multibeam receiver?

**Question 2:** Can high-efficiency multibeam receiver optics be designed and implemented in an antenna originally designed for single-beam receivers?

**Question 3:** How can LO power be efficiently distributed to each pixel with high-isolation?

## 1.8 Outline of this Thesis

In chapter 2, key methods and figures-of-merit that are used in this thesis frequently are introduced. In Chapter 3, the latest theoretical studies on receiver optics and the effect of aberrations are briefly reviewed. This is followed by the development of software code to calculate aperture efficiency with the effect of aberrations. In chapter 4, a method to design and analyze frequency independent optics for feed horns using commercial ray tracing and physical optics software is shown. This method was then used to design optics for a two-beam multibeam receiver. Chapter 5, explores a solution to allow the passage of multiple receiver beams through a small aperture utilizing re-imaging optics. In Chapter 6, the development of a novel wideband waveguide based Magic Tee junction suited for split-block fabrication is shown.

**CHAPTER 2**

# Analysis Methods and Figures-of-Merit

## 2.1 Introduction

This chapter introduces the basic concepts and analysis methods from optics, and antenna theory, that are used in this thesis.

## 2.2 Geometrical Optics

### 2.2.1 Fundamental Concepts

Fundamental concepts from geometrical optics for an optical system are introduced.

- **Aperture stop**: A physical stop that limits the extent of rays that can enter the optical system. The aperture stop defines the rays that can reach the image, or in other words, defines the total energy that enters the system.

- **Field stop**: The physical stop the limits the maximum chief ray angle. The field stop defines the angular field-of-view of the optical system.

- **Pupil(s)**: An image of the aperture stop. There may be multiple pupils in an optical system given by the number of optical elements. The first pupil seen from the object side (observer side) is called the **entrance pupil**. The last pupil seen from the image side is called the **exit pupil**. Entrance and exit pupils may coincide with physical apertures depending on the optical system.

- **Chief ray**: The rays that pass through the center of the aperture stop.

- **Marginal rays**: The edge rays that pass though the vertical edges (Meridional rays) and horizontal edges (Sagittal rays) of an aperture stop.

### 2.2.2 Analysis Methods and Figures-of-Merit

**Strehl ratio** : The Strehl ratio is widely used as a figure-of-merit for evaluating the imaging quality of an optical system (Born et al., 1999). The Strehl ratio is defined as the peak irradiance at a given image point $P$ with wavefront aberrations $\Phi_P$, over the peak irradiance at the same image point absent of aberrations.

If we define the rms of the wavefront as $\sigma = (\Delta\Phi_P)^2$,

$$\sigma_{\Phi_P} = (\Delta\Phi_P)^2 = \frac{\int_0^1 \int_0^{2\pi} \left(\Phi_P - \overline{\Phi_P}\right)^2 \rho d\rho d\theta}{\int_0^1 \int_0^{2\pi} \rho d\rho d\theta}. \tag{2.2.1}$$

Where, $\rho$ is the normalized radial component and $\theta$ is the azimuthal component on the exit pupil. The Strehl ratio $S$ may be written as an approximation as,

$$S(P) \sim 1 - \left(\frac{2\pi}{\lambda}\right)^2 (\Delta\Phi_P)^2 . \tag{2.2.2}$$

Where, $\lambda$ is the wavelength.

The approximate form of the Strehl ratio has an empirical formula given by Mahajan (1983),

$$S(\sigma_\Phi) \approx e^{-\left(\frac{2\pi\sigma_\Phi}{\lambda}\right)^2}. \tag{2.2.3}$$

In Mahajan (1983), it was stated that the exponential form for the Strehl ratio in Eq. (2.2.3) gave a better fit for the primary aberrations. This exponential form is often referred to as the 'Maréchal approximation' of the Strehl ratio. It was later shown in Ross (2009), the exponential form of the Strehl ratio can be derived by assuming the wavefront error can be characterized by a probability density function (PDF) with a Gaussian noise profile.

**Spot Diagrams** : Spot diagrams are a useful tool to check how the rays form an image. A grid of rays are defined entering the entrance pupil. The rays are then traced through the optical system and their final position at a given point is calculated. For an ideal imaging system, parallel rays entering the system will converge to a singular focal point. However, the presence of aberrations will introduce errors in the final position of the ray as ray aberrations which will spread them out. The specific aberration will show a characteristic spot diagram pattern. The combination of aberrations will show complex spot diagrams, but the diagram can be used effectively to quickly identify if particular aberrations show a strong presence (example in Fig. 2.1).

## 2.3 Physical Optics

Physical Optics (PO) is an approximation used for the analysis of electromagnetic fields reflecting at a reflector (Bird, 2015). Considering a reflector, the dimension of a physical reflector is usually much larger than the wavelength of the radiation. A good approximation for the surface currents on the reflector is to assume that on any point on the reflector, the induced current is the same as that on an infinite plane tangent to the point where the surface current is calculated.

If a feed is used to radiate a magnetic field $\mathbf{H_f}$ towards the reflector, the surface current on the reflector is given by,

$$\mathbf{J_s} = 2\hat{n} \times \mathbf{H_f}|_{\text{reflector}\Sigma}. \tag{2.3.1}$$

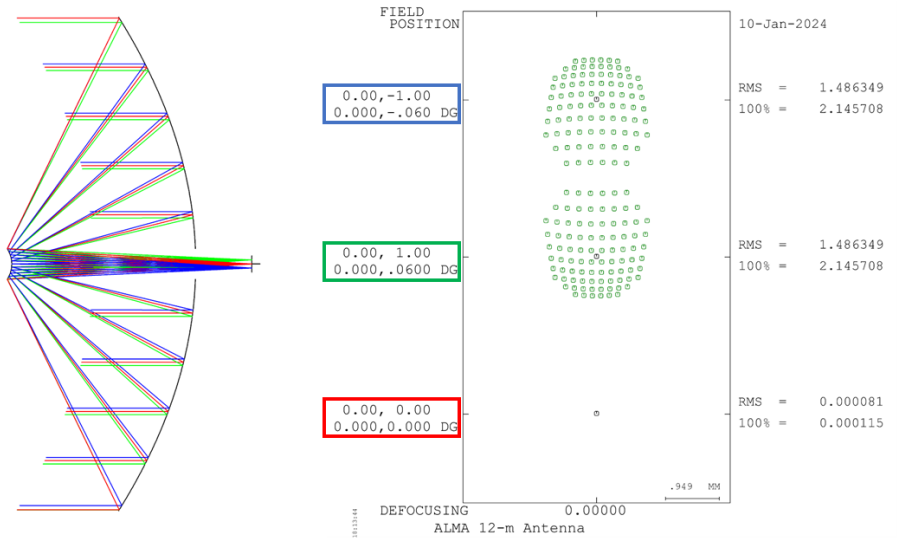


**Fig. 2.1** Example of a spot diagram using ALMA 12-m antenna. The green and blue rays have a 0.06 degree incident angle into the primary. The on-axis rays (red) converge to a singular point because there are no aberrations. The off-axis rays (green, blue) are affected by the field-curvature and are spread out.

Here, $\hat{n}$ is the unit normal vector on the reflector surface $\Sigma$. This is the physical optics approximation. The factor 2 accounts for the incident and reflected fields. The electric fields propagated from the surface currents will be given by,

$$\mathbf{E}(r,\theta,\phi) = -\frac{jk\eta_0}{4\pi}[\mathbf{F}(\theta,\phi) - \hat{r}(\mathbf{F}(\theta,\phi)\cdot\hat{r})], \tag{2.3.2}$$

where,

$$\mathbf{F}(\theta,\phi) = \int_{\Sigma} \mathbf{J_s} \exp{(jk\hat{r}\cdot\mathbf{r}')}\mathrm{d}S'. \tag{2.3.3}$$

The primed variables refer to the coordinates of the source on the surface of the reflector. The vector $\hat{r}$ is the unit vector for the radial component. Equation. (2.3.3) shows a Fourier transform relation.

## 2.4 Figures-of-Merit

### 2.4.1 Aperture Efficiency

The aperture efficiency is used as one main figure-of-merit to evaluate the optical performance of an antenna. The aperture efficiency $\eta_{\mathrm{A}}$ can generally be defined as,

$$\eta_{\mathrm{A}} = \frac{\text{Total power available to receiver}}{\text{Total incident power into the antenna}}.$$

Here, the subscript A denotes the an aperture antenna. The total power incident on an aperture will be proportional to the area. For an antenna with a physical aperture area $A_{\mathrm{phs}}$, the aperture

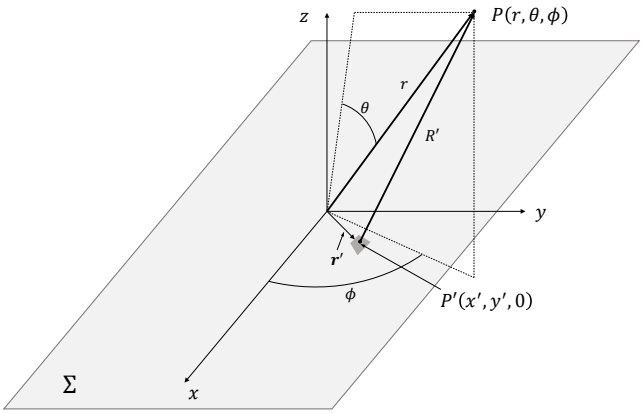


**Fig. 2.2** Coordinate system and calculated radiated fields at an observation point $P$ from an aperture surface currents at point $P'$.

efficiency will be given by,

$$\eta_{\mathrm{A}} = \frac{A_{\mathrm{e}}}{A_{\mathrm{phys}}}, \tag{2.4.1}$$

where, $A_{\mathrm{e}}$ is the effective aperture area. The directivity $D$ is a measure of an antennas ability to focus radiation towards a particular direction. The gain of the antenna $G$ is a measure of an antenna ability to focus radiation towards a particular direction compared to an ideal isotropic radiation pattern (Balanis, 2016). These two quantities are related by their radiation efficiency $\eta_{\mathrm{rad}}$ when transmitting or from reciprocity, related to their aperture efficiency when receiving. Thus, the gain of the antenna can be written as,

$$G(\theta, \phi) = \eta_{\mathrm{rad}} D(\theta, \phi). \tag{2.4.2}$$

If we denote, $D_{\mathrm{std}}$ as the standard directivity for an aperture type antenna with area $A$ which is defined in the *IEEE Standard for Definitions of Terms for Antennas* as,

$$D_{\mathrm{std}} = \frac{4\pi A}{\lambda^2}. \tag{2.4.3}$$

Equation. (2.4.2) becomes,

$$\eta_{\mathrm{A}} = \frac{G_{\mathrm{peak}}}{D_{\mathrm{std}}}. \tag{2.4.4}$$

Finally, the aperture efficiency of an aperture type antenna can be given by its peak gain as,

$$\eta_{\mathrm{A}} = \frac{G_{\mathrm{peak}} \lambda^2}{16\pi^2 D_{\mathrm{A}}^2}. \tag{2.4.5}$$

Where, $D_{\mathrm{A}}$ is the diameter of the aperture.

### 2.4.2 Quasioptical Theory

At submillimeter frequencies, quasioptical theory is a useful way to describe the propagation of a beam (Goldsmith, 1998). Quasi-optics serves as the intermediate point in terms of approximation complexity when compared to the simple description of geometrical optics and

the propagation described through diffraction integrals. The attractiveness of quasi-optics is it provides a simple and collected way to describe a beams propagation without requiring to solve rigorous diffraction integrals.

The theory of quasi-optics starts at the Helmholtz equation. If we assume a time variation of $\exp(j\omega t)$ where $\omega$ is the angular frequency, the Helmholtz equation will be given by,

$$(\nabla^2 + k^2)\Psi = 0. \tag{2.4.6}$$

Here, $\Psi$ may represent the electric or magnetic field components. We assume the beam has slowly varying amplitude perpendicular to the direction of propagation. We may write a quasi-plane wave trial solution as,

$$\Psi \rightarrow E = u(x, y, z)e^{-jkz}. \tag{2.4.7}$$

Here, $k = 2\pi/\lambda$ where $\lambda$ is the wavelength, and $u(x, y, z)$ is a complex scalar function. Substituting Eq.(2.4.7) into Eq.(2.4.7) we get,

$$\frac{\partial^2 E}{\partial^2 x} + \frac{\partial^2 E}{\partial^2 y} + \frac{\partial^2 E}{\partial^2 z} + k^2 E = 0. \tag{2.4.8}$$

Reducing further we get the reduced wave equation,

$$\frac{\partial^2 u}{\partial^2 x} + \frac{\partial^2 u}{\partial^2 y} + \frac{\partial^2 u}{\partial^2 z} - 2jk\frac{\partial u}{\partial z} = 0. \tag{2.4.9}$$

We assume the the wave amplitude varies slowly along the direction of propagation compared to the wavelength, then the second partial derivative of $z$ can be approximated to be zero. This assumption is referred to as the paraxial approximation. Applying this condition to Eq.(2.4.9) we finally get the paraxial wave equation,

$$\frac{\partial^2 u}{\partial^2 r} + \frac{1}{r}\frac{\partial u}{\partial r} - 2jk\frac{\partial u}{\partial z} = 0. \tag{2.4.10}$$

The solution to the paraxial wave equation is given by,

$$E(r, z) = \left(\frac{2}{\pi w(z)^2}\right)^{0.5} \exp\left(-\frac{r^2}{w(z)^2} - jkz - \frac{j\pi r^2}{\lambda R(z)} + j\phi_0(z)\right). \tag{2.4.11}$$

Here,

$$w(z) = w_0\left[1 + \left(\frac{\lambda z}{\pi w_0^2}\right)^2\right]^{\frac{1}{2}} \tag{2.4.12}$$

$$R(z) = z + \frac{1}{z}\left(\frac{\pi w_0^2}{\lambda}\right)^2 \tag{2.4.13}$$

$$\phi_0(z) = \arctan\left(\frac{\lambda z}{\pi w_0^2}\right). \tag{2.4.14}$$

Are the three parameters that describe the shape of the beam. Equation.(2.4.11) shows a Gaussian envelope in the field amplitude, where the beam radius $w(z)$ is the radius of the beam where

the field amplitude falls to $1/e$ from the on-axis value. This solution is refereed to as a *Gaussian beam*. The radius of curvature $R(z)$ shows the equiphase-fronts of the Gaussian beam follow a spherical shape.

# CHAPTER 3

# Aberrations in Multibeam Receivers

## 3.1 Introduction

This chapter shows the development of software code to calculate the effect of aberrations on aperture efficiency based on the latest theoretical research. The code was then used for an analysis of the ALMA 12-m antenna assuming a multibeam receiver with frequency independent illumination on the sub-reflector.

### 3.1.1 Aberrations in Cassegrain Antennas

A Cassegrain reflector will ideally have a perfect image at the on-axis Cassegrain focus. However, the off-axis positions will suffer from aberrations. The receiver optics will be affected by optical aberrations if they are not situated at the on-axis Cassegrain focus and will have lower aperture efficiency (Dragone, 1982). This is true for both single-beam receivers and multibeam receivers. The effect of aberrations are a critical aspect to consider for any array receiver. Padman introduced some basic equations for the Seidel aberrations (primary aberrations) for a Cassegrain antenna in Padman (1995). The effect of aberrations are in general frequency dependent because they represent the distorted wavefront of the incident wave which will have a different phase angle depending on the frequency.

Lamb (1999) derived some estimations for degradation of aperture efficiency due to aberrations for the ALMA 12-m antenna. Here, the estimations were based on a uniform aperture illumination from a feed which is a not a general case (especially for broadband feeds). These formulas were used as an initial figure-of-merit in Lamb et al. (2001) for the initial calculations to determine the requirements for the receiver optics in the ALMA antenna during the design stage. Imada and Nagai (2020) showed the comprehensive analysis of the effect of aberrations on aperture efficiency.

If we wish to design a multibeam receiver with aperture efficiency near identical to single-beam receivers, we must consider and analyze individual pixels comprehensively. Accordingly, a more up-to-date evaluation of the effect of aberrations on aperture efficiency is necessary and may also give better insight on how to better design high-efficiency receiver optics for multibeam receivers. Thus, we require a method to rapidly calculate the effect of aberrations on aperture efficiency for different optical settings including feed patterns, feed positions, and frequencies.

## 3.2 Method

### 3.2.1 Aperture Efficiency Affected by Aberrations

The theory from Imada and Nagai (2020) served as the basis of the software code developed here. The key principles, equations, and methods from Imada and Nagai (2020) are briefly summarized from Section. 3.3.2 to Section. 3.2.4. The implementation in software code (MATLAB) is later shown in Section. 3.3.

It was shown in Imada and Nagai (2020) that two fields are needed to define the aperture efficiency as shown in Fig. 3.1. First is an incident wave in to the antenna, the other is a feed pattern. It was then shown that aperture efficiency can be split into three factors Nagai et al. (2021), the spill-over efficiency at the entrance pupil, the spill-over efficiency at the exit pupil, and the beam coupling efficiency.

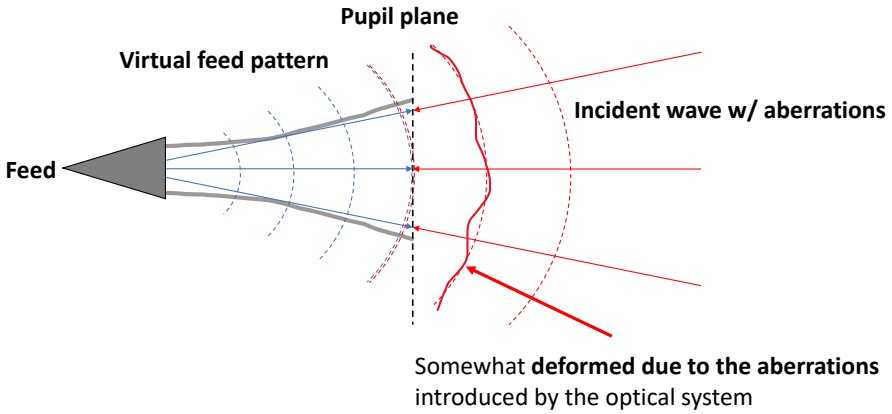


**Fig. 3.1** A diagram showing the feed pattern and incident wave (with aberrations) necessary for calculating aperture efficiency

### 3.2.2 System Setting

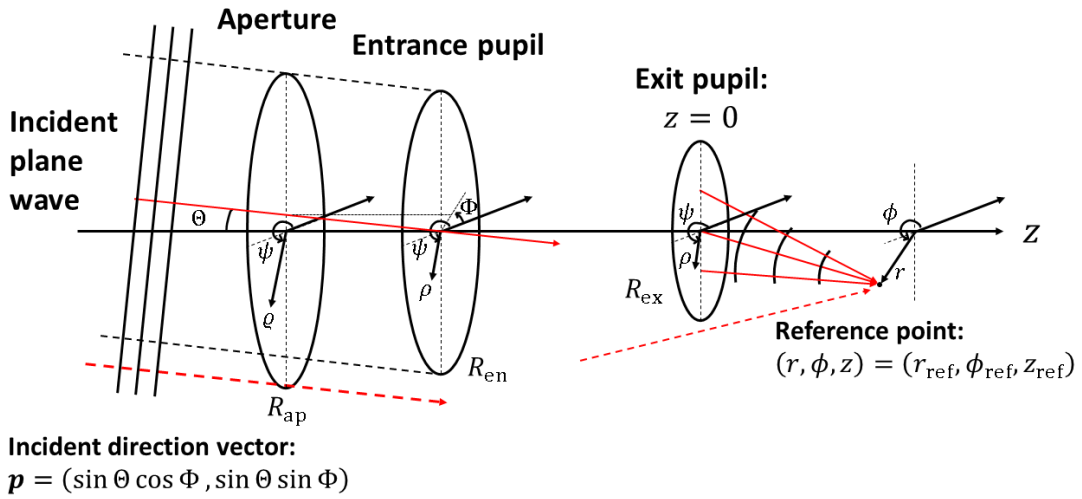


**Fig. 3.2** A modified diagram of Fig. 1 from Imada and Nagai (2020) showing the coordinate system setting.

The telescope optical system with a focal length $f$ and coordinate system in Fig. 3.2 is assumed. The optical system consists of an aperture, entrance and exit pupil, and an arbitrary reference plane (or the focal plane). The optical system is assumed as a cylindrically symmetric system with the exit pupil set as the system origin. The aperture radius is denoted $R_{\text{ap}}$ and the entrance and exit pupils are denoted $R_{\text{en}}$ and $R_{\text{ex}}$ respectively. An image is evaluated at a reference point with cylindrical coordinates $(r, \phi, z) = (r_{\text{ref}}, \phi_{\text{ref}}, z_{\text{ref}})$. The incident wave is assumed to be a plane wave incident with an incident and azimuthal angle of $(\Theta, \Phi)$. A point on the aperture and pupils have the polar coordinates $(\varrho, \psi)$ and $(\rho, \psi)$, respectively. The normalized radial component has a range of $\varepsilon \leq \rho \leq 1$, where $0 \leq \varepsilon \leq 1$ is the blockage. The vectors $\boldsymbol{p} = (\sin\Theta\cos\Phi, \sin\Theta\sin\Phi)$, $\boldsymbol{\varrho} = (\varrho, \psi)$, $\boldsymbol{\rho} = (\rho, \psi)$, and $\boldsymbol{r}_{\text{ref}} = (r_{\text{ref}}, \phi_{\text{ref}}, z_{\text{ref}})$ are defined for convenience.

### 3.2.3 Incident Wave

#### 3.2.3.1 Reference Wave

A uniform plane wave is incident into the optical system at an angle of $(\theta_{\text{inc}}, \Phi_{\text{inc}})$. The incident plane wave at the aperture and the entrance pupil can be written as,

$$E_{\text{ap}}(\boldsymbol{p}; \boldsymbol{\varrho}) = \frac{1}{\sqrt{\pi} R_{\text{ap}}} \exp[jkR_{\text{ap}}\varrho\sin\Theta\cos(\psi - \Phi)]. \tag{3.2.1}$$

$$E_{\text{en}}(\boldsymbol{p}; \boldsymbol{\rho}) = \frac{R_{\text{en}}}{\sqrt{\pi} R_{\text{ap}} R_{\text{ex}}} \exp[jkR_{\text{ap}}\rho\sin\Theta\cos(\psi - \Phi)]. \tag{3.2.2}$$

When there are no aberrations, an optical system will transform the plane wave into a spherical wave centered at an image point. This ideal center point may be set as a reference to measure how the wavefront aberrations causes deviations in the final image position. When the paraxial

approximation holds, the reference point $(r_{\rm ref}, \phi_{\rm ref}, z_{\rm ref})$ will have a radius measured from the exit pupil as,

$$\begin{aligned} R_{\rm ref} &= \sqrt{r_{\rm ref}^2 + z_{\rm ref}^2} \\ &\approx z_{\rm ref}. \end{aligned} \tag{3.2.3}$$

Then, a spherical wave centered at a reference point can be written as,

$$E_{\rm sph}(\boldsymbol{\rho}; \boldsymbol{r}_{\rm ref}) = \exp\left[-R_{\rm ex}\rho \sin\theta_{\rm ref} \cos\left(\psi - \phi_{\rm ref}\right) - \frac{R_{\rm ex}^2 \rho^2}{2 z_{\rm ref}}\right]. \tag{3.2.4}$$

Here, $(\rho, \psi)$ are the normalized components on the pupil.

### 3.2.3.2 Wavefront Aberrations

The wavefront aberrations are the optical-path-difference between the reference sphere and the incident wavefront (Fig. 3.3). Wavefront aberrations can be expanded into a series with an appropriate orthonormal basis. A commonly used one is the Zernike polynomials defined as the orthogonal set of functions on the unit circle[1] Mahajan (1981),

$$W(\boldsymbol{p}; \boldsymbol{\rho}; \boldsymbol{r}_{\rm ref}) = \sum_{m,n} A_n^m(\boldsymbol{p}; \boldsymbol{r}_{\rm ref}) Z_n^m(\boldsymbol{\rho}; \varepsilon), \tag{3.2.5}$$

where $m$ and $n$ are integers which must satisfy $n \geq |m|$ and $n - |m|$ is even. The coefficients for each term describes the magnitude of the individual aberrations and they depend on the incident angle of the wave into the antenna and the reference position.

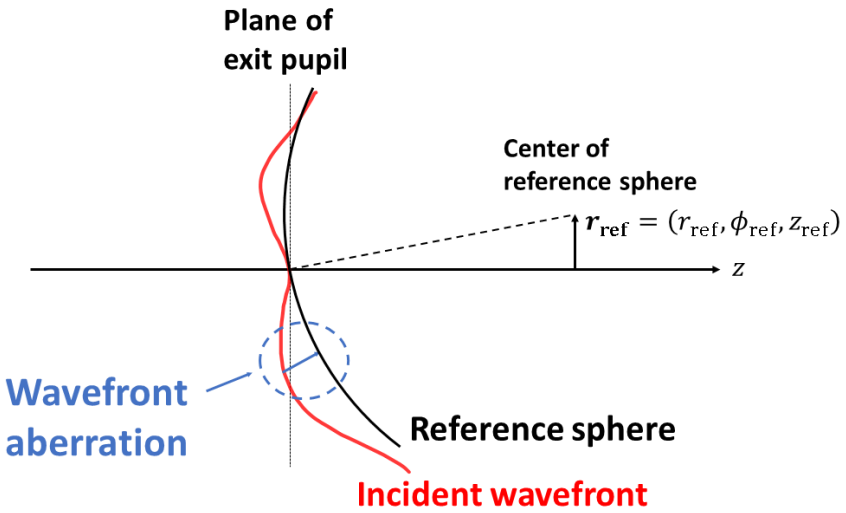


**Fig. 3.3** Diagram describing the relation between the incident wave, the reference sphere, and the wavefront aberrations.

[1]The wavefront aberrations expanded into a series of Zernike annular polynomials were also expanded into a Taylor series in Imada and Nagai (2020).

#### 3.2.3.3 Incident Wave at Exit Pupil

The incident wave is assumed to be a spherical wave centered at a reference point given by Eq. (3.2.4) with small aberrations given by Eq. (3.2.5). Finally, the incident wave into the antenna at the exit pupil $E_{\text{ex}}$ can be written as,

$$E_{\text{ex}}(\boldsymbol{p};\boldsymbol{\rho}) = \frac{R_{\text{en}}}{\sqrt{\pi}R_{\text{ap}}R_{\text{ex}}} E_{\text{sph}} \exp\left(-jkW\right). \tag{3.2.6}$$

### 3.2.4 Feed Pattern

A feed pattern is needed to calculate the aperture efficiency. A Common first approximation is a quasioptical Gaussian beam described with Gaussian-Laguerre beam modes Goldsmith (1998). A feed containing only the fundamental Gaussian beam mode with a beam waist $w_{\text{bw}}$ at a position $\boldsymbol{r}_{\text{bw}} = (r_{\text{bw}}, \phi_{\text{bw}}, z_{\text{bw}})$ will have a feed pattern $E_{\text{det}}(\boldsymbol{\rho}, \boldsymbol{r}_{\text{bw}}; w_{\text{bw}})$ as,

$$E_{\text{det}}(\boldsymbol{\rho};\boldsymbol{r}_{\text{bw}};w_{\text{bw}}) = \sqrt{\frac{2}{\pi}}\frac{1}{w(z')} L_0^0\left(\frac{2r'^2}{w^2(z')}\right) \cdot \exp\left[-\frac{r'^2}{w^2(z')} - jk(z'-z'_{\text{bw}}) - \frac{j\pi r'^2}{\lambda R(z')} - j\phi_0(z')\right], \tag{3.2.7}$$

where, the beam radius $w(z)$, radius of curvature $R(z)$, and phase slippage $\phi_0(z)$ are given as,

$$w(z) = w_0\left[1 + \left(\frac{\lambda z}{\pi w_0^2}\right)^2\right]^{\frac{1}{2}} \tag{3.2.8}$$

$$R(z) = z + \frac{1}{z}\left(\frac{\pi w_0^2}{\lambda}\right)^2 \tag{3.2.9}$$

$$\phi_0(z) = \arctan\left(\frac{\lambda z}{\pi w_0^2}\right). \tag{3.2.10}$$

Here, $L_p^m$ is the Laguerre polynomial, the primed coordinates are the coordinates along the beam axis tilted by $\theta_{\text{bw}}$ with an azimuthal angle $\phi_{\text{bw}}$ from the $z$-axis given by,

$$\begin{cases} x' = x\cos\theta_{\text{bw}}\cos\phi_{\text{bw}} + y\cos\theta_{\text{bw}}\sin\phi_{\text{bw}} - z\sin\theta_{\text{bw}} \\ y' = -x\sin\phi_{\text{bw}} + y\cos\phi_{\text{bw}} \\ z' = x\sin\theta_{\text{bw}}\cos\phi_{\text{bw}} + y\sin\theta_{\text{bw}}\sin\phi_{\text{bw}} + z\cos\theta_{\text{bw}}. \end{cases} \tag{3.2.11}$$

### 3.2.5 Aperture Efficiency

The aperture efficiency is split into three factors: Spill-over efficiency at the entrance pupil, spill-over efficiency at the exit pupil, and the beam coupling efficiency at the exit pupil according to Nagai et al. (2021). The beam coupling efficiency is evaluated at the exit pupil.

$$\eta_{\text{A}} = \eta_{\text{spill, en}}\eta_{\text{spill, ex}}\eta_{\text{bcp}}. \tag{3.2.12}$$

Here,

$$\eta_{\text{spill, en}}(\boldsymbol{p};\varepsilon) = \frac{R_{\text{en}}^2 \int_\varepsilon^1 \mathrm{d}\rho \int_0^{2\pi} \mathrm{d}\psi |E_{\text{en}}(\boldsymbol{p};\boldsymbol{\rho})|^2}{R_{\text{ap}}^2 \int_\varepsilon^1 \mathrm{d}\varrho \int_0^{2\pi} \mathrm{d}\psi \varrho |E_{\text{ap}}(\boldsymbol{p};\boldsymbol{\varrho})|^2} \cos\Theta, \tag{3.2.13}$$

$$\eta_{\text{spill, ex}}(\boldsymbol{r}_{\text{bw}}, w_{\text{bw}};\varepsilon) = \frac{\int_\varepsilon^1 \mathrm{d}\rho \int_0^{2\pi} \mathrm{d}\psi \rho |E_{\text{det}}(\boldsymbol{\rho};\boldsymbol{r}_{\text{bw}})|^2}{\int_\varepsilon^\infty \mathrm{d}\rho \int_0^{2\pi} \mathrm{d}\psi \rho |E_{\text{det}}(\boldsymbol{\rho};\boldsymbol{r}_{\text{bw}})|^2}, \tag{3.2.14}$$

and,

$$\eta_{\text{bcp}}(\boldsymbol{p};\boldsymbol{r}_{\text{bw}}) = \frac{\left| \int_\varepsilon^1 \mathrm{d}\rho \int_0^{2\pi} \mathrm{d}\psi \rho E_{\text{ex}}(\boldsymbol{p};\boldsymbol{\rho}) E_{\text{det}}^*(\boldsymbol{\rho};\boldsymbol{r}_{\text{bw}}) \right|^2}{\left( \int_\epsilon^1 \mathrm{d}\rho \int_0^{2\pi} \mathrm{d}\psi \rho |E_{\text{ex}}(\boldsymbol{p};\boldsymbol{\rho})|^2 \right) \left( \int_\epsilon^1 \mathrm{d}\rho \int_0^{2\pi} \mathrm{d}\psi \rho |E_{\text{det}}(\boldsymbol{\rho};\boldsymbol{r}_{\text{bw}})|^2 \right)}. \tag{3.2.15}$$

## 3.3 Development of Software Code

### 3.3.1 Implementation

The system setting from Imada and Nagai (2020) can be applied to the ALMA antenna. Here, the key methods and basic equations from Imada and Nagai (2020) were developed into a software code to calculate the aperture efficiency with the effect of aberrations for the ALMA 12-m antenna.

### 3.3.2 System Setting for ALMA 12-m Antenna

The ALMA 12-m antenna is set as the optical system. The ALMA 12-m antenna is a Cassegrain antenna consisting of a 12-m parabolic primary reflector and a 0.75 m hyperbolic reflector. The important parameters of the antenna are summarized in Table. 3.1. If there are no additional optics in the system besides the antenna, the sub-reflector (secondary reflector), in most cases, acts as an aperture stop and as the exit pupil in a radio telescope. The ALMA 12-m antenna is designed to have the on-axis rays at the edge of the primary reflector reflect at the edge of the sub-reflector both can acting as a stop. For off-axis rays, the sub-reflector acts as the aperture stop in the system.

A diagram of the optical system considered here is shown in Fig. 3.8. The exit pupil can then be set as the origin of the optical system. Here, The sub-reflector vertex is set as the system origin and we assume a cylindrical coordinate system in $(r, \phi, z)$, where $r$ is the radial component, $\phi$ is an azimuthal component, and $z$ is the axial component with the positive direction perpendicular to the sub-ref vertex. The entrance and exit pupils have a radius $R_{\text{en}}$ and $R_{\text{ex}}$ respectively.

### 3.3.3 Ray Tracing Software

Modern commercial ray tracing software can not only be used for optical design, but also for various optical analyses. Here, the commercially available ray tracing software CODE V

**Table 3.1** Parameter list of ALMA 12m antenna geometry.

| Parameter name | Label | Value |
|---|---|---|
| Primary reflector diameter | $D_{\rm p}$ | 12 [m] |
| Secondary reflector diameter | $D_{\rm s}$ | 0.75 [m] |
| Primary reflector focal distance | $f_{\rm p}$ | 4.8 [m] |
| Secondary reflector focal distance | $f_{\rm s}$ | 6.177 [m] |
| Equivalent focal distance | $f_{\rm eq}$ | 96 [m] |
| Magnification | $M$ | 20 |
| Primary vertex to secondary vertex distance | $d_{\rm p}$ | 4.506 [m] |
| Secondary vertex to Cassegrain focus distance | $d_{\rm s}$ | 5.883 [m] |

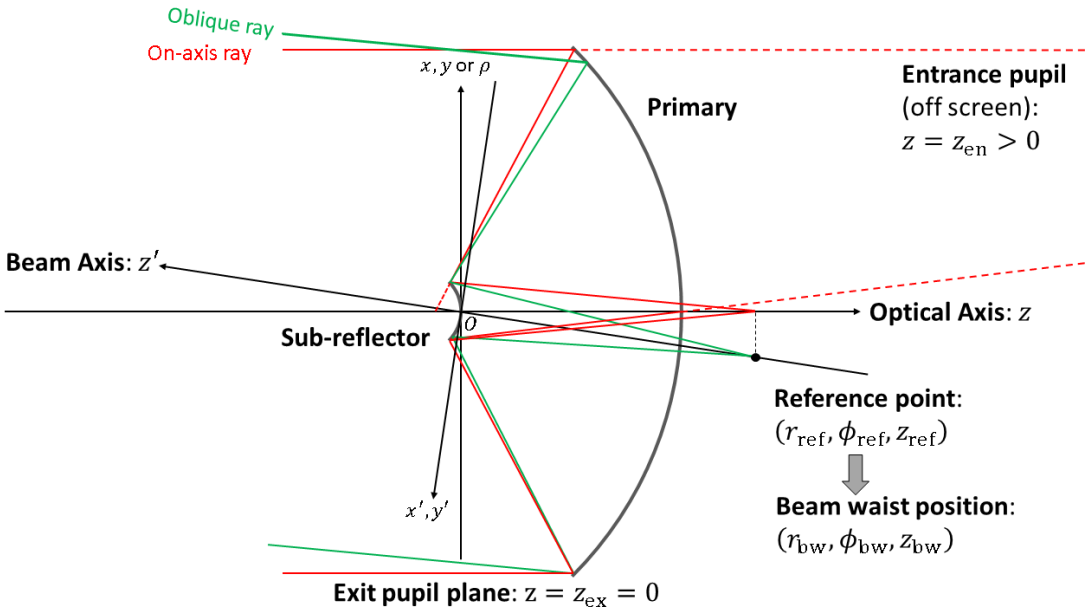


**Fig. 3.4** A diagram of the ALMA 12-m antenna and the system setting in this analysis.

ver. 2023.03[2] was used for the modeling of the optical system and the analysis of aberrations.

CODE V defines the direction of the rays entering the system with two field angles, the X-angle (XAN) and the Y-angle (XAN) shown in Fig. 3.5. The coordinate system in Imada and Nagai (2020) can be converted to the field angles used in CODE V as,

$$\begin{cases} \tan \mathrm{XAN} &= \tan\theta_{\rm inc}\sqrt{1-\frac{1}{1+\tan^2\phi_{\rm inc}}} \\ \tan \mathrm{YAN} &= \frac{\tan\theta_{\rm inc}}{\sqrt{1+\tan^2\phi_{\rm inc}}}. \end{cases} \tag{3.3.1}$$

[2]https://www.synopsys.com/optical-solutions/codev.html

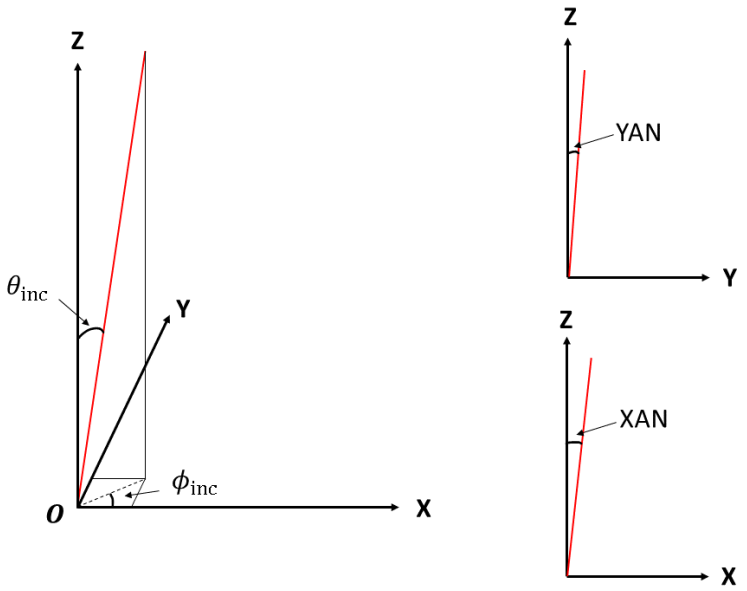


**Fig. 3.5** Conversion between incident angles $(\theta_{\text{inc}}, \phi_{\text{inc}})$ from Imada and Nagai (2020) and field angles in CODE V.

CODE V has various analysis tool that can be utilized. Here, the pupil map analysis tool was used to take the wavefront at the exit pupil and expand it into a series of Zernike polynomials (Fig. 3.6). An image position can be set using the same reference point.

The ALMA 12-m antenna was modeled in CODE V and is shown in Fig. 3.7. A reference point is set using a given incident angle into the primary reflector. The reference point radial coordinate and azimuthal coordinate can be given by the incident angle. However, due to the large thickness (depth) of the primary and sub-reflector, the Gaussian image point will not coincide with the Cassegrain focus of the telescope.

### 3.3.4 Feed Pattern

A radio telescope often specifies the illumination pattern on the sub-reflector from the feed. A Gaussian beam will produce a truncated Gaussian illumination given by a truncation edge taper level $T_{\text{e}}$ in dB defined as,

$$T_{\text{e}}(\text{dB}) = -10 \log_{10} \left[ \exp \left( -\frac{2r_{\text{sub}}^2}{w_{\text{sub}}^2} \right) \right]. \tag{3.3.2}$$

Here, $r_{\text{sub}}$ is the sub-reflector radius and $w_{\text{sub}}$ is the beam radius at the sub-reflector. Thus, the beam radius can be obtained with a fixed edge taper value with the relation,

$$w_{\text{sub}} = \sqrt{\frac{20 r_{\text{sub}}^2}{T_{\text{e}} \log 10}}. \tag{3.3.3}$$

The beam waist of a Gaussian beam may be determined by knowing the beam radius $w$ and

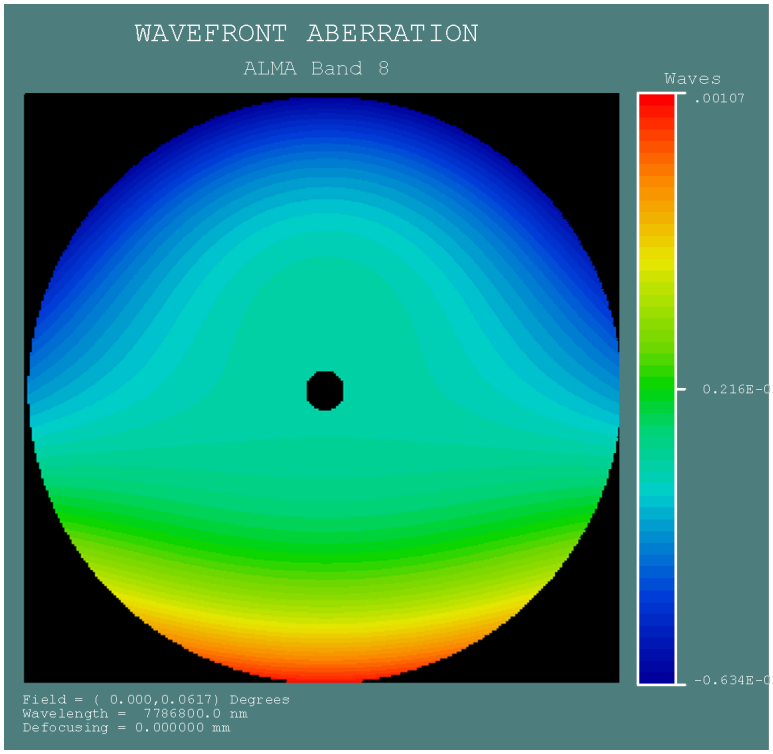


**Fig. 3.6** Pupil map of wavefront aberrations in CODE V for ALMA 12-m antenna using ALMA band 8 position. The color map and corresponding scale shows the deviation from the reference sphere given by the number of wavelengths in nm (7.787e+06 nm for 385 GHz).

radius of curvature of the beam $R$ at an arbitrary position.

The curvature center of the beam wavefront can be set to match the reference sphere center to fix $R$. Thus, the radius of curvature of the beam at the sub-reflector $R_{\text{sub}}$ will be equal to the reference sphere radius given by Eq. (3.2.3) as,

$$R_{\text{sub}} = z_{\text{ref}}. \tag{3.3.4}$$

The beam waist and beam waist position can be derived using Eq. (3.3.3) and Eq. (3.3.4) with the relation,

$$\begin{cases} w_{\text{bw}} = \dfrac{w_{\text{sub}}}{\sqrt{1+\left(\frac{\pi w_{\text{sub}}^2}{\lambda R_{\text{sub}}}\right)^2}} \\ z_{\text{bw}} = \dfrac{R_{\text{sub}}}{1+\left(\frac{\lambda R_{\text{sub}}}{\pi w_{\text{sub}}^2}\right)^2}, \end{cases} \tag{3.3.5}$$

where $\lambda$ is the wavelength.

When the incident wave is incident at an oblique angle $(\theta_{\text{inc}}, \Phi_{\text{inc}})$ from the antenna center axis, the reference point will have a non-zero radial component $r_{\text{ref}}$. The angle between the reference point and the exit pupil will be given by $\theta_{\text{ref}} = \text{atan}(r_{\text{ref}}/z_{\text{ref}})$. The beam axis is rotated to match the angle between the antenna center axis and reference position,

$$\theta_{\text{bw}} = \pi - \theta_{\text{ref}}. \tag{3.3.6}$$

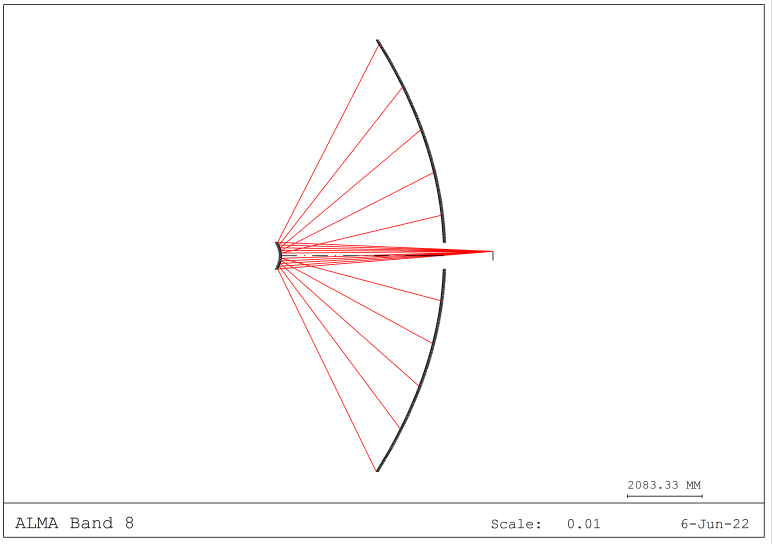


**Fig. 3.7** The ALMA 12-m antenna modeled in CODE V. The incident angle is set to match the ALMA band 8 receiver position.

A feed pattern containing only a fundamental Gaussian beam is considered. The ALMA 12-m antenna has a sub-reflector with a diameter of 750 mm (radius $r_{\text{sub}} = 375$ mm). The beam radius at different edge taper levels are shown in Fig. 3.9. Here, the edge taper was set to 10.9 dB since the theoretical maximum aperture efficiency is given at this value. The beam waist position was derived using Eq. (3.3.5).

### 3.3.5 Calculation Setup

A set of inputs are defined for the calculation according to the variables from Section. 3.2. The input variables are summarized in Table. 3.2. Here, the incident angles determines the reference point coordinates. The final outputs are the Aperture Efficiency $\eta_{\text{A}}$ at a given beam waist position $(r_{\text{bw}}, \phi_{\text{bw}}, z_{\text{bw}})$ and frequency, and the Strehl ratio $S$ at a given reference position $(r_{\text{ref}}, \phi_{\text{ref}}, z_{\text{ref}})$ and frequency, and beam waist $w_{\text{bw}}$.

**Table 3.2** List of input and output variables.

| Variable name (Unit) | Relevant label in code | Description |
|---|---|---|
| Center frequency (GHz) | f_c | Center frequency in range |
| Fractional bandwidth | FBW | Fractional bandwidth |
| Frequency points | nfreq | Number of frequency points in range |
| Grid spacing | xspacing, yspacing | number of points to calculate in grid |
| Incident angles (deg) | XAN, YAN | Incident angles for CODE V, |
| Illumination edge taper (dB) | input_Te | Edge taper of Gaussian beam |

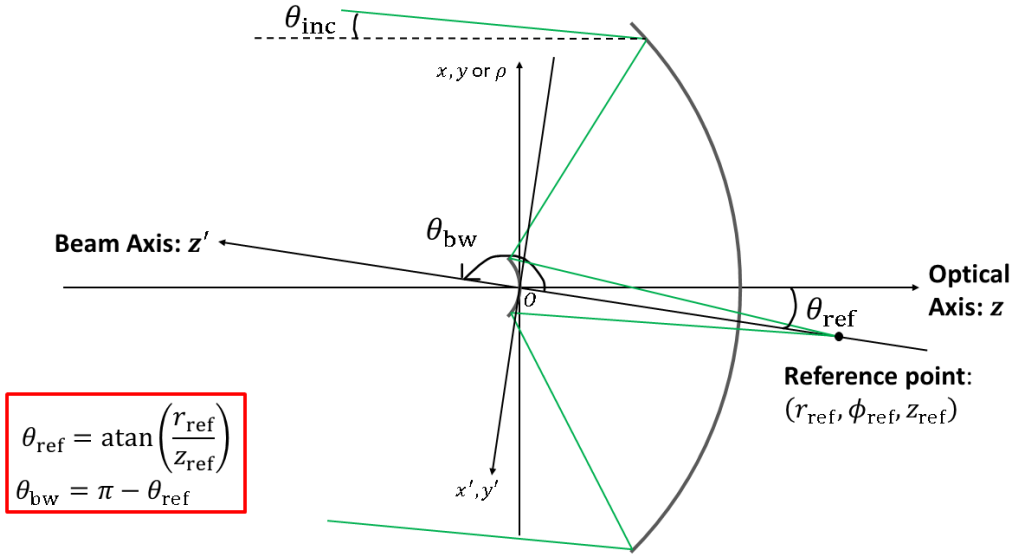


**Fig. 3.8** A diagram of the ALMA 12-m antenna and the system setting in this analysis.

## 3.4 Analysis of ALMA 12m Antenna

### 3.4.1 Feed Placed On-Axis

The reference point was set at the on-axis Cassegrain focus with $z_{\rm ref} = 5882.813$ mm. The aperture efficiency and Strehl ratio at 35, 442, and 950 GHz are summarized in Table. 3.3.

**Table 3.3** On-axis aperture efficiency and Strehl ratio.

| Frequency (GHz) | $\eta_{\rm A}$ | SR | $z_{\rm bw}$ | $w_{\rm bw}$ |
|---|---|---|---|---|
| 35 (GHz) | 0.8034 | 1.0000 | 5764.7118 | 4.3991 |
| 442 (GHz) | 0.8034 | 1.0000 | 5882.0569 | 4.3991 |
| 950 (GHz) | 0.8034 | 1.0000 | 5882.6489 | 4.3991 |

### 3.4.2 Reference Placed Along Focal Plane

The reference point was moved laterally along the focal plane from the Cassegrain focus at a fixed reference position of $z_{\rm ref} = 5882.813$ mm to calculate the aperture efficiency of the antenna and the Strehl ratio. The receiver beam at the sub-reflector is fixed with the edge taper value.

Effectively, this is calculating the illumination from a single-beam receiver at different positions along the focal plane. Consequently, this is also simulating the same situation as frequency independent illumination at the sub-reflector Goldsmith (1998), but is not specifying any receiver optics and treating it as a black-box.

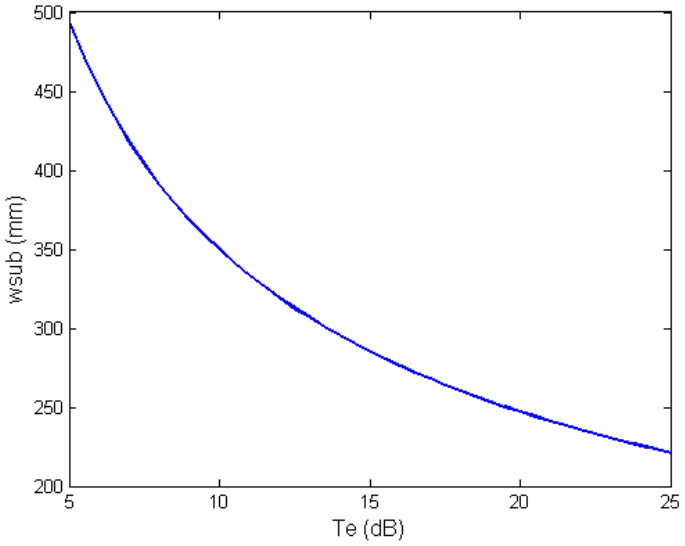


**Fig. 3.9** Beam radius at sub-reflector $w_{\text{sub}}$ for different edge taper values $T_{\text{e}}$.

### 3.4.2.1 Frequency Dependence

The aperture efficiency and Strehl ratio was calculated at three bands with 50 % fractional bandwidth with center frequencies $f_c = 30, 300$, and $1000$ GHz. The frequency dependence was checked at two positions: the reference point positioned $r_{\text{ref}} = 100$ mm and $300$ mm away laterally from the Cassegrain focus. The aperture efficiencies and Strehl ratios are shown in Fig. 3.10 for $r_{\text{ref}} = 100$ mm and Fig.3.11 for $r_{\text{ref}} = 300$ mm.

The aperture efficiency and Strehl ratio in Fig. 3.10 both have a small frequency dependent degradation to them due to the effect of aberrations. Notably, the degradation of Strehl ratio does not return the same degradation in aperture efficiency. The frequency dependence becomes much stronger as expected at $r_{\text{ref}} = 300$ mm as shown in Fig. 3.11.

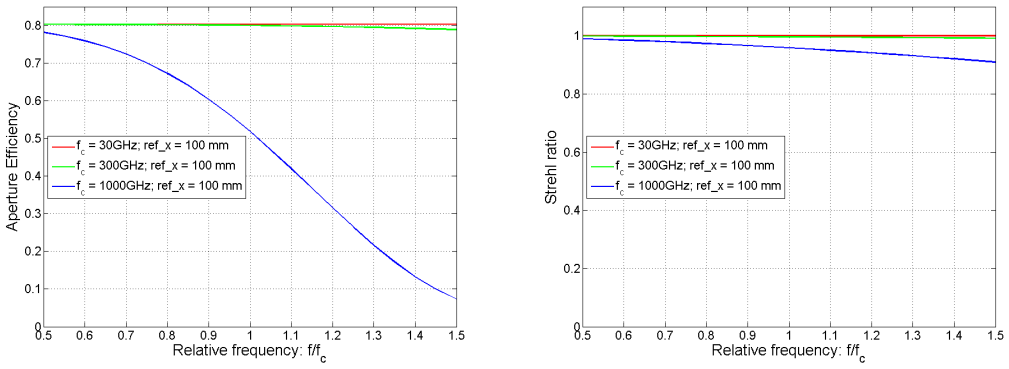


**Fig. 3.10** Aperture efficiency and Strehl ratio at different frequencies at $r_{\text{ref}} = 100$ mm.

### 3.4.2.2 Positional Dependence

Three frequency points 35 GHz, 442 GHz, and 950 GHz are fixed and serve as a reference to compare the effect of aberrations at the lowest, highest, and a frequency in-between the two, for

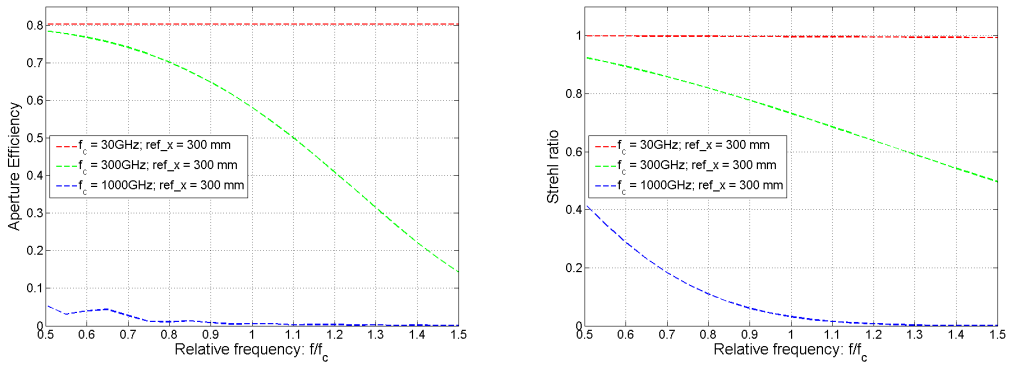


**Fig. 3.11** Aperture efficiency and Strehl ratio at different frequencies at $r_{\text{ref}} = 300$ mm.

ALMA. These three frequency point correspond to the lowest frequency in ALMA band 1, the center frequency in ALMA band 8, and the highest frequency in ALMA band 10 respectively. The reference point was moved laterally $\pm 300$ mm from the nominal Cassegrain focus of the antenna. Positional dependence of aperture efficiency and Strehl ratio for the three frequencies are shown in Fig. 3.12. The cross-sections along the x-axis are shown in Fig. 3.13.

It can be seen that aberrations have little to no effect at lower frequencies. This can be explained simply as the wavefront errors become smaller compared to the wavelength thus having minimal effect on the mismatch between the phase of the incident wave and feed pattern. At the higher frequencies the effect of aberrations become much more significant due the the wavefront errors having a comparable size to the wavelength causing more phase deviation.

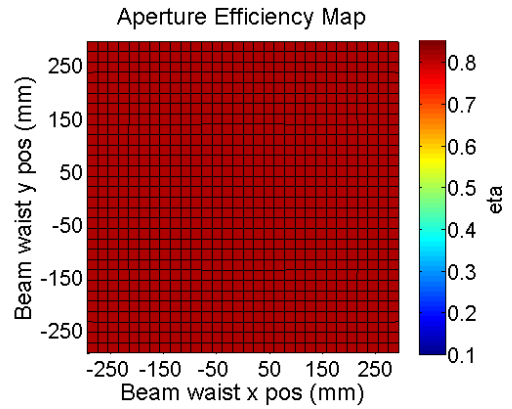


**(a)** $\eta_A$ at 35 GHz

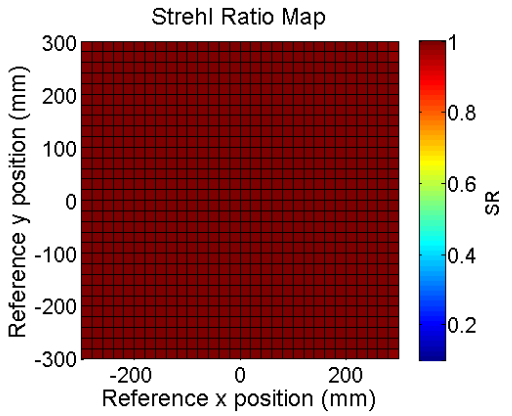


**(b)** Strehl ratio at 35 GHz

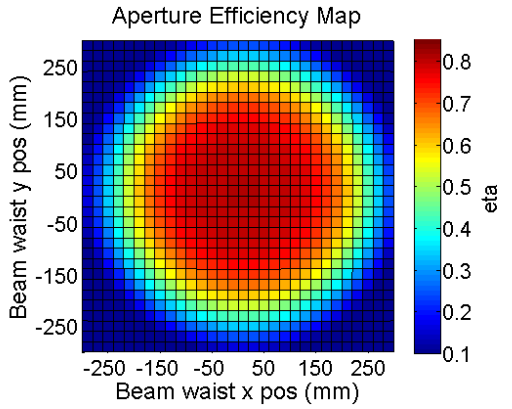


**(c)** $\eta_A$ at 442 GHz

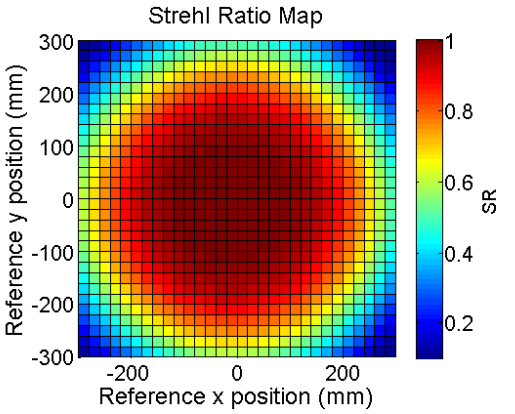


**(d)** Strehl ratio at 442 GHz

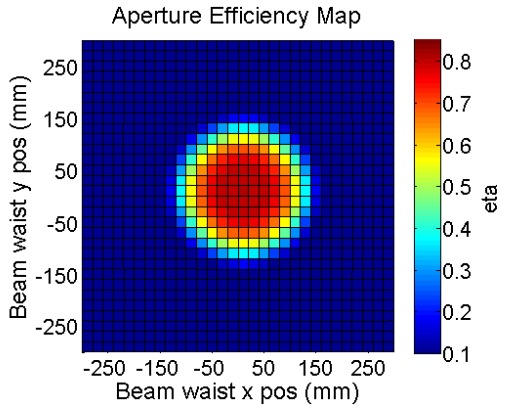


**(e)** $\eta_A$ at 950 GHz

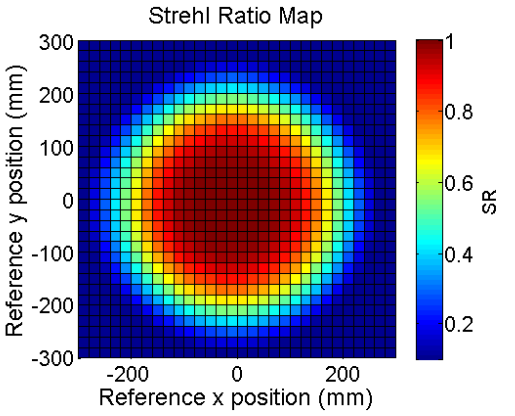


**(f)** Strehl ratio at 950 GHz

**Fig. 3.12** The aperture efficiency and Strehl ratio distributions along the focal plane. The left column shows the aperture efficiency distribution. The right column shows the Strehl ratio distribution.

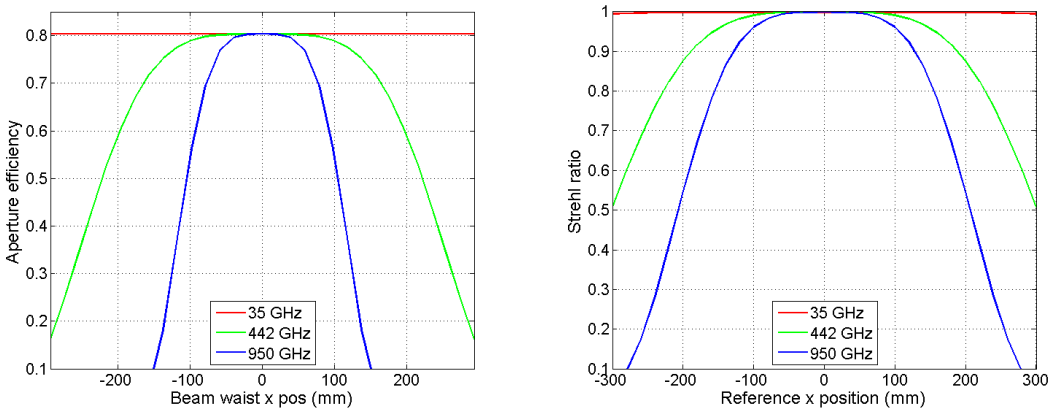


**(a)** Cross-section of $\eta_A$

**(b)** Cross-section of SR

**Fig. 3.13** Cross-section of aperture efficiency and Strehl ratio distribution along the x-axis on the focal plane.

### 3.4.3 Reference Axially Repositioned

The focus position of the antenna will change depending on the incident angle. Thus a simple lateral offset from the Cassegrain focus will start to deviate from this position resulting in defocusing effects. The reference point may be axially re-positioned onto the antenna focus for a given position to eliminate the defocusing effects.

The reference position considering the field curvature can be approximated by using the Petzval surface Born et al. (1999), or by using ray tracing software. Here, CODE V was used to obtain the axial movement $\Delta z_{\text{ref}}$ to reposition the reference point onto the best focus position (Where the transverse ray aberrations are minimized) which will be referred to as the ”off-axis Cassegrain focus” (Fig. 3.15).

The radius of curvature of the beam will be given by the adjusted reference position as $R_{\text{sub}} = z_{\text{ref}} + \Delta z_{\text{ref}}$, which will return a corresponding beam waist position given by Eq. (3.3.5).

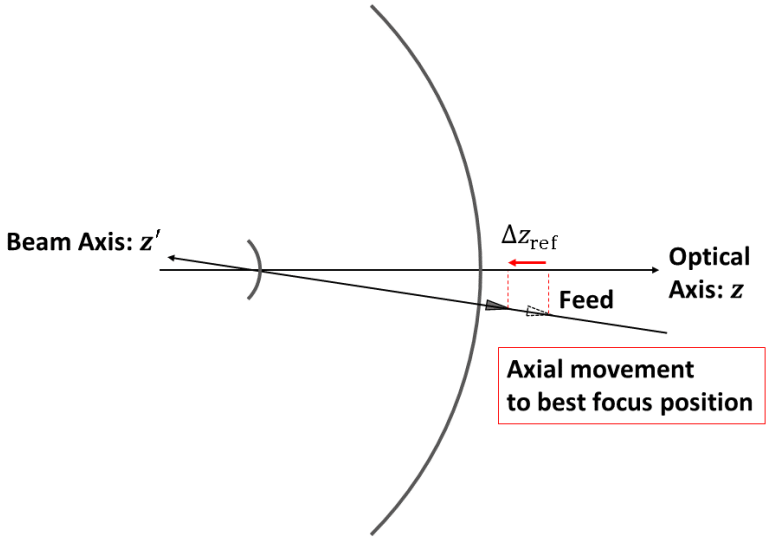


**Fig. 3.14** Diagram of the axial repositioning of the feed to the focus.

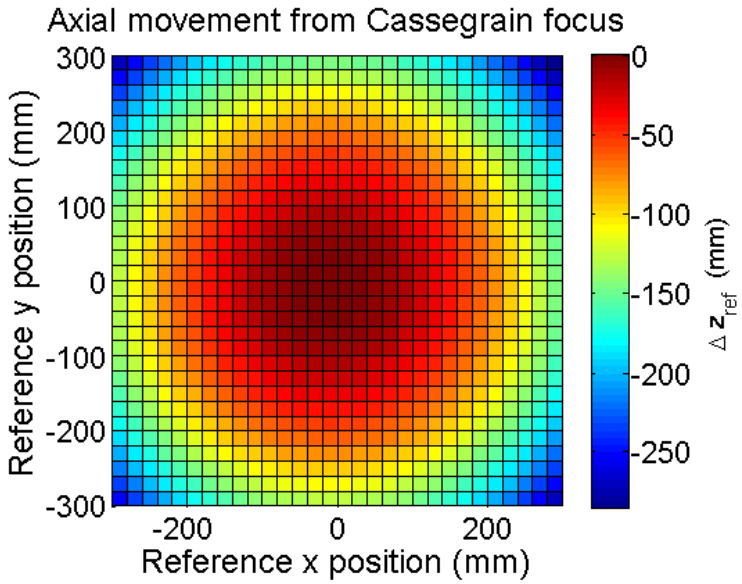


**Fig. 3.15** Axial adjustment for reference position from plane containing Cassegrain focus to eliminate defocus. Each position has a different incident angle and a corresponding amount of axial defocus.

### 3.4.3.1 Frequency Dependence

The aperture efficiency and Strehl ratio calculated with the repositioned reference point (and corresponding beam waist position) to the off-axis Cassegrain focus with $r_{\text{ref}} = 100$ mm is shown in Fig. 3.16 and $r_{\text{ref}} = 300$ mm is shown in Fig. 3.17.

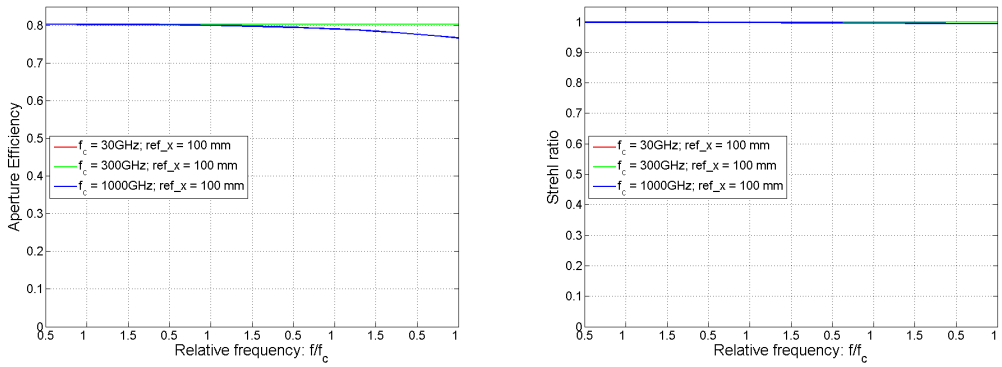


**Fig. 3.16** Aperture efficiency and Strehl ratio at different frequencies at $r_{\text{ref}} = 100$ mm and axial repositioning.

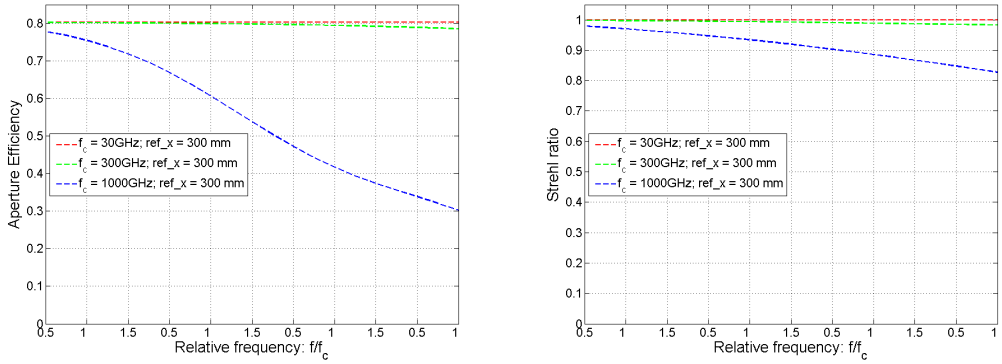


**Fig. 3.17** Aperture efficiency and Strehl ratio at different frequencies at $r_{\text{ref}} = 300$ mm and axial repositioning.

### 3.4.3.2 Positional Dependence

The aperture efficiency and Strehl ratio were calculated with the axial repositioning of the feed and are shown in Fig. 3.18. The cross sections along the x-axis are shown in Fig. 3.19.

It is evident that the defocusing effects were the most dominant aberration term in the system. By adjusting the feed to eliminate the defocus, the effect of aberrations are minimal on the aperture efficiency, both for their frequency dependence and positional dependence.

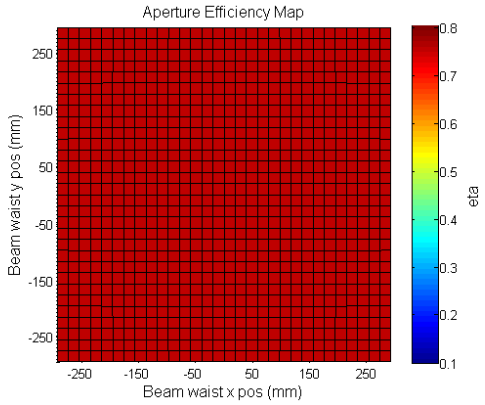


**(a)** $\eta_A$ at 35 GHz

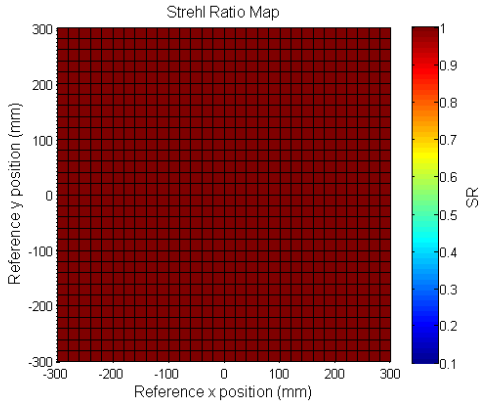


**(b)** Strehl ratio at 35 GHz

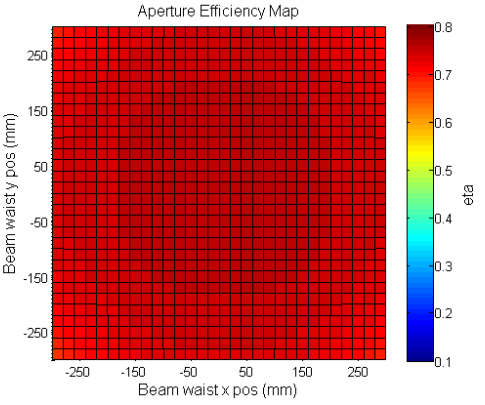


**(c)** $\eta_A$ at 442 GHz

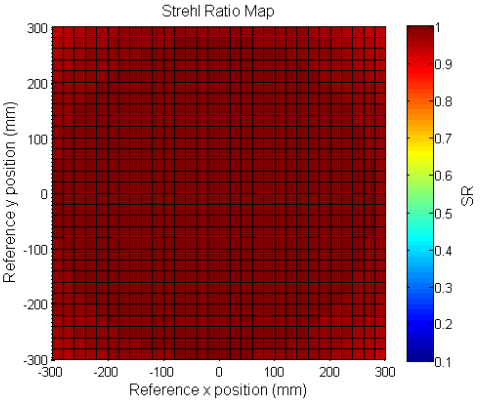


**(d)** Strehl ratio at 442 GHz

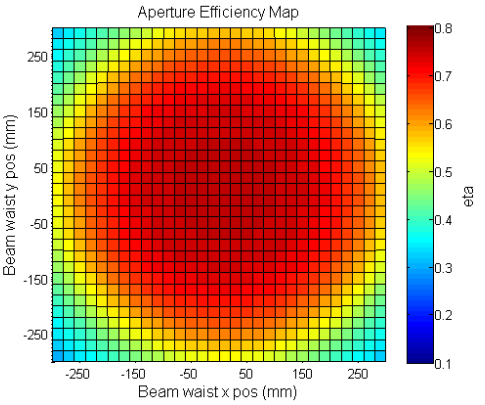


**(e)** $\eta_A$ at 950 GHz

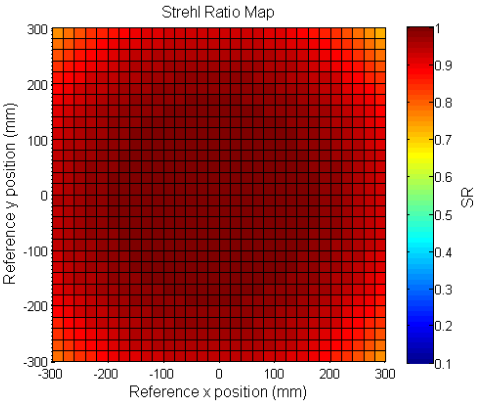


**(f)** Strehl ratio at 950 GHz

**Fig. 3.18** The aperture efficiency and Strehl ratio distributions along the focal plane. The left column shows the aperture efficiency distribution. The right column shows the Strehl ratio distribution.

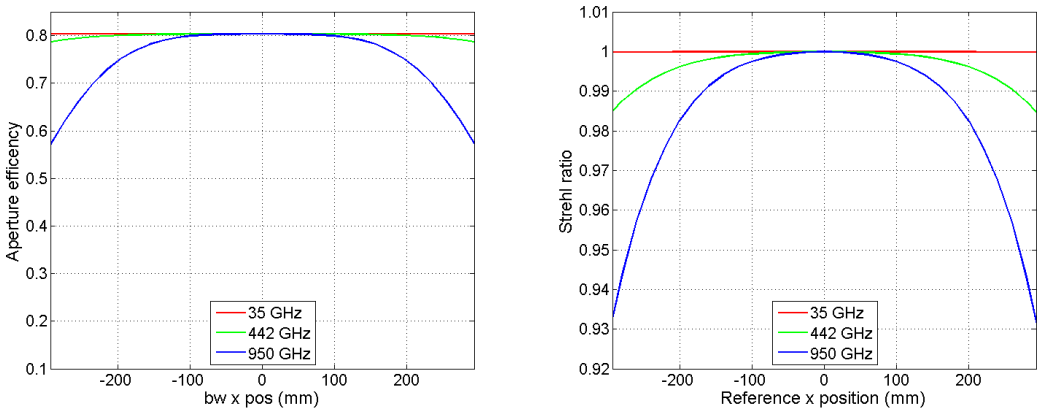


**(a)** $\eta_A$ **(b)** Strehl ratio

**Fig. 3.19** (a) Aperture efficiency with repositioned feed, (b) Strehl ratio with repositioned reference point.

## 3.5 Discussion

### 3.5.1 Implications and Possible Additions

The implementation of the latest theoretical research of aberrations on aperture efficiency in software has allowed the rapid calculation of aperture efficiency at different positions.

The use of ray tracing software has the obvious demerit of requiring the software and having it available. However, the overwhelming advantage is being able to obtain information concerning aberrations for complex optical systems. Simple settings such as a bare Cassegrain reflector illuminated by a feed horn can be analytically considered. Complex systems with more optical elements will become too complex for analytical studies and will require the use of software. Here, the simplest analysis only considering the final beam at the sub-reflector which coincided with the exit pupil was conducted. If the exit pupil is at a different position due to the presence of other optical elements, this software will serve extremely convenient as aberrations contributions will add together from each optical element (Born et al. 1999). These settings can be easily simulated in ray tracing software. Here, a feed only containing a fundamental Gaussian beam mode was considered. A different analytical feed pattern such as an ideal hybrid-mode feed horn (Wylde, 1984) may be assumed.

Feed patterns obtained from other simulation software can be utilized effectively as well. Full simulations in physical optics including the antenna may require hours to simulate in some cases. However, only simulating receiver beam to the sub-reflector will not require too much time. As a result, the electric fields from a feed may be obtained relatively easily in quick succession. The resulting fields from the feed in the PO simulations can then be used for the calculation of aperture efficiency here.

We may possibly use beam measurement results from real feed horns. Gonzalez et al. (2016) shows a re-configurable near-field beam measurement system to measure near-field patterns of

feed horns. The near-field measurement results may be imported into physical optics software, and their propagation can be simulated to obtain their fields at the exit pupil. The aberrations can still be obtained through ray tracing software. We can then calculate the simulated aperture efficiency of the antenna without the physical antenna.

A focal plane array and aperture plane array introduced in Padman (1995) may be simulated with the developed software code with a few additions. A focal plane array assuming direct illumination from offset feed horns can be simulated. The beam waist position can fixed at a position, not derived from the edge taper at the sub-reflector. The beam waist position can then be used to propagate a beam towards the sub-reflector producing the illumination on the sub-reflector. Tilt angles and illumination offsets can also implemented simulating the efficiency loss due to asymmetric illumination from offset feeds in a focal plane array.

### 3.5.2 Aperture Efficiency from Constant illumination

The most dominant source of degradation from this analysis was the defocusing caused by the field-curvature. This is consistent with the results seen in the previous literature in Lamb (1999). Third order aberrations were also minimal for relatively small incident angles evident from the very high Strehl ratio.

The analysis done was assuming a constant beam size at the sub-reflector mimicking the frequency independent beam at the sub-reflector from a single-beam receiver. As a result, one conclusion from this analysis is aberrations are not limiting for frequency independent design of receiver optics if the focus of the antenna is properly matched to the phase center of the beam.

For a separation corresponding to several beam waists, we do not see much difference between the aperture efficiencies because they act as their own optical system with their own pupil. This is an attractive trait for high-aperture efficiency receiver optics.

A multibeam receiver with frequency independent optics could achieve high and constant aperture efficiency for all pixels. This is attractive if the aim is maximizing all aperture efficiencies of the pixels for a small number of pixels. Frequency independent multibeam receiver optics will only be separated by a few tens of millimeters corresponding to the size of a focusing element. The effect of aberrations will not be significant at submillimeter wave frequencies for neighboring pixels as long as the receiver itself is situated close to the antenna center axis.

This analysis so far has ignored system details by treating the tertiary optics (which are necessary for FID) as a block box and only considering the final beam on the sub-ref. In reality, the feed positions may be considerably far away from each other and we could see a slight variation of aperture efficiency between pixels. Tertiary optics may also introduce aberrations if off-axis conics are used as they will introduce their own aberrations. Further analysis including effects from tertiary optics will be necessary to evaluate this concept in depth.

## 3.6 Summary of this Chapter

This chapter presented the development of a software code to calculate the effect of aberrations on aperture efficiency based on the latest theories on receiver optics. Off-axis feeds in a

multibeam receiver will be affected by aberrations degrading their aperture efficiency. Previous calculations based on simple descriptions of aberrations and feeds were sufficient for simple systems. However, they could not describe a complex optical system with many optical elements.

The software code developed here utilizes commercial ray tracing software to obtain the simulated wavefront aberrations from an optical system. This has the distinct advantage of retrieving information about aberrations from a potentially complex optical system with several focusing elements. A feed pattern is assumed and the coupling between a spherical wave with the aberrations obtained from the ray tracing software is used to calculate aperture efficiency.

This software code was used to analyze the aperture efficiency of the ALMA 12-m antenna. Here, a feed only containing a fundamental Gaussian beam mode was assumed. The analysis simulated the aperture efficiency of black-box receiver optics producing a constant beam size at the sub-reflector mimicking a frequency independent illumination. The beam waist position is then offset in two scenarios 1) laterally offsetting away from the Cassegrain focus 2) Lateral offsets with axial defocusing to the focus position. Analysis 1) showed a distinct frequency and positional dependence of aperture efficiency and Strehl ratio. This is the combination of several aberrations, but mostly the defocusing from the field curvature. Analysis 2) returned the expected constant aperture efficiency because the defocusing term in the wavefront aberrations were minimized. This analysis showed that, for receiver optics that produce a constant illumination at the sub-reflector, aberrations are not a limiting factor for aperture efficiency at sub-millimeter wavelengths.

More calculations can be conducted assuming different multibeam receiver architectures such as focal plane arrays. The software code may also include aberrations from receiver tertiary optics with additional modifications if necessary.

**CHAPTER 4**

# Tertiary Optics Design and Analysis Using Ray Tracing and Physical Optics for Multibeam Receivers

## 4.1 Introduction

This chapter discusses the design and analysis of tertiary optics utilizing geometrical optics and physical optics. The main objective of this chapter is to establish a method to design the tertiary receiver optics for each individual pixel in the multibeam receiver array to satisfy the imaging condition for frequency independent optics.

### 4.1.1 Tertiary Optics for Feed Horns

In many cases, a receiver will require additional optical elements to match a receiver beam to the antenna. These additional optics are referred to as the tertiary optics. The three main roles of the tertiary optics are:

- Repositioning and refocusing the incident wave to a desired position.
- To match the beam size of the horn to the antenna to produce a desired illumination pattern.
- To create an image of the sub-reflector/horn aperture to satisfy the imaging conditions for frequency independent design of the optics.

Modern astronomical receivers utilize conical corrugated horns owning to their symmetrical beam shape, low sidelobe levels, and superior polarization discrimination. An ideal corrugated horn under the balanced hybrid condition will excite the hybrid $\mathrm{HE}_{11}$-mode (Clarricoats and Olver, 1984). For a corrugated horn with diameter $2a$ and slant length $R_{\text{horn}}$, the electric fields at the horn aperture are linearly polarized and is given as a truncated Bessel function with a spherical phase-front (Wylde, 1984),

$$\boldsymbol{E}_{\text{horn}} = J_0(k_c r) \exp\left(-\frac{j\pi r^2}{\lambda R_{\text{horn}}}\right) \hat{y}, \tag{4.1.1}$$

where, $k_c = 2.405/a$. the fields at the horn aperture are determined by the horn aperture diameter and the slant length of the horn.

It was shown in Wylde (1984) when the hybrid-mode can be expanded into a series of Gaussian-Laguerre beam modes. Here, 97.9 % of the power in the hybrid-mode is contained in the fundamental Gaussian beam mode described in quasi-optical theory (Fig. 4.1). This

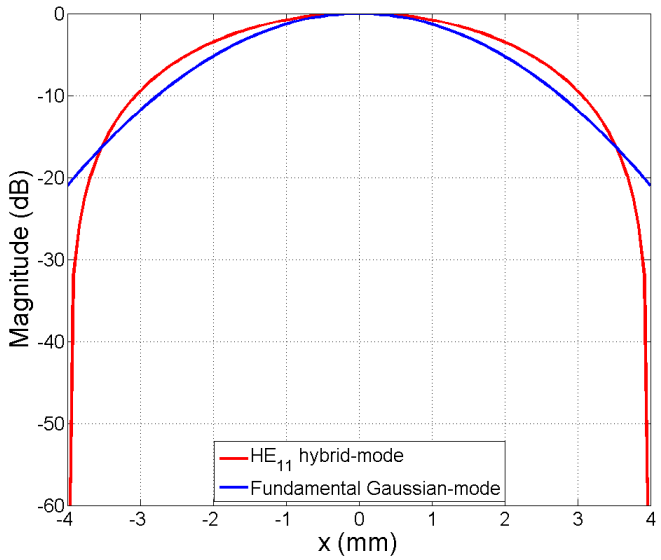


**Fig. 4.1** Comparison between fundamental hybrid beam mode and fundamental Gaussian beam mode for a corrugated horn with $2a = 7.99$ and $R_{\text{horn}} = 24.43$.

enables us to approximate the propagation from a feed horn with quasi-optical Gaussian beam propagation. It was also found that the maximum coupling between a fundamental Gaussian beam with a beam radius $w$ and a corrugated feed horn with a diameter $2a$ occurs when $w = 0.644a$.

This approximation allows us to describe the shape of the feed horn and its field distribution at the aperture with two parameters, the horn radius $a$ and the horn slang length $R_{\text{horn}}$.

### 4.1.2 Receiver Optics for Focal Plane Arrays

Focal plane arrays have been utilized in many multibeam receivers to achieve high-pixel counts and close beams on the sky. The typical array architectures are introduced in Padman (1995). A traditional focal plane array has a frequency dependent aperture efficiency due to the how the receiver optics are designed.

The aperture efficiency of an antenna will be determined by the electric field distribution produced by a receiver feed at the exit pupil (Nagai et al.,2021). For a Cassegrain antenna, the sub-reflector generally acts as an aperture stop to reduce noise from ground pick-up. As a result, the field distribution at the sub-reflector will be imaged at a pupil (Imada et al., 2015). The receiver optics must be designed to produce a illumination pattern at the sub-reflector that returns a high-degree of coupling efficiency, which in turn returns high-aperture efficiency.

A feed produces an illumination at the sub-reflector given by the receiver beam. The propagation of a receiver beam depends on the frequency. If we assume a feed horn only containing a fundamental Gaussian beam mode, it will produce a truncated Gaussian illumination at the sub-reflector with some truncation edge taper level. The beam radius at a given propagation distance away from its beam waist is given by Eq. (2.4.14). A horn with a relatively wide fractional bandwidth of 40% placed at the Cassegrain focus of the ALMA 12-m antenna will experience a beam radius differences and beam waist position differences of approximately 40% at the fre-

quency band ends. This frequency dependence becomes greater for wider bandwidth feed horns. The frequency dependence of the aperture efficiency will be given by the frequency dependence of the illumination at the sub-reflector which may range from approximately 8% (Lamb, 2003) for optimum gain feed horns (Padman et al., 1987) and greater for larger feed horns. In reality, the aperture efficiency will be further lowered by the effect of aberrations, especially if a planar array of feed horns are implemented where defocusing effects may be come significant at high-frequencies.

For FPAs operating in a narrow bandwidth, the frequency dependence may not be too significant since there may only be a few percent difference between the maximum and minimum values across the whole frequency band. This slight degradation may be justified in a large format array since the large number of pixels can justify the slightly lower sensitivity. However, if we assume only a small number of pixels, the trade-off may not be fully justifiable.

### 4.1.3 Frequency Independent Design for Multibeam Receivers

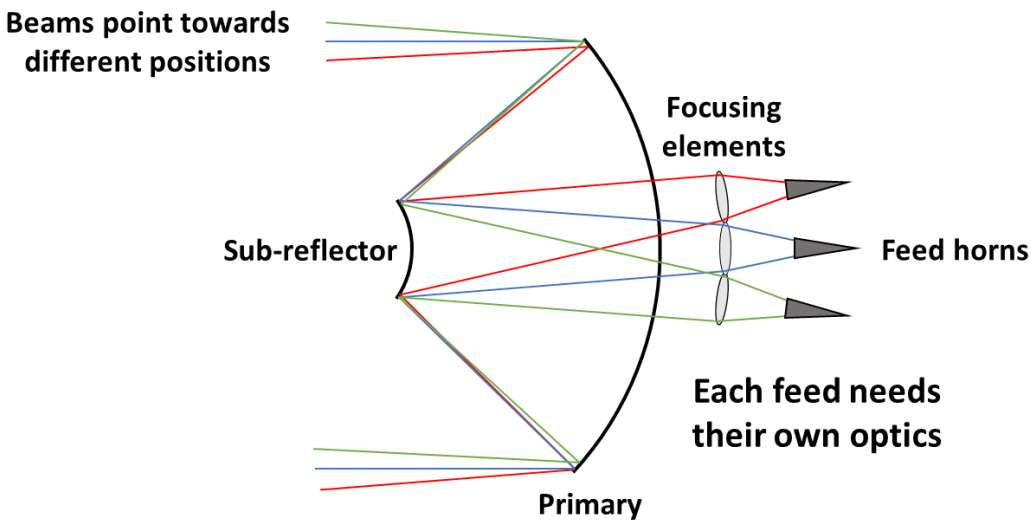


**Fig. 4.2** Simple diagram depicting the optical system for a frequency independent array.

For a multibeam receiver, each feed in the array will be placed at different positions. It was shown in Chapter. 3 that the most dominant aberration is the defocusing due to the field curvature. Consequently, accounting for the defocus and aligning a feeds phase center with the Cassegrain focus returns high-aperture efficiency. The sub-reflector can be physically repositioned to change the effective focal length of the antenna to match the focus of the telescope to a specific feed horn. This is one tactic utilized in single-beam receivers. However, the simultaneous focusing to multiple feeds will be difficult as the change in focus will not be the same for each feed position. The repositioned sub-reflector will also intentionally introduce spherical aberrations which will also degrade the aperture efficiency. As a result, we cannot only rely on the sub-reflector to match an array of feed horns to the antenna and additional optical elements

will be necessary for the receiver.

One option to explore is extending the imaging condition for frequency independent design in single-beam receiver optics to the individual feed horn in a multibeam receiver. Considering the diagram shown in Fig. 4.2, a focusing element can be paired with every feed horn to satisfy the imaging condition necessary for frequency independent illumination at the sub-reflector. However, this configuration will require individual solutions to the additional optics as every feed is placed at a different position. Thus, we require a method to obtain solutions and designs for the individual tertiary optics for each feed.

The use of ray tracing and geometrical optics is attractive here as it can describe the optic in a simple way and can provide formulas to derive necessary parameters such as focal lengths of optical elements. However, ray tracing cannot fully describe the receiver optics as it does not include the effect of diffraction. The effect of diffraction can be done with Physical Optics (PO). However, utilizing PO for optical design is not ideal as it requires orders of magnitude more time compared to ray tracing simulations in some cases. We may use each method appropriately for the design and analysis of the tertiary optics for each individual pixel.

## 4.2 Methods and Figures-of-Merit

### 4.2.1 Frequency Independent Design for Feed Horns

A core concept for single-beam receiver optics with broadband performance for a Cassegrain antenna is frequency independent illumination at the sub-reflector (Lamb, 2003). Chu (1983) derived the necessary conditions for a receiver beam to achieve frequency independent illumination at a given plane. The frequency independent design of a quasioptical beam was discussed in Goldsmith (1998). The general theory using using Fresnel diffraction was shown in Imada et al. (2015).

Consider the setting shown in Fig.4.3. A feed with a Gaussian beam radius $w_{\text{in}}$ at the horn aperture is assumed. In general, the beam size of a receiver $w(z;\nu)$ depends on the frequency $\nu$ and the propagation distance $z$. If an optical element (a lens or mirror) with a focal length $f$ is placed a distance $d_{\text{in}}$ away from the horn aperture, an image of the horn aperture will be created at a position $d_{\text{out}}$ away from the lens.

If the input and output distances satisfy the common relation,

$$\frac{1}{f} = \frac{1}{d_{\text{in}}} + \frac{1}{d_{\text{out}}}, \tag{4.2.1}$$

the output beam size $w_{\text{out}}$ will be a geometrically scaled image of the input beam size as,

$$w_{\text{out}} = \frac{d_{\text{in}}}{d_{\text{out}}} w_{\text{in}}. \tag{4.2.2}$$

This relation is the well known "Lens equation" for a thin lens[1]. The basic condition for frequency independent design is to have the position of the horn aperture from a lens satisfy

[1] A lens with negligible thickness

Eq.(4.2.1) to produce an image at the sub-reflector. Here, since the fields at the horn aperture are frequency independent, its image at the sub-reflector is also frequency independent. This imaging condition occurs if, and only if, the horn aperture sub-reflector positions satisfies the lens equation. Conversely, for an arbitrary lens at a fixed position away from the horn and sub-reflector, the focal length must be solved to satisfy this imaging condition for a constant beam size to be created.

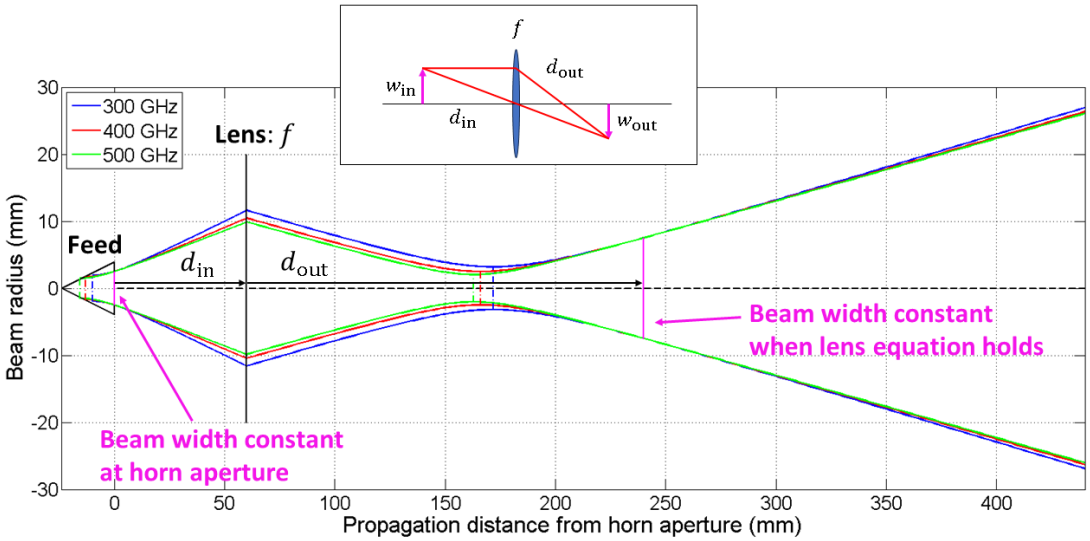


**Fig. 4.3** Diagram of a feed horn and its frequency independent beam at a lens output. The top diagram depicts the image formed with the same lens considering geometrical optics.

For the case of a radio telescope with a sub-reflector doubling as an aperture stop, the frequency independent condition is equivalent to creating the exit pupil from geometrical optics at the horn aperture. It was emphasized in Imada et al. (2015) that, electric fields at a pupil scale geometrically because a pupils are images of each other. This allows us to treat the electric field components at a pupil as geometrical objects whose size depends on the magnification between the pupils.

### 4.2.2 Definition of Beam Curvature Center

Radio telescopes often have antenna reflectors with a considerable depth due to having a relatively low F-number. For example, the ALMA 12-m antenna has a primary reflector diameter of 12 m with a focal length of 4.8 m resulting in an F-number of $f/D = 0.4$. This results in the depth of the primary reflector from the vertex to the plane of the rim is 1875 mm. The ALMA antenna is a classical Cassegrain reflector with a magnification of $M = 20$. This requires a sub-reflector with a back focal length of $f_{\mathrm{sub}} = 294.15$ mm (Distance between foci $f_s = 6176.95$ mm). The sub-reflector has a diameter of 750 mm, this results in a sub-reflector with a thickness of 111.32 mm.

If we assume quasi-optical Gaussian beam propagation, the beam waist size will change depending on how and where the desired edge taper is defined. If we consider the situation in

Fig. 4.4, we can define a plane along the rim of the sub-reflector and the Cassegrain focus[2]. Here, the radius of curvature of the beam will be roughly 5994.13 mm (ALMA originally used $R = 6000$ mm). If we define the radius of curvature from the vertex, it will be 5882.81 mm. The centers of these definitions will still be the same since the focus position of the telescope is not changed. However, the final beam radius on the sub-reflector will be defined at a different position, thus returning a slightly different beam waist size.

The beam waist and its position can be determined with the beam radius and the radius of curvature at a given position. If we use the beam radius (given by the edge taper) and the radius of curvature, then the beam waist will be given by,

$$\begin{cases} w_0 = \dfrac{w_{\text{sub}}}{\sqrt{1+\left(\frac{\pi w_{\text{sub}}^2}{\lambda R_{\text{sub}}}\right)^2}} \\ z_0 = \dfrac{R_{\text{sub}}}{1+\left(\frac{\lambda R_{\text{sub}}}{\pi w_{\text{sub}}^2}\right)^2}. \end{cases} \tag{4.2.3}$$

For a sub-reflector thickness $\Delta t = 111.32$ mm from the plane at the vertex to the plane along the rim, the radius of curvature to the rim of the sub-reflector will be given by $R_{\text{rim}} = R_{\text{vert}} + \Delta t$, where $R_{\text{vert}}$ is the radius of curvature at the vertex. The radius of curvature is taken as positive when the curvature is concave towards the direction of propagation and negative when convex towards the direction of propagation.

If we assume an illumination edge taper of 12 dB, using (4.2.3), at 442 GHz the beam waist for both cases will be,

$$\begin{cases} w_{0,\text{vert}} = 3.98\,\text{mm} \\ w_{0,\text{rim}} = 4.06\,\text{mm} \end{cases} \tag{4.2.4}$$

The two beam waists differ by about 2 % within the frequency band. This difference should not affect the final performance of the optics significantly, as we should only see slight differences in spill-over efficiency.

However, there will be differences in beam axis angles (chief ray angles) if this reference plane is not kept consistent. If a receiver beam is not placed along the antenna axis, a beam pointing to the center of the sub-reflector and the center of the plane containing the rim will have a different tilt angle. In the case the beam is tilted to point towards the center of the plane containing the edge, the beam will no longer produce a centered illumination.

This is also an issue if we are to utilize geometrical optics and ray tracing since beam axis angles and ray angles will not be consistent with each other. Thus, it is necessary to keep a consistent system setting between the different optical analysis methods.

For this thesis, the curvature center of the beam will be measured from the vertex of the sub-reflector. The plane of the sub-reflector will also be placed at the vertex.

[2] $R = 6005.85$ mm if we define the radius of curvature from the Cassegrain focus to the edge of the sub-reflector

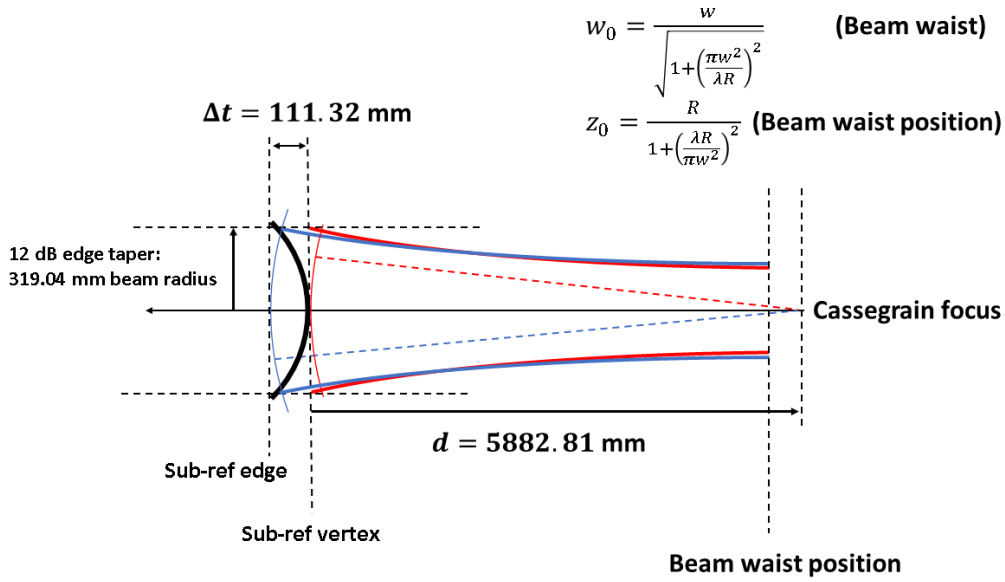


**Fig. 4.4** Difference between beam waist sizes for different reference planes.

### 4.2.3 Aperture Efficiency at Sub-Reflector

For the specific case of the ALMA antenna, the aperture efficiency is defined and evaluated at the sub-reflector. Here, a receiver beam is assumed to couple an ideal spherical wave with matching phase. The ideal spherical wave is assumed to be centered at a given phase center. The spherical wave will have a constant field amplitude across the sub-reflector and can represented as a top-hat function with a constant amplitude $E_0$.

Consider a uniform plane wave with a wavelength $\lambda$ enters into the antenna. The plane wave can be assumed transformed into a converging truncated spherical wave after reflection at the primary and sub-reflector. The spherical wave converges towards a phase center point given by the Cassegrain focus and will have a radius $R$ at the sub-reflector. We denote this as the target reference wave,

$$\mathbf{E}_{\text{target}} = |E_0| \exp(-j\vec{k} \cdot \vec{r}) \quad \text{where } |E_0| = \begin{cases} 1 \ (\Omega \leq \Omega_{\text{sub}}) \\ 0 \ (\Omega > \Omega_{\text{sub}}) \end{cases} \tag{4.2.5}$$

where $|\vec{k}| = k = 2\pi/\lambda$ is the wave number, $\vec{r}$ is the position vector where the origin set at the phase center (Cassegrain focus), and the bold font indicates complex fields. Now consider a linearly polarized feed. The fields at the sub-reflector from the receiver beam output from the receiver tertiary optics is denoted as $\mathbf{E}_{\text{beam}}$. Using the overlap integral, the aperture efficiency can be defined as,

$$\eta_{\text{sub}} = \frac{|\iint_{\Omega_{\text{sub}}} \mathbf{E}_{\text{target}} \cdot \mathbf{E}^*_{\text{beam}} d\Omega|^2}{\iint |\mathbf{E}_{\text{beam}}|^2 d\Omega \iint |\mathbf{E}_{\text{target}}|^2 d\Omega}. \tag{4.2.6}$$

Here, $\Omega_{\text{sub}}$ is the solid angle of the sub-reflector from the phase center. If we denote the fields at the sub-reflector from the receiver beam along the reference spherical surface as $\mathbf{E}_{\text{sub}}$, the phase of $\mathbf{E}_{\text{sub}}$ will be measured from the reference sphere center as $\mathbf{E}_{\text{sub}} = \mathbf{E}_{\text{beam}} \exp(-j\vec{k} \cdot \vec{r})$. We

may then rearrange Eq. (4.2.6) to get the formula,

$$\eta_{\text{sub, beam}} = \frac{|\iint_{\Omega_{\text{sub}}} 1 \cdot \mathbf{E}_{\text{sub}} d\Omega|^2}{\iint |\mathbf{E}_{\text{sub}}|^2 d\Omega \iint_{\Omega_{\text{sub}}} |1|^2 d\Omega}. \tag{4.2.7}$$

Thus we may easily calculate the aperture efficiency at the sub-reflector by getting the fields along the reference sphere from the receiver beam at the sub-reflector. Equation (4.2.7) is a close representation of the definition used by ALMA.

If we assume some power is input into a feed and is completely propagated to free-space with no loss, then the total power in the propagated fields will be exactly equal to the total power input into the receiver.

Consider an input power of $P_{\text{feed}}$ is input to a receiver feed as shown in Fig. 4.5. The feed will propagate a receiver beam and will produce an electric field pattern $\mathbf{E}_{\text{sub}}$ at the sub-reflector. If we assume no losses, then the total power incident at the sub-reflector will be given as,

$$\iint |\mathbf{E}_{\text{sub}}|^2 d\Omega = P_{\text{feed}}. \tag{4.2.8}$$

By defining total power that reaches the sub-reflector from the feed, we can quantify the power that was not incident at the sub-reflector and was spilled-over at the tertiary optics with the formula,

$$\eta_{\text{sub, feed}} = \frac{|\iint_{\Omega_{\text{sub}}} 1 \cdot \mathbf{E}_{\text{sub}} d\Omega|^2}{\iint_{\Omega_{\text{sub}}} |1|^2 d\Omega \cdot P_{\text{feed}}}. \tag{4.2.9}$$

Equation (4.2.7) does not include the spill-over efficiency at the primary (spill-over at the entrance pupil), and the spill-over efficiency from the receiver optics. As a result, this definition will in general return higher aperture efficiency values compared to Eq. 2.4.5 and Eq. (4.2.9). The three definitions for aperture efficiency are summarized in Table. 4.1.

**Table 4.1** Summary of aperture efficiency definitions.

| | | Includes spill-over | | |
|---|---|---|---|---|
| $\eta$ | Defined position | At primary | At sub-ref | At tertiary optics |
| $\eta_{\text{A}}$ | On the sky | YES | YES | YES |
| $\eta_{\text{sub, feed}}$ | At sub-ref | NO | YES | YES |
| $\eta_{\text{sub, beam}}$ | At sub-ref | NO | YES | NO |

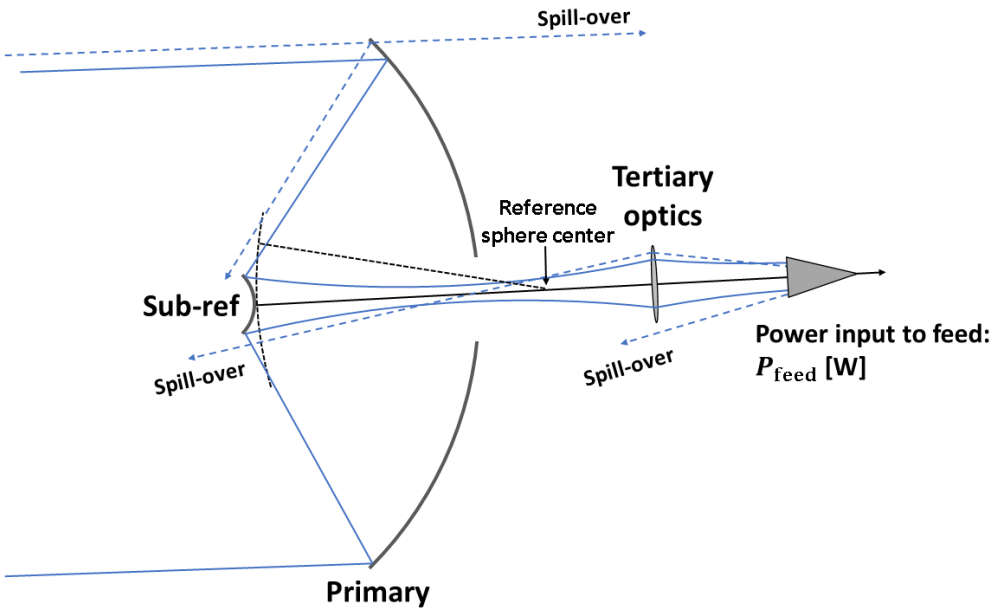


**Fig. 4.5** A simple diagram depicting the spill-over at the antenna reflectors and at the receiver tertiary optics.

The equations introduced above assume ideal propagation and no loss of efficiency due to materials. All equations do not include the following:

1. Loss due to surface roughness (Ruze, 1965).
2. Ohmic loss from reflectors.
3. Loss due to dielectrics and variability of refractive index.

These effects may be included as different factors if necessary and the final aperture efficiency can be represented as a product of all factors.

The fields along a spherical surface can be easily obtained through commercial electromagnetic simulation software such as GRASP. If the receiver beams phase exactly matches the reference sphere, the phase difference will be zero and we should see a flat phase distribution along the spherical surface.

## 4.3 Alternative Optics Designs for ALMA Band 8

The imaging condition for frequency independent design requires solving the lens equation to obtain the necessary focal length of a focusing element to match a receiver feed to a target illumination. The use of a lens or a mirror will depend case by case for the specific receiver. Here, we consider mirrors as the focusing element.

The current ALMA band 8 optics consists of a single-mirror system using an ellipsoidal mirror. The details of the current ALMA band 8 optics and its optical performance is shown in Appendix. A.

The design and analysis of single-mirror optics are shown in Appendix. B. A single-mirror system has limited design freedom if a feed horn is assumed. For the case of the current ALMA

band 8 feed horn, the position of the mirror must be 6009 mm away from the sub-reflector which will physically interfere with the final 15K shield in the ALMA cryostat.

### 4.3.1 Two-Mirror Design

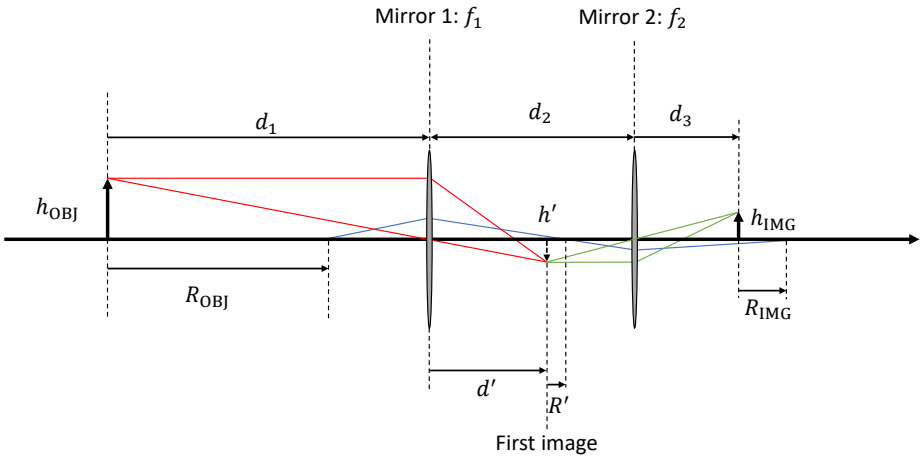


**Fig. 4.6** System setting for Two-mirror tertiary optics.

The solution to the position and focal length for the tertiary optics necessary for the imaging condition can be solved if the horn parameters are fixed. Two-mirror tertiary optics are considered here, however the required number of focusing elements will depend case by case.

For two focusing elements, the sub-reflector will be imaged twice. The first mirror will directly image the sub-reflector and create an intermediate image (as a pupil), and it will also image the off-axis Cassegrain focus. The second mirror will image the intermediate image and the image of the Cassegrain focus to create a final image. The horn aperture and phase center can then be situated to match the final images to satisfy the frequency independent conditions.

A two-mirror (two-lens) system is shown in Fig. 4.6. Two mirrors are separated by a distance $d_2$. An object (OBJ) situated a distance $d_1$ away from mirror 1 with focal length $f_1$ will produce an image a distance $d'$ away from mirror 1. Simultaneously, a point $R_{\mathrm{OBJ}}$ away from the object will produce an image $R'$ away from the image of the object.

The object-image relation for the first mirror will satisfy the lens equation,

$$\begin{cases} \frac{1}{f_1} &= \frac{1}{d_1} + \frac{1}{d'} \\ \frac{1}{f_1} &= \frac{1}{d_1 - R_{\mathrm{OBJ}}} + \frac{1}{d' + R'}. \end{cases} \tag{4.3.1}$$

$$\begin{cases} \frac{1}{f_2} &= \frac{1}{d_2 - d'} + \frac{1}{d_3} \\ \frac{1}{f_2} &= \frac{1}{d_2 - d' - R'} + \frac{1}{d_3 + R_{\mathrm{IMG}}}. \end{cases} \tag{4.3.2}$$

The final image size $h_{\mathrm{IMG}}$ and object image size $h_{\mathrm{OBJ}}$ will be related by the first image size

$h'$,

$$h' = -\frac{d'}{d_1} h_{\text{OBJ}} = -\frac{d_2 - d'}{d_3} h_{\text{IMG}}. \tag{4.3.3}$$

The system of equations given by Eq. (4.3.1), Eq. (4.3.2) and Eq. (4.3.3) returns five equations with ten variables. Here,

$$\begin{cases} d' &= K' d_2 \\ R' &= \frac{R_{\text{OBJ}} d'^2}{d_1^2 - R_{\text{OBJ}}(d' + d_1)}, \end{cases} \tag{4.3.4}$$

and

$$K' = \frac{\frac{h_{\text{IMG}}}{h_{\text{OBJ}}}}{\frac{d_3}{d_1} + \frac{h_{\text{IMG}}}{h_{\text{OBJ}}}}. \tag{4.3.5}$$

Finally, $d_2$ can be solved to obtain,

$$\begin{aligned} d_2 = \frac{(R_{\text{OBJ}} R_{\text{IMG}} d_3 + R_{\text{OBJ}} d_3^2 - R_{\text{IMG}} d_1^2 + R_{\text{OBJ}} R_{\text{IMG}} d_1) K'^2}{R_{\text{OBJ}} R_{\text{IMG}} K'(K' - 1)} \\ + \frac{2 d_1 (d_1 - R_{\text{OBJ}}) K' + (R_{\text{OBJ}} - d_1) d_1}{R_{\text{OBJ}} K'(K' - 1)}. \end{aligned} \tag{4.3.6}$$

The mirror focal lengths can be solved with Eq. (4.3.1) and Eq. (4.3.2) using Eq. (4.3.4) and Eq. (4.3.6). When the object and image heights and curvature centers are fixed, the mirror focal lengths $f_1$ and $f_2$, and the distance between mirrors $d_2$ can be solved as a function of $d_1$ and $d_3$. The focal lengths $f_1$, $f_2$, and the distance $d_2$ as a function of $d_1$ and $d_3$ with fixed $h_{\text{OBJ}}$, $h_{\text{IMG}}$, $R_{\text{OBJ}}$, and $R_{\text{IMG}}$ are shown in Fig. 4.7 and Fig. 4.8.

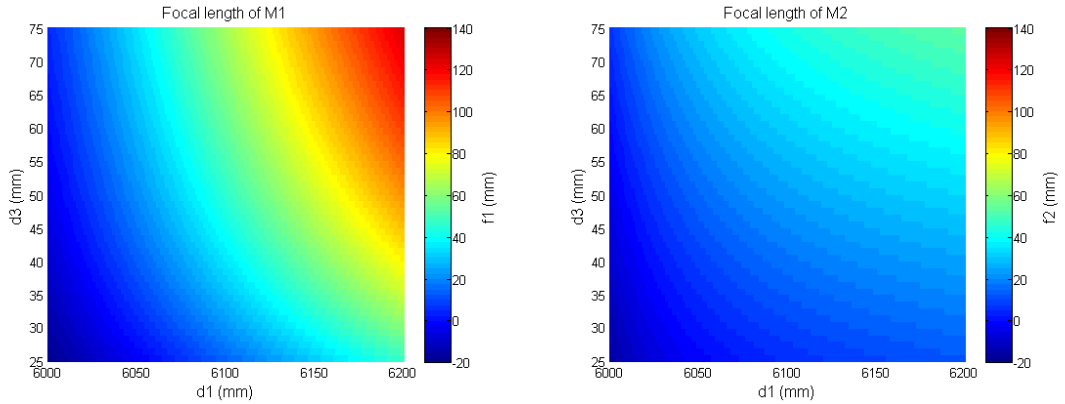


**(a)** Focal length $f_1$ of first mirror

**(b)** Focal length $f_2$ of second mirror

**Fig. 4.7** (a) The focal length of mirror 1 and (b) the focal length of mirror 2, as functions of $d_1$ and $d_3$. Here, $h_{\text{OBJ}} = 316.266$ mm and $h_{\text{IMG}} = 2.571$ mm, and, $R_{\text{OBJ}} = 5866.097$ mm and $R_{\text{IMG}} = 24.43$ mm.

The parameters describing the object height can be fixed by using the target illumination at the sub-reflector. An illumination edge taper value that returns a beam radius at the sub-reflector $w_{\text{sub}}$ can be assumed and used for $h_{\text{OBJ}}$. The curvature radius can be set to match the radius to the off-axis Cassegrain focus $R_{\text{sub}}$ which can represent $R_{\text{OBJ}}$.

We may fix the parameters describing the horn according to Section. 4.1.1. The image height

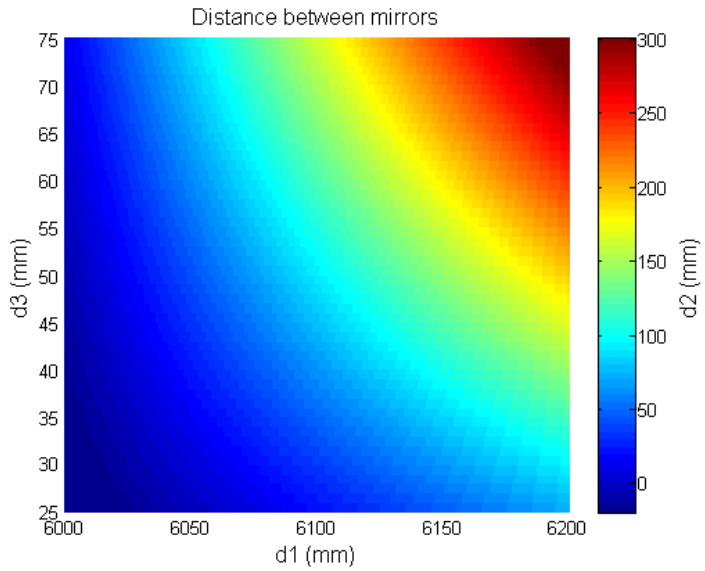


**Fig. 4.8** The distance between mirrors $d_2$ as a function of $d_1$ and $d_3$. Here, $h_{\text{OBJ}} = 316.266$ mm and $h_{\text{IMG}} = 2.571$ mm, and, $R_{\text{OBJ}} = 5866.097$ mm and $R_{\text{IMG}} = 24.43$ mm.

is set as the beam radius at the horn aperture $w_{\text{horn}}$ and $R_{\text{IMG}}$ is set as the horn slant length $R_{\text{horn}}$.

Here, at least two parameters still need to serve as free parameters to obtain solutions if the target illumination and horn parameters are fixed. The relative position of the mirrors from the sub-reflector and horn can be easily fixed by the positional constraints from the antenna. Thus, the distance from the sub-reflector to mirror 1 $d_1$ and the distance from mirror 2 to the horn aperture $d_3$ were set as free parameters.

#### 4.3.1.1 Modeling and Analysis with Ray Tracing

The ALMA band 8 receiver feed horn was used for as a feed horn in this analysis. ALMA band 8 feed horn is described in Sekimoto et al. (2008). The band 8 horn has a horn aperture diameter of 7.99 mm and an axial length of 24.1 mm. The fields beam size at the horn aperture is given by $w_{\text{horn}} = 2.571$ and $R_{\text{horn}} = 24.430$.

A Two-mirror tertiary optics for the band 8 horn was designed with the combination of $d_1 = 6125$ mm and $d_3 = 45$ mm. The target illumination is set again to obtain a 12.21 dB edge taper to compare with the current target for the band 8 receiver with $w_{\text{wub}} = 316.266$ mm and $R_{\text{sub}} = 5866.09668$. The solution to the mirror focal lengths and distance between them are given by,

$$\begin{cases} f_1 &= 53.54 \text{ mm}, \\ f_2 &= 23.42 \text{ mm}, \\ d_2 &= 102.84 \text{ mm}. \end{cases} \tag{4.3.7}$$

The Two-mirror optics shown in Fig. 4.9 were modeled in CODE V. The main panel shows the view facing the Y-Z plane and the top left panel shows the top-down view facing the X-Z plane. Two ellipsoidal mirrors were modeled with focal lengths and separation given by

Eq. 4.3.7. The reflection angle between the chief ray (equivalent to the beam axis, center ray of red bundle in Fig. 4.9) was set to 41.01 degrees. The feed aperture plane was placed 45 mm away from M2 according to Eq. (4.3.7) with the final beam axis situated parallel to the antenna center axis.

The image of the sub-reflector can be seen aligning with the horn aperture plane with the rays converging at a point 24.43 mm away corresponding to the horn phase center.

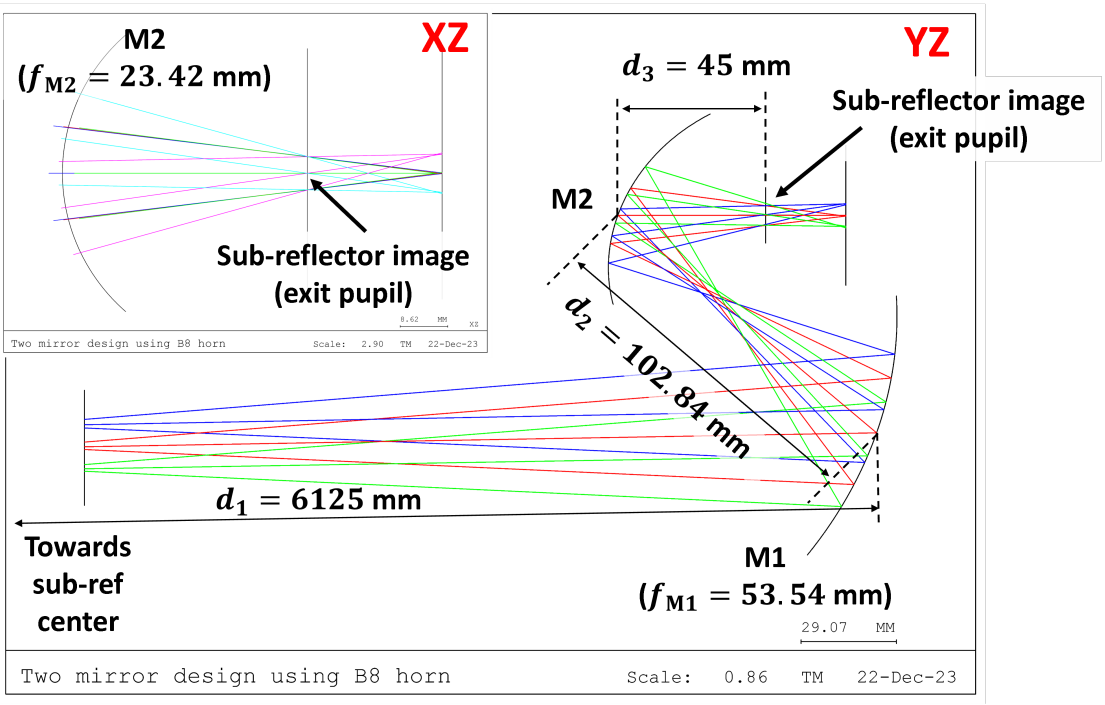


**Fig. 4.9** Two-mirror tertiary optics modeled in CODE V.

One small issue is, solutions with smaller distances between mirrors will require a higher power second mirror with a shorter effective focal length. Shorter focal lengths yields conic surfaces with larger curvature (smaller curvature radii). If the conic surface is drawn from the major axis[3], then the maximum diameter achievable is twice the minor axis for the on-axis reflection along the major vertex of the surface. Off-axis reflection angles will yield a much smaller reflector since the surface must be offset to have the rays reflect at the off-axis position. The mirror surface will require defining a rim from the offset position which may limit the rim diameter depending on the conic surface. This may be resolved if we relax the constraint of using the current band 8 horn parameters and assume a larger horn with either or both a larger diameter and longer slant length.

### 4.3.1.2 Physical Optics Analysis

The two-mirror optics from Section. 4.3.1.1 was modeled in GRASP and is shown in Fig. 4.10. Physical optics simulations were conducted at 385 GHz, 442 GHz, and 500 GHz to obtain the illumination on the sub-reflector, far-fields on the sky, and to calculate aperture efficiency. An ideal hybrid-mode feed horn with a diameter 7.99 mm and slant length 24.43 mm was used as

[3] A conic surface with a negative conic constant

the feed. A power of $4\pi$ (W) is fed to the horn and the fields from the feed are propagated to each element in the order of, the feed to the tertiary optics, the tertiary optics to the sub-reflector, the sub-reflector to the primary reflector, and the primary reflector to the sky. The cryostat window can be seen in the lower left in Fig. 4.10. However, the window was not included in the calculations since the beam will pass through its center and we expect little effects from the beam truncation.

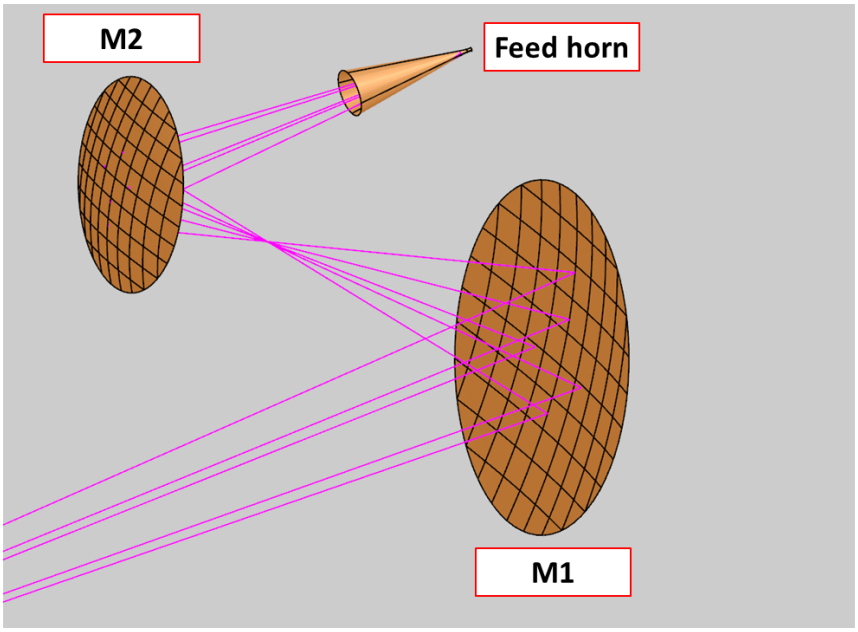


**Fig. 4.10** Two-mirror tertiary optics modeled in GRASP.

#### 4.3.1.3 Fields at Sub-Reflector

The fields on the sub-reflector were calculated on a reference spherical surface with radius $R = 5866.097$ mm centered at the off-axis Cassegrain focus. The field magnitude at the sub-reflector is shown in Fig. 4.11. The dotted lines in Fig. B.4 shows the angular extent of the sub-reflector from the off-axis Cassegrain focus. The phase difference between the receiver beam at the sub-reflector and the reference sphere is shown in Fig. 4.12. The left column in Fig. 4.11 and Fig. 4.12 shows the two-dimensional distributions along the reference spherical surface at the sub-reflector and the right column shows the symmetrical cut along $v = 0$ and the asymmetrical cut along $u = 0$.

The illumination at the sub-reflector has a consistent shape disregarding the asymmetry in the asymmetrical cuts. The noticeable deformation may be caused by some unwanted higher-order modes being generated by the reflection at the mirrors. The phase pattern also shows some higher order terms, particularly a very minor fourth order term similar to spherical aberrations[4]. The magnitude of the phase errors caused by aberrations from the tertiary optics are relatively small. However, some aberrations may constructively interfere to cause a noticeable difference under certain circumstances, which may be a potential cause for the frequency dependence of the indentation. The result of the distortion is a overall higher spill-over at the sub-reflector. The

[4]This is not spherical aberrations from the antenna

field magnitude shows slightly higher magnitude beam skirts outside of the sub-reflector range compared to the single-mirror optics. This higher spill-over will directly lower the aperture efficiency.

Understanding the exact cause of the distortions in the beam will require both the analysis of aberrations which can be done in ray tracing software or by analyzing the phase pattern, and a modal analysis to understand which higher-order modes are being generated. This is left as a future investigation.

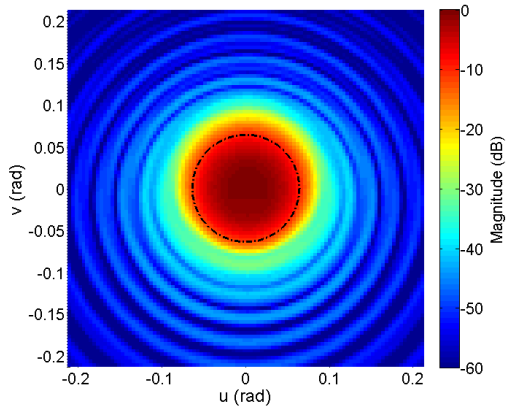


**(a)** 385 GHz

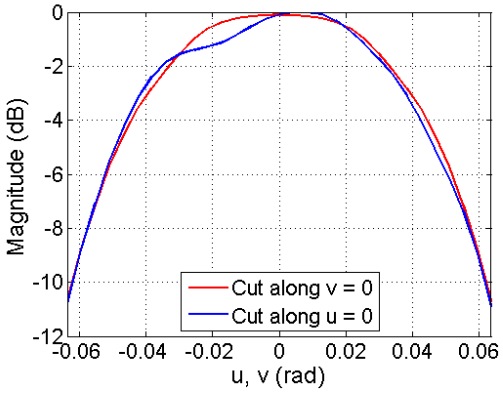


**(b)** 385 GHz

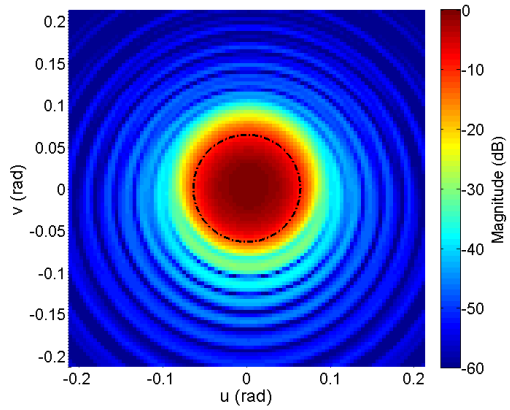


**(c)** 442 GHz

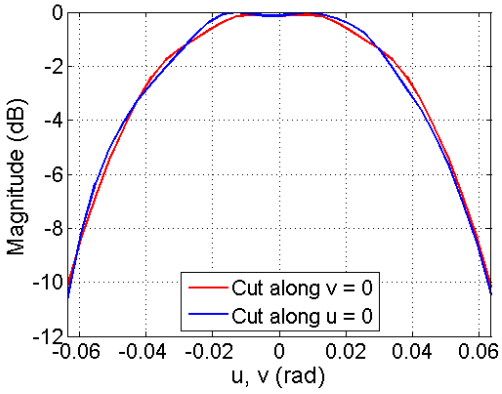


**(d)** 442 GHz

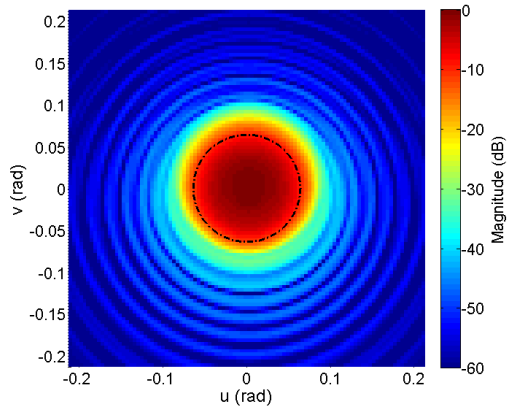


**(e)** 500GHz

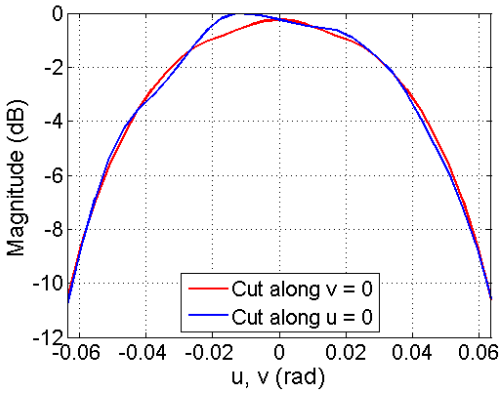


**(f)** 500 GHz

**Fig. 4.11** The field magnitude on the sub-reflector with the two-mirror tertiary optics.

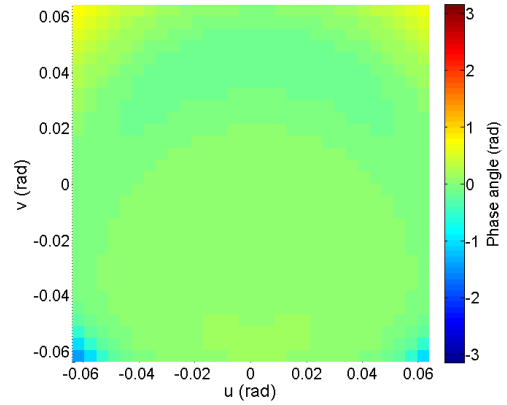


**(a)** 385 GHz

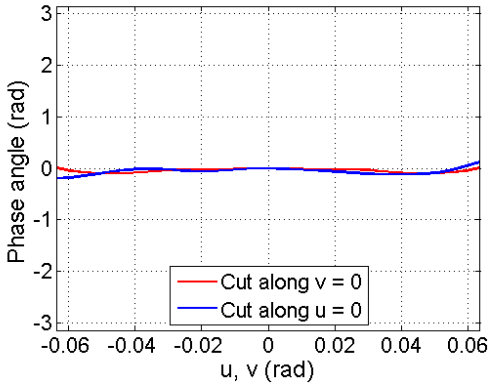


**(b)** 385 GHz

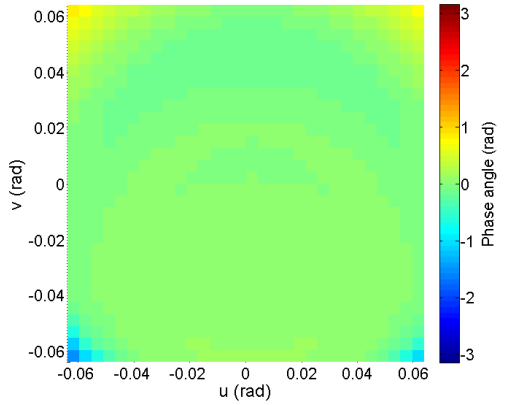


**(c)** 442 GHz

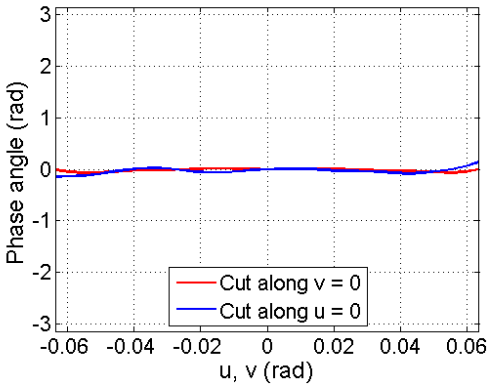


**(d)** 442 GHz

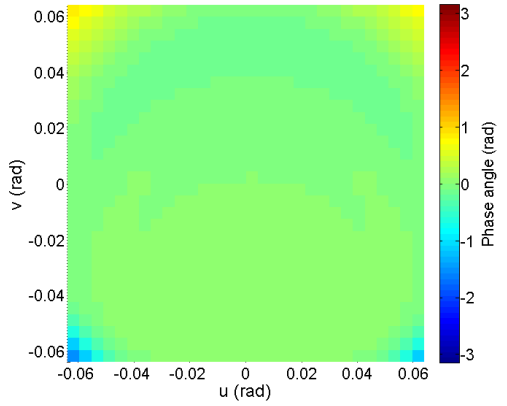


**(e)** 500GHz

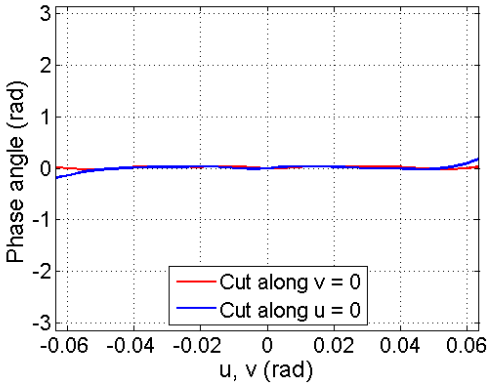


**(f)** 500 GHz

**Fig. 4.12** The phase difference between the reference sphere and the receiver beam at the sub-reflector from the two-mirror optics.

#### 4.3.1.4 Beams on Sky

The far-fields on the sky were calculated with the $u - v$ plane origin was offset by 0.0617 degrees ($1.076 \times 10^{-3}$ radians) from the antenna bore-sight direction to align the origin with the calculated peak position of the beams. The far-fields for the Co-polarization (Co-Pol) and

cross-polarization (Xs-Pol) patterns are shown in Fig. 4.13. The symmetrical and asymmetrical cuts are shown in Fig. 4.14.

The far-fields using the two-mirror optics show good beam symmetry and low sidelobes even with the distortion present at the sub-reflector fields. The maximum Xs-Pol was significantly lower than the single-mirror optics in Appendix. B with Xs-pol lower than -39.0 dB at 385 GHz. There is a slightly stronger presence of coma aberrations which introduces an asymmetric first sidelobe in Fig. 4.14 (b). The peak position was not noticeably affected by the coma aberration and was still centered at $v = 0.0617$ degrees.

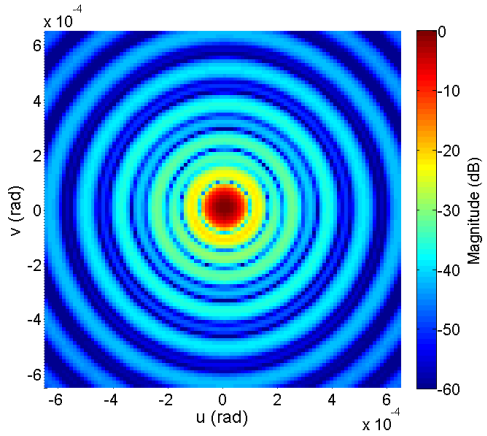


**(a)** Co-Pol: 385 GHz

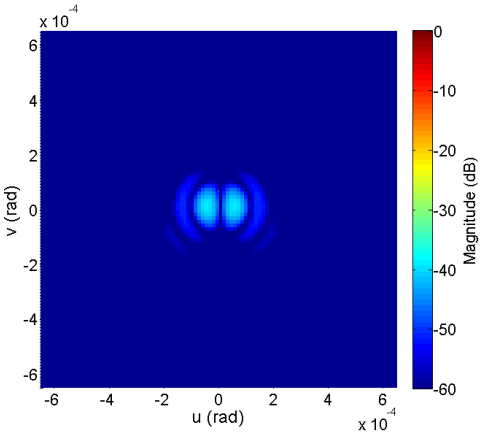


**(b)** Xs-Pol: 385 GHz

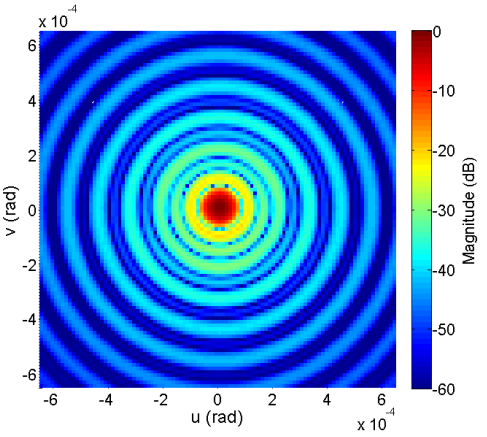


**(c)** Co-Pol: 442 GHz

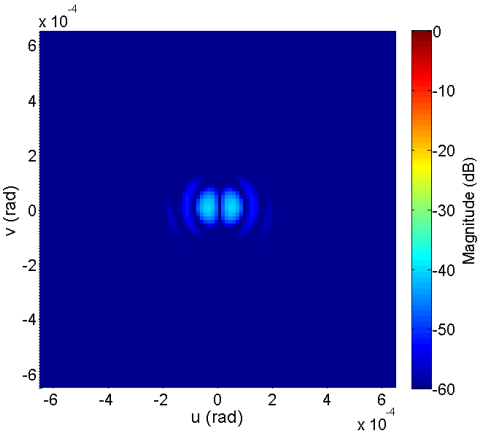


**(d)** Xs-Pol: 442 GHz

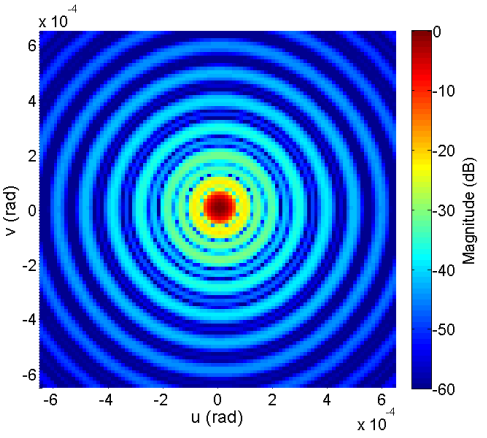


**(e)** Co-Pol: 500 GHz

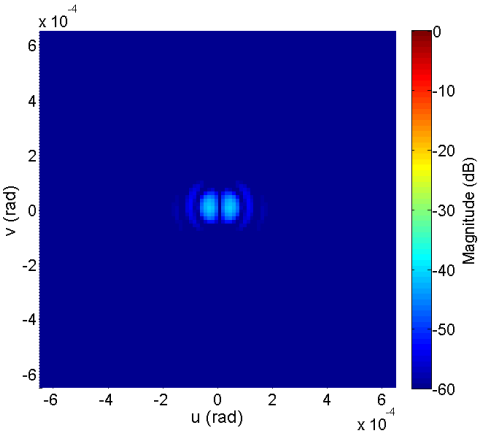


**(f)** Xs-Pol: 500 GHz

**Fig. 4.13** The far-fields on the sky using two-mirror tertiary optics.

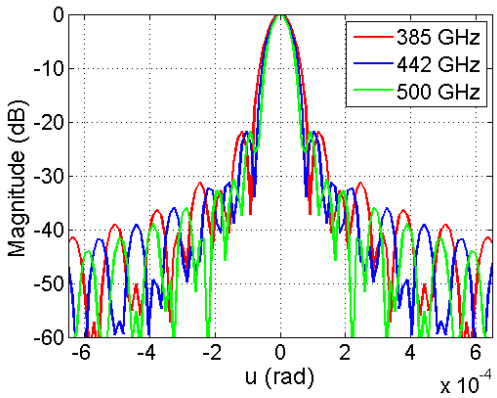


**(a)** Co-Pol: Cut along $v = 0$

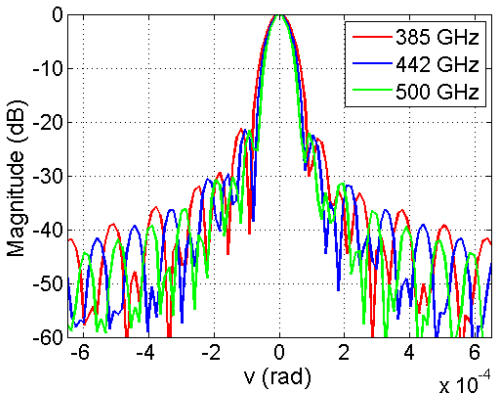


**(b)** Co-Pol: Cut along $u = 0$

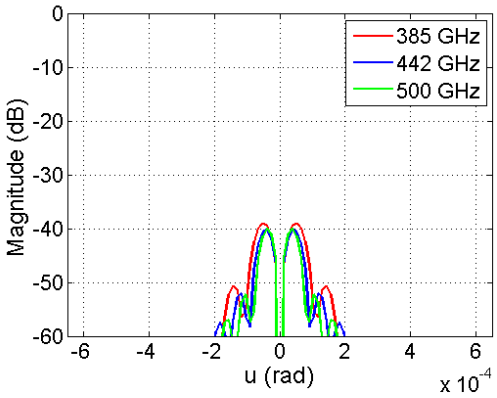


**(c)** Xs-Pol: Cut along $v = 0$

**Fig. 4.14** The cuts of the far-fields on the sky using two-mirror optics.

#### 4.3.1.5 Aperture Efficiency

The aperture efficiency of the antenna using Eq (2.4.5) was calculated using the peak gain value from the far-fields, and the aperture efficiencies evaluated at the sub-reflector from Section. 4.2.3 were calculated using the fields at the sub-reflector. The total power from the feed is $4\pi$ as indicated in Section. B.1.2.

The aperture efficiency values for the two-mirror optics is summarized in Table. 4.2. An overall high aperture efficiency of greater than 0.80 on the sky was obtained. However, there exists a slight frequency dependence compared to the single-mirror optics. The aperture efficiency on the sky varies by roughly 1.5% at the frequency band edges. The origin of this frequency dependence is most-likely the combination of the distortion seen in the fields at the sub-reflector and the spill-over at the mirrors.

**Table 4.2** Aperture efficiencies of two-mirror tertiary optics.

| | 385 (GHz) | 442 (GHz) | 500 (GHz) | $1 - \frac{\eta_{385}}{\eta_{500}}$ (%) |
|---|---|---|---|---|
| $\eta_A$ | 0.8290 | 0.8382 | 0.8417 | 1.51 |
| $\eta_{\text{sub, feed}}$ | 0.8507 | 0.8583 | 0.8619 | 1.30 |
| $\eta_{\text{sub, beam}}$ | 0.8576 | 0.8632 | 0.8658 | 0.95 |

## 4.4 Few-Pixel Multibeam Receiver Design

### 4.4.1 Stacked Unit Cells

#### 4.4.1.1 Minimum Spacing Between Pixels

Frequency independent design for individual pixels from Fig. 4.2 requires designing focusing elements for each feed. The imaging condition for frequency independent design from Section. 4.3.1 can be used for individual pixels. The mirrors require sufficiently large size to minimize the truncation of the beam. Thus, the minimum separation between focusing elements without them physically overlapping will be one of the most compact configurations for an array.

A two-dimensional array will require placing focusing elements laterally and horizontally. In other words, each receiver pixel will have both a lateral and horizontal tilt and rotation angles to their beam axis from the antenna center axis. For the two-mirror design in Section. 4.3.1, horizontal pixels will only require having sufficient spacing between both M1 mirrors horizontally. However, The lateral pixels will require extra considerations for a compact layout.

One efficient layout is a "stacked" design where the first mirror of the second pixel is situated on top of the second mirror of the first pixel laterally shown in Fig. 4.15. Each "unit cell" will require calculating the focal lengths of the mirrors at each position since the incident angle, positions of mirrors will be different. Horn parameters can be set independently for each pixel.

Here, we consider the simplest case of a two-beam multibeam receiver but still focus on overcoming the challenging design of the lateral pixels.

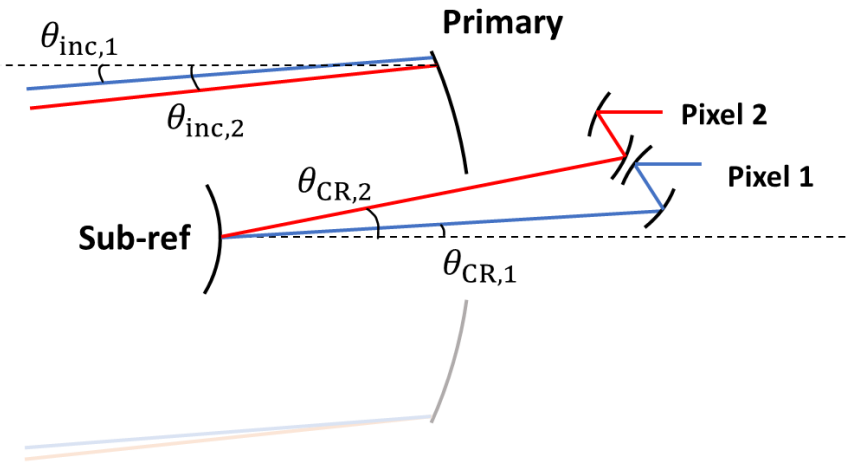


**Fig. 4.15** Concept of Stacked unit cell design.

#### 4.4.1.2 Beam Separation

In this configuration, the pixels will be separated by their lateral chief ray angle difference ($\theta_{CR}$ in Fig. 4.15). Here, the chief ray angle must be sufficiently large to have both beams completely separated towards their respective tertiary optics.

The beam separation on the sky will be given by the incident angle difference into the primary reflector ($\theta_{inc}$ in Fig. 4.15). If the tertiary optics are directly imaging the sub-reflector, and the sub-reflector is the aperture stop in the system, the chief ray angle will be the angle between the antenna center axis and the chief ray. For chief ray angles, the incident angle into the antenna will be given by the effective focal length $F_{eff}$ of antenna as,

$$\theta_{inc} = \frac{d_s \theta_{CR}}{F_{eff}}, \tag{4.4.1}$$

where, $d_s$ is the distance from the vertex of the sub-reflector to the on-axis Cassegrain focus. The expected beam separation $\delta\theta = \theta_{inc,\,2} - \theta_{inc,\,1}$ will be given by the difference between the two chief rays in the two-beam design.

We may determine $\theta_{CR}$ by fixing the position of the mirror using $d_1$ from Eq. (4.3.1). The distance from the sub-reflector to mirror 1 for pixel 2 can be set as roughly the distance between the sub-reflector and mirror 2 of pixel 1. Thus, by fixing the mirror positions, the chief ray angles can be set, in turn returning the incident angle difference. Minimizing the chief ray angle difference will also provide the smallest beam separation on the sky.

### 4.4.2 Design in Ray Tracing Software

The two-mirror design method from 4.3.1 was used to determine the positions and focal lengths of the mirrors. Here, the band 8 horn parameters were used for both pixels. A two-beam multibeam receiver using two-mirror tertiary optics was modeled in CODE V and is shown in

Fig. 4.16. Each pixel had their respective optics solved for their horns and positions. The two beams are labeled as pixel 1 (PX 1) and pixel 2 (PX 2) respectively. The mirrors were set as ellipsoids. The parameters for each pixel are listed in Table. 4.3.

**Table 4.3** List of parameters for both pixels in two-beam multibeam receiver design.

| | Value | |
|---|---|---|
| Parameter (Unit) | PX 1 | PX 2 |
| $\theta_{\text{CR}}$ (deg) | 1.006 | 1.430 |
| $d_1$ (mm) | 6125.000 | 6071.879 |
| $d_2$ (mm) | 68.921 | 56.865 |
| $d_3$ (mm) | 35.000 | 40.000 |
| $f_1$ (mm) | 40.205 | 31.248 |
| $f_2$ (mm) | 15.694 | 15.556 |
| $R_{\text{horn}}$ (mm) | 24.43 | 24.43 |
| $w_{\text{horn}}$ (mm) | 2.571 | 2.571 |
| $w_{\text{sub}}$ (mm) | 316.266 | 316.266 |
| $R_{\text{sub}}$ (mm) | 5866.097 | 5849.549 |

The design was able to have two independent bundles of rays enter into their respective pixels. Each pixel was able to create an image of the sub-reflector approximately at each horn aperture position. However, the close up view of M2 and the horn aperture plane shown in Fig. 4.17 reveals there is a noticeable difference between the calculated sub-reflector image position (horn aperture plane) and the ray traced image in the X-Z plane. This indicates the presence of Sagittal astigmatism. The Strehl ratio for both pixels return very high values of at $\text{SR}_{\text{PX1}} = 0.9996$ for PX 1 and $\text{SR}_{\text{PX2}} = 0.9977$ for PX 2. Both pixels are by no means aberration limited, however, we should expect the defocused image of the sub-reflector at the horn image will directly affect the shape of the beam as seen previously in the two-mirror design. The chief ray angle for PX 2 was set slightly too small and the edge of M1 of PX 2 may overlap with the beam from PX 1.

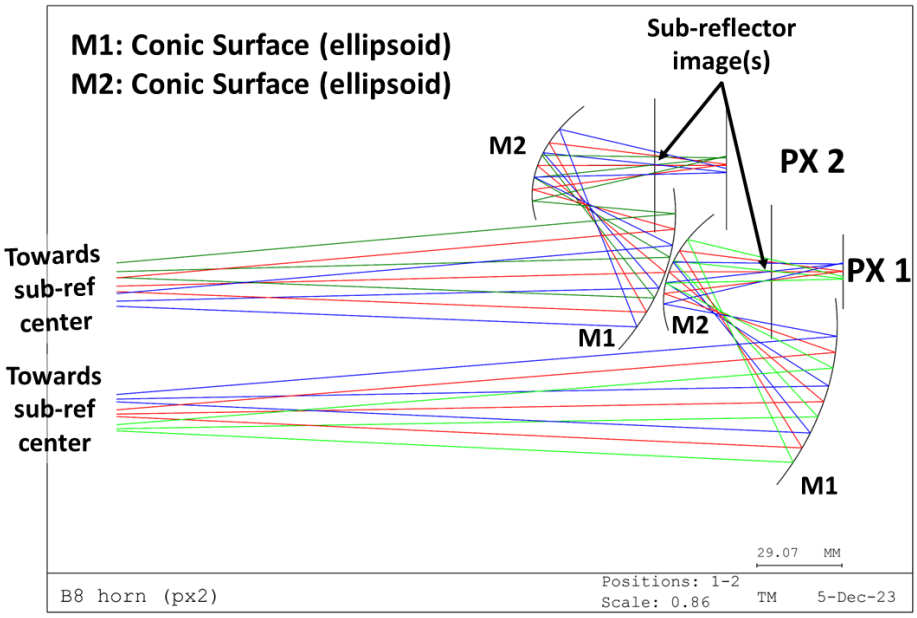


**Fig. 4.16** Stacked unit cell design of a two beam multibeam receiver in CODE V.

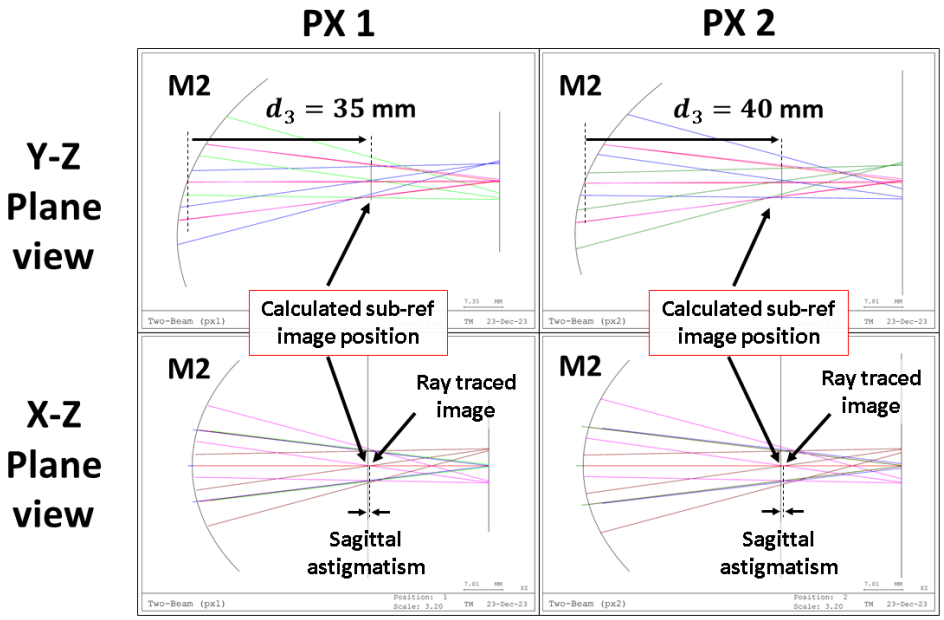


**Fig. 4.17** Cross-section and close up views of final image.

### 4.4.3 PO simulations

We conduct PO simulations at 385 GHz, 442 GHz, and 500 GHz to obtain the fields at the sub-reflector, far-fields on the sky, and to calculate aperture efficiency, as done in the same manner as in the previous sections. The two-beam multibeam receiver optics from Section, 4.4.2 were modeled in GRASP and is shown in Fig. 4.18. Each pixel was simulated by propagating a beam from feed to sky independently.

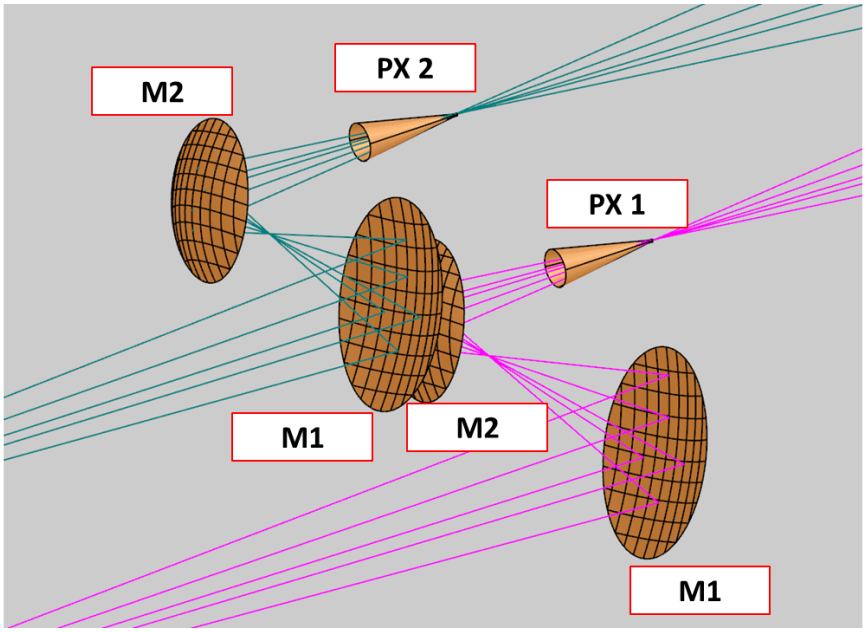


**Fig. 4.18** Stacked unit cell design of a two beam multibeam receiver in GRASP.

#### 4.4.3.1 Fields at Sub-Reflector

The illumination on the sub-reflector was calculated by setting two different reference spheres centered at the corresponding off-axis Cassegrain focus for each pixel. The field magnitude distribution is shown in Fig. 4.19, and their symmetrical and asymmetrical cuts are shown in Fig. 4.20. The left column shows the plots for PX 1 and the right for PX 2. The dotted line shows the angular extent of the sub-reflector seen from the respective off-axis Cassegrain focus. The cuts correspond to the area inside the dotted lines in Fig. 4.19 showing the profiles inside the angular range of the sub-reflector between $-0.064 \leq u, v \leq 0.064$ radians. The phase difference distribution between the reference sphere and the receiver beam is shown in Fig. 4.21 with the cuts shown in Fig. 4.22. The phase plots are limited to the range of the sub-reflector.

The field magnitude reveals a heavily distorted illumination at the sub-reflector. A larger fraction of power is also seen spilled out of the sub-reflector with a much more gradual decay. The cuts show the same distortion seen in the two-mirror optics in the previous section but at a amplified scale. The phase patterns show more deviation from the reference sphere surface. Particularly, we see a even term polynomial function in the symmetrical cuts including a distinct fourth-order term in the symmetrical cuts which resembles spherical aberrations. The illumination edge taper is consistent at the three frequencies showing a -12 dB truncation at in the symmetrical cuts. However, the mirrors are adding more aberrations into the system which all sum together to produce a distorted beam shape that depends on the frequency.

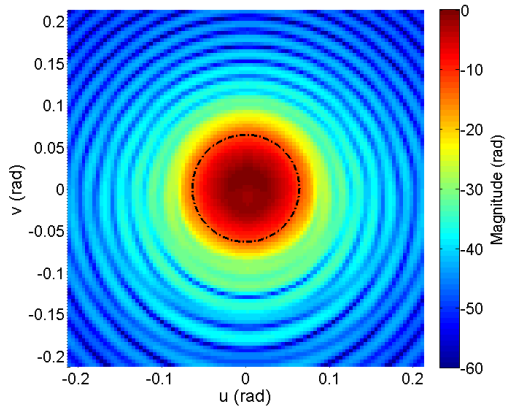


**(a)** PX 1: 385 GHz

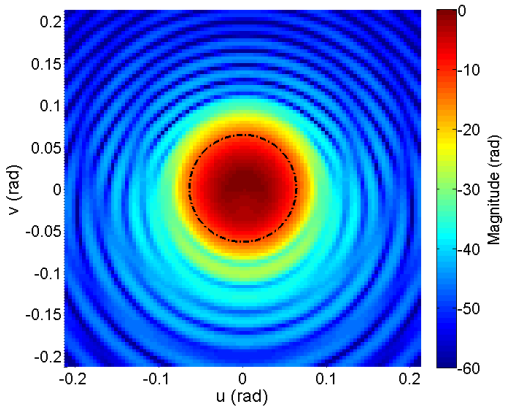


**(b)** PX 2: 385 GHz

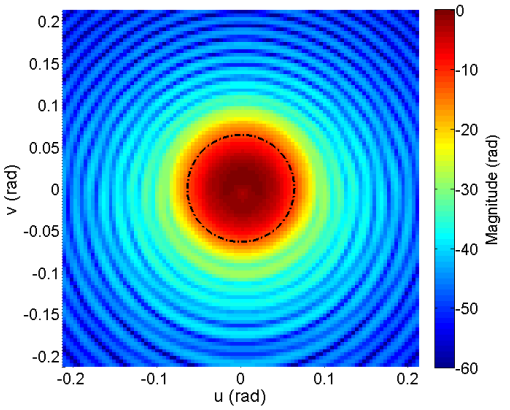


**(c)** PX 1: 442 GHz

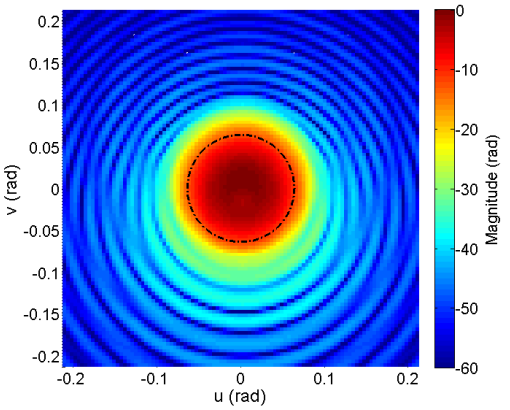


**(d)** PX 2 :442 GHz

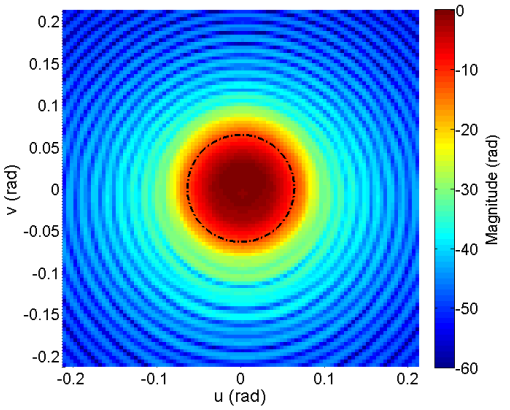


**(e)** PX 1: 500GHz

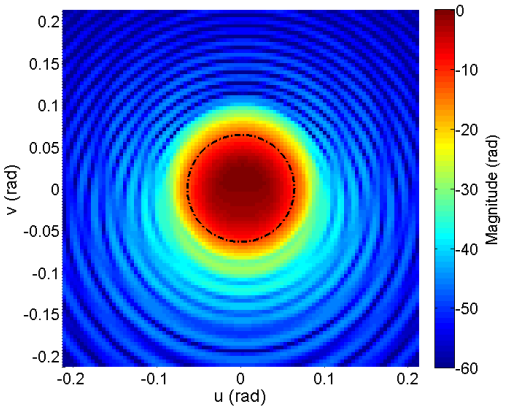


**(f)** PX 2: 500 GHz

**Fig. 4.19** The symmetrical and asymmetrical cuts of the field magnitude at the sub-reflector from the two-beam multibeam receiver.

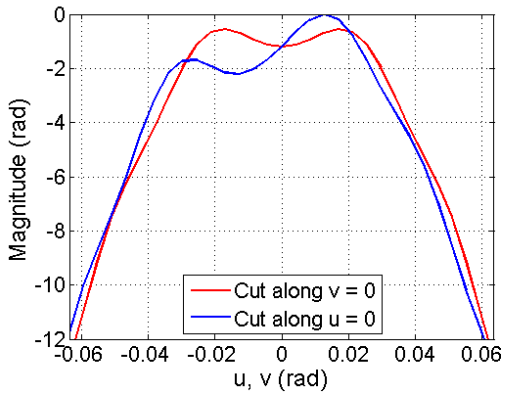


**(a)** PX 1: 385 GHz

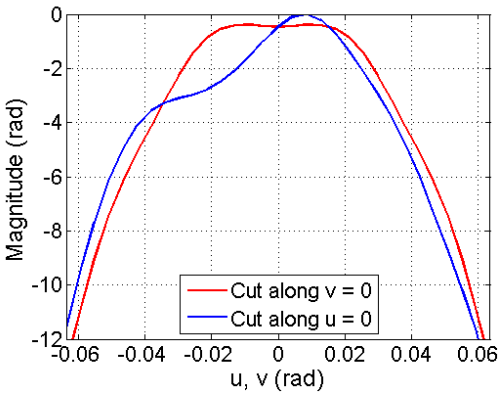


**(b)** PX 2: 385 GHz

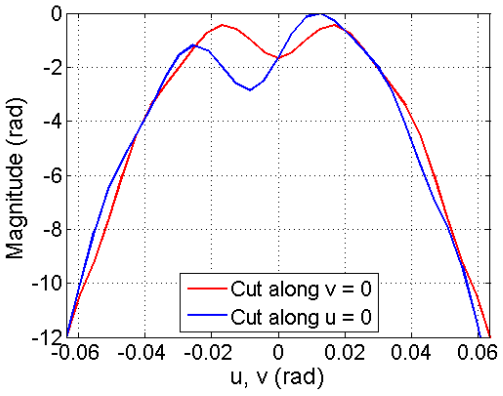


**(c)** PX 1: 442 GHz

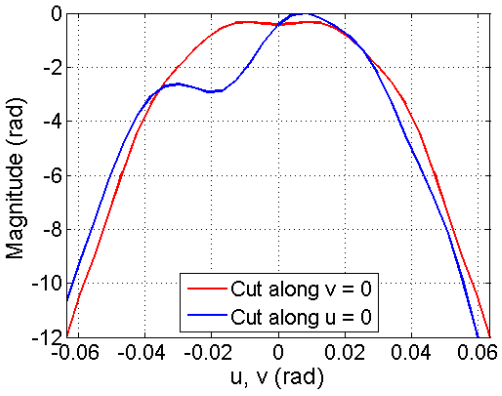


**(d)** PX 2 :442 GHz

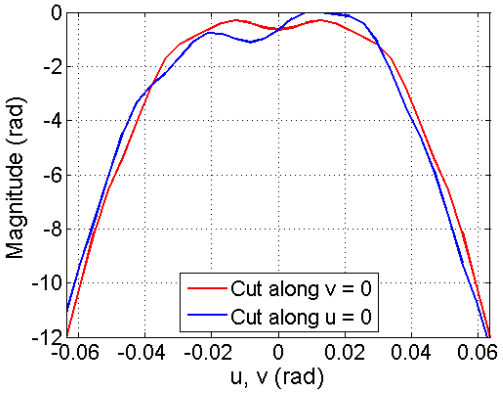


**(e)** PX 1: 500GHz

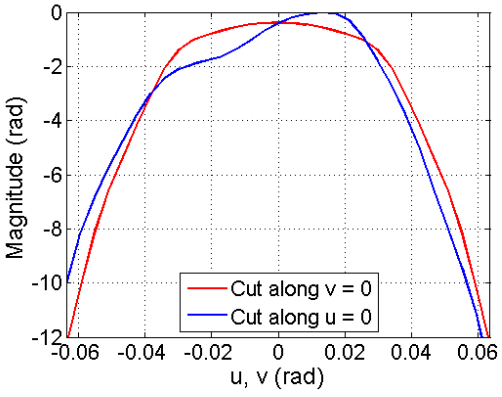


**(f)** PX 1: 500 GHz

**Fig. 4.20** The symmetrical and asymmetrical cuts of the field magnitude at the sub-reflector from the two-beam multibeam receiver.

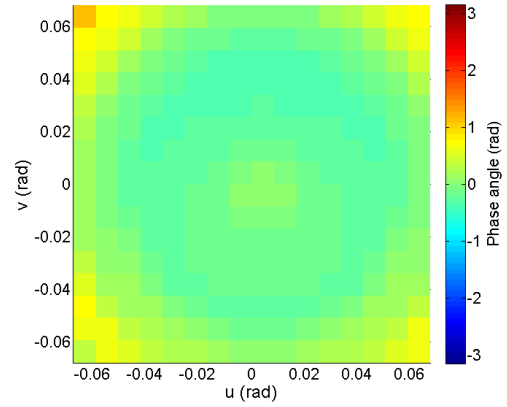


**(a)** PX 1: 385 GHz

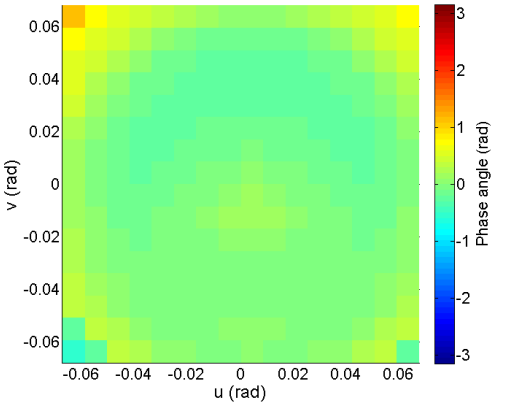


**(b)** PX 2: 385 GHz

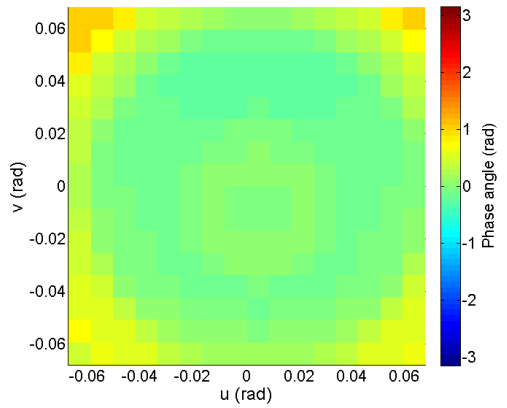


**(c)** PX 1: 442 GHz

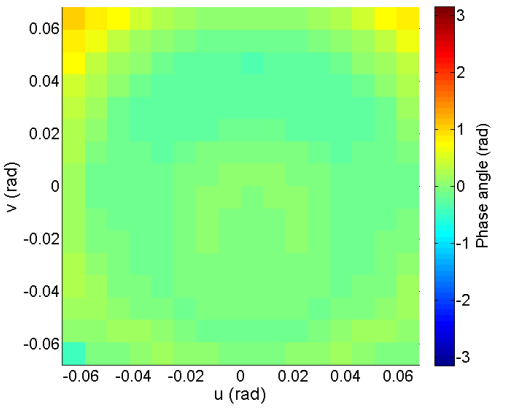


**(d)** PX 2 :442 GHz

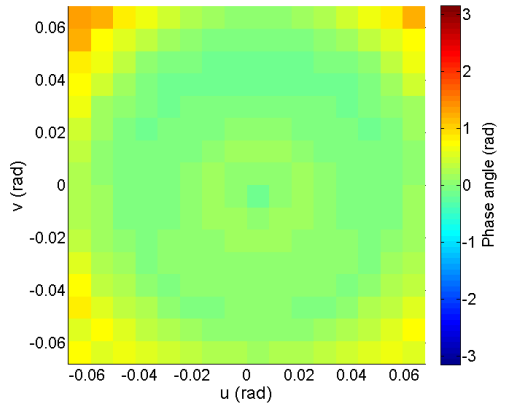


**(e)** PX 1: 500 GHz

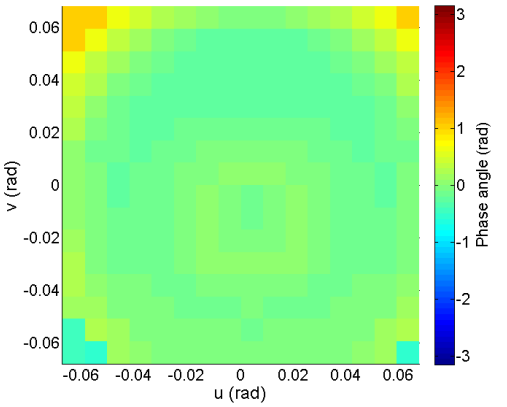


**(f)** PX 1: 500 GHz

**Fig. 4.21** The phase difference distribution between the reference sphere and the receiver beam from the two-beam multibeam receiver.

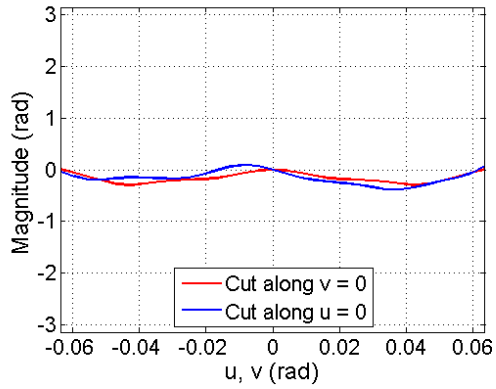


**(a)** PX 1: 385 GHz

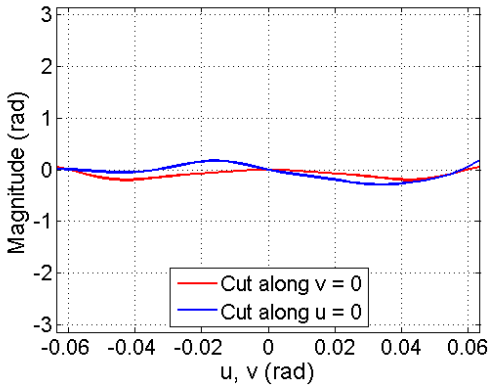


**(b)** PX 2: 385 GHz

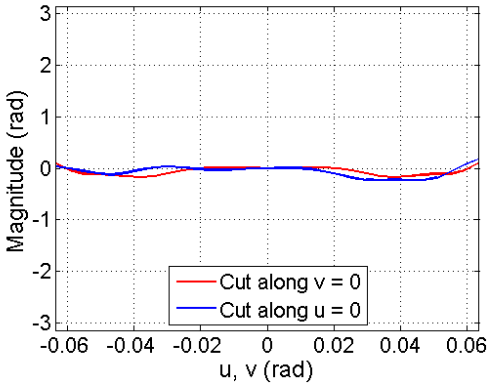


**(c)** PX 1: 442 GHz

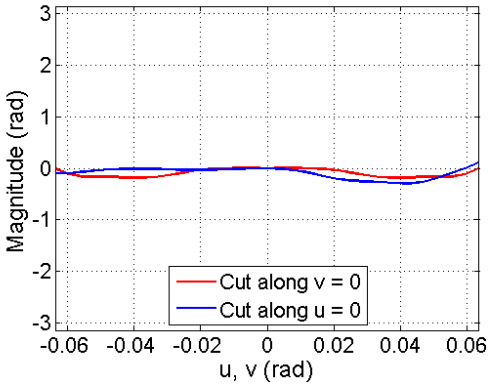


**(d)** PX 2 :442 GHz

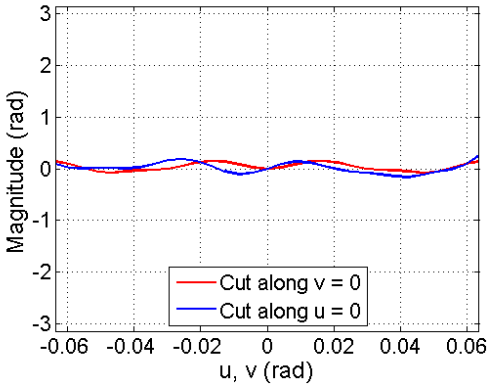


**(e)** PX 1: 500 GHz

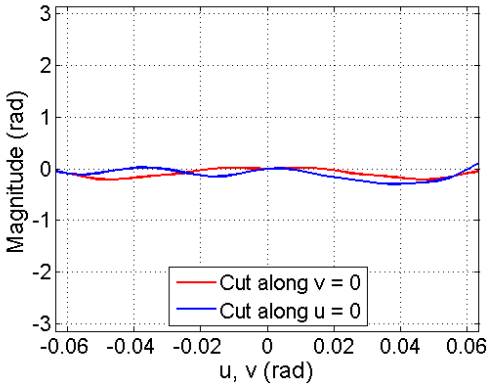


**(f)** PX 1: 500 GHz

**Fig. 4.22** The symmetrical and asymmetrical cuts of the phase difference at the sub-reflector from the two-beam multibeam receiver.

#### 4.4.3.2 Beams on Sky

The far-fields on the sky were calculated with the $u-v$ plane centered at each pixels expected peak position given by their incident angles. The far-fields of both pixels are shown in Fig. 4.23 for the Co-Pol, Fig. 4.24 for the Xs-pol, and Fig. 4.25 for the cuts.

The far-fields directly show the effect of the distorted illumination at the sub-reflector. The asymmetrical cuts along $u = 0$ show the first sidelobe is being affected heavily by the aberrations introduced by the mirrors.

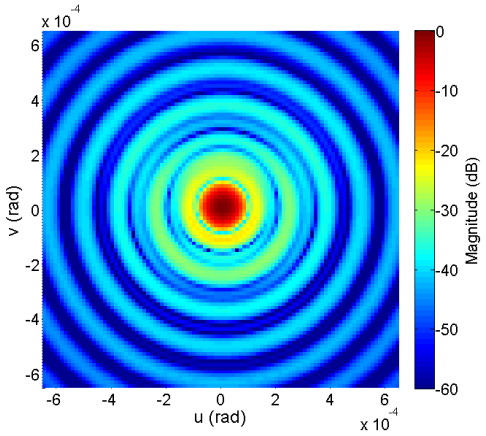


**(a)** PX 1: 385 GHz

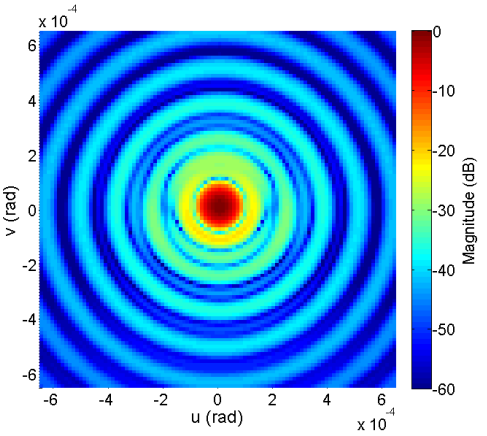


**(b)** PX 2: 385 GHz

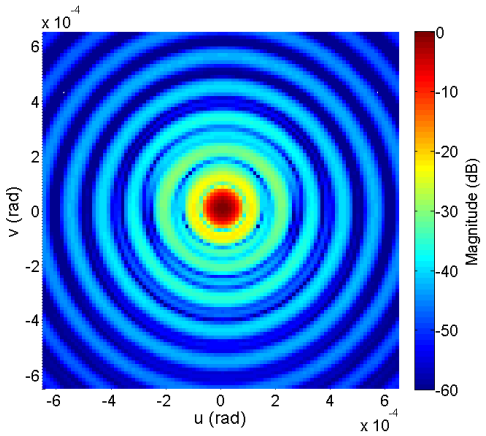


**(c)** PX 1: 442 GHz

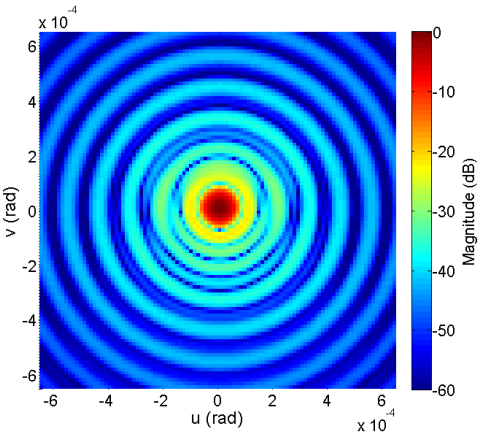


**(d)** PX 2: 442 GHz

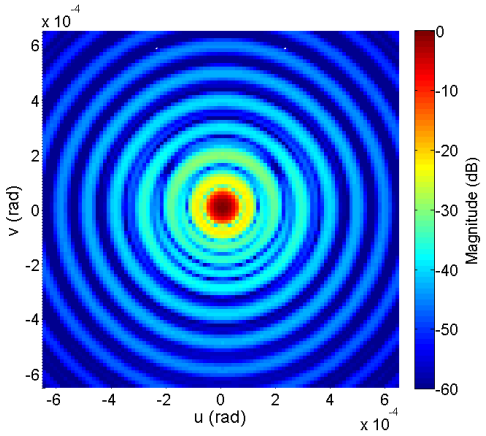


**(e)** PX 1: 500 GHz

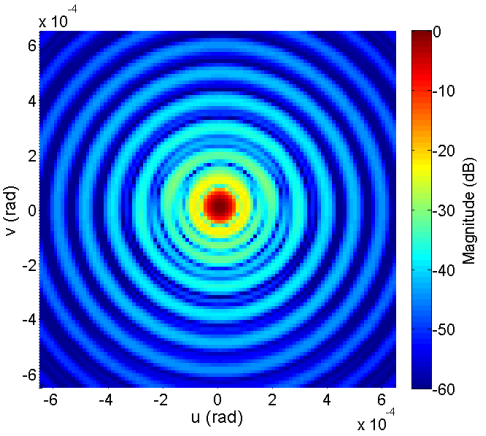


**(f)** PX 2: 500 GHz

**Fig. 4.23** The Co-Pol far-field pattern on the sky from both pixels of the two-beam multibeam receiver.

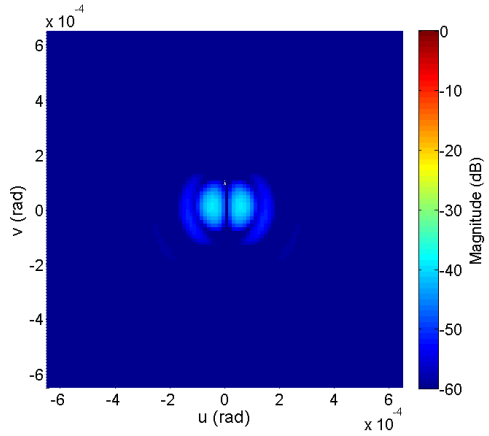


**(a)** PX 1: 385 GHz

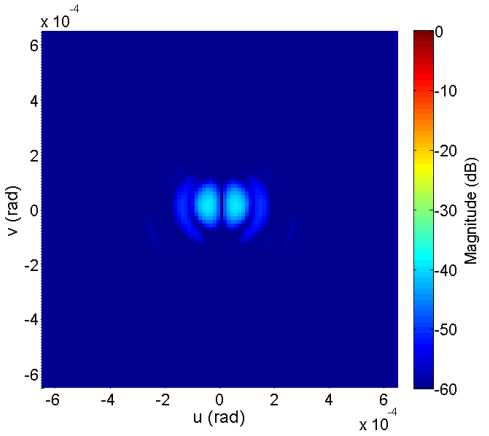


**(b)** PX 2: 385 GHz

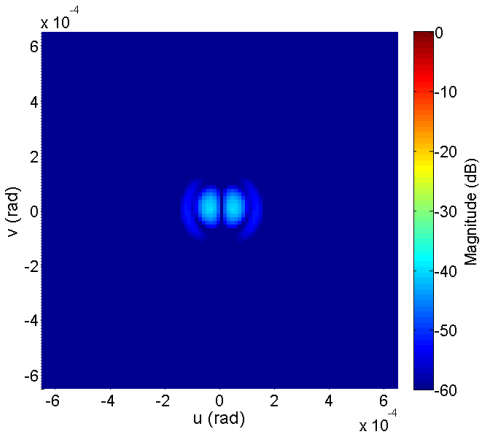


**(c)** PX 1: 442 GHz

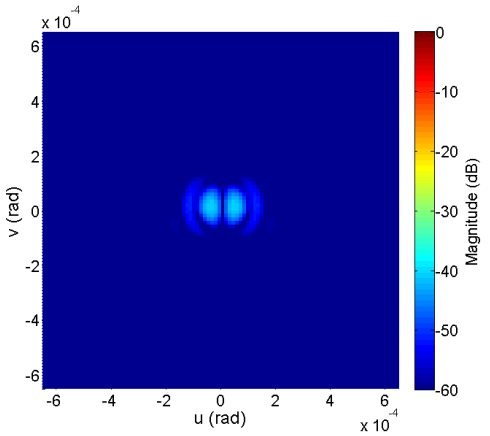


**(d)** PX 2: 442 GHz

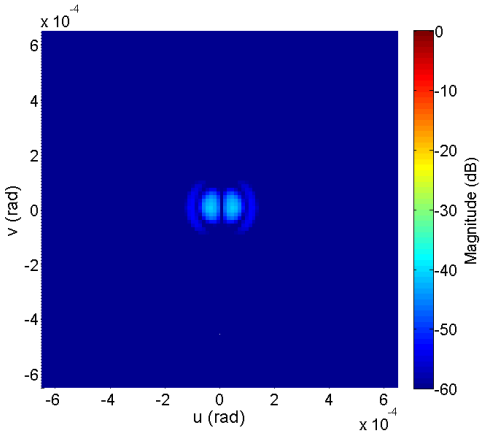


**(e)** PX 1: 500 GHz

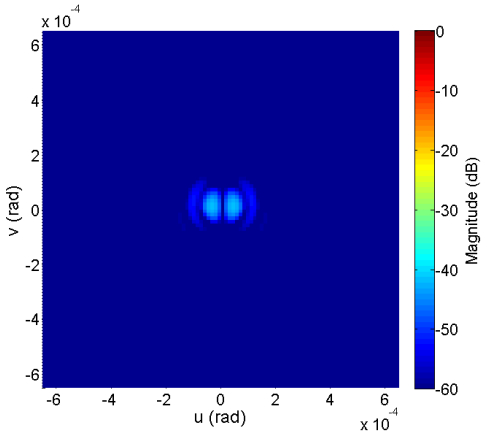


**(f)** PX 2: 500 GHz

**Fig. 4.24** The Xs-Pol far-field pattern on the sky from both pixels of the two-beam multibeam receiver.

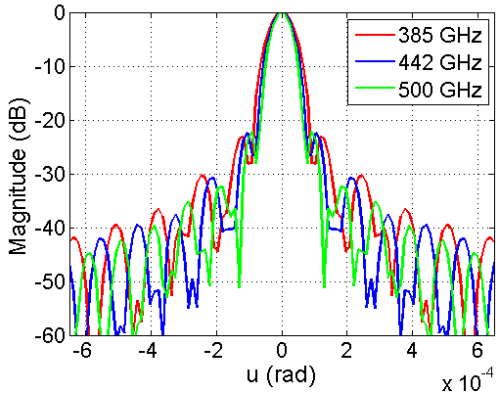


**(a)** PX 1 Co-Pol: Cut along $v = 0$

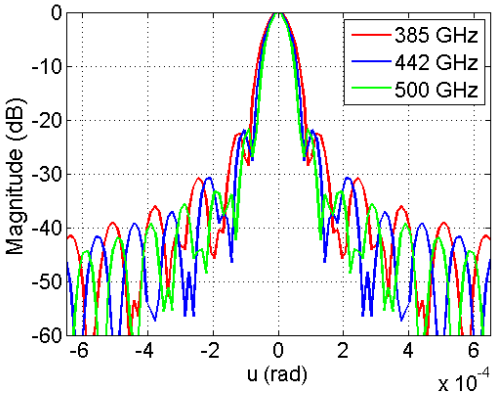


**(b)** PX 2 Co-Pol: Cut along $v = 0$

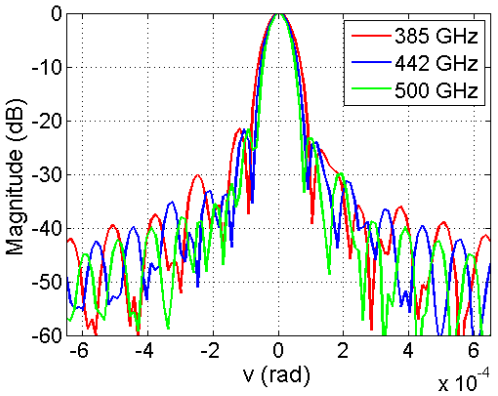


**(c)** PX 1 Co-Pol: Cut along $u = 0$

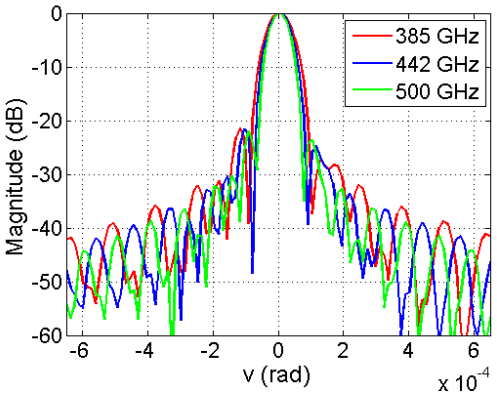


**(d)** PX 2 Co-Pol:Cut along $u = 0$

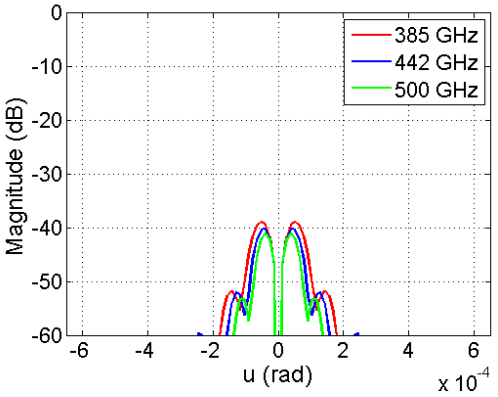


**(e)** PX 1 Xs-Pol: Cut along $v = 0$

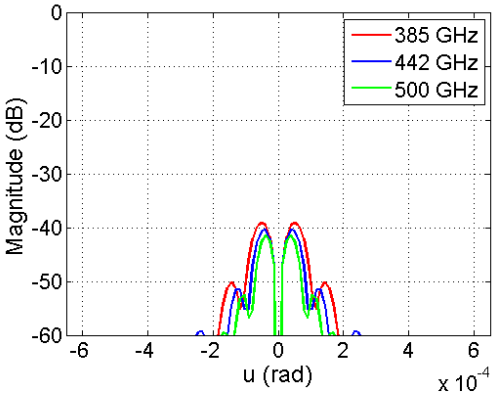


**(f)** PX 2 Xs-Pol: Cut along $v = 0$

**Fig. 4.25** The symmetrical and asymmetrical cuts of the Co-Pol and Xs-Pol patterns from the two-beam multibeam receiver.

#### 4.4.3.3 Beam Peak Positions and Separation

The $u$-$v$ plane origins were offset for both beams corresponding to their expected peak position. The beams had minimal beam squint and were centered at their origins. The relative peak positions of beams are overlaid and are shown in Fig. 4.26. The relative peak positions have a peak-to-peak separation on the sky of $\delta\theta = 0.026$ degrees. The beam size is $\lambda/D = 6.49 \times 10^{-5}$ radians or 0.0037 degrees at 385 GHz and $\lambda/D = 5.00 \times 10^{-5}$ radians or 0.0029 degrees at 500 GHz. Thus, this two-beam multibeam receiver has a relative peak-to-peak separation of about 7 beams at 385 GHz and 9 beams at 500 GHz.

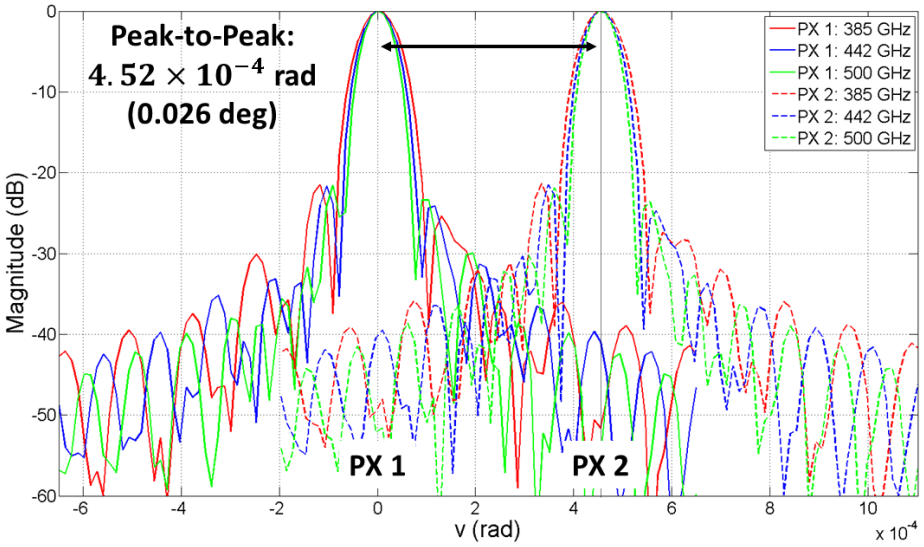


**Fig. 4.26** The overlay of the asymmetrical cuts of two-beam optics showing their relative peak positions. PX 1 was centered at $v = 0$.

#### 4.4.3.4 Aperture Efficiency

The aperture efficiencies are summarized in Table. 4.4. The aperture efficiency on the sky was lower than 0.80, however, the aperture efficiency defined at the sub-reflector shows greater than 0.80 for almost all frequencies of both definitions. Both definitions at the sub-reflector assume some ideal conditions such as an ideal spherical wave for the incident wave and negligible spill-over at the receiver optics. As a result, the maximum difference between the aperture efficiency on the sky and at the sub-reflector was 5.2% showing these definitions may overestimate the maximum aperture efficiency by a notable factor.

## 4.5 Optimizations Using Ray Tracing

### 4.5.1 Optimization Method

Mirrors surfaces can be altered to freeform surfaces and can be optimized to direct rays towards a desired direction. This can be used to reduce the aberrations and create an image at a

**Table 4.4** Aperture efficiencies of two-beam multibeam optics

| | | 385 [GHz] | 442 [GHz] | 500 [GHz] | $1 - \frac{\eta_{385}}{\eta_{500}}$ (%) |
|---|---|---|---|---|---|
| PX 1 | $\eta_A$ | 0.7666 | 0.7815 | 0.7906 | 3.04 |
| | $\eta_{\text{sub, feed}}$ | 0.7886 | 0.8016 | 0.8118 | 2.86 |
| | $\eta_{\text{sub, beam}}$ | 0.8089 | 0.8187 | 0.8264 | 2.12 |
| PX 2 | $\eta_A$ | 0.7794 | 0.7890 | 0.7973 | 2.25 |
| | $\eta_{\text{sub, feed}}$ | 0.8076 | 0.8187 | 0.8351 | 3.29 |
| | $\eta_{\text{sub, beam}}$ | 0.8185 | 0.8269 | 0.8285 | 1.21 |

desired position. The optimization method will depend on the application.

To satisfy the imaging condition for frequency independent design in the ALMA antenna, the exit pupil must be placed at the horn aperture. Conversely, since the horn aperture coincides with the exit pupil, any ray from the center of the sub-reflector must pass intersect at the center of the exit pupil because it is a chief ray. This can be set as the target for the optimization. Additionally, the horn aperture plane will need to be perpendicular to the beam axis dictating the center chief rays incident angle.

The target constraint for the optimization are the following:

1. Chief rays must pass through the position corresponding to the horn aperture center.
2. The center chief ray (equivalent to the beam axis) must intersect the horn aperture center and the phase center plane with a local incident angle of $\theta = 0$.

Five rays were defined, the center chief ray, two meridional rays (+Y, -Y), and two sagittal rays (+X, -X). The incident angles of the meridional and sagittal rays into the antenna are set to the maximum beam size of $\pm 0.004$ degrees for their corresponding ray direction.

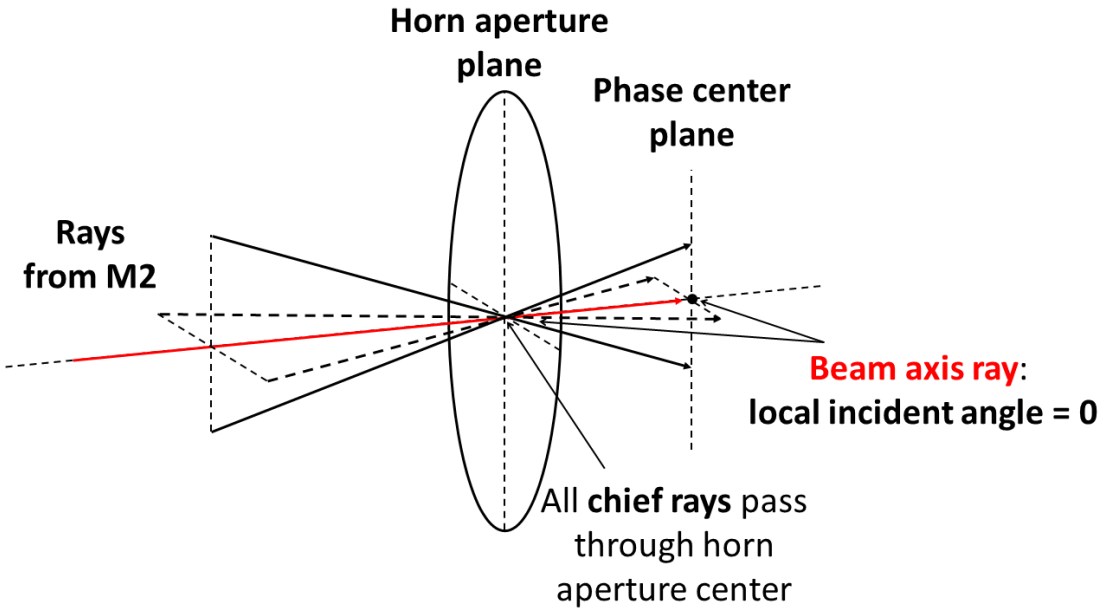


**Fig. 4.27** Diagram showing the optimization constraints on the chief rays.

### 4.5.2 Optimized Two-Beam Optics

A base anamorphic asphere was used as the freeform surface. This surface is characterized with two independent conic constants and curvature radii for the $x$ and $y$ axes. The base anamorphic asphere is given in the *CODE V Documentation Library* as,

$$z = \frac{(\text{CUX})x^2 + (\text{CUY})y^2}{1 + \sqrt{1 - (1 + \text{KX})(\text{CUX})^2x^2 - (1 + \text{KY})(\text{CUY})^2y^2}}. \tag{4.5.1}$$

Here, CUX, CUY are the $x$ and $y$ curvature at the vertex and are given by CUX $= 1/$RX and CUY $= 1/$RY, where RX and RY are the $x$ and $y$ curvature radii. The parameters KX and KY are the $x$ and $y$ conic constants.

The mirror positions (vertex coordinates $(x, y, z)$ and rotation angle about the $x$-axis $\alpha$), and the surface parameters KX, KY, RX, and RY were set as free parameters with a small range. The horn positions were fixed in place. The final optimized parameters are listed in Table. 4.5.

**Table 4.5** Optimized surface parameters for Two-Beam optics.

| | PX 1 value | | PX 2 value | |
|---|---|---|---|---|
| Parameter (Unit) | Mirror 1 | Mirror 2 | Mirror 1 | Mirror 2 |
| KX | -0.6899 | -0.2044 | -0.7989 | -0.2191 |
| KY | -0.6870 | -0.1396 | -0.7960 | -0.1938 |
| RX (mm) | -64.384 | 35.079 | -54.9433 | 34.107 |
| RY (mm) | -61.220 | 38.178 | -53.1403 | 35.276 |
| $d_1$ (mm) | 6122.562 | | 6070.333 | |
| $d_2$ (mm) | 76.331 | | 77.389 | |
| $d_3$ (mm) | 47.162 | | 46.923 | |
| $\theta_{\text{CR}}$ (deg) | 1.01 | | 1.55 | |
| $\theta_{\text{refl}}$ (deg) | 43.09 | | 50.70 | |

The optimized design is shown in Fig. 4.28. The incident angle for PX 2 was changed to $\theta_{\text{CR}} = 0.095$ degrees to allow more clearance for the mirrors to move during the optimization. The horn position was also positioned further away from PX 1 to account for the altered chief ray angle. The cross-section views in Fig. 4.29 show the ray traced sub-reflector images coincides with the horn aperture plane.

The spot diagrams for both pixels in Fig. 4.30 and Fig. 4.31 show the astigmatism contribution was mostly eliminated after the optimizations. The only remaining noticeable spot pattern is the coma, which is expected as the receivers still have a large offset from the antenna center axis and the odd-term aberrations cannot be fully eliminated unless we add more optical elements adding more degrees of freedom in the optimization. On the one hand, we may aim to reduce the coma aberration and remedy the asymmetric sidelobes it causes. On the other hand, the effect of coma on aperture efficiency is minor and will only lead to a marginal improvement in the aperture efficiency. Moreover, the peak position was not affected much by the beam squint. As a result, the overall effect of coma does not need to be prioritized and the other aberrations

such as defocus, spherical, and astigmatism should be prioritized.

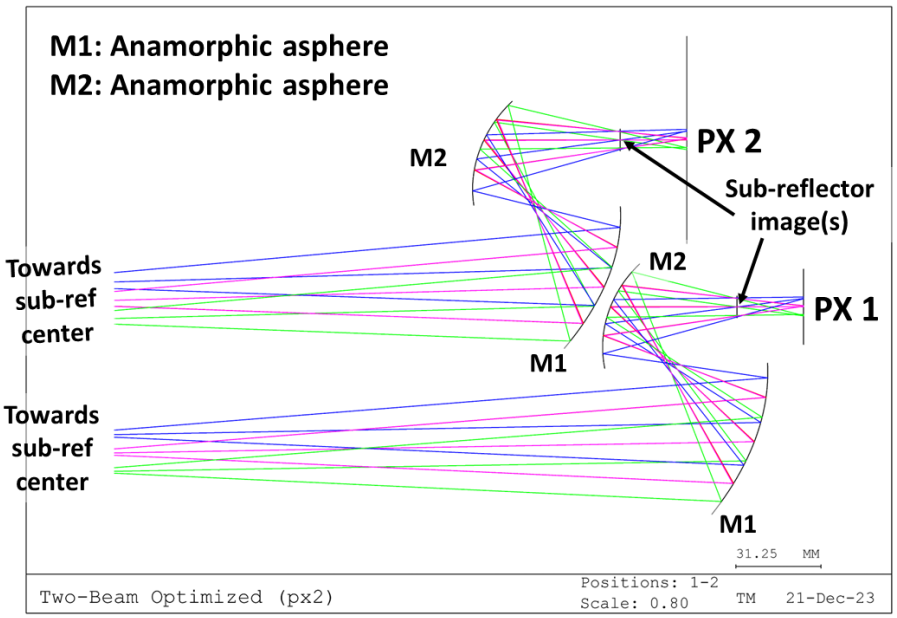


**Fig. 4.28** Stacked unit cell design of a two beam multibeam receiver in CODE V.

### 4.5.3 Modeling and Analysis with PO

The optimized mirror surfaces were recreated in GRASP using the built-in pseudo spline surface function. A grid of surface points were sampled and interpolated to generate a best fit surface. The grid density along the rim vicinity was set to be twice that of the center region to account for the large curvature at the vertex along the minor axis. The model is shown in Fig. 4.32. Mirror 2 of PX 2 had a small minor axis radius of curvature of RX 34 mm which limits the maximum aperture diameter to roughly 70 mm. However, due to the reflection angle, the surface section near the minor axis vertex was required which led to some minor interpolation issues (the top of M2 can has a clipped edge). This can be resolved by sampling more points towards the minor vertices, however it will require more calculation time.

PO simulations were conducted at 385 GHz, 442 GHz, and 500 GHz to obtain the fields at the sub-reflector, far-fields on the sky, and to calculate aperture efficiency. Each case used the same settings for the calculation as in section 4.4.3. The only difference was the reference sphere center for PX 2 was changed to match the new position due to the larger chief ray angle and the origin of the $u - v$ plane for the far-fields was centered at the expected peak position.

#### 4.5.3.1 Fields at Sub-Reflector

The field magnitude at the sub-reflector from both pixels, the phase differences between the reference spheres, and their symmetrical and asymmetrical cuts are summarized in Fig. 4.33, Fig. 4.34, Fig. 4.35, and Fig. 4.36, respectively.

The field magnitude shows more power was concentrated inside the sub-reflector range compared to the un-optimized two-beam optics. Some distortion caused by the rim of M2 of PX 2 can be seen. The interference pattern can be explained as a large phase mismatch is being

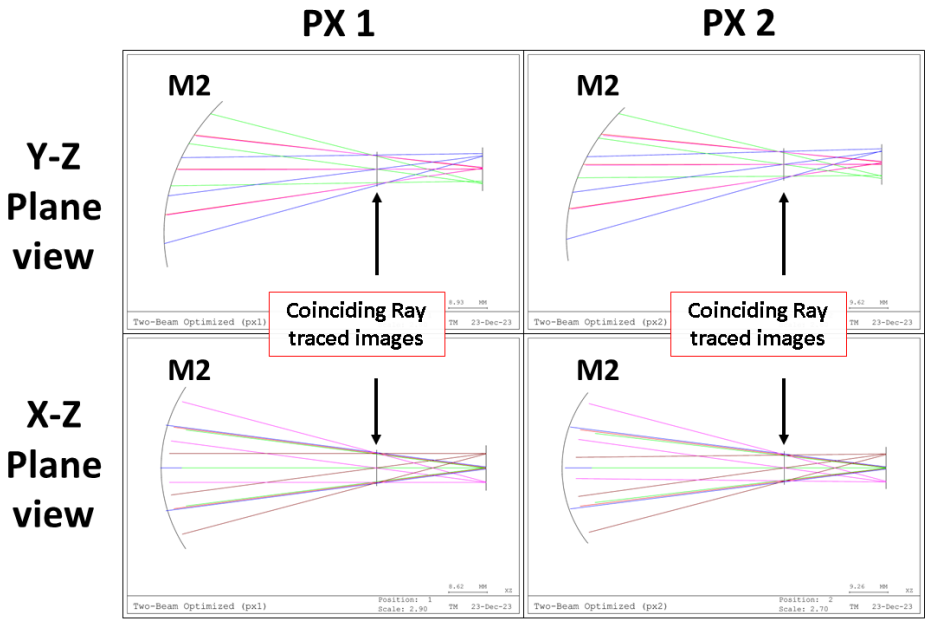


**Fig. 4.29** Cross-section and close up views of final image of optimized two-beam multibeam receiver.

induced by the different curvature from optimized surface shape and the interpolated surface shape. The field magnitude profiles show a bulge at the center which can be explained by the shaping of the reflectors into asymmetric shapes.

The phase patterns still show some ripples caused by the aberrations introduced by the mirrors, however they have a much more subtle magnitude inside the range of the sub-reflector compared to the un-optimized optics.

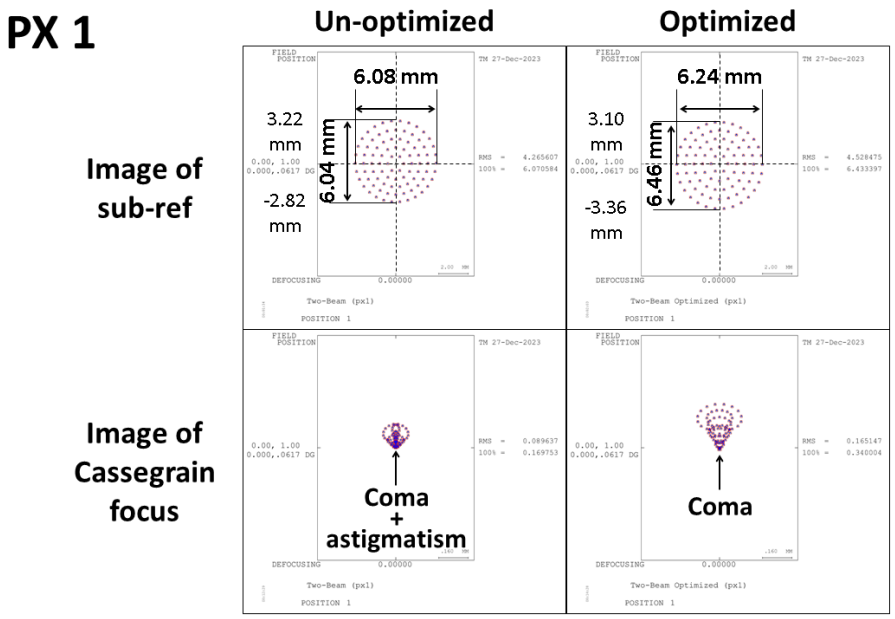


**Fig. 4.30** The comparison between spot diagrams before and after the optimization for PX 1.

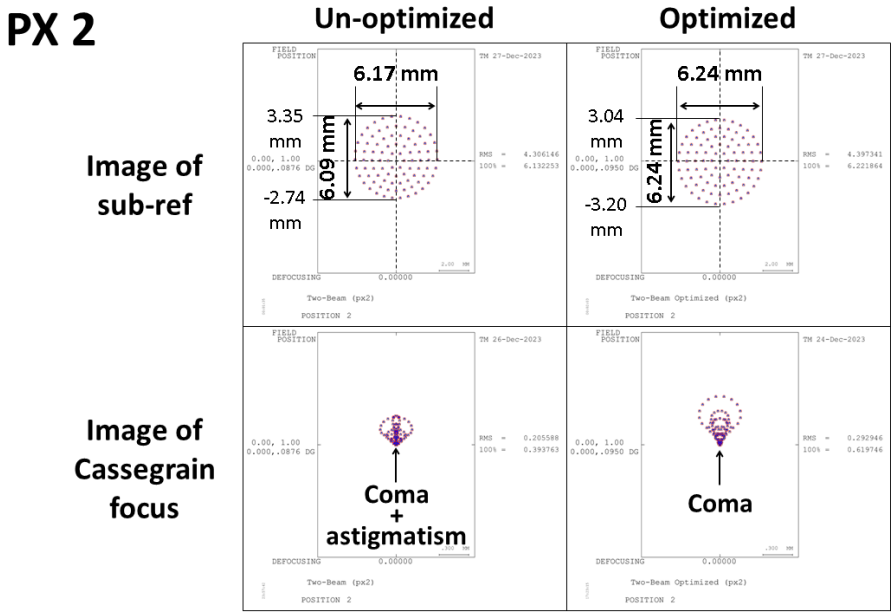


**Fig. 4.31** The comparison between spot diagrams before and after the optimization for PX 1.

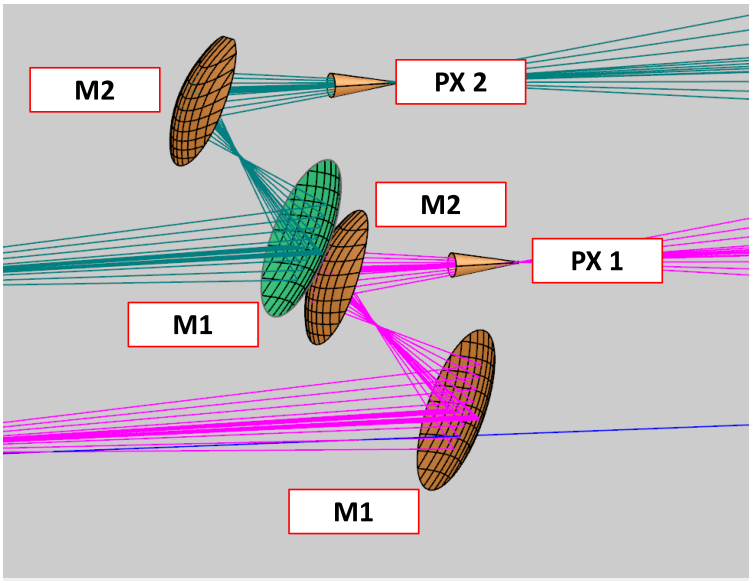


**Fig. 4.32** Two-Beam optics after optimizations modeled in GRASP.

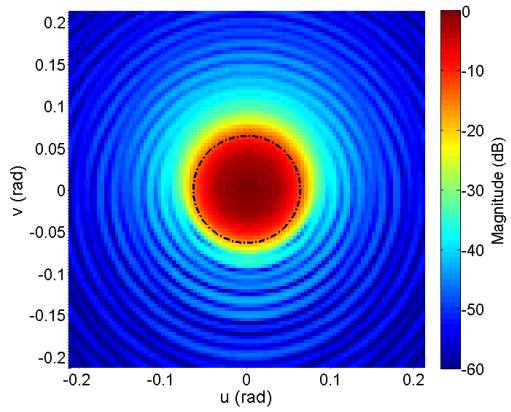


**(a)** PX 1: 385 GHz

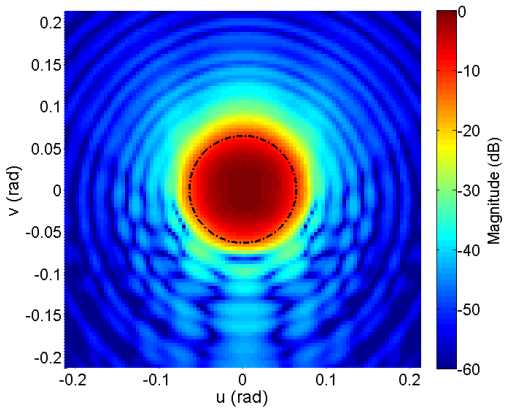


**(b)** PX 2: 385 GHz

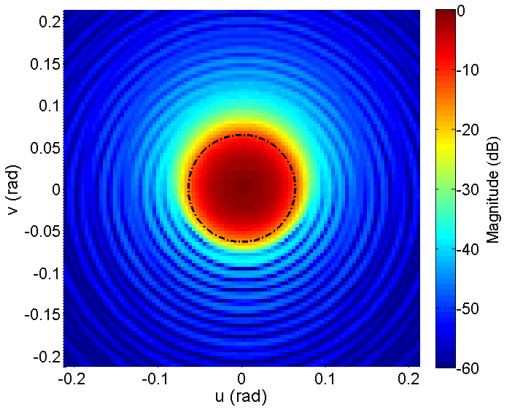


**(c)** PX 1: 442 GHz

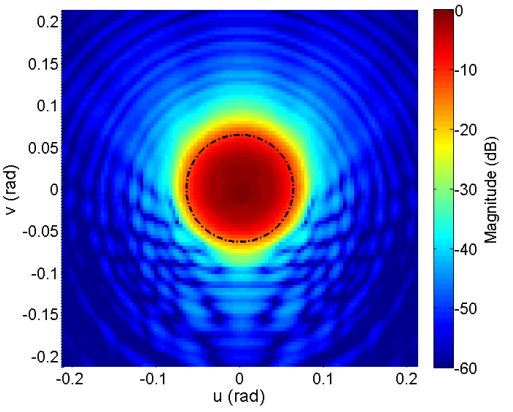


**(d)** PX 2: 442 GHz

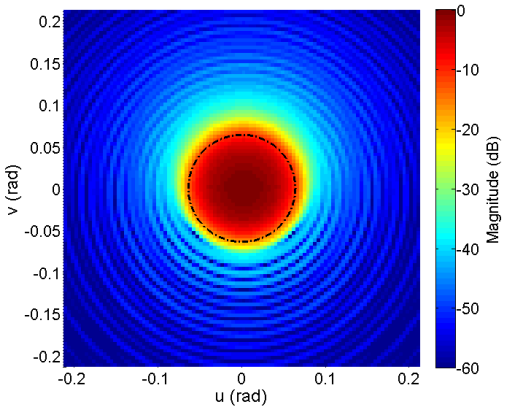


**(e)** PX 1: 500 GHz

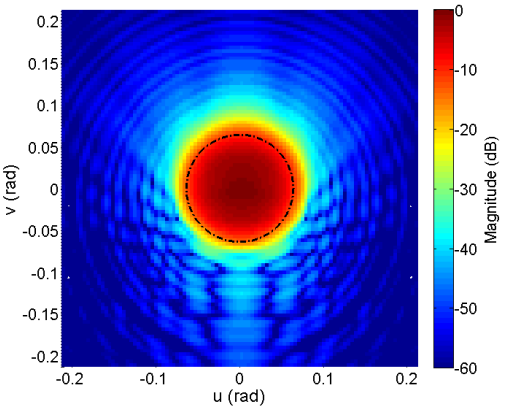


**(f)** PX 2: 500 GHz

**Fig. 4.33** Field magnitude at the sub-reflector using the two-beam optics with optimized surface shapes.

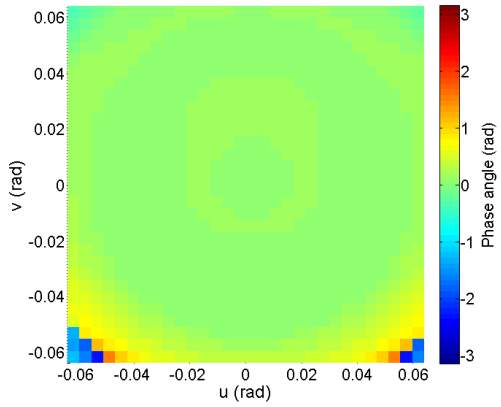


**(a)** PX 1: 385 GHz

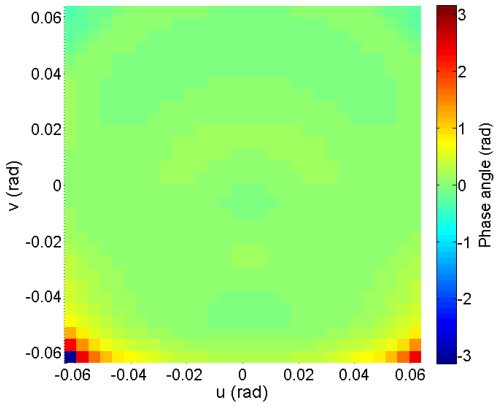


**(b)** PX 2: 385 GHz

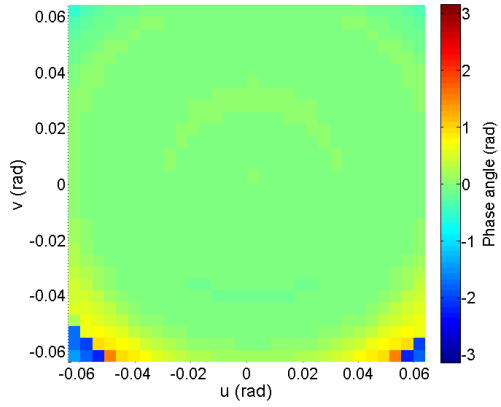


**(c)** PX 1: 442 GHz

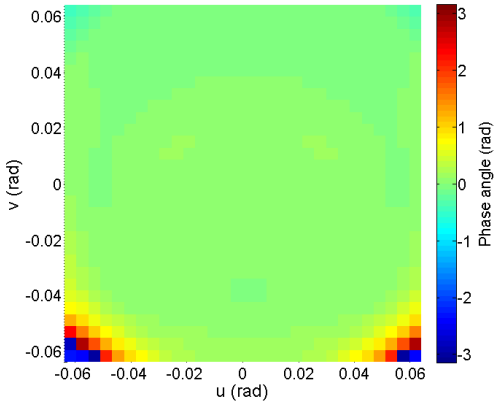


**(d)** PX 2: 442 GHz

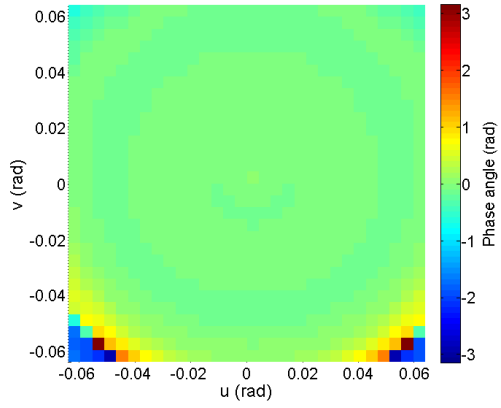


**(e)** PX 1: 500 GHz

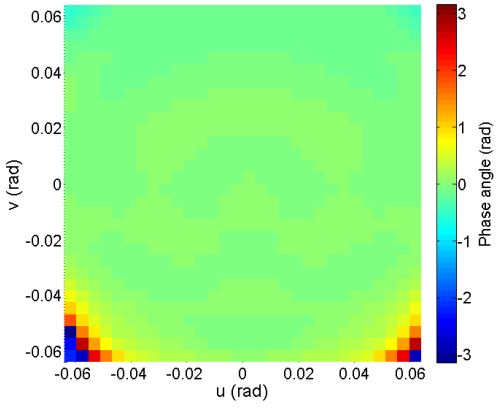


**(f)** PX 2: 500 GHz

**Fig. 4.34** The phase difference between the reference sphere and receiver beam using the with optimized surface shapes.

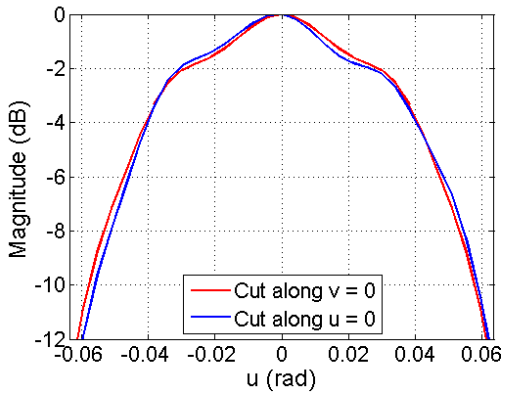


**(a)** PX 1: 385 GHz

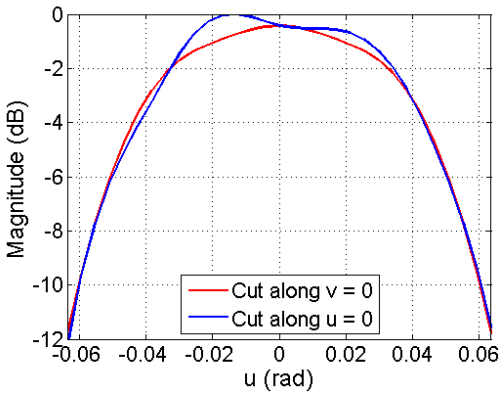


**(b)** PX 2: 385 GHz

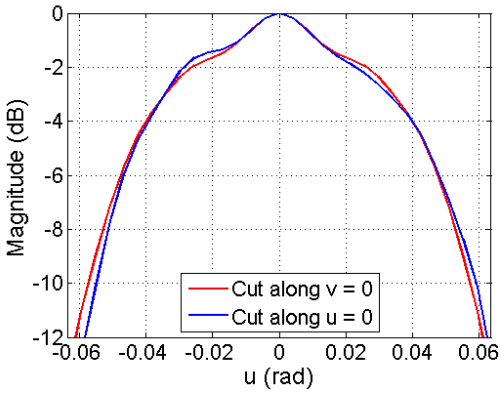


**(c)** PX 1: 442 GHz

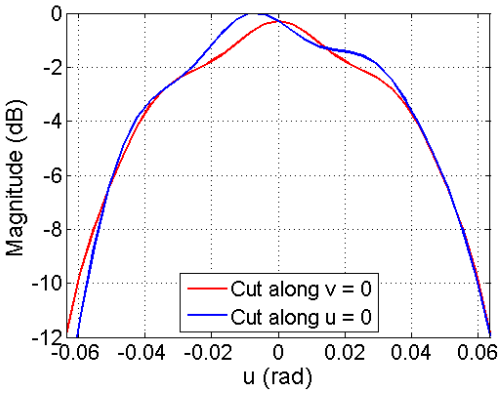


**(d)** PX 2: 442 GHz

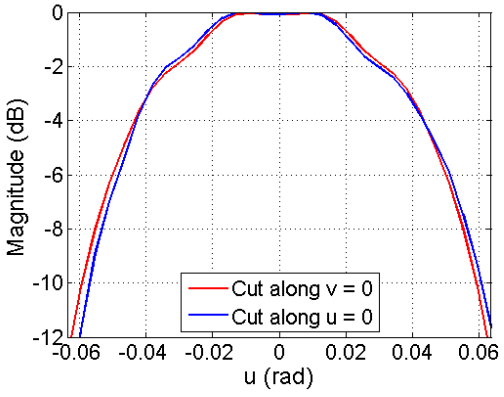


**(e)** PX 1: 500 GHz

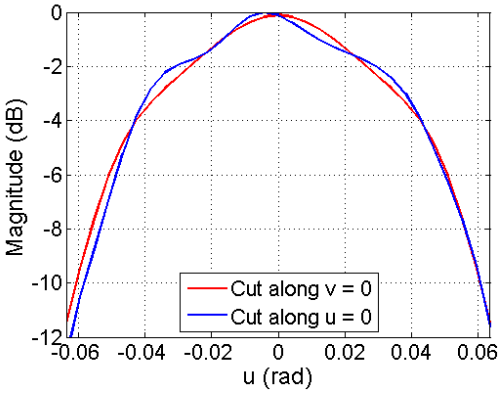


**(f)** PX 2: 500 GHz

**Fig. 4.35** The symmetrical and asymmetrical cuts of the field magnitude at the sub-reflector using the two-beam optics with optimized surface shapes.

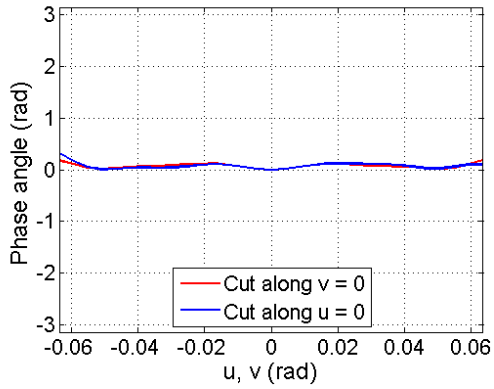


**(a)** PX 1: 385 GHz

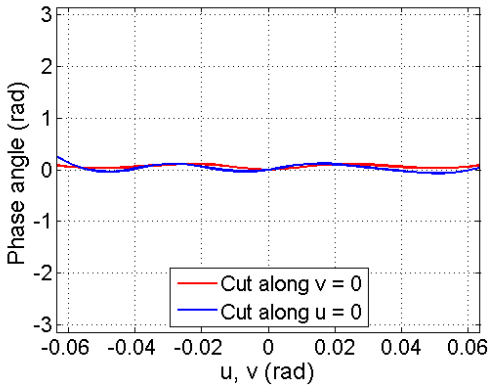


**(b)** PX 2: 385 GHz

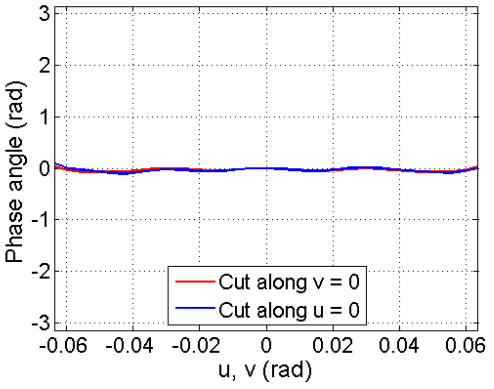


**(c)** PX 1: 442 GHz

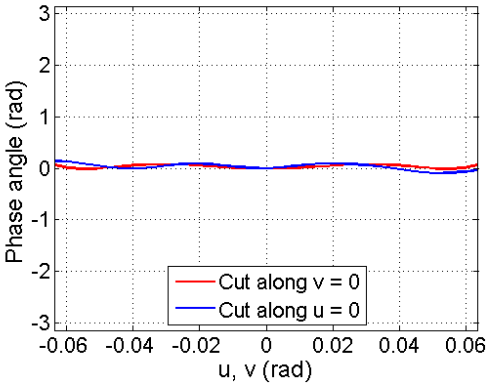


**(d)** PX 2: 442 GHz

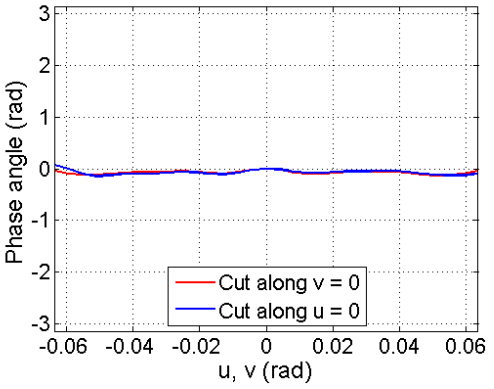


**(e)** PX 1: 500 GHz

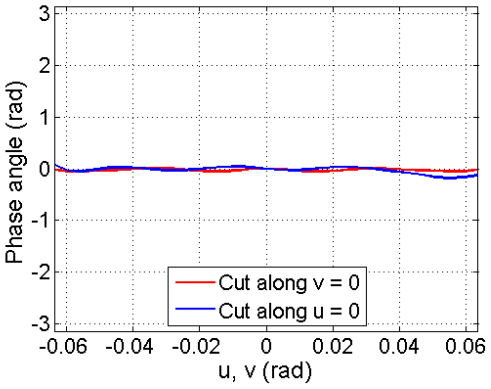


**(f)** PX 2: 500 GHz

**Fig. 4.36** The symmetrical and asymmetrical cuts of the phase difference at the sub-reflector using the two-beam optics with optimized surface shapes.

#### 4.5.3.2 Far-Fields

The $u-v$ planes origins were centered at the two expected peak positions for their respective pixels. The Co-Pol pattern on the sky is shown in Fig. 4.37 and the Xs-Pol pattern in Fig. 4.38, and their cuts in Fig. 4.39.

The Co-Pol pattern show more concentric sidelobes compared to the un-optimized optics expect for PX 2 which shows a distorted feature in the positive $v$ direction. There will be in general more coma aberrations because the pixel position was moved further offset from the antenna center axis. However, this distortion can be attributed to the interpolated and clipped mirror 2 of PX 2 and can be assumed to be an artificial feature. We may expect to see a more symmetrical beam shape if we sample more points near the minor vertex of M2 of PX 2 for the interpolation.

The shaped mirrors had very little contribution to the Xs-pol with the maximum Xs-pol level only increasing by 0.2 dB compared to the un-optimized optics.

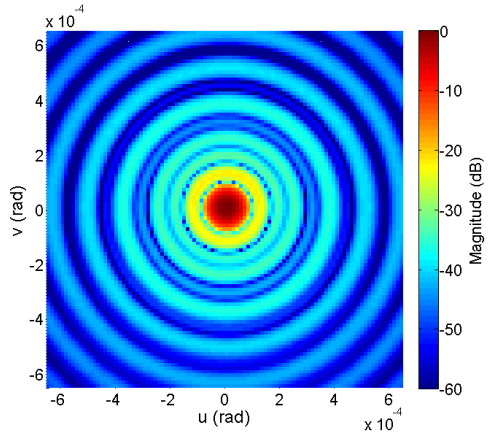


**(a)** PX 1: 385 GHz

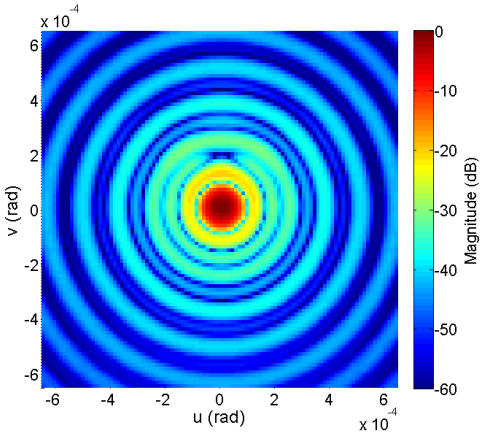


**(b)** PX 2: 385 GHz

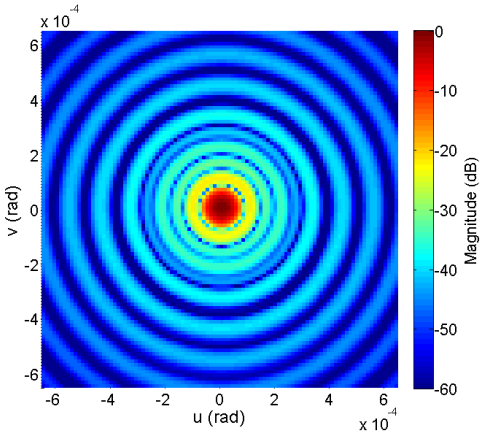


**(c)** PX 1: 442 GHz

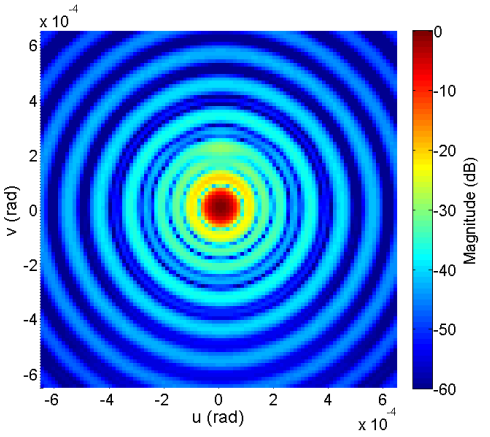


**(d)** PX 2: 442 GHz

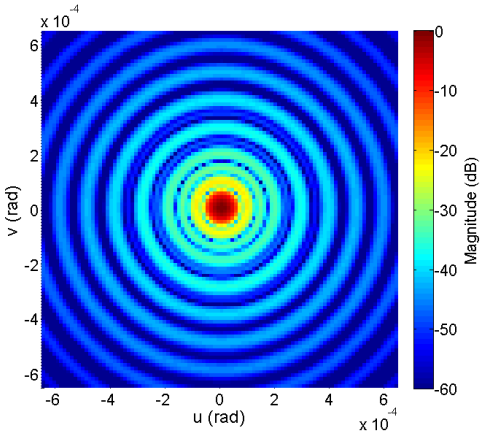


**(e)** PX 1: 500 GHz

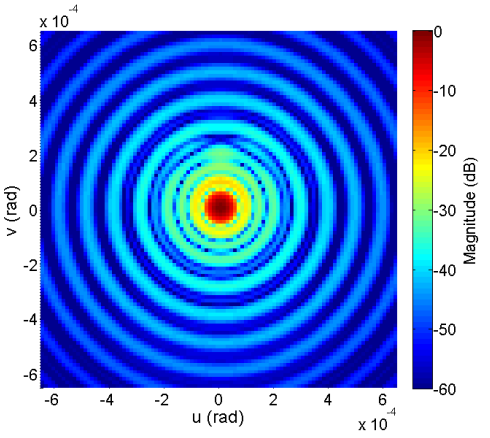


**(f)** PX 2: 500 GHz

**Fig. 4.37** The Co-Pol on the sky from two-beam design with optimized mirrors.

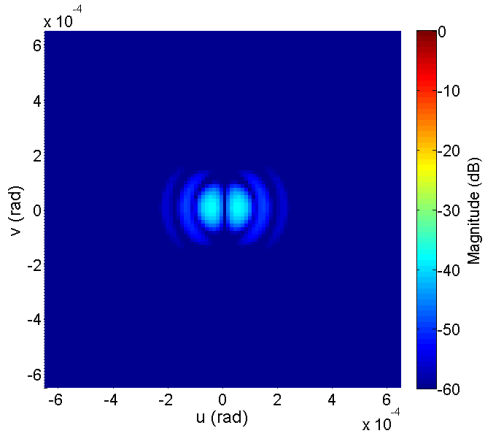


**(a)** PX 1: 385 GHz

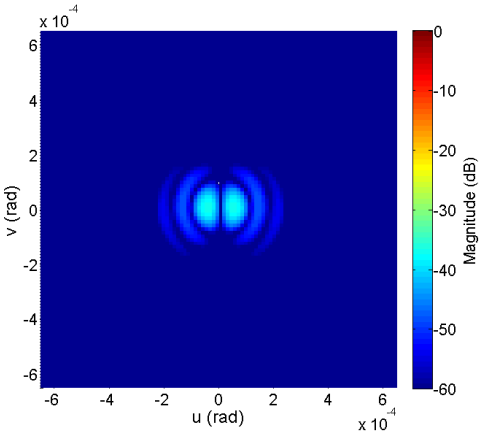


**(b)** PX 2: 385 GHz

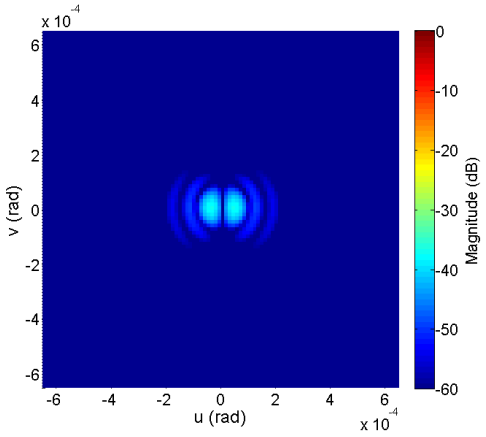


**(c)** PX 1: 442 GHz

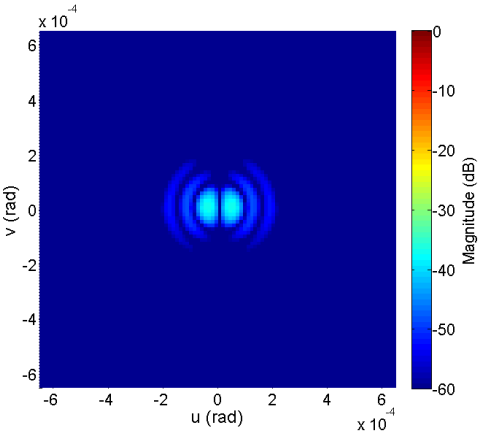


**(d)** PX 2: 442 GHz

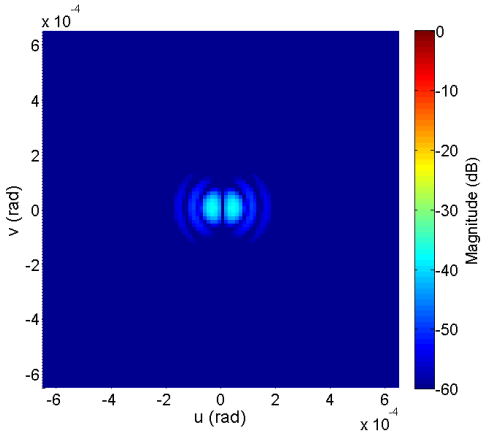


**(e)** PX 1: 500 GHz

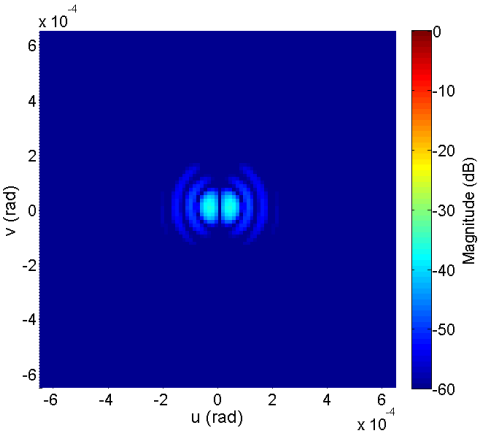


**(f)** PX 2: 500 GHz

**Fig. 4.38** The Xs-Pol on the sky from two-beam optics with optimized mirrors.

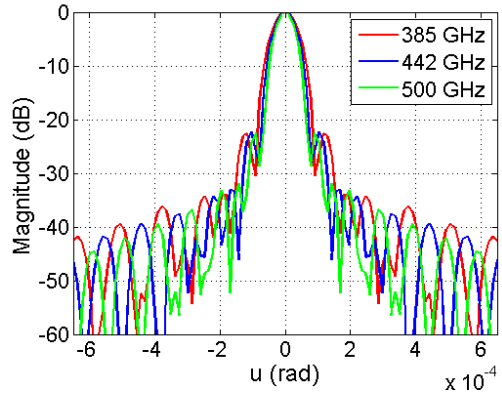


**(a)** PX 1: cut along v = 0

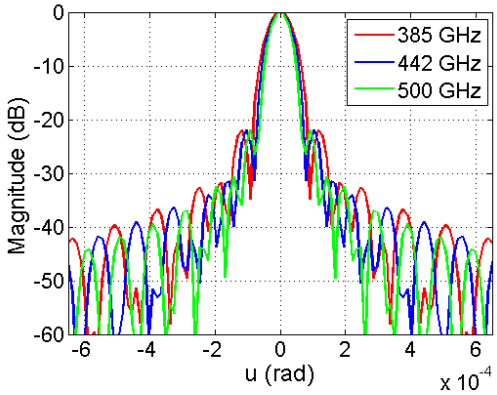


**(b)** PX 2: cut along v = 0

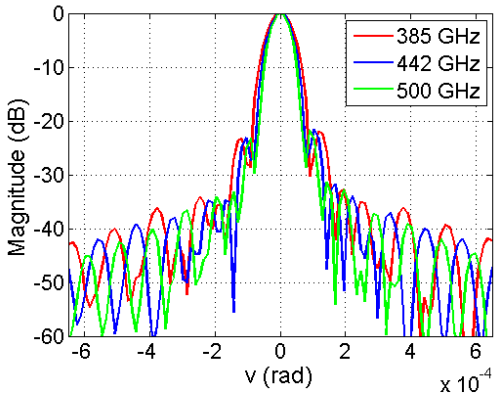


**(c)** PX 1: cut along u = 0

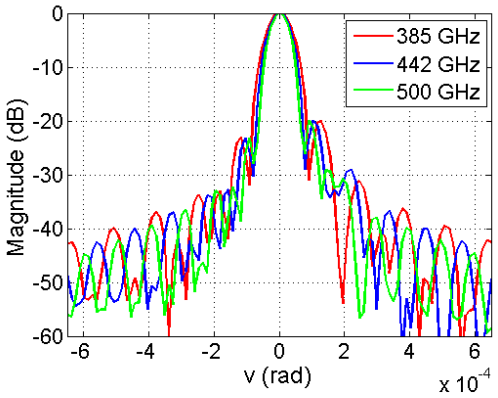


**(d)** PX 2: cut along u = 0

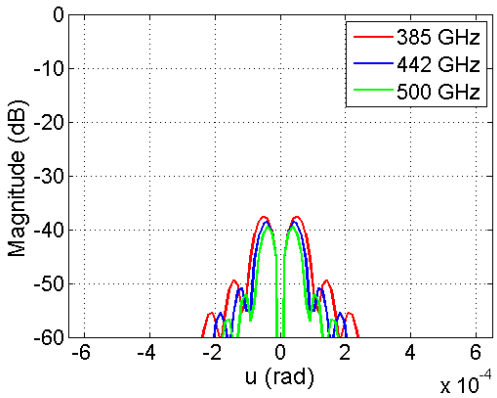


**(e)** PX 1: Cut along v = 0

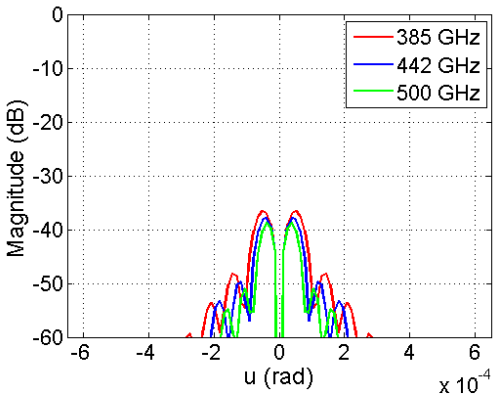


**(f)** PX 2: Cut along v = 0

**Fig. 4.39** The symmetrical and asymmetrical cuts of the Co-Pol and Xs-Pol patterns of the two-beam optics with optimized mirrors.

#### 4.5.3.3 Peak Positions and Separation

The relative peak positions were centered at their $u$-$v$ plane origins. The relative peak positions of the two-beam optics with the optimized mirrors are shown in Fig. 4.40. The relative peak-to-peak separation on the sky is $\delta\theta = 0.033$ degrees. This translates into a separation of roughly 9 beams at 385 GHz and 11 beams at 500 GHz.

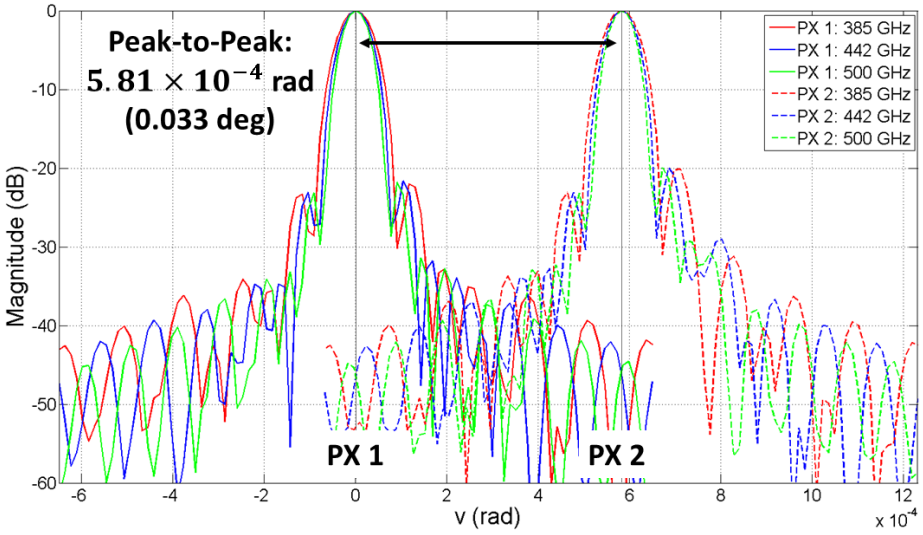


**Fig. 4.40** Overlay of asymmetrical cuts on the sky of two-beam optics with optimized mirrors. PX 1 was centered at $v = 0$.

#### 4.5.3.4 Aperture Efficiency

The aperture efficiencies of the two-beam optics with optimized mirrors are summarized in Table. 4.6. The optimization yielded a higher aperture efficiency on the sky of higher than 0.80 and is overall higher compared to the un-optimized optics. The frequency dependence was also weaker with a maximum deviation of 1.3 % at the band edges.

**Table 4.6** Aperture efficiencies of two-beam multibeam optics after optimizations

| | | 385 (GHz) | 442 (GHz) | 500 (GHz) | $1 - \frac{\eta_{385}}{\eta_{500}}$ % |
|---|---|---|---|---|---|
| PX 1 | $\eta_A$ | 0.8252 | 0.8294 | 0.8358 | 1.27 |
| | $\eta_{\text{sub, feed}}$ | 0.8387 | 0.8438 | 0.8480 | 1.10 |
| | $\eta_{\text{sub, beam}}$ | 0.8435 | 0.8476 | 0.8510 | 0.88 |
| PX 2 | $\eta_A$ | 0.8295 | 0.8355 | 0.8385 | 1.07 |
| | $\eta_{\text{sub, feed}}$ | 0.8507 | 0.8565 | 0.8606 | 1.15 |
| | $\eta_{\text{sub, beam}}$ | 0.8552 | 0.8598 | 0.8632 | 0.93 |

## 4.6 Discussion

### 4.6.1 Implications and Conflicting Constraints

#### 4.6.1.1 Implications of Design

The proposed unit cell design is one configuration that has close to the minimum spacing between focusing elements in the lateral direction. However, the focusing elements need to be sufficiently large to reduce the effect of truncation on the beam. At band 8 frequencies, the

beam radius will be in the order of a few millimeters depending on the propagation distance and transformation by the focusing element. The mirrors must be several times the diameter of the beam meaning we must have focusing elements with a few tens of millimeter diameter or larger.

Horizontal pixels will have the same separation between mirrors and will thus have a similar beam separation on the sky. The combination of horizontal and vertical pixels as a two-dimensional array will return a two-dimensional grid of beams on the sky. However, they will be extremely sparse at the order of around 10 beam widths of separation.

The final optimized two-beam optics has a total height of roughly 155 mm measured laterally from mirror edge to mirror edge. The current ALMA band 8 receiver cartridge has a base diameter of 170 mm. This shows, be it under many ideal assumptions and neglecting many physical components, the proposed design can work within the bounds of the existing receiver cartridge. The physical layout, also considering the horizontal pixels, may be optimized together with the optics to have a compact layout to fit inside a receiver cartridge. This will require constraining the positional limits of the receiver cartridge and some considerations will be needed for the other front-end components such as the waveguide blocks.

#### 4.6.1.2 Issues with Stacked Unit Cell Design

One unaddressed issue is, this proof-of-concept design has ignored many mechanical constraints introduced by the antenna itself. In particular, the small cryostat window for ALMA band 8 will impose serious limitations for the chief ray difference between pixels. The diagram in Fig. 4.41 shows the proposed two-beam design situated to align the beam from PX 1 with the current band 8 window position. The ALMA band 8 cryostat window has a diameter of 35 mm. The ALMA 12-m antenna has its receiver cabin 5882.813 mm away from the vertex of the sub-reflector. The band 8 window is placed 103.3 mm away from the center of the receiver cabin. This window is sufficiently large for the current single beam-receiver, but will be very limiting if multiple beams are to pass through and be directed towards the sub-reflector. For beams to enter into the cryostat window, the window diameter limits a maximum chief ray angle difference of $\delta\theta_{\text{in}} < 35/5882.3$ rad $= 0.34$ degrees. In practice, this will be even smaller due to the truncation at the edge of the window. PX 2 has a chief ray angle difference of $\delta\theta_{\text{CR}} = 0.54$ degrees from PX 1, which exceeds the maximum chief ray angles permitted by the window.

In general, there exists rays that can enter the window and points towards the large offset position for PX 2. However, this requires changing the tertiary optics or tilting the feed. Regardless, theses rays do not originate from the sub-reflector rendering them useless for the purpose of receiver optics. We may consider the possible option to add additional cryostat windows for each beam. However, this will require modifying the existing receiver cabin, especially the dewar top plate. Moreover, this solution does not address the large separation of the beams on the sky.

A minor limitation will also be the fabrication of the mirror on opposing surfaces. Current machining of mirrors is done on a single face. The stacked approach will require designing a mirror block with both surfaces machined on opposite sides. This may be face difficulties machining accurate surfaces for surfaces with large curvature (mirrors with small focal lengths) and may require using more complex machining methods such as 5-axis Computer Numerical

Control (CNC) machining.

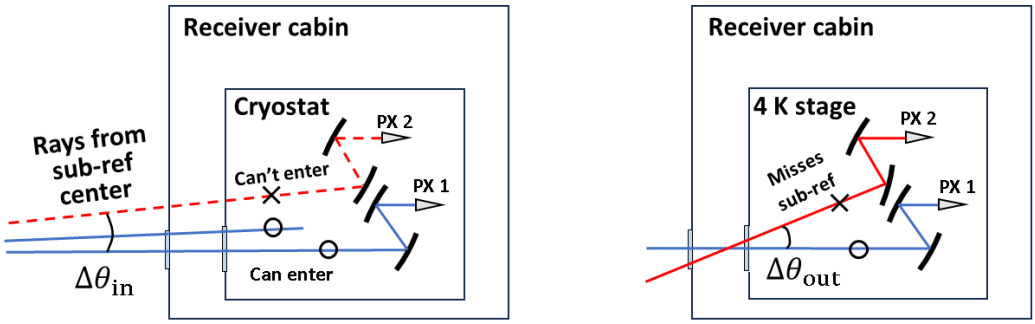


**Fig. 4.41** Issues with chief ray angles into and out of cryostat.

### 4.6.2 Tertiary Optics Design using Ray Tracing

The design of tertiary optics using ray tracing showed that for certain conditions, such as frequency independent illumination at the sub-reflector, ray tracing and geometrical optics can describe and predict the optical system well which was shown and is consistent with Imada et al. (2015). The simplicity of ray tracing is extremely attractive when considering multiple receiver feeds which all require independent optical solutions. The initial design and optimization in ray tracing software is a one method to obtain good performing optics before moving on to more rigorous simulations and optimization methods.

This method only calculates the required focal lengths and distances between mirrors to create the image of the sub-reflector and phase center at the horn. It cannot control the aberrations in the system as it assumes the paraxial approximation and the thin lens equation which ignores aberrations.

In this analysis, we only focused on the design for the existing band 8 horn. The frequency bandwidth will be determined by the feed horns bandwidth. The ALMA band 8 feed horn has a fractional bandwidth of 26%. However, the method presented here, and the general principle of frequency independent design, can obtain solutions for an arbitrary feed horn. We may design a horn with a wider bandwidth and solve the optics to work with that horn for a wideband and frequency independent design.

## 4.7 Summary of this Chapter

This chapter aimed to address how to design high-efficiency optics for individual pixels in a multibeam receiver. The optics are based on the established theories for single-beam receivers

implementing frequency independent optics. Recent connections between theories in diffraction and electromagnetic propagation have been linked to geometrical optics and ray tracing when the imaging condition for frequency independent design is established. This allows us to use ray tracing for design of receiver optics.

Here, ray tracing was used to calculate the required focal lengths and positions of focusing elements to obtain the frequency independent illumination. Ray tracing was used to design optics for the current ALMA band 8 horn. The optics were also optimized to force the exit pupil to align with the horn aperture. A two-beam multibeam receiver was designed and optimized using the proposed method. Follow up Physical optics simulations showed the optics returned high-aperture efficiency of $\eta_{\mathrm{A}} \geq 0.80$ on the sky for both pixels.

There were a few issues that arose from this analysis. One is the pixels in the two-beam multibeam receiver had a large separation leading to very sparse beams on the sky of greater than ten beam widths. The other is the fact that one of the beams could not be pointed towards the sub-reflector because of the existence of a cryostat window. The window has a diameter sufficient for single-beam receivers, but does not leave much room to allow two or more beams through from different angles. Additional optics are needed to allow the beams to pass through the small cryostat apertures.

# CHAPTER 5

# Multibeam Optics for Small Cryostat Apertures

## 5.1 Introduction

This chapter explores the use of re-imaging optics to design frequency independent multi-beam receiver optics to pass several receiver beams through a small cryostat aperture.

### 5.1.1 Physical and Mechanical Limitations for Multibeam Optics

As stated in Ch. 1, Radio telescopes aiming to implement multibeam receivers will face challenges concerning the constraints from the antenna. One challenge is designing multibeam receiver optics to work within the bounds of an existing radio telescope. Particularly, radio telescopes housing cryogenically cooled receivers generally have compact receiver cabins with small vacuum windows and thermal shields for a single beam to pass through.

Multibeam heterodyne receivers are physically much larger than single beam receivers with their feeds spatially distributed along the focal plane. Often times the feed array requires tertiary optics to direct each beam towards the sub-reflector. The tertiary optics are also needed for each feed to create frequency-independent illumination on the sub-reflector Chu (1983). The frequency independent illumination thus requires more space to accommodate focusing elements for each feed. Additionally, if each beam is to produce a centered illumination, then the difference between beam axis pointing towards the sub-reflector will become large to accommodate the individual focusing elements for each feed.

The design of a few-pixel multibeam receiver that satisfies the imaging condition necessary for frequency independent illumination at the sub-reflector was demonstrated in Chapter 4. A couple of issues arose with the proposed design:

- All receiver beams could not pass through a shared cryostat aperture because of the large angular difference of the beam axes.
- The beams on the sky had a large separation on the sky as a direct result of the large angular separation of the beam axes.

### 5.1.2 Re-Imaging Optics

To guide multiple beams through a small cryostat window, we require additional focusing elements to take beams entering the window within a narrow angle and separate them with a large angle to direct them to the various feed positions. Re-imaging optics have been utilized

in focal plane arrays. However, most focal plane arrays are designed for a dedicated cryostat and typically have sufficient room for multiple focusing elements to overcome limitations imposed by a cryostat. Re-imaging optics for focal plane arrays also cannot provide the frequency independent illumination as they image the frequency dependent fields at the focal plane. Decentered focusing and diffractive elements have been used in optics to dynamically steer beams of light in Bawart et al. (2020). A similar approach can be applied by using decentered lenses to refract the beam axis away from the optical axis to steer a beam incident into a cryostat window and redirect it towards a different focusing element for each individual feed. This will also address the large beam separation on the sky as the beam axis angles that can enter into the window will be limited to small angles.

## 5.2 Method

### 5.2.1 Design Concept

A fundamental concept in optics is a "pupil", which is the image of the aperture stop Born et al. (1999). Since the pupil is the image of the aperture stop, any ray from the center of the aperture stop (referred to as the chief ray) will pass through the center of the pupil. A pupil can be created at an arbitrary position with a focusing element such as a lens. Any chief ray that does not pass through the center of the focusing element will pass through the center of the pupil at an angle. This angle will depend on the focal length of the focusing element.

A radio telescope often uses the sub-reflector as an aperture stop, thus any focusing element that images the sub-reflector will create a pupil. These optics may serve the role of re-imaging optics for the antenna. Imada et al. (2015), shows that an arbitrary electric field input to one pupil will produce a geometrically scaled image of the input fields at an output pupil independent of frequency. This relation can be applied to the traditional design of frequency independent receiver optics. The frequency independent fields from a receiver horn aperture can be imaged on a pupil using tertiary receiver optics with the usual methods (examples in Chu, 1983 and Gonzalez, 2016). Thus, any beam that is directed towards the center of the pupil will produce a frequency-independent illumination centered on the sub-reflector.

Additionally, depending on the effective focal length of the re-imaging optics, small chief ray angles may be transformed into larger angles out of the pupil. This will be necessary if large mirrors or lenses are used in the tertiary receiver optics for the frequency independent design.

## 5.3 Design Equations

### 5.3.1 Basic Equations

An object at a distance $d_{\text{in}}$ away from a thin lens with focal length $f$ will produce an image $d_2$ distance away from the lens (Fig. 5.1) and will satisfy the lens equation,

$$\frac{1}{f} = \frac{1}{d_{\text{in}}} + \frac{1}{d_{\text{out}}}. \tag{5.3.1}$$

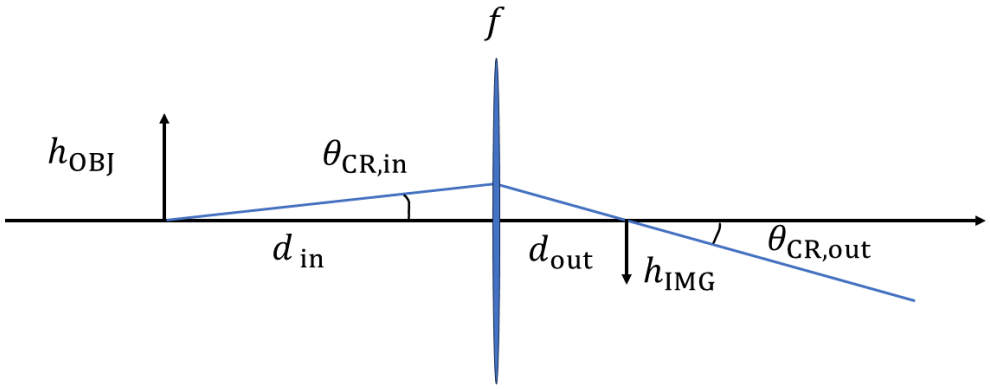


**Fig. 5.1** Diagram of a simple lens

The ratio between the object height $h_{\text{OBJ}}$ and image height $h_{\text{IMG}}$ will be given by,

$$h_{\text{IMG}} = -\frac{d_{\text{out}}}{d_{\text{in}}} h_{\text{OBJ}}. \tag{5.3.2}$$

The distances $d$ may be positive or negative to indicate an object in front or behind the lens, to indicate real or virtual images, and to indicate the orientation of the image with respect to the object (i.e. a negative height indicates an inverted image).

The relation between the ray angle entering and exiting the lens will be given by the position of the object and the focal length of the lens. If the object is the aperture stop, considering small angles into the lens, a chief ray input into the lens $\theta_{\text{CR, in}}$, the output chief ray angle $\theta_{\text{CR, out}}$ will be given by,

$$\theta_{\text{CR,out}} = -\frac{d_{\text{in}}}{d_{\text{out}}} \theta_{\text{CR,in}}. \tag{5.3.3}$$

### 5.3.2 Targets for Final Beam

The illumination on the sub-reflector can be described with two parameters, the edge taper level, and the radius of curvature. In the case of frequency-independent illumination, the edge taper will give a constant beam radius $w_{\text{Sub}}$ on the sub-reflector. The target beam radius can be derived from the edge taper (Goldsmith, 1998) as,

$$w_{\text{sub}} = \sqrt{\frac{20 \log_{10} e \cdot r_{\text{sub}}^2}{\text{ET}}}. \tag{5.3.4}$$

Here, $r_{\text{sub}}$ is the radius of the sub-reflector, and ET is the edge taper in dB.

The center of curvature of the beam wavefront will be set to match the off-axis Cassegrain focus position $R_{\text{CF}}$, which depends on the incident angle of the plane wave into the antenna.

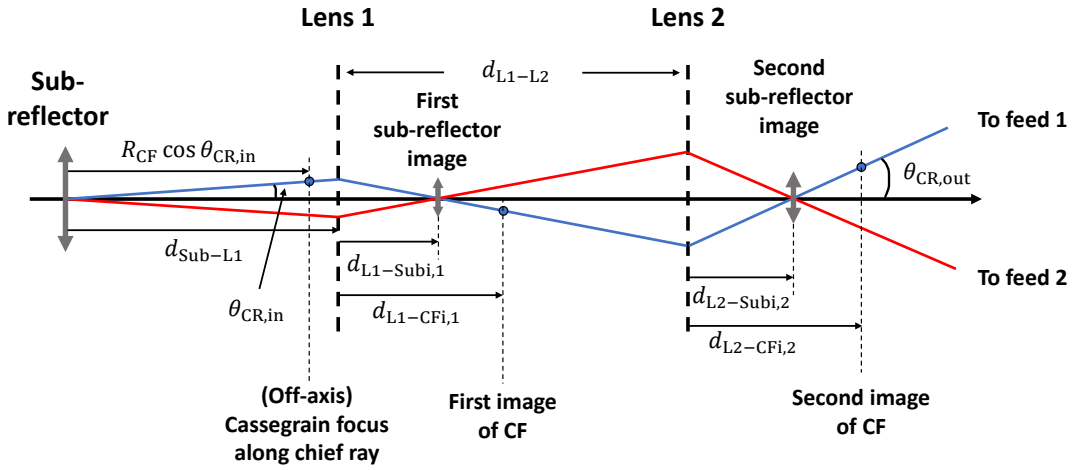


**Fig. 5.2** Re-imaging optics system setting.

The radius of curvature will be different for each feed position, which can be easily obtained using ray tracing software.

### 5.3.3 Two-Lens Re-Imaging Optics

A two-lens system for the re-imaging optics is shown in Fig. 5.2. To differentiate between various lengths and distances, distances along lens axes are written with $d$, curvature radii with $R$, beam radii with $w$, and focal lengths with $f$. The subscripts denote where distances are measured from or specify an object (e.g. the distance from lens 1 to lens 2 $d_{\mathrm{L1\text{-}L2}}$, beam radius at sub-reflector $w_{\mathrm{sub}}$). Images are denoted with an "i, number" at the end of subscripts as an object may be imaged multiple times (e.g. the second image of the beam radius at the sub-reflector $w_{\mathrm{Subi,\,2}}$). The variable names and their notations are listed in table 5.1.

The first lens with focal length $f_{\mathrm{L1}}$ will produce an image of the sub-reflector and the Cassegrain focus (CF). The second lens with focal length $f_{\mathrm{L2}}$ will take the first image of the sub-reflector and Cassegrain focus, and create the second image of the sub-reflector and Cassegrain focus.

$$\begin{cases} \frac{1}{f_{\mathrm{L1}}} = \frac{1}{d_{\mathrm{Sub\text{-}L1}}} + \frac{1}{d_{\mathrm{L1\text{-}Subi,\,1}}} \\ \frac{1}{f_{\mathrm{L1}}} = \frac{1}{d_{\mathrm{CF\text{-}L1}}} + \frac{1}{d_{\mathrm{L1\text{-}CFi,\,1}}}, \end{cases} \tag{5.3.5}$$

$$\begin{cases} \frac{1}{f_{\mathrm{L2}}} = \frac{1}{d_{\mathrm{L1\text{-}L2}} - d_{\mathrm{L1\text{-}Subi,\,1}}} + \frac{1}{d_{\mathrm{L2\text{-}Subi,\,2}}} \\ \frac{1}{f_{\mathrm{L2}}} = \frac{1}{d_{\mathrm{L1\text{-}L2}} - d_{\mathrm{L1\text{-}CFi,\,1}}} + \frac{1}{d_{\mathrm{L2\text{-}CFi,\,2}}}. \end{cases} \tag{5.3.6}$$

The imaged beam radius at the output of the second lens $w_{\mathrm{subi,\,2}}$ will be given by,

$$w_{\mathrm{Subi,\,2}} = \left( -\frac{d_{\mathrm{L2\text{-}Subi,\,2}}}{d_{\mathrm{L1\text{-}L2}} - d_{\mathrm{Subi,\,1\text{-}L2}}} \right) * \left( -\frac{d_{\mathrm{L1\text{-}Subi,\,1}}}{d_{\mathrm{Sub\text{-}L1}}} \right) * w_{\mathrm{Sub}}. \tag{5.3.7}$$

**Table 5.1** List of variables in system

| Parameter | notation |
|---|---|
| Chief ray angle into Re-imaging optics | $\theta_{\text{CR, in}}$ |
| Chief ray angle output from re-imaging optics | $\theta_{\text{CR, out}}$ |
| Radius of curvature from CF | $R_{\text{CF}}$ |
| Axial distance from CF to Lens 1 | $d_{\text{CF-L1}} =$ $d_{\text{Sub-L1}} - R_{\text{CF}} \cos\theta_{\text{CR, in}}$ |
| Beam radius at sub-reflector | $w_{\text{sub}}$ |
| Beam radius at feed aperture | $w_{\text{horn}}$ |
| Radius of curvature of beam at feed aperture | $R_{\text{horn}}$ |
| Focal length of lens 1 | $f_{\text{L1}}$ |
| Focal length of lens 2 | $f_{\text{L2}}$ |
| Distance between lenses | $d_{\text{L1-L2}}$ |
| Distance from sub-ref center to lens 1 | $d_{\text{Sub-L1}}$ |
| Distance from lens 1 to first image of sub-ref | $d_{\text{L1-Subi,1}}$ |
| Distance from lens 1 to first image of CF | $d_{\text{L1-CFi,1}}$ |
| Distance from lens 2 to second image of sub-ref | $d_{\text{L2-Subi,2}}$ |
| Distance from lens 2 to second image of CF | $d_{\text{L2-CFi,2}}$ |
| Distance from Mirror 1 to third image of sub-ref | $d_{\text{M1-subi, 3}}$ |
| Distance from Mirror 1 to third image of CF | $d_{\text{M1-CFi, 3}}$ |
| Distance for chief ray from lens 2 to Mirror 1 | $d_1$ |
| Distance Between Mirror 1 and Mirror 2 | $d_2$ |
| Distance from Mirror 2 to feed aperture | $d_3$ |
| Focal length of Mirror 1 | $f_{\text{M1}}$ |
| Focal length of Mirror 2 | $f_{\text{M2}}$ |

The system of equations for the tertiary optics can be constructed in the same way as the re-imaging optics. The image of the sub-reflector and the image of the Cassegrain focus are imaged by the tertiary optics to match the positions of the beam radius at the horn aperture and phase center of the horn, respectively.

$$\begin{cases} \frac{1}{f_{\mathrm{M1}}} = \frac{1}{d_1 - d_{\mathrm{L2\text{-}Subi,\,2}}/\cos\theta_{\mathrm{CR,\,out}}} + \frac{1}{d_{\mathrm{M1\text{-}Subi,\,3}}} \\ \frac{1}{f_{\mathrm{M1}}} = \frac{1}{d_{\mathrm{L2\text{-}CFi,\,2}}} + \frac{1}{d_{\mathrm{M1\text{-}CFi,\,3}}}, \end{cases} \tag{5.3.8}$$

$$\begin{cases} \frac{1}{f_{\mathrm{M2}}} = \frac{1}{d_2 - d_{\mathrm{M1\text{-}Subi,\,3}}} + \frac{1}{d_3} \\ \frac{1}{f_{\mathrm{M2}}} = \frac{1}{d_2 - d_{\mathrm{M1\text{-}CFi,\,3}}} + \frac{1}{d_3 + R_{\mathrm{horn}}}. \end{cases} \tag{5.3.9}$$

The beam radius of the horn $w_{\mathrm{horn}}$ can be matched to $w_{\mathrm{subi,2}}$ if the relation,

$$\begin{aligned} w_{\mathrm{horn}} = &\left(-\frac{d_3}{d_2 - d_{\mathrm{M1\text{-}Subi,\,3}}}\right) \\ &* \left(-\frac{d_{\mathrm{M1\text{-}Subi,\,3}}}{d_1 - d_{\mathrm{L2\text{-}Subi,2}}/\cos\theta_{\mathrm{CR,\,out}}}\right) * w_{\mathrm{Subi,\,2}}, \end{aligned} \tag{5.3.10}$$

is satisfied.

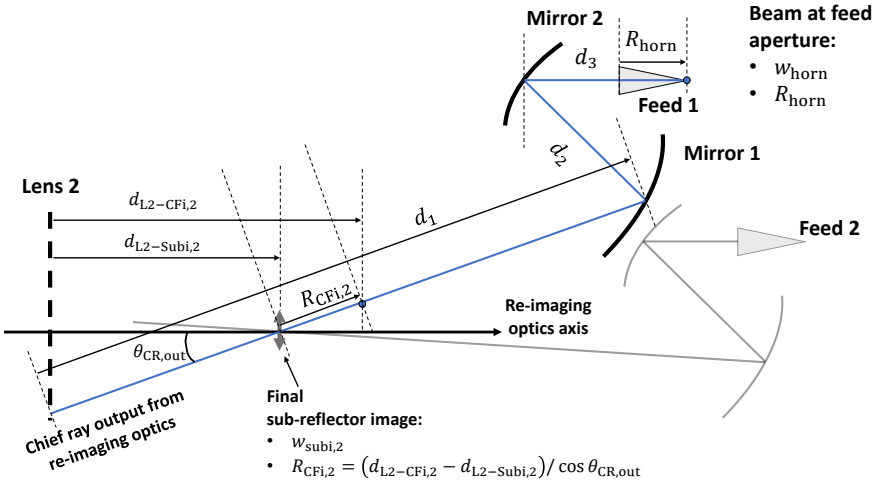


**Fig. 5.3** Tertiary optics system setting.

### 5.3.4 Choosing Free Parameters

The equations from 5.3 give us five equations with nine parameters for the re-imaging optics, and five equations with eleven parameters for the tertiary optics for a given beam. We may appropriately select parameters from each optical system to be fixed to obtain solutions. In general, any of the free parameters can be fixed, however, some parameters may be less constrained and much easier to fix (e.g. distance between horn aperture and mirror). Therefore, it is desirable to fix the parameters that are relatively simple to fix, and find solutions to the remaining parameters that work within the strong constraints.

The off-axis Cassegrain focus $R_{\mathrm{CF}}$ and output chief ray angle $\theta_{\mathrm{CR,\,out}}$ can be easily given by fixing the input chief ray angle for each feed. The chief ray angle may be set to have a large

difference at the output of the re-imaging optics to completely separate the beams and direct them to their respective tertiary optics.

The optics can be constructed to match the illumination on the sub-ref and the fields at the feed aperture. The curvature center at the sub-reflector will be given by $R_{\text{CF}}$, which is determined previously by fixing the chief ray angle. We may also easily fix the illumination edge taper at the sub-reflector to determine $w_{\text{sub}}$.

This leaves us with six free parameters to obtain solutions for the optics. Here, $d_{\text{Sub-L1}}$, $d_{\text{L1-L2}}$, $f_{\text{L1}}$, $f_{\text{L2}}$, $d_1$, $d_3$, were set as the free parameters and the equations were solved to finally obtain, $f_{\text{M1}}$, $f_{\text{M2}}$, and $d_{\text{M1-M2}}$.

### 5.3.5 Physical and Mechanical Constraints

The antenna and cryostat will impose strong constraints on the optics and will limit the number of usable solutions. Some examples of strong mechanical constrains imposed by the antenna/cryostat are:

- The Chief ray (corresponding to a beam axis for simplicity) should not enter into the first window too far offset from the center to avoid major lob-sided beam truncation.
- The beams must be separated and diverge away from each other with a sufficiently large angle at the output of the re-imaging optics.
- The sub-reflector image must be able to match to the receiver tertiary optics with practical focal lengths and distance between focusing elements.

The various constraints will depend on the antenna and cryostat and requirements for the receiver optics.

By applying these kind of constraints onto the solutions for the full receiver optics containing the re-imaging lenses and tertiary mirrors, we may filter out all cases that cannot be implemented. We may then choose an appropriate solution that is most convenient.

## 5.4 Designing a Two-Beam Multibeam Receiver

### 5.4.1 Design for ALMA 12-m Antenna

The ALMA 12-m antenna and its cryostat, and the Band 8 receiver (385 - 500 GHz) was considered for the design of a two-beam multibeam receiver. A diagram of the ALMA 12-m antenna cryostat is shown in Fig. 5.4.

The ALMA cryostat is composed of several stages that are gradually cooled from ambient temperature down to 110 K, 15 K, and 4 K. Each stage interface has a small window with a dielectric slab (also used to filter infrared radiation) separating each stage.

The band 8 receiver cryostat window is positioned in the plane containing the on-axis Cassegrain focus 5882.8125 mm away from the sub-ref vertex. The window has a radial distance 103.3 mm away from the antenna center axis. The band 8 cryostat window has a diameter of $\phi = 35$ mm. The 110 K stage and 15 k stages have $\phi = 40$ mm diameter windows. The

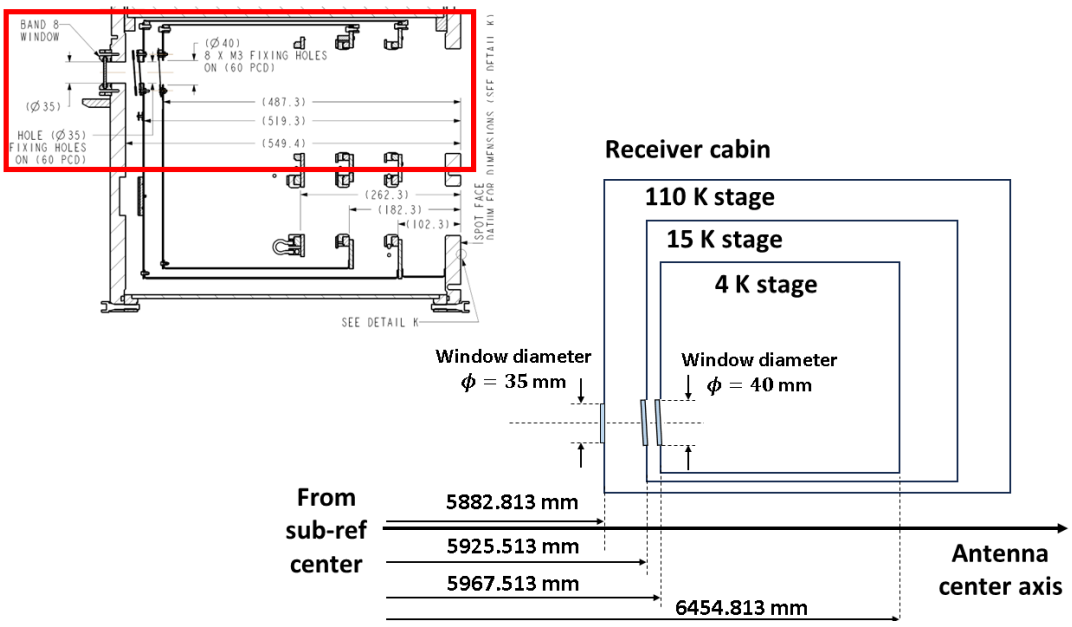


**Fig. 5.4** Diagram of ALMA 12-m antenna cryostat from schematic. The schematic is shown in the upper left. The bottom right shows a simplified diagram, which is a mirrored image of the red area along the antenna axis for better visualization. Schematic credit: ALMA (ESO/NAOJ/NRAO).

dewar and 110 K window, 110 K and 15 K windows are separated by 55.2 mm, 32 mm respectively. This gives us a cylinder with diameter 35 mm and length 84.7 mm that the beams can pass through.

### 5.4.2 Parameter Search

The target illumination edge taper was set to 12.21 dB ($w_{\text{sub}} = 316.266$ mm) to match and compare with the current illumination of the band 8 receiver. The curvature center of the beam was set to match the off-axis Cassegrain focus of the telescope and was set to $R_{\text{CF}} = 5862.723$ mm for beam 1 and $R_{\text{CF}} = 5867.656$ mm for beam 2 for the incident angles $\theta_{\text{inc}} = 0.0658, 0.0572$, respectively.

A parametric search was done to extract a number of acceptable solutions for the re-imaging optics and receiver tertiary optics. Each free parameter $d_{\text{Sub-L1}}$, $d_{\text{L1-L2}}$, $f_{\text{L1}}$, $f_{\text{L2}}$, $d_{\text{in}}$, and $d_{\text{out}}$, was given a sparse range, and all solutions for $f_{\text{M1}}$, $f_{\text{M2}}$, and $d_{\text{M1-M2}}$ were calculated for each free parameter combination. An initial value set was chosen from the batch of usable solutions. The initial solution was then manually adjusted to produce a final acceptable solution. The final parameters are listed in table. 5.2 and table. 5.3.

### 5.4.3 Modeling in Ray Tracing Software

The ray tracing software CODEV was used to model the re-imaging optics and tertiary optics. The re-imaging optics are set as dielectrics lenses with a refractive index of $n = 1.5$ (a commonly used material is High Density Polyethylene: HDPE). The Re-imaging optics are composed of two bi-convex lenses with radius of curvature of 78.64 mm, 37.89 mm, and thick-

**Table 5.2** Final Parameters for Re-imaging Optics

| Parameter | Value (mm) |
|---|---|
| $f_{\text{L1}}$ | 80 |
| $f_{\text{L2}}$ | 40 |
| $d_{\text{Sub-L1}}$ | 5930 |
| $d_{\text{L1-L2}}$ | 25 |

**Table 5.3** Final Parameters for Tertiary Optics

| Parameter | Beam 1 value (mm) | Beam 2 value (mm) |
|---|---|---|
| $f_{\text{M1}}$ | 55.080 | 35.062 |
| $f_{\text{M2}}$ | 94.281 | 26.236 |
| $d_{\text{M1-M2}}$ | 75.184 | 53.859 |
| $d_1$ | 135 | 65 |
| $d_3$ | 25 | 23 |

ness 8 mm, 12 mm, respectively. The tertiary optics are composed of a set of ellipsoidal mirrors. The optical axes for the tertiary optics are aligned with the chief ray output from the re-imaging optics.

The re-imaging optics and tertiary optics for both feeds are shown in Fig. 5.5. The tertiary optics adopts the unit-cell design from 4.4. The first mirror for beam one is stacked on top of the second mirror for beam two to create a compact layout.

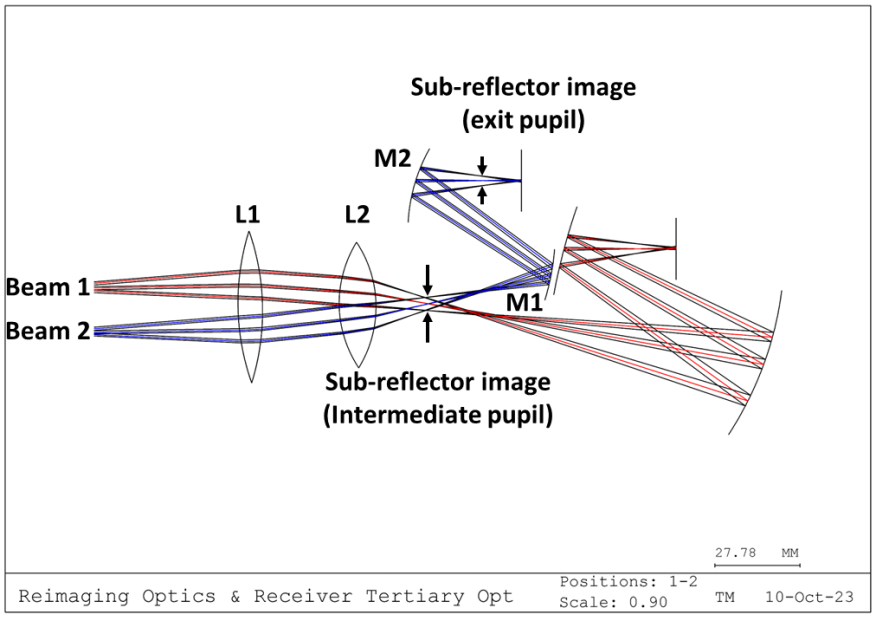


**Fig. 5.5** The design of a two beam Multibeam receiver in CODE V

The re-imaging optics produces an image of the sub-reflector with a magnification factor of $M = 0.00567$. The Tertiary optics produces an image of the pupil that is aligned with the feed

aperture. The rays finally converge to a phase center position. The phase center position was 3 mm closer from the calculated position. The final image plane was moved forward 3 mm to remove the defocus. This leaves us with a beam with $w_{\text{horn}} = 1.4$ and $R_{\text{horn}} = 11$ mm at the feed aperture. This difference can be explained with the approximations associated with using the thin lens equations on relatively thick lenses. The final image point can be better predicted by accounting for the lens thickness in the equations, or can be optimized in the ray tracing software.

The incident angle for the parallel rays entering into the antenna were set to $\theta_{\text{inc}} = 0.0658, 0.0572$ for beam 1 and beam 2, respectively. This gives a pointing difference of $\delta\theta = 0.0658 - 0.0572 = 0.0086$ degrees. This resulted in completely separated beams with a separation angle of 25 degrees between chief rays exiting the re-imaging optics.

## 5.5 Results

### 5.5.1 Simulations in Physical Optics Software

The design from CODE V was modeled in GRASP and is shown in Fig. 5.6. PO simulations were done to obtain the far-fields on the sky and the illumination on the sub-reflector. The beam from feed 1 (feed with magenta rays in Fig. 5.6) and feed 2 (feed with blue rays in Fig. 5.6) were set as Gaussian beams with a beam radius and radius of curvature of $w_{\text{horn}} = 1.4$ mm and $R_{\text{horn}} = 11.02$ mm to match the values from the initial calculations and the ray tracing results. The simulation was done at 385, 442, and 500 GHz which corresponds to ALMA band 8 frequencies. The two beams were successfully propagated to the sky passing through all windows from their large offset position relative to the window. The beams on the sky, illumination on the sub-reflector, and their x-y cuts are shown in Fig. 5.7 to Fig. **??**.

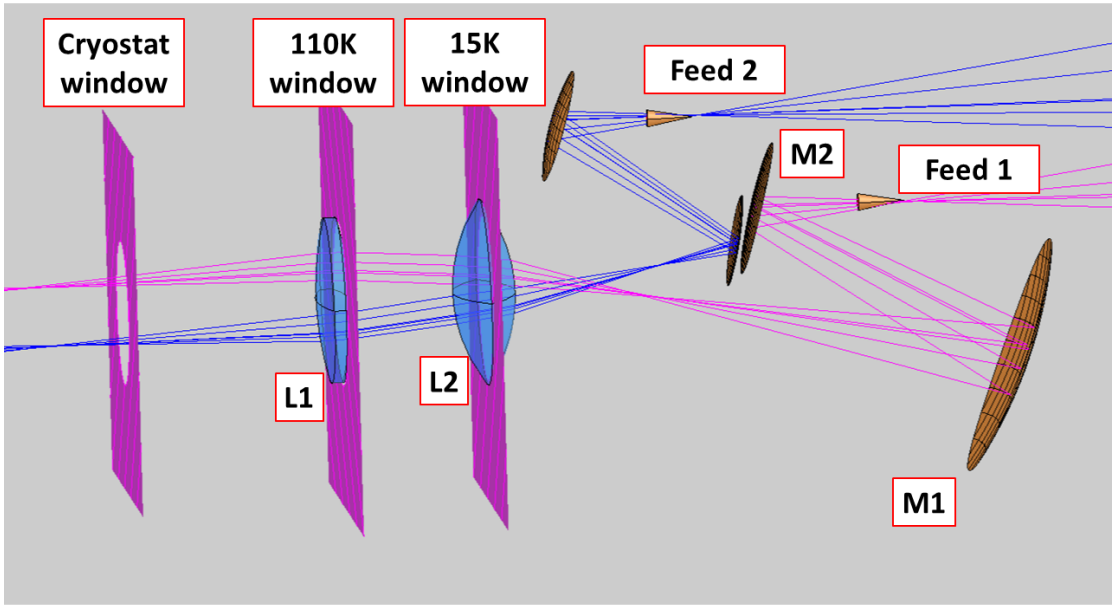


**Fig. 5.6** The re-imaging optics and tertiary optics in GRASP

### 5.5.2 Fields at Sub-Reflector

The fields on the sub-reflector was calculated along a spherical surface with radius $R_{\mathrm{CF}}$ centered at the off-axis Cassegrain focus for each beam. The field magnitudes on the sub-reflector were successfully obtained and are shown in Fig. 5.7 with their x-y cuts shown in Fig. 5.8. The two-column figures show the results for both feeds with pixel 1 shown in the left column and pixel 2 shown in the right column.The dotted line in Fig. 5.7 represents the angular range of the sub-reflector. The cuts show the profile inside the range of the sub-reflector.

The illumination edge taper from the PO simulations is roughly -11.2 dB. The slight difference from the target illumination can be mostly attributed to the limitations of geometrical optics. Some distortion can be seen in the beam due to the use of decentered lenses, which is expected.

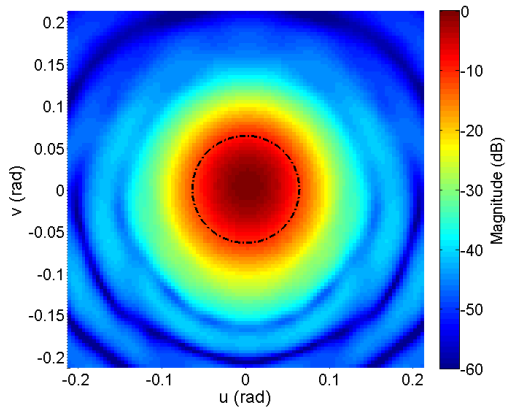


**(a)** PX 1: 385 GHz

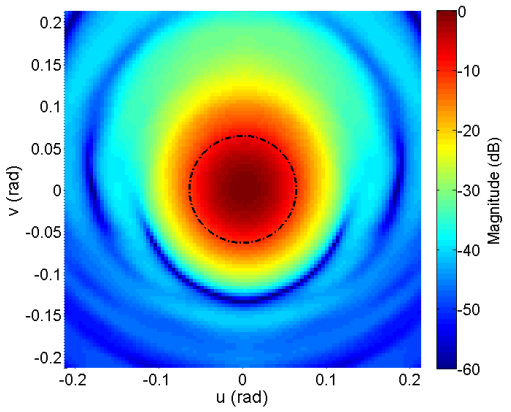


**(b)** PX 2: 385 GHz

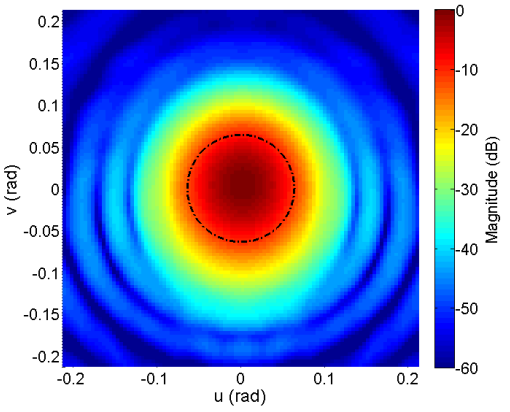


**(c)** PX 1: 442 GHz

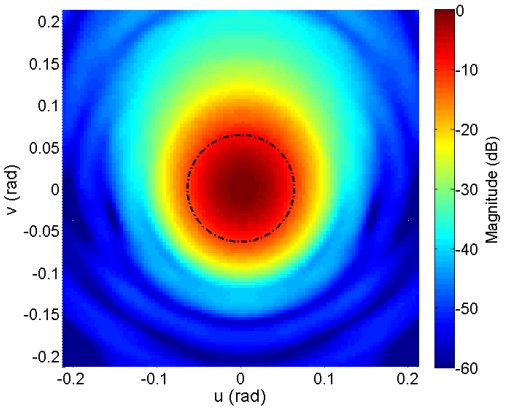


**(d)** PX 2: 442 GHz

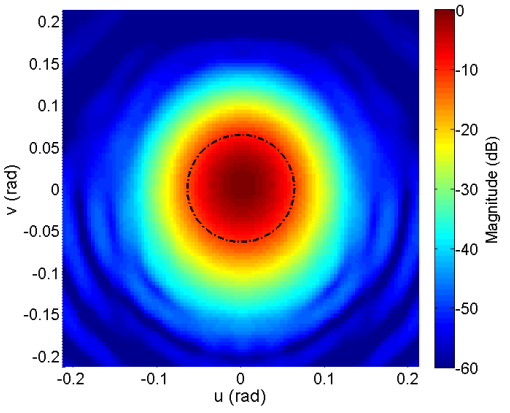


**(e)** PX 1: 500 GHz

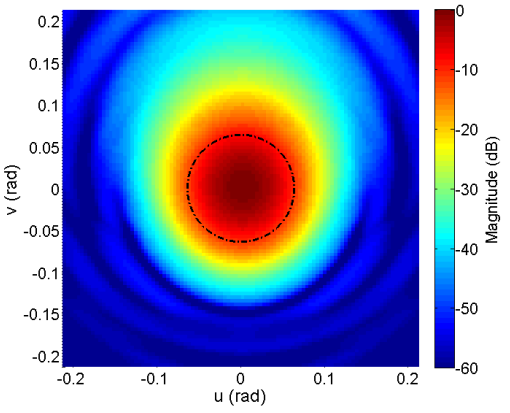


**(f)** PX 2: 500 GHz

**Fig. 5.7** Illumination on sub-reflector produced by each feed. The dotted line shows the angluar range of the sub-reflector.

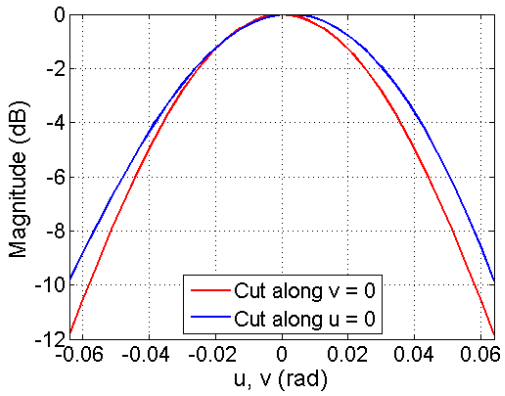


**(a)** PX 1: 385 GHz

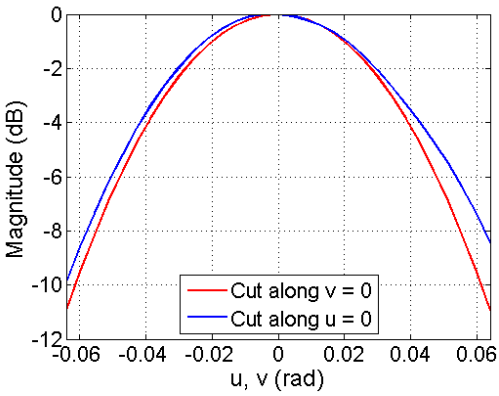


**(b)** PX 2: 385 GHz

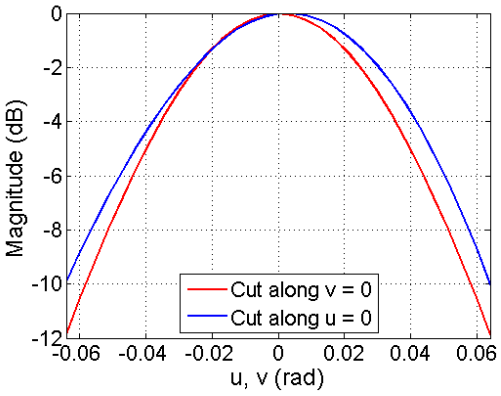


**(c)** PX 1: 442 GHz

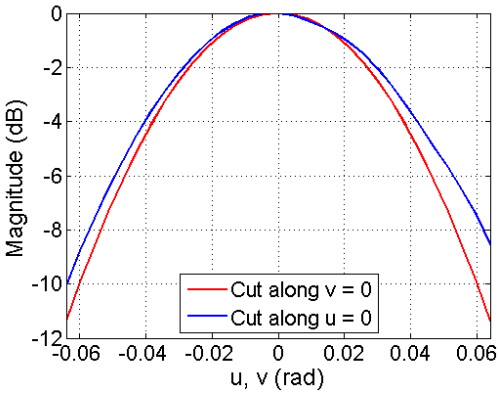


**(d)** PX 2 :442 GHz

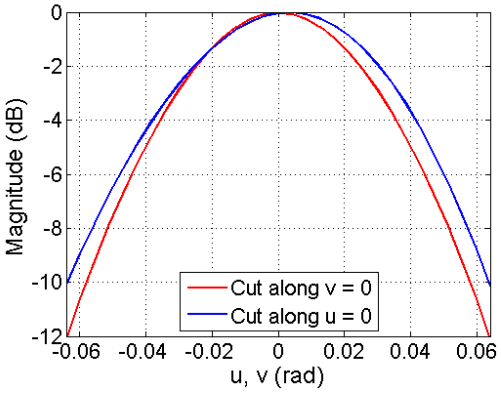


**(e)** PX 1: 500GHz

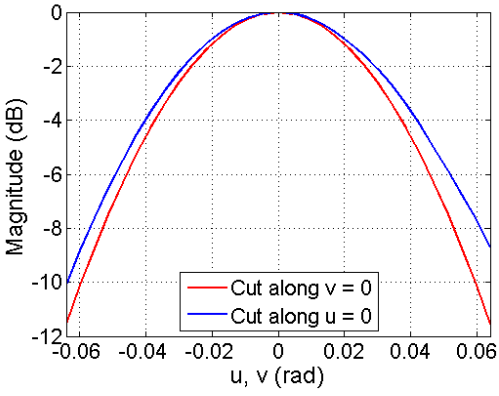


**(f)** PX 2: 500 GHz

**Fig. 5.8** The cuts of the field magnitude at the sub-reflector along $u = 0$ and $v = 0$.

### 5.5.3 Beams on the Sky

The Far-fields on the sky were calculated with the $u$-$v$ plane centered at $(u, v) = (0, 0.001076)$ to check the relative separation between beam peak positions. This origin corresponds to the expected peak position for a beam passing through the center of the cryostat window. The far-fields for the co-polarization and cross-polarization are shown in Fig. 5.9 and Fig. 5.10 with their $u$-$v$ cuts shown in Fig. 5.11. The relative beam positions are overlaid and shown in Fig. 5.12.

The peak positions in Fig. 5.12 were $v = -6.5\times10^{-5}$ radians for beam 1 and $v = 7.8\times10^{-5}$ radians for beam 2, which returns a peak-to-peak separation of $\delta\theta = 0.0082$ degrees. The beam size for the ALMA 12-m antenna at band 8 frequencies is $\lambda/D = 0.0037$ degrees at 385 GHz and $\lambda/D = 0.0029$ degrees at 500 GHz. Thus, the beam separation is approximately 2.2 beam-widths at 385 GHz and 2.8 beam-widths at 500 GHz. This relatively small separation was achieved because the re-imaging optics were able to change the effective F-number of the rays.

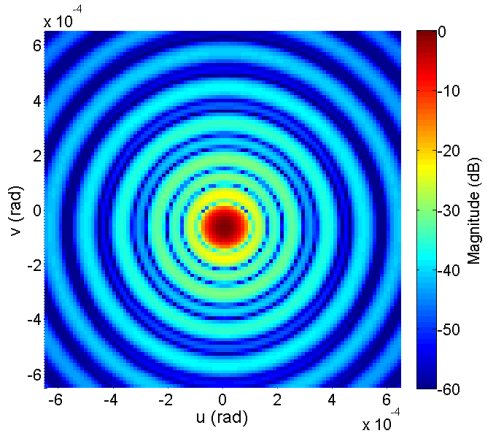


**(a)** PX 1: Co-Pol 385 GHz

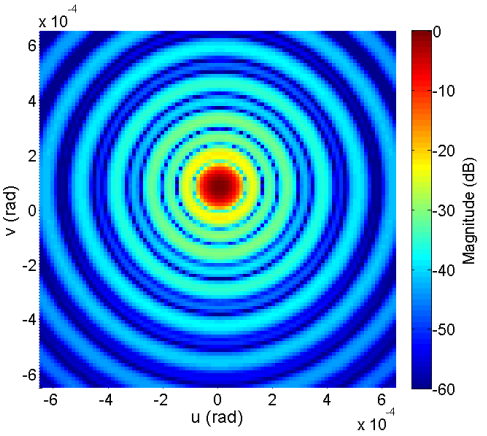


**(b)** PX 2: Co-Pol 385 GHz

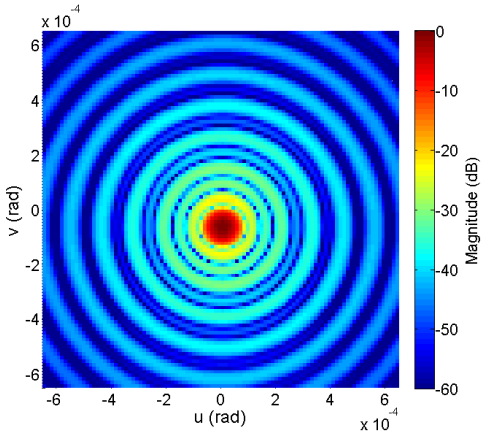


**(c)** PX 1: Co-Pol 442 GHz

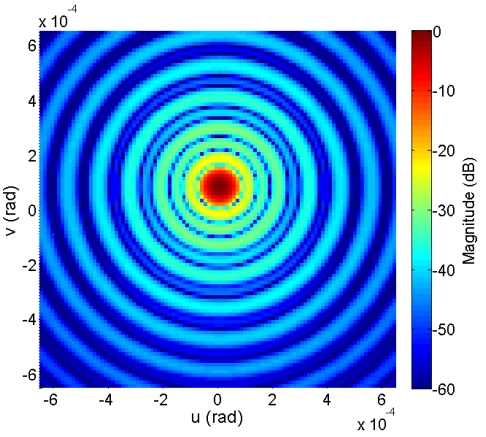


**(d)** PX 2: Co-Pol 442 GHz

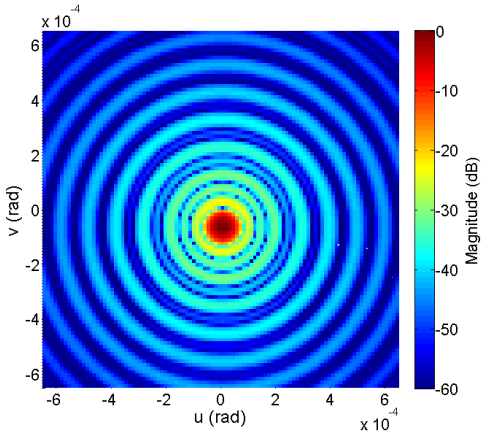


**(e)** PX 1: Co-Pol 500 GHz

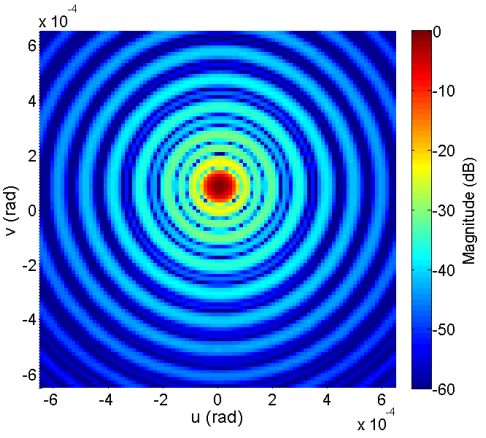


**(f)** PX 2: Co-Pol 500 GHz

**Fig. 5.9** Co-polarization of far-fields on the sky from each pixel.

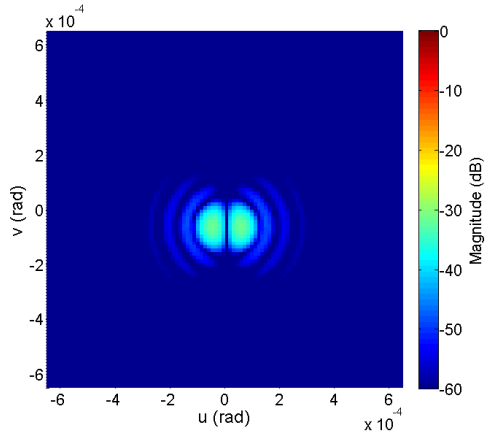


**(a)** PX 1: 385 GHz

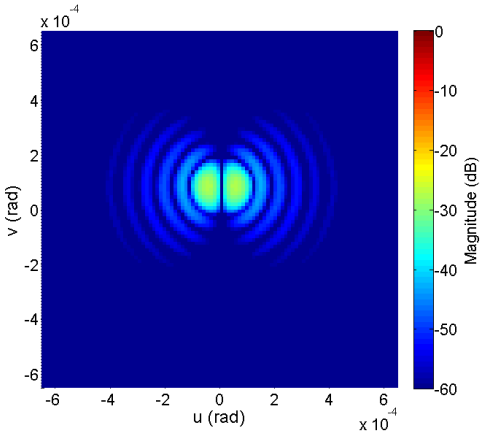


**(b)** PX 2: 385 GHz

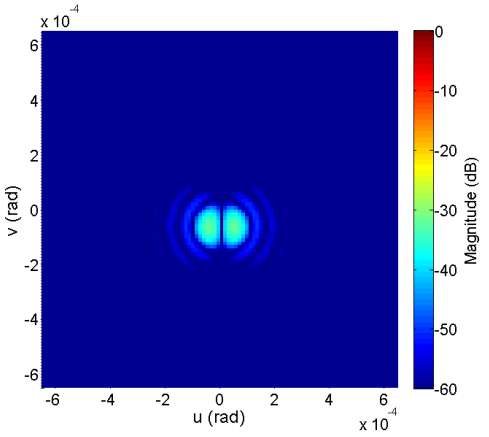


**(c)** PX 1: 442 GHz

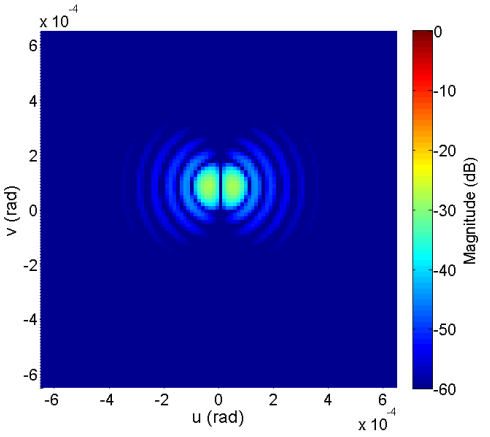


**(d)** PX 2: 442 GHz

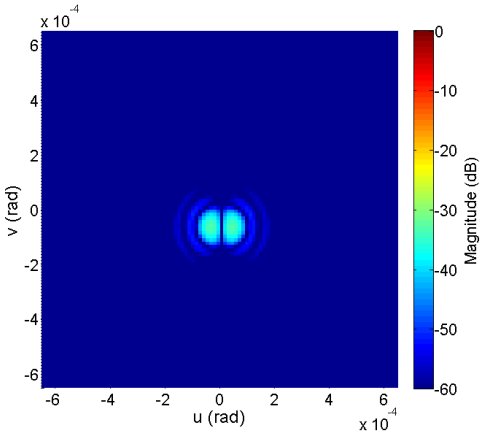


**(e)** PX 1: 500 GHz

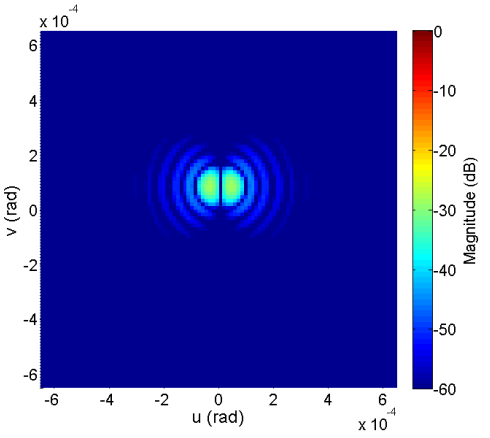


**(f)** PX 2: 500 GHz

**Fig. 5.10** Cross-polarization of far-fields on the sky from each pixel.

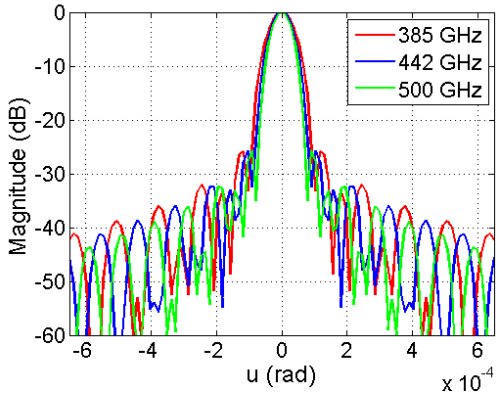


**(a)** PX 1 Co-Pol: Cuts along $v = 0$

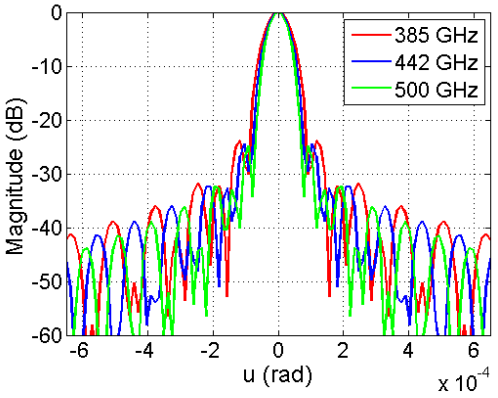


**(b)** PX 2 Co-Pol: Cuts along $v = 0$

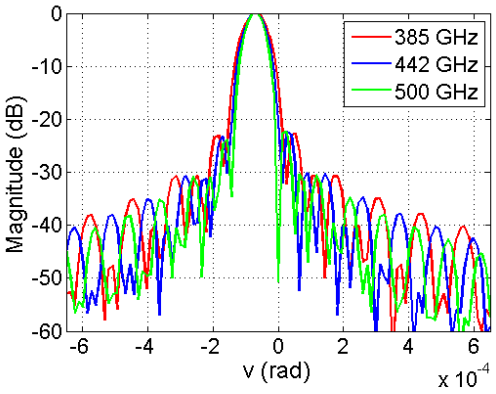


**(c)** PX 1 Co-Pol: Cuts along $u = 0$

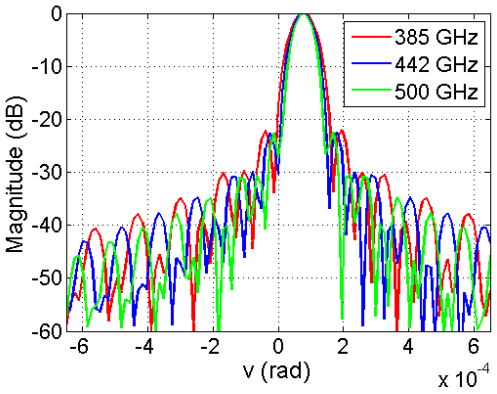


**(d)** PX 2 Co-Pol: Cuts along $u = 0$

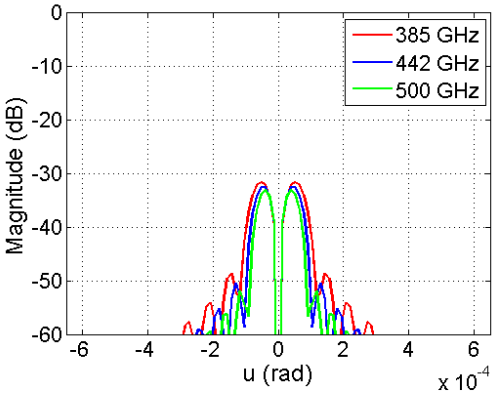


**(e)** PX 1 Xs-Pol: Cuts along $v = 0$

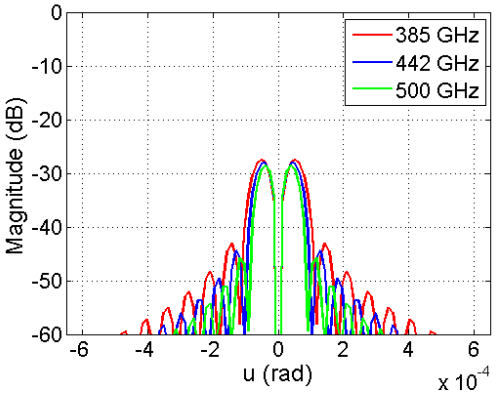


**(f)** PX 2 Xs-Pol: Cuts along $v = 0$

**Fig. 5.11** Far-field symmetrical and asymmetrical cuts and comparison between pixels.

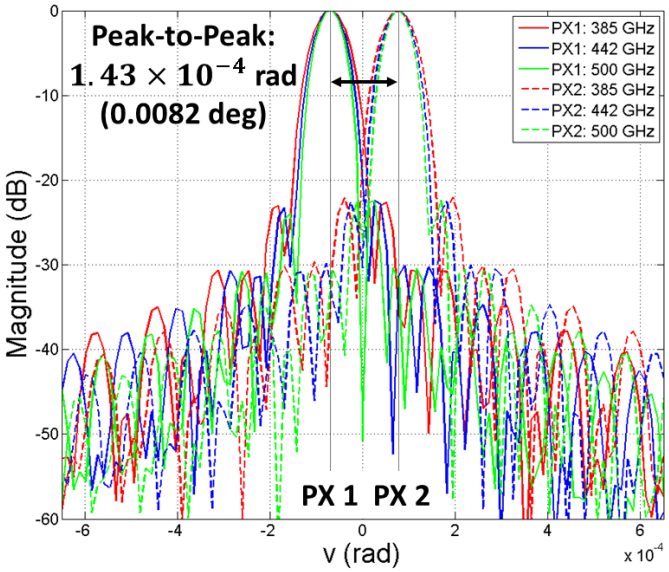


**Fig. 5.12** Overlay of co-pol cuts along $u = 0$ for both pixels.

### 5.5.4 Aperture Efficiency

The aperture efficiencies for both pixels are summarized in Table. 5.4.

**Table 5.4** Aperture efficiencies of two-beams using re-imaging optics

| | | 385 (GHz) | 442 (GHz) | 500 (GHz) | $1 - \frac{\eta_{385}}{\eta_{500}}$ (%) |
|---|---|---|---|---|---|
| PX 1 | $\eta_{\text{A, 1}}$ | 0.6368 | 0.6401 | 0.6401 | 0.52 |
| | $\eta_{\text{sub, feed 1}}$ | 0.6625 | 0.6700 | 0.6733 | 1.60 |
| | $\eta_{\text{sub, beam 1}}$ | 0.7914 | 0.7979 | 0.8010 | 1.20 |
| PX 2 | $\eta_{\text{A, 2}}$ | 0.6392 | 0.6455 | 0.6500 | 1.66 |
| | $\eta_{\text{sub, feed 2}}$ | 0.6561 | 0.6621 | 0.6665 | 1.56 |
| | $\eta_{\text{sub, beam 2}}$ | 0.7888 | 0.7916 | 0.7953 | 0.82 |

The aperture efficiency for beam 1 was calculated to be $\eta_{\text{A, 1}} = 0.6368$ and $\eta_{\text{A, 2}} = 0.6392$ for beam 2 at 385 GHz. It was found that the spill-overs at Lens 1 (first lens on the left in Fig. 5.6) and the cryostat window (Left most aperture in Fig. 5.6) was around 0.91 and 0.83 respectively for both beams. Setting a smaller incident angle into the cryostat window will reduce this effect. However, the output chief ray angle will correspondingly become small as well. Thus, the position of the lenses, angles in to and out of the lenses may require further considerations during the design and parameter search constraints. Additional lenses or mirrors may be added if necessary to explore more solutions. However, not only will the added complexity increase the number of variables, adding more optical elements in general will degrade the receiver noise temperature, significantly for additional dielectric lenses.

## 5.6 Discussion

### 5.6.1 Limitations of Method and Possible Improvements

The results from the PO simulations show some deviation from the target illumination from the initial calculations. This is mostly due to the limitations of ray tracing, geometrical optics, and quasioptical Gaussian beam propagation, as they may only serve as first approximations to predict beam sizes and positions. The design of the tertiary optics follows the method introduced in Chapter. 4 to design for feed horns.

The design method presented here is only able to provide a select few solutions from the entire solution space. Thus, this method is best suited for setting up an initial design for the re-imaging and tertiary optics when given strong mechanical and physical constraints. Physical optics may not be able to fully describe the dielectric lenses effect on the beams, thus more sophisticated electromagnetic methods will be further required to analyze its effect.

The design parameters may be further optimized in software to obtain the best optics that satisfies all requirements. An example is utilizing ray tracing to optimize lens and mirror shapes to reduce the beam distortion. The feed and optics may also be optimized together to provide the optimal illumination on the sub-reflector to maximize the aperture efficiency. This includes the option to vary the horn parameters (given by $w_{\text{horn}}$ and $R_{\text{horn}}$) to find the optimal spacing between re-imaging optics and horns, focal lengths of mirrors, and distances between horns and tertiary optics mirrors.

A 2-D array of feeds may be designed by including the azimuthal angle for the chief ray. The mirrors will also require additional rotations to finally reflect all chief rays to be parallel to each other, if it is required (e.g. for implementing parallel feeds).

### 5.6.2 Minimum Window Size Estimations

The final aperture efficiency for the beams were degraded mainly by the truncation at the cryostat window and spill-over at lens 1. However, the coupling efficiency between the feed and the target beam at the sub-reflector can be roughly estimated by dividing the final aperture efficiency on the sky with the spill-over efficiency at the sub-reflector. Focusing on the results at 385 GHz, as it has the largest beam size entering the re-imaging optics, the relative power hitting the sub-reflector from the feed was 0.746 and 0.726 for PX 1 and PX 2, respectively. The estimated coupling efficiency can then be derived as $0.637/0.746 \approx 0.854$ for PX 1 and $0.639/0.726 \approx 0.880$ for PX 2. Doing the same operation for the two-beam optics from Section. 4.4.3, we may directly compare the difference between estimated coupling efficiency of the two optics. The spill-over efficiency from PX 1 and PX 2 for the two-beam optics were 0.967 and 0.959, respectively. This returns an estimated beam coupling efficiency of $0.825/0.967 \approx 0.853$ and $0.830/0.959 \approx 0.865$ for PX 1 and PX 2 at 385 GHz.

This shows the feeds are relatively well matched with the antenna. If the spill-over efficiencies at the windows and re-imaging optics lenses are raised to near unity, then we can expect to see aperture efficiency values close to 0.80 on the sky. The degradation due to truncation can be addressed if we find solutions to the re-imaging optics with smaller incident angles into the cryostat window, or by consider larger windows.

The beam waist for a Gaussian beam produced by beam 1 and beam 2 are both 4.6 mm at the output of the re-imaging optics near their off-axis Cassegrain focuses. The beam waists are roughly 22 mm away from the cryostat window. The resulting beam radii at the cryostat window will be about 4.8 mm. Each beam enters the window offset from its center with the largest offset being 7.5 mm for beam 2. For both beams to have sufficient clearance to enter the window, the window diameter must be enlarged by the offset distance for each beam. This results in a final window diameter of $35 + 7.5 * 2 = 50$ mm which is 1.4 times larger than the current window.

The spill-over at lens 1 can be addressed by enlarging the lens diameter. However, the maximum diameter of a lens will be limited by the curvature radius and thickness of the lens. Additionally, the window size will also need to increase accordingly in this case as the diameter of Lens 1 was set to match the diameter of the window of the stage it was positioned in. The minimum diameter may be found by calculating the beam size at the lens. For the following discussions, we assume the same increase from 35 mm to 50 mm to match the cryostat window.

Ideally, a 50 mm window should not impose any mechanical challenges since the ALMA cryostat has larger diameter apertures for the lower frequency bands (e.g. ALMA band 1 window diameter is $\phi = 110$ mm). However, practically, in the case of ALMA, this requires redesigning the dewar top plate and integrating onto each individual antenna in the array which may require a major effort.

### 5.6.3 Additional Estimations of Degradation

#### 5.6.3.1 Effect of Dielectric Lenses

The re-imaging optics assumed ideal lenses with no loss. In reality, dielectric elements will introduce significantly more loss compared to a mirror which must be addressed. A useful formula to evaluate the loss introduced by a dielectic was given in Lamb (2003) as,

$$1 - L^{-1} = \frac{2\pi n \omega t}{c} \tan\delta. \tag{5.6.1}$$

Here, $n$ is the refractive index, $\omega$ is the frequency, $t$ is the thickness of the material, $c$ is the speed of light, and $\tan\delta$ is the loss tangent. The loss tangent is defined in Pozar (2011) as,

$$\tan\delta = \frac{\omega\epsilon'' + \sigma}{\omega\epsilon'}, \tag{5.6.2}$$

where, $\epsilon'$ and $\epsilon''$ are the real and imaginary components of the complex permittivity of the material $\epsilon = \epsilon' - j\epsilon''$, and $\sigma$ is the conductivity of the material. High-Density Polyethylene was assumed as the lens material. The lenses in the re-imaging optics may be placed outside of the cryostat or inside the 4 K stage depending on the solution. The loss tangent for HDPE at submillimeter wavelengths and different temperatures has been discussed in Jacob et al. (2002), Riddle et al. (2003), and Chao et al. (2021). An accurate measure of the loss tangent at the specific frequency and temperature will be required to quantify the dielectric loss. For a rough estimate, we assume a loss tangent of $\tan\delta = 4 \times 10^{-4}$. Using $t = 8$ mm for lens 1 and $t = 12$ mm for lens 2, Eq.(5.6.1) returns a loss of 5 % and 7 % from each lens which amounts to a total power loss of roughly 12 % at 500 GHz.

The re-imaging optics solution explored here unfortunately estimates considerable loss from the dielectrics alone, which negates the point of the complex optics design to achieve high aperture efficiency. However, this was only one solution out of the potentially many solutions. We may find an optimal solution to the lens variables that provides the lowest amount of dielectric loss. If solutions estimating only a few percent loss can be found, the few percent loss may be a valid trade-off to maintain the high-aperture efficiency and achieving the frequency independent design of the optics. This will require searching through several iterations of re-imaging optics solutions and tertiary optics solutions. Another option is exploring the use of zoned lenses to significantly reduce the lens thickness (Goldsmith, 1992).

Another source of loss is from reflection at the lens interface. The discontinuity between the relative permittivity of free-space and the lens material will cause a portion of the beam to reflect at the lens interface. Reflections can be mitigated by adding matching element structures on the lens surface to gradually change the impedance. This surface treatment is regarded as the anti-reflection coating (AR).

One note of potential issue is, most AR coatings on lenses are for a single lens-feed combination where the feed is aligned with the lens. However, the re-imaging optics demonstrated here utilizes decentered lenses shared between pixels. Here, the receiver beam also do not pass through the center of the lenses. Additionally, the chief ray angle for each beam was set independently and in practice can be different from each other leading to different incident angles into the lens. The relation between beam distortion due to tilted beams entering into the lens offset from its vertex and AR coating may require additional consideration.

#### 5.6.3.2 Additional Thermal Load for Larger Window

The previous section proposed the possibility of a larger cryostat window to alleviate the strong constraints from the small diameter. The direct consequence from a larger window is more heat allowed to enter the cryostat adding additional thermal load to the cryocooler. The added thermal load must be considered when considering cryogenically cooled receivers as the cooling capacity will be one hard limit for the maximum number of pixels that can be considered. However, if the additional thermal contributions are relatively small, this may serve as a valid trade-off for increasing the efficiency of the optics and number of pixels. However, the full thermal contributions must be calculated. This includes the contribution from the lenses, additional heat entering the cryostat, and additional components from the multibeam receiver. The total number of components should scale by a factor of number of pixels integrated on the receiver. Thermal heat transfer analyses from Ekin (2006) can be done to evaluate the additional thermal contribution to the cryostat.

Details of the ALMA cryostat, cryocooler, and cryogenics are described in Yokogawa et al. (2003). The ALMA cryostat utilizes a 3-stage GM cryocooler with a maximum cooling capacity of 0.75 W at 3.80 K, 10 W at 12.8 K, and 40 W at 98 K.

Emissive heat flux from a surface with a temperature $T$ and area $A$ is given by the Stefan-Boltzmann equation (Ekin, 2006),

$$Q = \sigma \varepsilon A T^4. \tag{5.6.3}$$

Here, $\sigma = 5.67 \times 10^{-8}$ $[\mathrm{W}/(\mathrm{m}^2 \cdot \mathrm{K}^4)]$ is the Stefan-Boltzmann constant and $\varepsilon$ is the emissivity of the surface. An increase in window diameter from 35 mm to 50 mm will increase the total area of the window by a factor of $(50/35)^2 \approx 2.04$, doubling the total heat load entering the 110 K stage of the cryostat. In reality, infrared filters are used to block a majority of the thermal radiation entering the cryostat so we may expect much lower results.

If we consider the worst case scenario of no IR filters, we may roughly estimate the total load to the 4K stake. We may focus on the re-imaging optics as the optical system to determine the rays that can enter the cryostat. Assuming the vacuum window acts as an aperture stop, it will also act as an entrance pupil. If we assume Lens 1 limits the maximum chief ray angle allowed to enter the optical system, it acts as a field stop. The rays that can enter the re-imaging optics will be determined by the entrance window of the re-imaging optics given by the cone of rays that subtends the first lens and the cryostat window as shown in Fig. 5.13.

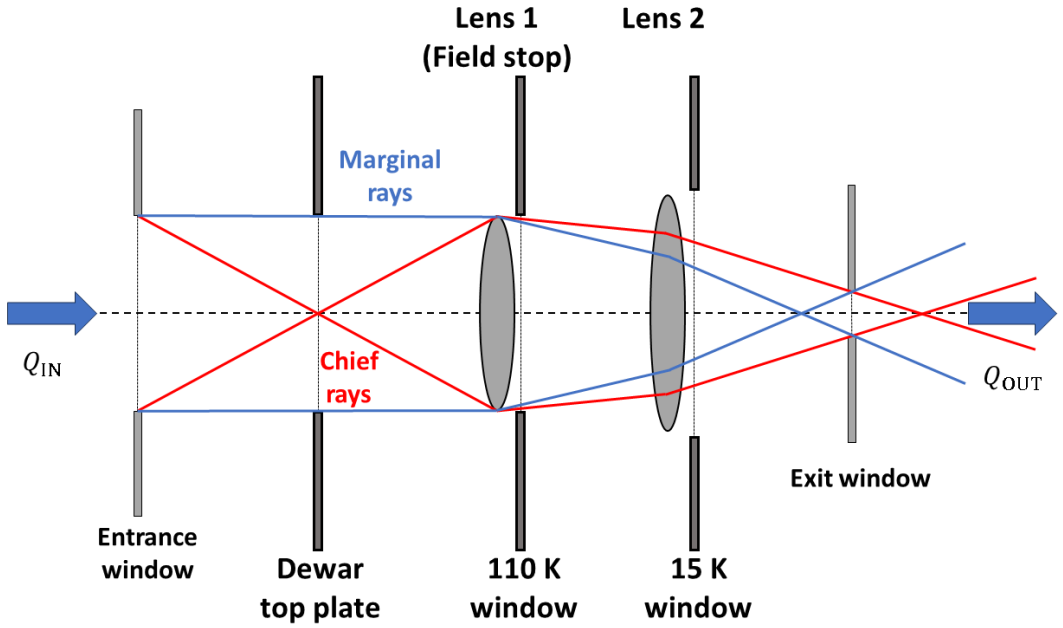


**Fig. 5.13** Entrance window of re-imaging optics.

The radiative heat transfer between two black bodies will be given by the temperature difference between the two facing surfaces (Ekin, 2006). For a surface with area $A_1$ and temperature $T_1$, the total heat exchange to a surface with area $A_2$ and temperature $T_2$ will be given by,

$$Q = \sigma(T_2^4 - T_1^4)A_1F_{12}, \tag{5.6.4}$$

where, $F_{12}$ is the geometrical factor given by,

$$F_{12} = \frac{1}{A_1}\int_{\mathrm{A2}}\int_{\mathrm{A1}} \frac{\cos\phi_1 \cos\phi_2}{\pi r^2}\mathrm{d}A_1\mathrm{d}A_2. \tag{5.6.5}$$

Some useful formulas for power transmission from a heat source through a dielectric are provided in Lamb (1993). From the total incident heat load entering the window, a portion will be reflected, absorbed, and transmitted by the dielectrics. For a dielectric material with thickness $t$,

$$Q = \lambda \frac{T_{\mathrm{H}} - T_{\mathrm{L}}}{t} A. \tag{5.6.6}$$

If the input hot temperature is 295 K, and the edge of the lens is at 110 K, and assuming a thermal conductivity of $\lambda = 0.3\ \mathrm{Wm^{-1}K^{-1}}$ for HDPE (Yang et al., 2016), a lens with 8 mm thickness using Eq.(5.6.6) returns, $Q \approx 6.7$ W for a 35 mm window and $Q \approx 13.6$ W for a 50 mm window. The increased window size will double the heat entering into the 110 K stage. This is expected as the relative size of the entrance window will increase with an increase of both the vacuum window and first lens.

The current single-beam cartridges have a total heat load of 0.35 W at the 4 K stage as shown in the ALMA cryostat front-end design report in Orlowska (2005). The biggest contributor of heat, especially at the 4 K stage, are the amplifiers which require roughly a third of the total cooling capacity. This fact alone limits the total number of pixels possible to roughly three, assuming the total heat load simply scales with the number of pixels.

## 5.7 Summary of this Chapter

This chapter aimed to address how multibeam receiver optics can be designed within a confined space such as a compact cryostat. A method to design re-imaging optics to guide multiple beams through small cryostat windows was presented. Re-imaging optics were designed by placing lenses in appropriate locations to creating a pupil at an intermediate position in the optical system. The re-imaging optics takes the beam on the sub-reflector and re-images them on the intermediate pupil. The tertiary optics were set to match a beam from a feed to the beam output from the pupil for the frequency independent condition. The re-imaging optics and tertiary optics parameters can be solved using a simple parametric search. The method was applied to design a two-beam multibeam receiver to fit inside the ALMA 12-m antenna and its cryostat. Beam were successfully directed through the cryostat from large offset positions inside the cryostat. The presented design showed significant truncation of the beams at the edge of the cryostat window, but otherwise suggests high beam coupling efficiency between the target illumination and the feed. The method produces an acceptable design that can be further refined.

# CHAPTER 6

# Wideband Magic Tee Waveguide Junctions

## 6.1 Introduction

This chapter discusses a novel design to a wideband high-performance E-plane Magic Tee waveguide junction for split-block fabrication that can be applied in current heterodyne receivers, and future applications for LO distribution in multibeam heterodyne receivers.

### 6.1.1 Waveguide Blocks used in Radio Receivers

Radio telescope (sub)mm-wave receivers use low-loss waveguide components, and low-noise amplifiers and/or superconducting mixers to receive extremely weak astronomical signals. Additionally, science requirements usually require wideband performance. This wideband low-noise specification pushes for compact and complex waveguide networks which combine several waveguide components in a single block.

### 6.1.2 Fabrication Methods

Machining methods with high-accuracy are necessary as fabrication errors can be fatal for state-of-the-art high-performance waveguide components at millimeter wavelengths. The fabrication of waveguide components will depend case-by-case for the application. The fabrication method can be categorized into subtractive and additive manufacturing. Subtractive manufacturing includes the vast variety of direct machining methods such as Computer Numerical Control machining (CNC machining). Additive manufacturing includes methods such as 3D printing.

**N-Section Construction** :A waveguide block is usually fabricated as E-plane split-blocks to avoid cutting waveguide currents of the fundamental $TE_{10}$ mode, which would increase loss in the case of non-perfect metal contact between blocks (Pozar, 2011). A waveguide can be constructed with subtractive manufacturing by directly removing material from a metal block to create waveguide channels. A waveguide is constructed by dividing it into sections, then machining each section as channels on the block, which are all then constructed connected to form the waveguide walls.

Figure 6.1 depicts a simple rectangular waveguide constructed with a two-part E-plane split-block. It is also generally desirable to have as few blocks as possible to minimize alignment errors. Waveguide components designed and developed at the National Astronomical Observatory of Japan Advanced Technology Center often employ two-piece construction with a E-plane split-block.

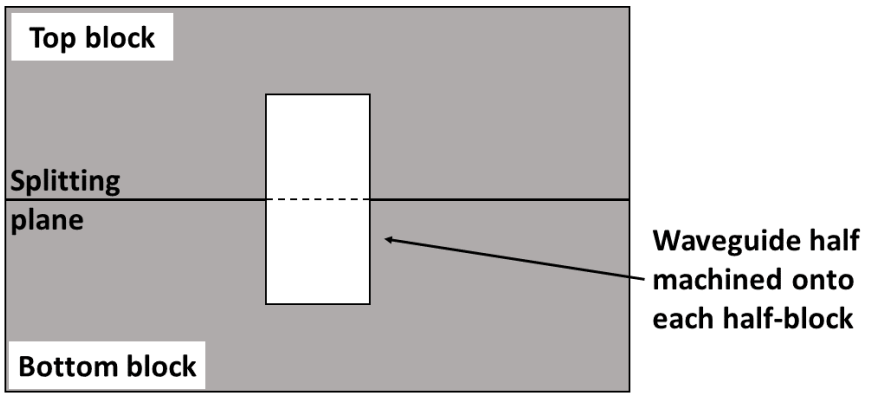


**Fig. 6.1** A diagram showing the desirable construction of a waveguide onto a metal block. The waveguide is split at the center crosswise and each waveguide half is machined onto the two half blocks.

Direct machining of wavaguide components can be done with single-axis turning, 3/5-axis computer numerical control (CNC) machining, and wire-cut electric discharge machining (Wire-cut EDM). These methods offer reliable high-accuracy fabrication even for complex geometries.

The main drawbacks for direct machining is some limitations in fabricable structures. Structures are created by removing metal from a block. Thus, areas where a tool cannot reach physically cannot be fabricated. Some fabricable structures are also undesired such as deep horizontal grooves which requires special tools which are either not commercially available, or are prone to breaking due to unusual bit aspect ratios.

**Metal 3D Printing** : A relatively new branch of additive manufacturing is metal 3D printing. Metal 3D printing has seen a surge of application due to recent advances in 3D printing technologies and readily available commercial 3D printers. All metal additive manufacturing can be broadly categorized into laser beam powder bed fusion systems (PBF-L), laser beam directed energy deposition systems (DED-L), electron beam powder bed fusion systems (PBF-EB), and other systems such as plastic casting combined with casting and nano-scale technologies (Milewski, 2017). Each method has their pros and cons and is best suited case-by-case for manufacturing a component. In this thesis, we are mainly interested in PBF-L technology.

Metal 3D printing of waveguide components have been demonstrated for diverse applications at various frequencies. Polymer based printing with copper deposition for ambient temperature waveguide components has been demonstrated for communications systems at X-band frequencies (8 to 12 GHz) in Guo et al. (2019). Recently, an all metal 3D printed millimeter wave waveguide components have been successfully demonstrated at

cryogenic temperatures for radio astronomy in Gonzalez et al. (2021).

### 6.1.3 Challenges Towards Multibeam

#### 6.1.3.1 3-Port Junctions in LO Circuits

In complex waveguide circuits, power dividers/combiners are common and 3-port T/Y-junctions have been used traditionally to distribute Local Oscillator (LO) signals to Superconductor-Insulator-Superconductor (SIS) sideband separating mixers (2SB) (Asayama et al., 2021) or integrated in Orthomode Transducers (OMT) to recombine same-polarization signals (Gonzalez et al., 2021). In many of those cases, the two ports of a power divider/combiner are connected to devices optimized for low-noise performance and which usually present very poor return loss. Due to the poor isolation of a T/Y-junction, a considerable amount of the large reflected signal finds its way to the other port, also connected to a component with poor return loss. This creates standing waves which degrade the system performance.

Consider the setting in Fig. 6.2 where a two-beam multibeam receiver has side-band separating mixers. A common LO signal is sent to both pixels and is divided using T-junctions and a fraction of the input power is coupled to the mixers (Red arrows in Fig. 6.2). Mixers have intrinsically unmatched input impedance which results in a noticeable reflected component of the input LO power (green and blue arrows in Fig. 6.2). The reflected component is then fed back into the T-junction where, since there is no output isolation, it is propagated to the neighboring mixer in the 2SB unit, and to the neighboring pixel in the multibeam receiver. This reflection can cause instability in the frequency response as ripples, or have a detrimental impact in the form of exciting resonant frequencies. The resonance will render certain frequencies inoperable in the worst case. The ripples will also cause an increase in LO noise due the unmatched phase between the input LO and the reflected LO. Hence, mitigating the reflected component is crucial for maintaining the highest performance.

One solution we may explore is utilizing a high-isolation power divider which can lead a reflected component to a matched termination where it can be absorbed isolating the neighboring ports. This can be done with 4-port devices such as a Magic Tee junction.

#### 6.1.3.2 Integrating 4-Port Junctions in Boifot Junction OMTs

A similar situation hypothesised in the previous section has been reported internally concerning an Ortho-mode Transducer (OMT). The wideband OMT being developed for ALMA band 7+8 (275 to 500 GHz, FBW: 58 %) utilizes a Boifot junction type double-ridged waveguide OMT to separate orthogonal polarizations (Gonzalez and Kaneko, 2021). The horizontal polarization (H-Pol) is sent through two branching arms which then recombine using a Y-junction.

Recent fabrication has led to minor issues concerning the yield of components. A few fabricated samples showed resonant frequencies in both the vertical and horizontal polarization response.

Recently, it was found from an analysis conducted by Ryo Sakai at the Advanced Technology Center at NAOJ, that the cause of the resonances were from fabrication errors in the double ridge structure. The resonance was caused by standing waves in the H-Pol ring of the OMT.

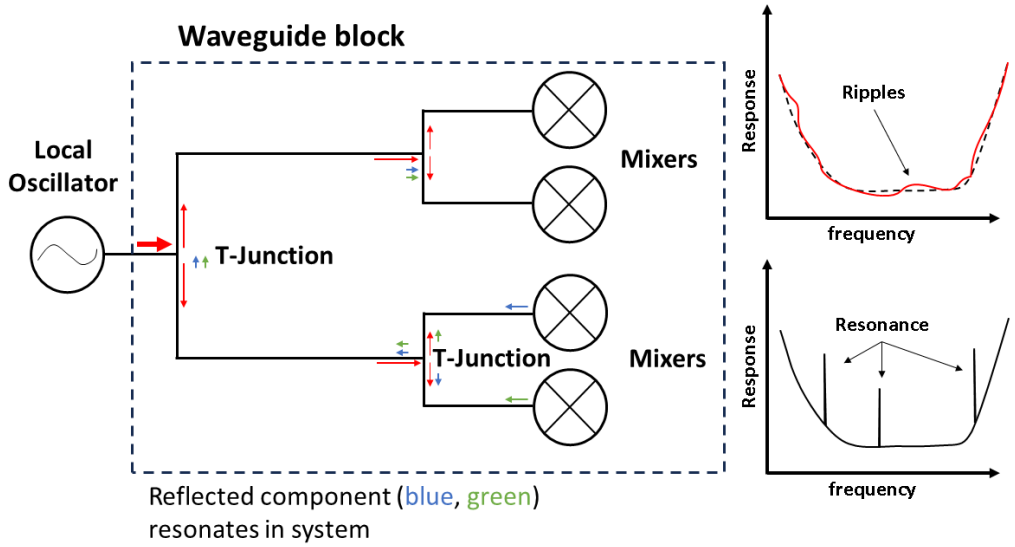


**Fig. 6.2** Diagram of signal reflections propagating to a neighboring pixel.

This resonance could be broken if isolation is introduced in the H-Pol ring.

This resonance may be addressed by replacing the Y-junction in the OMT with a junction with high-isolation. Even with the presence of small fabrication error causing leakage to the other orthogonal output, the leaked signal can be properly terminated at the junction. This will effectively increase the yield of usable components, which a crucial aspect for mass production of components. Increased yield of components is also attractive for multibeam receivers as the same component may require being fabricated N times for N number of pixels in the array.

## 6.2 Magic Tees for Split-Block

### 6.2.1 Magic Tee Waveguide Junction

Magic Tees are four-port waveguide junctions that have high port-to-port isolation. The simplest Magic Tee is composed of three intersecting empty waveguides as shown in Fig. 6.3. An ideal Magic Tee will have a scattering matrix given by,

$$S = \frac{1}{\sqrt{2}} \begin{bmatrix} 0 & 1 & 1 & 0 \\ 1 & 0 & 0 & 1 \\ 1 & 0 & 0 & -1 \\ 0 & 1 & -1 & 0 \end{bmatrix}. \tag{6.2.1}$$

An ideal Magic Tee will have two pairs of isolated of ports, the two colinear ports and the difference and sum ports. A Magic Tee may serve the role of a 180-degree power divider for signals input into port 4 (Blue arrows in Fig. 6.3).

The Magic Tee is one solution that can address the issues caused by poor port isolation stated in Section.6.1.3. A Magic Tee may replace the role of a three-port power divider to increase the

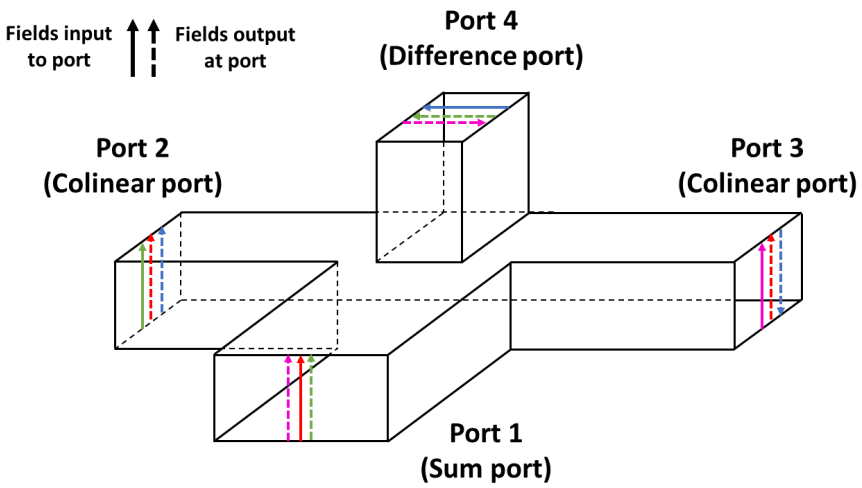


**Fig. 6.3** Diagram of a simple empty Magic Tee. Fields input at the ports are represented with solid arrows, and the resulting fields output at the other ports are represented with dashed arrows. Each color shows an ideal operation of a Magic Tee.

isolation between neighboring circuits in a LO distribution circuit. A Magic Tee integrated in a Boifot junction OMT may reduce the degradation effects due to fabrication errors and increase the total yield of components.

### 6.2.2 A High-Performance Magic Tee for (Sub)millimeter Wave Radio Receivers

Magic Tees have seen a variety of use in telecommunication and radar systems. Telecommunications and radar have vastly different requirements in terms of bandwidth, loss, and design compared to astronomical receivers. Thus, the diverse catalog of Magic Tee designs may not be suitable for addressing the issues demonstrated in Section. 6.1.3.

A Magic Tee for astronomical receivers must have low-loss, and high-isolation in a wide bandwidth. High-performance Magic Tees have been developed, however they lack the wideband performance[1] (Chu et al., 2014, Li et al., 2016), utilize striplines which complicates fabrication (Wang et al., 2015, Wang and Ling, 2019), or have H-plane power dividers (Chatterjee et al., 2015, Ameri et al., 2023, Hwang, 2009, Khorsandy et al., 2019).

Astronomical receivers often utilize two-part split-blocks for the waveguide block and junctions are designed as E-plane power dividers. If we wish to address the argument of replacing conventional T/Y-junctions, we require a design that can be implemented in current E-plane split-blocks. A few E-plane power divider Magic Tees have been proposed or demonstrated (Kerr and Horner, 2000, Zhu et al., 2011, Farahbakhsh, 2020, He et al., 2017, Peng et al., 2022). However they either lack the bandwidth, target performance, or construction method for the interest here. Hence, we require a waveguide based E-plane power divider Magic Tee junction that has high-performance across a wide bandwidth that can be implemented in a split-block.

[1]For Astronomical receivers

## 6.3 Design

### 6.3.1 Design Targets

Waveguide components used in radio telescope receivers require wide bandwidth to maximize the observable spectrum. The design targets are set to align the performance with other high-performance waveguide components used in astronomical receivers. The design targets are used for the optimization targets in software.

- Bandwidth as wide as possible.
- All port return loss higher than 20 dB and ideally higher than 25 dB.
- Isolation between sum and difference ports (port 1 and port 4), and between colinear ports (port 2 and port 3) higher than 20 dB and ideally higher than 25 dB.

### 6.3.2 Design Constraints

The direct machining of waveguides onto a block is usually done at NAOJ with 3-axis computer numerical control (CNC) machining (Fig. 6.4). Waveguides oriented perpendicular to the splitting plane will require the use of wire-cut EDM in some situations. These fabrication methods will impose strong constraints on the fabricable structures and final design of the component. Some constraints and general rules to be followed are listed below.

- Overhangs and cavities perpendicular to the machining direction require special tools and should be avoided to keep the machining simple.
- Sharp corners parallel to the machining direction will have rounded edges due to the machining bit. The fillet radius should have values realizable through standard machining bits.
- The maximum height of a structure should not exceed the split-block height to reduce the amount of excessive material to be removed and to limit potentially fragile structures to be exposed beyond the splitting plane.

Because of these limitations, structures oriented parallel to the splitting plane will be severely limited and/or cannot be fabricated.

The two colinear arms and difference port share a common plane where the waveguide centers can be situated on a plane parallel to difference port direction and can divide the waveguides cross-wise as demonstrated in Fig. 6.5. This plane is appropriate to serve as the splitting plane for the construction of a E-plane split-block Magic Tee.

## 6.4 Design of a 30-50 GHz Magic Tee

A Magic Tee shown in Fig. 6.6 was designed at extended Q-band frequencies of 30 - 50 GHz. This frequency range was chosen to relax the required tolerances for the component and because of the widely available commercial measurement instruments. The input rectangular

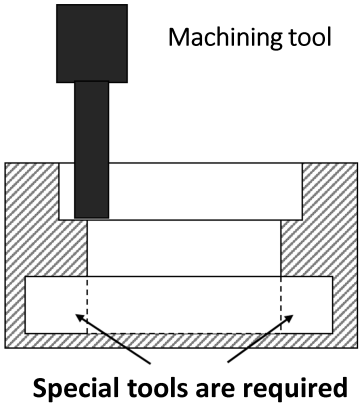


**Fig. 6.4** Limitations of structures fabricable through vertical 3-axis machining. Cavities perpendicular to the machining direction is one example of a structure requiring special tools such as a lathe. The use of special tools is generally avoided when possible to keep the machining as simple and inexpensive as possible.

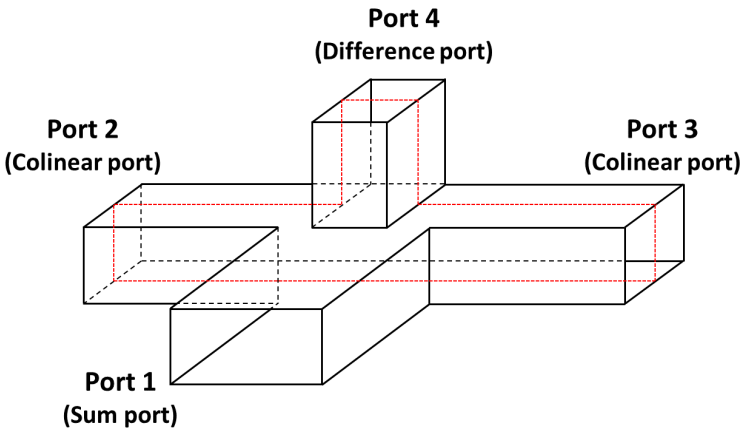


**Fig. 6.5** The common plane where the waveguides can be cut cross-wise in a simple Magic Tee.

waveguides for port 1 to port 3 are standard WR-22, with dimensions $5.69\ \mathrm{mm} \times 2.84\ \mathrm{mm}$. Ports 1 to 3 are all situated parallel to the splitting plane which divide the input waveguides crosswise. Port 4 is placed perpendicular to the splitting plane and connects to the other port arms at the center junction. All fillet radii were kept larger than 0.8 mm to utilize standard machining bits.

The detailed design is shown in Fig. 6.7. Port 1 (difference port) is a stepped waveguide with an iris connecting to the center junction. Ports 2 and 3 are E-bend WR-22 waveguides that flare away from each other to accommodate the waveguide flange on the final block. Port 4 (sum port) is a simple waveguide with rounded edges. The fillet radius for port 4 was kept relatively large so that the possibility for 3-axis machining could remain. Port 4 connects directly to the center junction. The junction is divided into two sections along the splitting plane and each section has two sections with variable height and width shown in Fig. 6.8. The Magic Tee is split along the center which cuts the input waveguides for ports 1 to 3 crosswise as shown in Fig. 6.9. This is the splitting plane for the split-block.

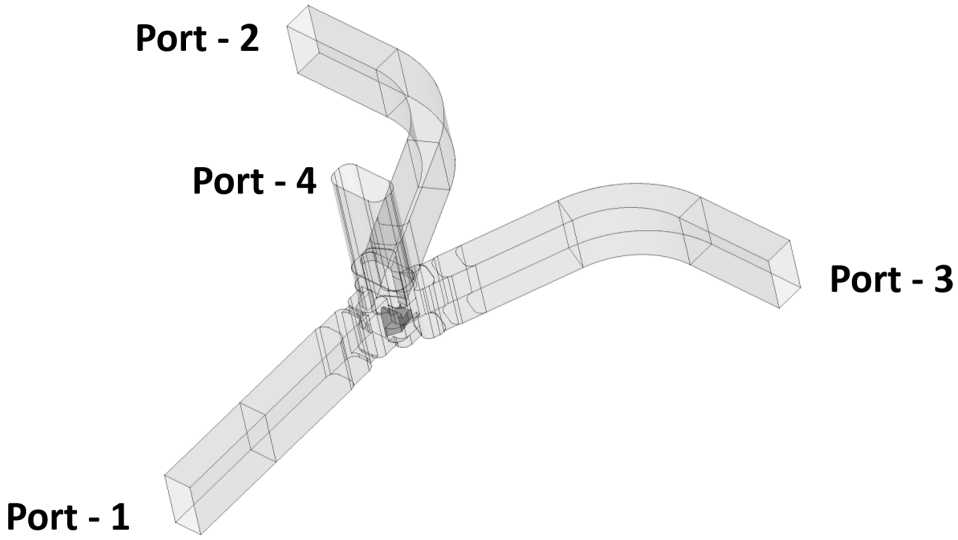


**Fig. 6.6** Proposed design of Magic Tee.

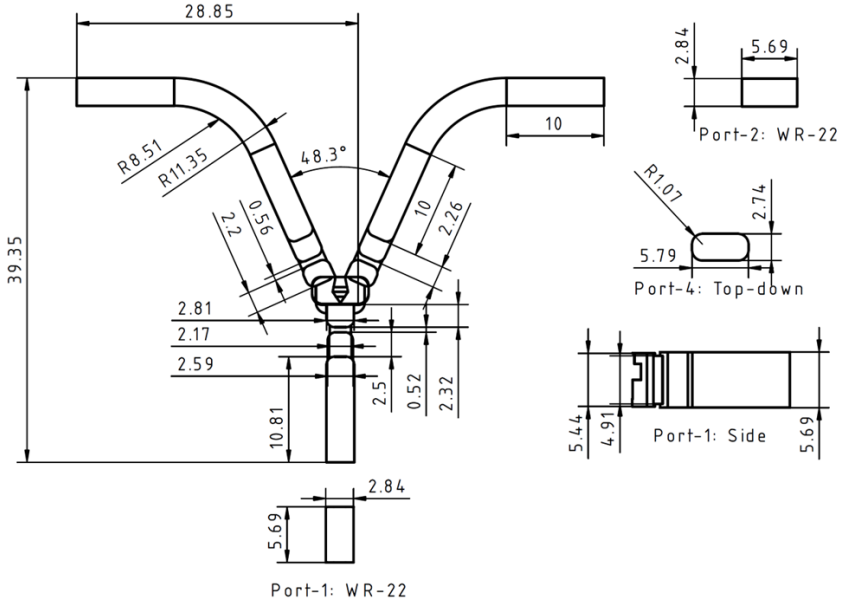


**Fig. 6.7** Mechanical drawing of proposed design and the dimensions of each waveguide inputs. Details of each port are shown in the detailed views. Port-2 and Port-3 have symmetrical designs.

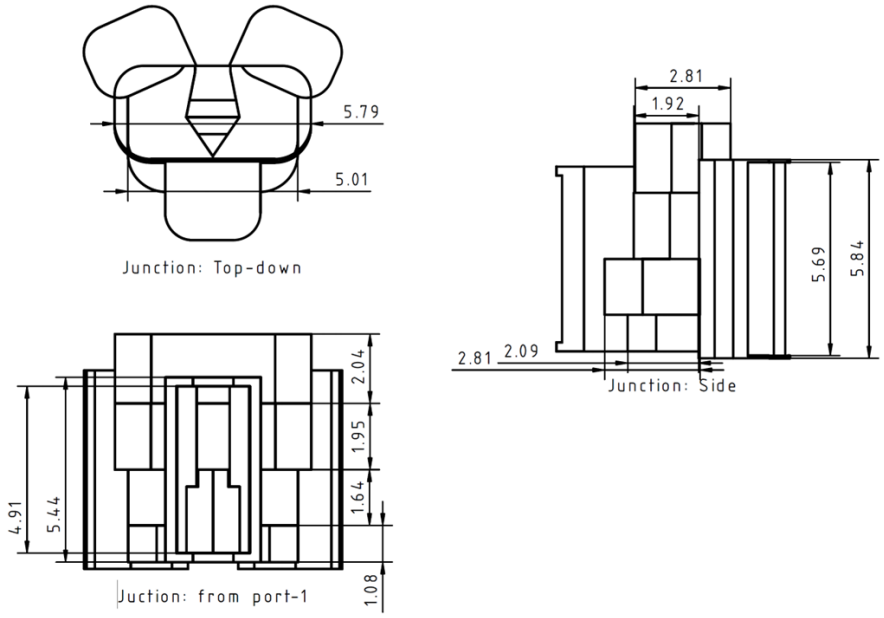


**Fig. 6.8** Mechanical drawing of center junction with the top-down and side perspectives

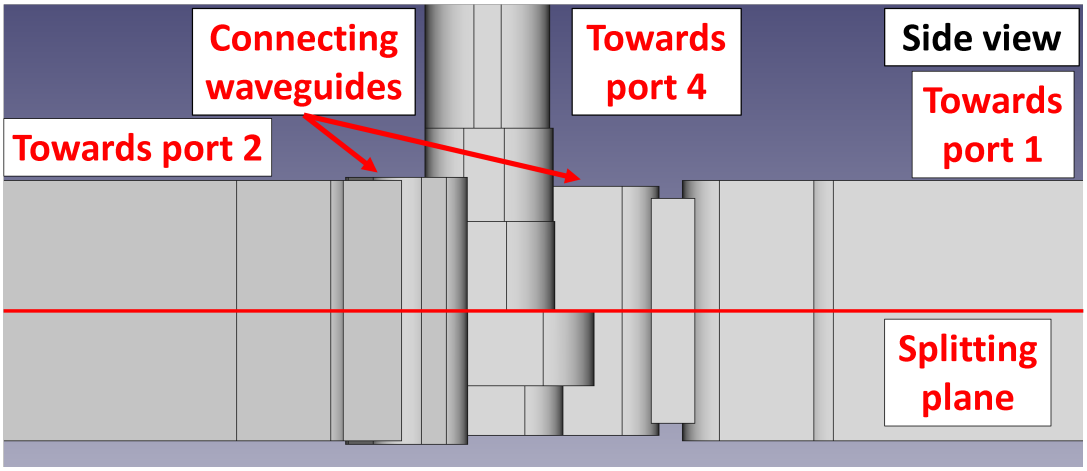


**Fig. 6.9** Side view of center Junction. Towards the left is port 2 and to right is port 1. The red line shows the splitting plane for the split-block.

### 6.4.1 Matching Elements

Matching elements placed inside the center junction have been used to increase the bandwidth of magic tees. Typical matching structures consist of conducting cones and pillars which point towards the difference port (e.g. Peng et al., 2022, Chatterjee et al., 2015). These structures may be fabricated in a split-block but may require special tools, which complicates the fabrication process. Here we focused on simple structures fabricable using 3-axis CNC machining.

Different structures shown in Fig. 6.10 were simulated to find a matching element that return the required performance while still being machinable with 3-axis CNC. The first design iteration was a simple rectangular fin and post. The port reflection was mostly dictated by the shape and area seen from the port, thus flat walls perpendicular to a port were avoided by using a

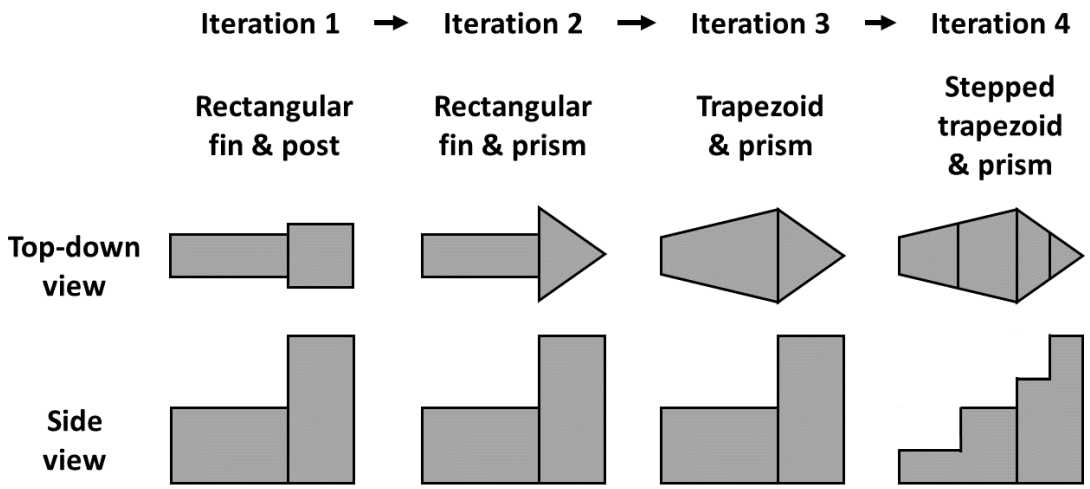


**Fig. 6.10** Design evolution of matching element structure. The top-down view is looking down from port 4 and the side view has port-1 on the right side.

triangular shape and steps were added to create a gradual transition. The port isolation between ports 1 and 4 were intrinsically high for a fin-post structure. The port isolation between ports 2 and 3 were mostly affected by the height and width of the fin. Fillets between the fin and post were removed by using a trapezoidal shape that connects to the prism which simplifies the fabrication.

Trial-and-error of machinable features ultimately converged to a stepped trapezoid and prism as shown in Fig. 6.11. The height was limited to the splitting-plane to avoid fragile structures protruding past this plane. The matching element is placed inside the bottom block inside the junction. The detailed design and dimeions of thematching element is shown in Fig. 6.12.

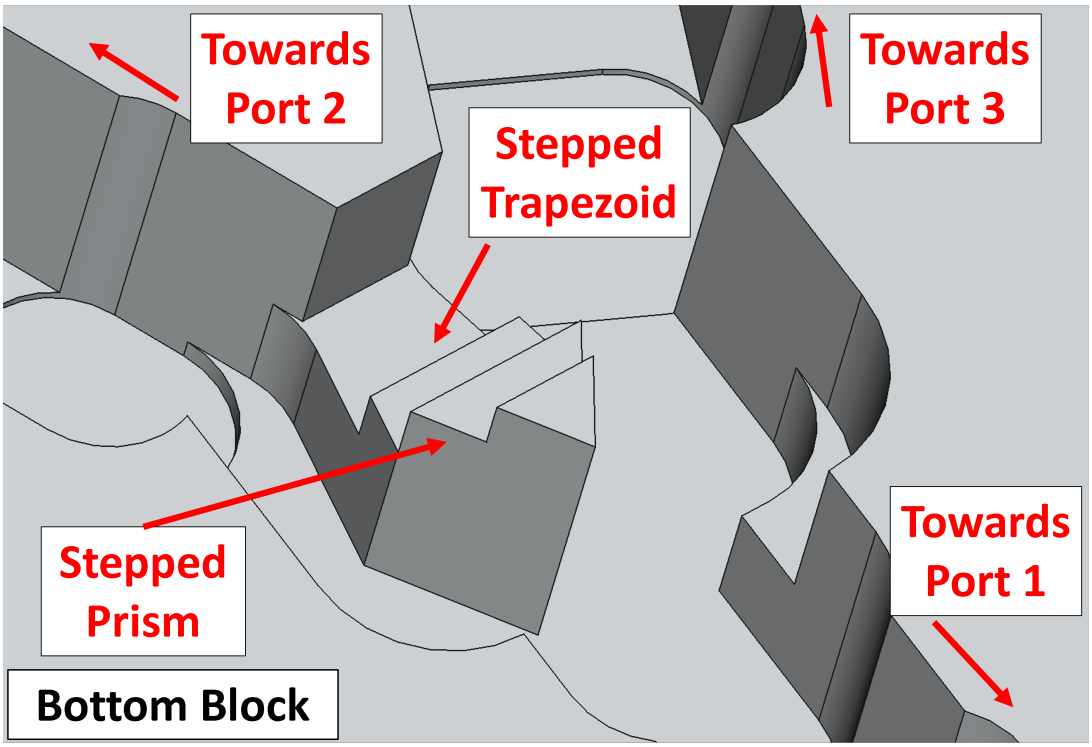


**Fig. 6.11** CAD view of matching element structure.

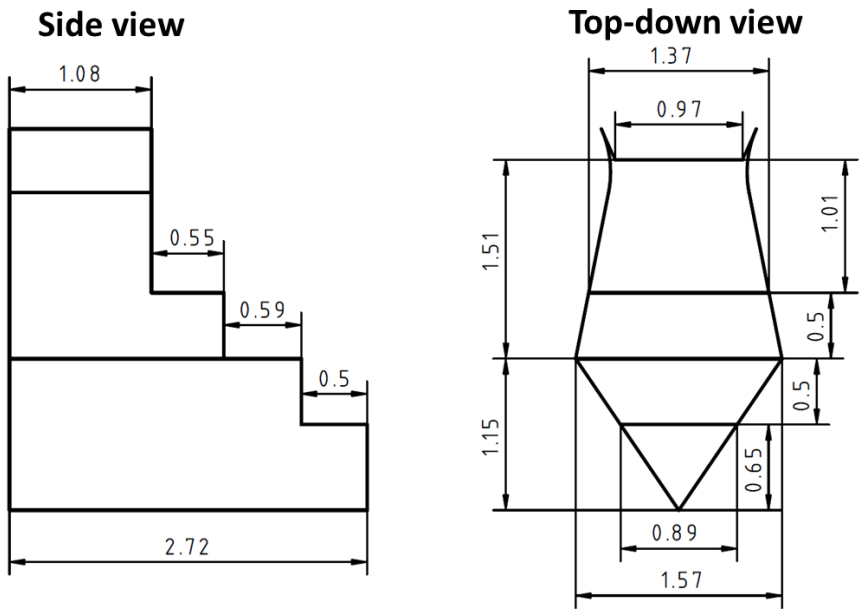


**Fig. 6.12** Mechanical drawing of final matching element structure and dimensions. The dimension units are in mm.

### 6.4.2 Simulation Results

The Magic Tee was optimized to reach the requirements and target performance listed in 6.3.1. The Magic Tee was simulated in WASP-NET from 28 to 52 GHz. The S-parameters for the port reflection, isolation, and transmission are shown in Fig. 6.13. The simulations were

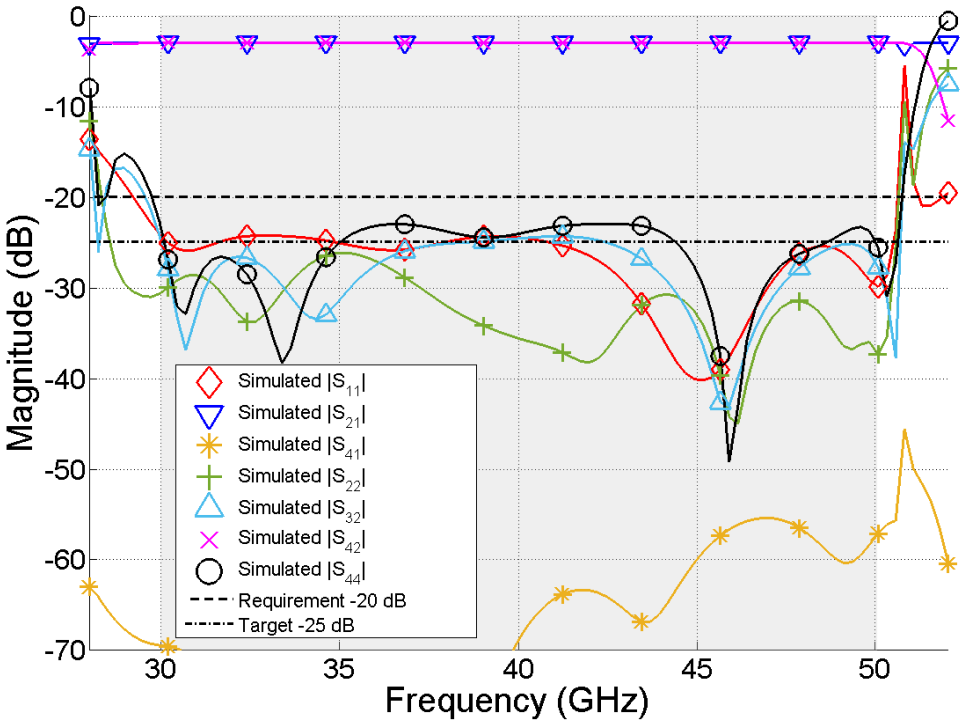


**Fig. 6.13** Simulated return loss shown as $S_{ii}$ and isolation between ports as $S_{41}$ and $S_{32}$. $S_{22}$ and $S_{33}$ are the same due to symmetry. The target 30-50 GHz frequency range is shaded.

conducted with a WR-22 rectangular waveguide transition at port 4.

The simulated Magic Tee was able to achieve higher than 22 dB for all port return loss and port isolation satisfying the requirement but fell short to reach the target of 25 dB within the target frequency band.

One note for potential conflict is the existence of a trapped mode at 51 GHz. Although the trapped mode is clear of the target frequency band, it may shift in frequency depending on the tolerance of the final component. Maintaining high-tolerance will be necessary to keep the trapped mode from entering the target frequency range.

## 6.5 Fabricated Component

The designed magic tee integrated in a split-block is shown in Fig. 6.14. All CAD models and fabricated component were produced and manufactured by KMCO [2] (Kawashima corporation). Each block has the dimensions $54.06\ \mathrm{mm}$ (width)$\times 65.00\ \mathrm{mm}$ (length)$\times 14.67\ \mathrm{mm}$ (height), with the final block having a total height of 29.34 mm. The waveguide flanges are UG383/U. The exterior of the manufactured block is shown in Fig. 6.15, and the view of the internals shown in Fig. 6.16.

[2] https://kmco.co.jp/

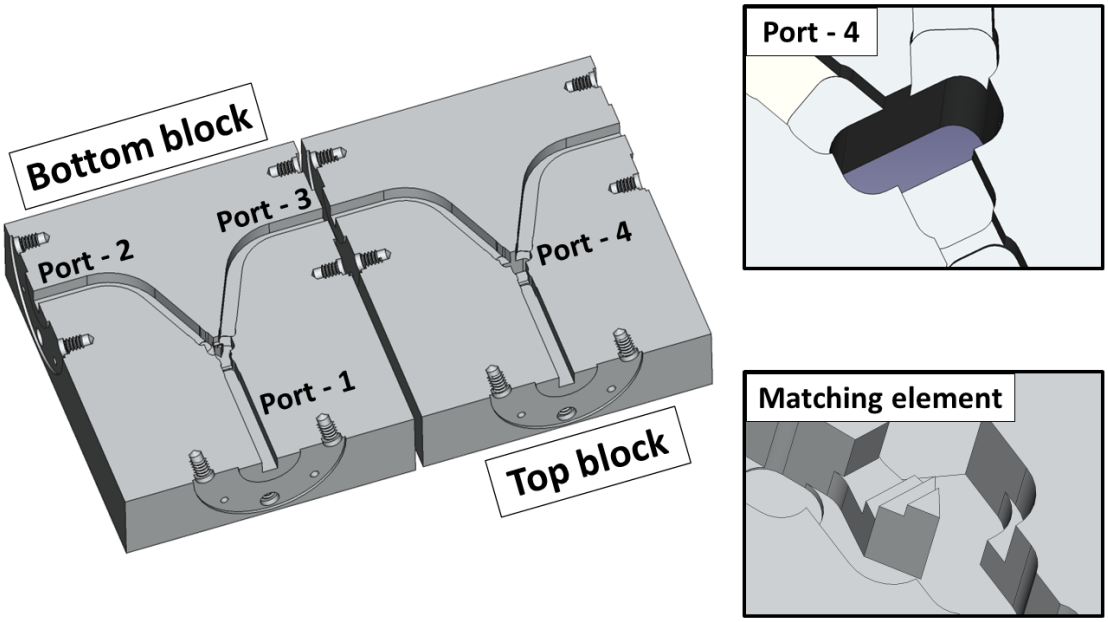


**Fig. 6.14** CAD model of proposed Magic Tee with flanges integrated in a two-part block. This is a simplified model to clearly show the waveguide channels and flange, and omits the securing screws, flange alignment pins, and other finer mechanical considerations.

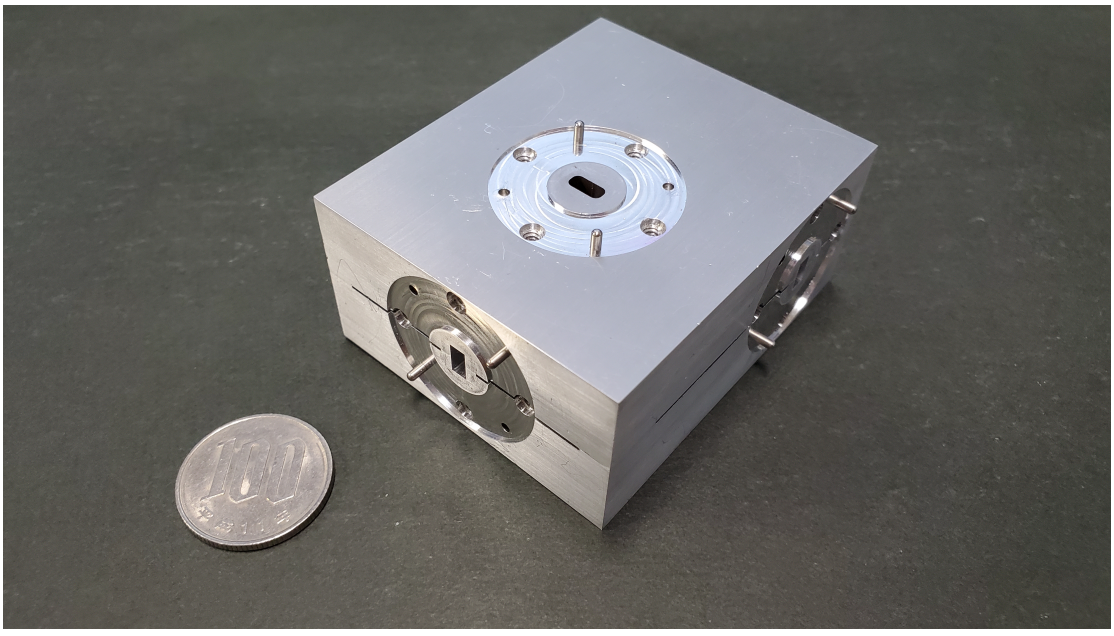

**Fig. 6.15** Photo of final Magic Tee block. A 100 Yen coin is shown in the left for scale.

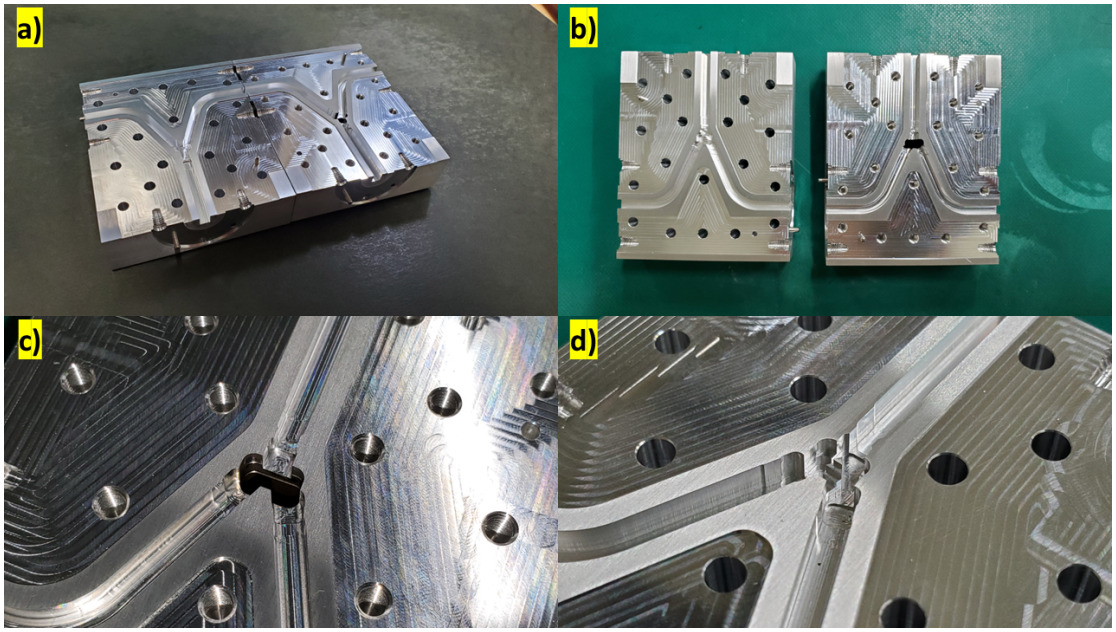


**Fig. 6.16** Photo of open final Magic Tee block. a) Overview of both blocks, b) Top-Down view, c) Port 4 in top block, d) Matching element in bottom block.

## 6.6 VNA Measurements

Vector Network Analyzer (VNA) measurements were conducted to obtain S-parameters. The measurement setup is shown in Fig. 6.17. A two-port VNA (model number) and two terminations were used to measure ports sequentially. A WR-22 Attenuator was used as a substitute termination as only a single WR-22 standard load was available. The open end of the attenuator reflects a portion of the signal back into the Magic Tee which slightly degrades the measured S-parameters. The characteristics of the standard load and the open-ended attenuator are shown in Fig. 6.18. The attenuator reflects roughly a maximum of -20 dB within the target frequency band. By connecting the attenuator to the isolated port, the combination of the low transmission with the attenuator should minimize the total reflected power. The attenuator was connected to an isolated port when measuring the port reflections. However, the isolation measurements cannot be free from this reflection due to their being two non-isolated ports. Accurate measurements of the port isolation requires connecting two matched load at the remaining ports, which can be easily done with two standard WR-22 loads.

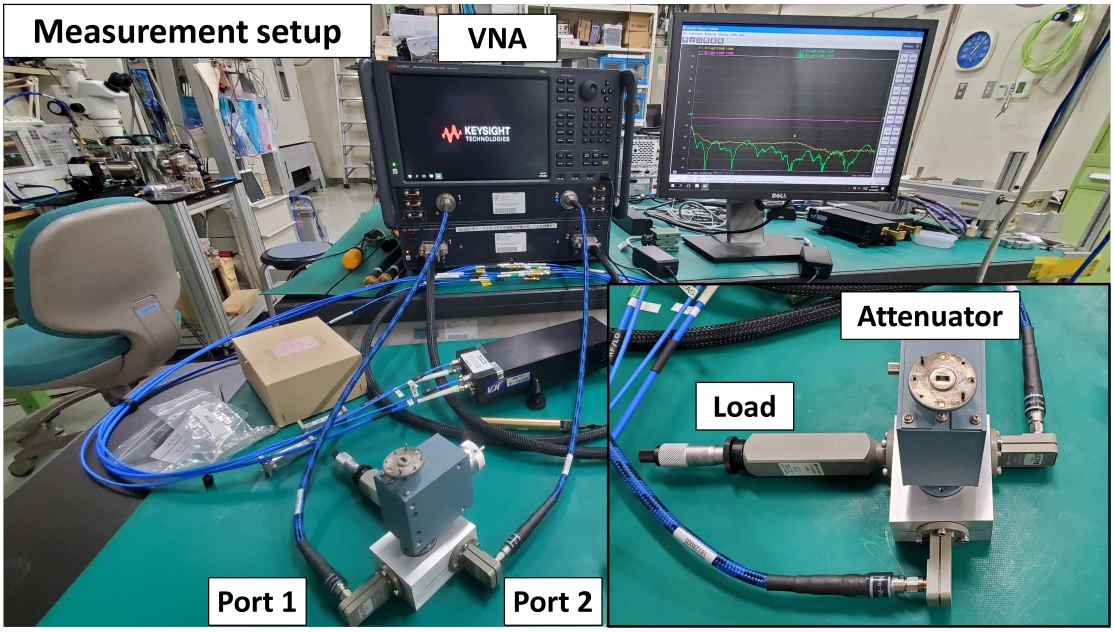


**Fig. 6.17** Photo of the VNA setup. The background photo shows the VNA connected to the Magic Tee and the lower right crop shows the open attenuator and load terminations.

The measurements were done from 28 to 50 GHz due to the limits of the VNA. Comparison between the measurement results with simulations are shown in Fig. 6.19 and Fig. 6.20. The measurements are in close agreement with the simulations despite some fluctuations due to the use of an attenuator as a termination. There is a noticeable deviation between the measured and simulated return loss at the frequency ends. The lower end deviation can be attributed to the combination of the unmatched termination using the attenuator and the characteristics of the load. The higher end may be related to the rectangular waveguide transition at port 4.

The return loss shows higher than 20 dB for all port reflection except for port 4 which shows degraded performance at frequencies higher than 48.9 GHz. The slight differences between the simulated and measured port reflection can be attributed to the use of an unmatched load, the fabrication tolerances, and the alignment tolerances with the VNA waveguide ports. However, the measurement results show some ripples due to the unmatched termination. Thus, follow-up measurements with a 4-port VNA or with another matched termination is required to conclusively determine if this is the true performance or errors introduced by the measurement setup. Nevertheless, the port 4 reflection shows acceptable performance just shy of the requirement. The particular use case we are interested in is replacing a T/Y-junction. In this application, port 4 will not serve a critical role and can be terminated with an absorber. Thus the requirement of low return loss for port 4 may be relaxed depending on the application. The detailed discussion is presented in Section. 6.8.2.

The isolated port transmission coefficients in Fig. 6.20 show some ripples in the measurements due to the unmatched termination. However, the port isolation still achieved the requirement of -20 dB. In reality, the isolation may be higher but finally limited by the symmetry of the component from the fabrication, particularly the $|S_{41}|$.

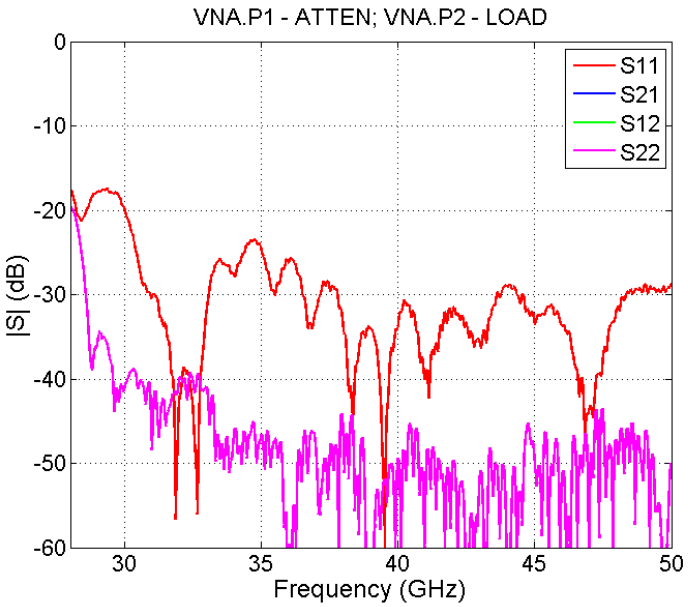


**Fig. 6.18** Reflection introduced by an open attenuator and load. The attenuator was connected to port 1 with the opposite port left open and port 2 was connected to a WR-22 Load.

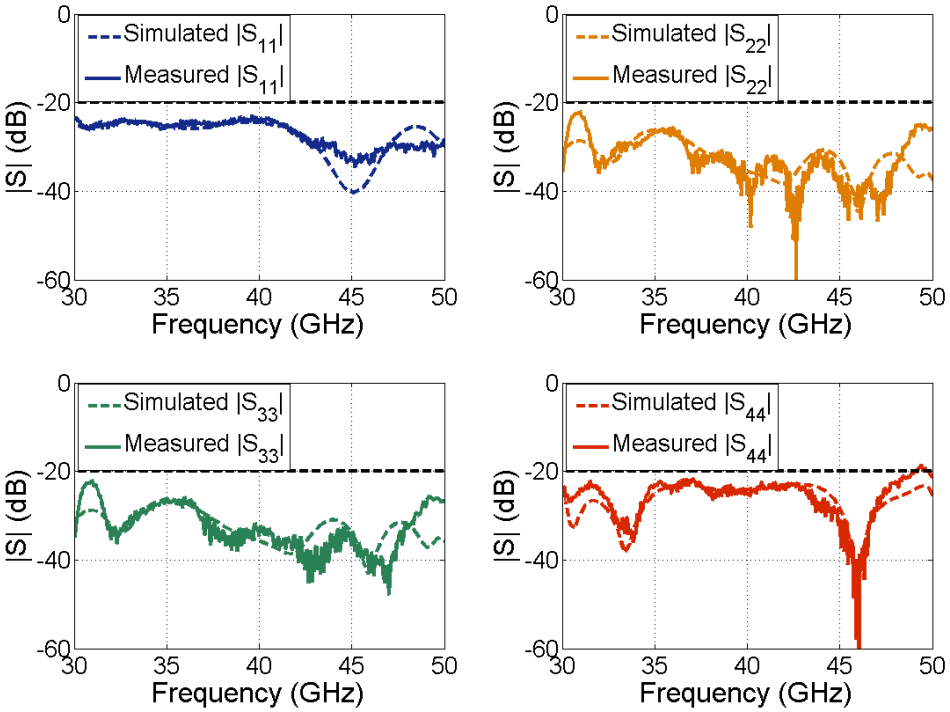


**Fig. 6.19** Comparison between measured and simulated return loss. The dashed lines are the simulated and the solid lines are the measured return losses. The black dashed line shows the requirement of -20 dB.

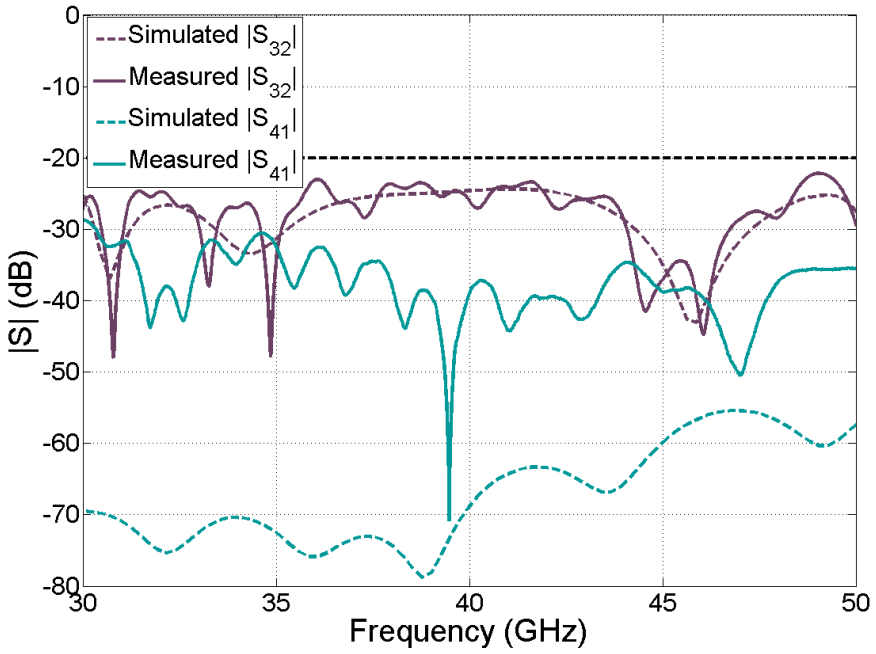


**Fig. 6.20** Comparison between measured and simulated port isolation. The dashed lines are the simulated transmission between isolated ports and the solid lines are the measured. The black dashed line shows the requirement of -20 dB.

## 6.7 Some Tests with 3D Printing

This section explores the application of metal 3D printing technology to fabricate high-performance Magic Tees. The main objective here is to identify limitations, possible improvements, and provide information towards the next steps for fabricating complex 3D printed waveguide components.

### 6.7.1 Metal 3D Printing

Recent advancements in metal 3D printing techniques have made previously challenging or otherwise impossible structures to fabricate with direct machining, possible (Duda and Raghavan, 2016). Powder bed fusion (PBF) metal 3D printing has seen a variety of applications in many different fields, and they have recently been utilized for the fabrication of millimeter wave radio receiver feed horns in Gonzalez et al. (2021).

Many 3D printing methods must be mindful of overhanging structures in the component. As a component is built layer-by-layer, large overhanging structures must have supports underneath them to prevent deformations (dotted box in Fig. 6.21). As a result, overhangs must have accessible support structures that can be removed with post processing. However, the inside of a waveguide, especially at millimeter wavelengths, will have limited access to the inside due to their small dimensions. Overhangs can be directly printed if the component is tilted so the overhang angle is much shallower. The general rule-of-thumb is to have the overhang oriented no less than 45-degrees along the printing direction.

Metal 3D printing is also currently limited in frequency to around 50 GHz due to surface

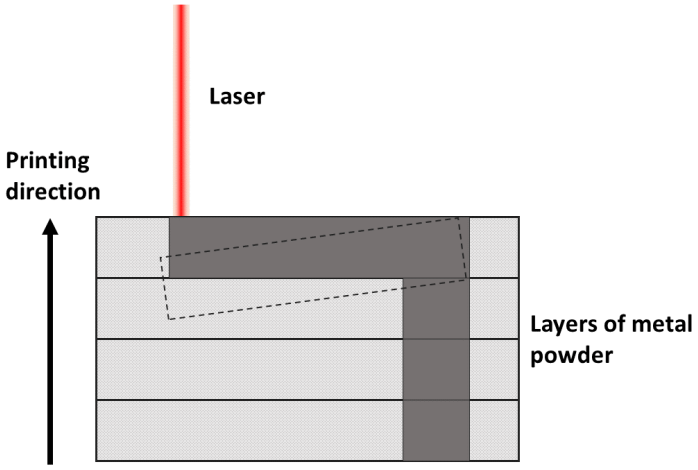


**Fig. 6.21** Diagram showing fabrication through powder bed fusion metal 3D printing. The dashed box shows an overhanging structure perpendicular to the printing direction which is susceptible to sagging and thus typically requires support structures.

roughness. However, fine-tuning the fabrication process and applying post processing to the fabricated component can extend the highest frequency range.

One interesting application for 3D printing is the possibility to take multiple individual components and fabricate a single continuous component. This will potentially eliminate alignment issues between components and will also simplify the characterization process as the number of components can be reduced. An example is shown in Huang et al. (2018) where a fully 3D printed feed and orthomode transducer cluster was fabricated as a single component.

The matching element geometry demonstrated in Section. 6.4.1 had limited design freedom because of the machining method. 3D printing may offer more freedom to design complex structures which cannot be fabricated with direct machining.

### 6.7.2 Fabricated Prototypes

The same 30 to 50 GHz Magic Tee was fabricated via 3D printing. The 3D printed components are shown in Fig. 6.22. The printing was done at the Advanced Technology Center (ATC) at the National Astronomical Observatory of Japan. Five components were fabricated labeled No.1 to No.5. Each component was tilted 45 degrees in different orientations during the fabrication. The components labeled No. 1 and No. 2 were tilted 45-degrees along two axes, and the components labeled No. 3 to No. 5 were tilted 45-degrees along a single axis. Post processing was done to machine the alignment holes and threads for the waveguide flanges.

### 6.7.3 VNA Measurements

The same VNA setup from Section. 6.6 was used to obtain S-parameters. Only the components No.1 to No.3 were measured due to insufficient time. The return loss and isolation for each 3D printed sample is compared with the simulations and is shown in Fig. 6.23 and Fig. 6.24, respectively. The return loss is generally lower across all measured components compared to the direct machined component. Nevertheless, the overall performance is is close to 20 dB for both

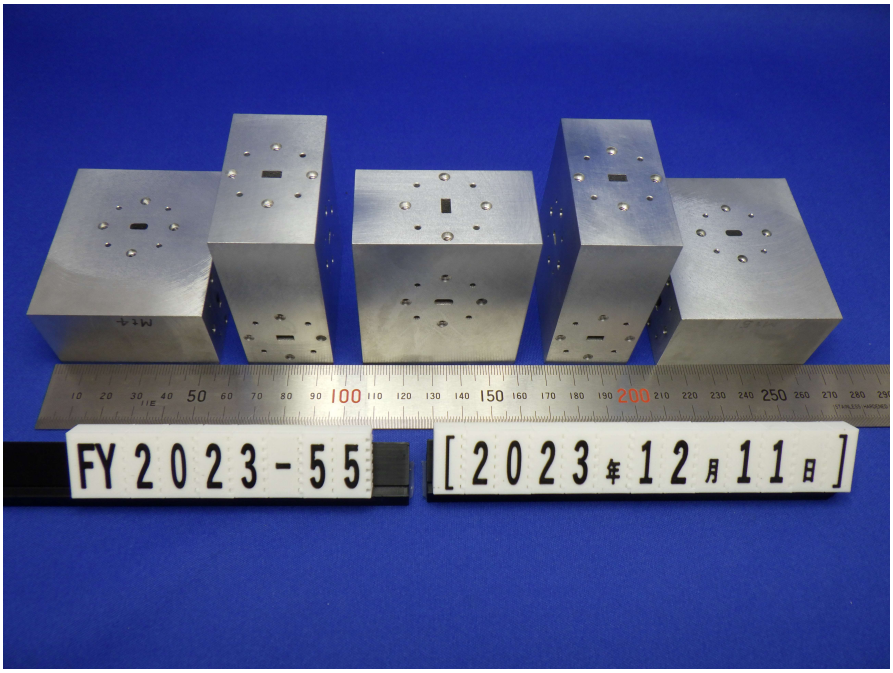


**Fig. 6.22** Metal 3D printed Magic Tees with the flanges (Photo provided by Hikaru Iwashita at ATC machining shop).

the return loss and isolation which shows promising potential. One complication is the trapped mode at 51 GHz from the simulation can be seen moving into the target frequency band.

The 3D printed Magic Tees shows generally worse performance compared to the machined prototype which was expected as the design was intended for direct machining. In particular, the matching element has many stepped structures all of which are only a few hundred microns in scale.

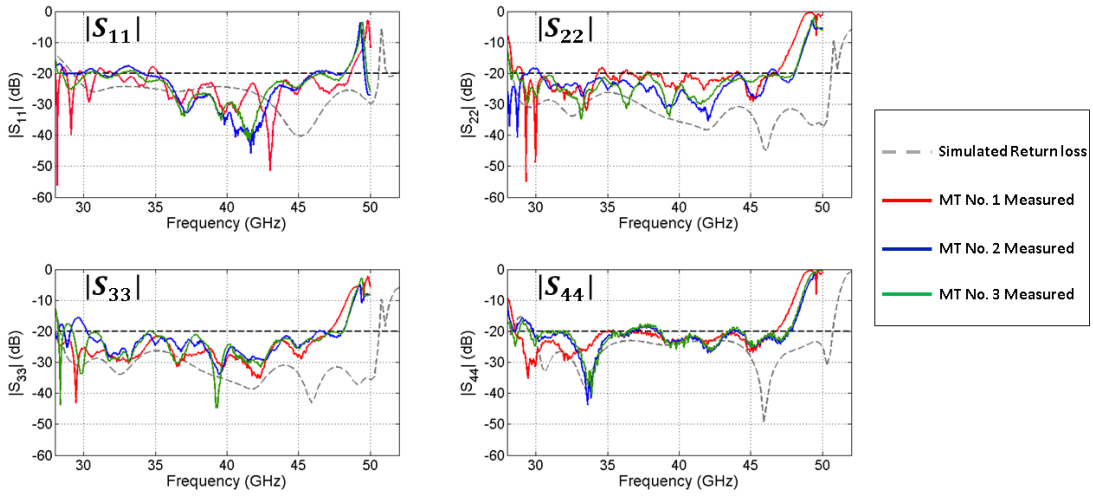


**Fig. 6.23** Comparison between simulated and measured return loss of 3D printed samples.

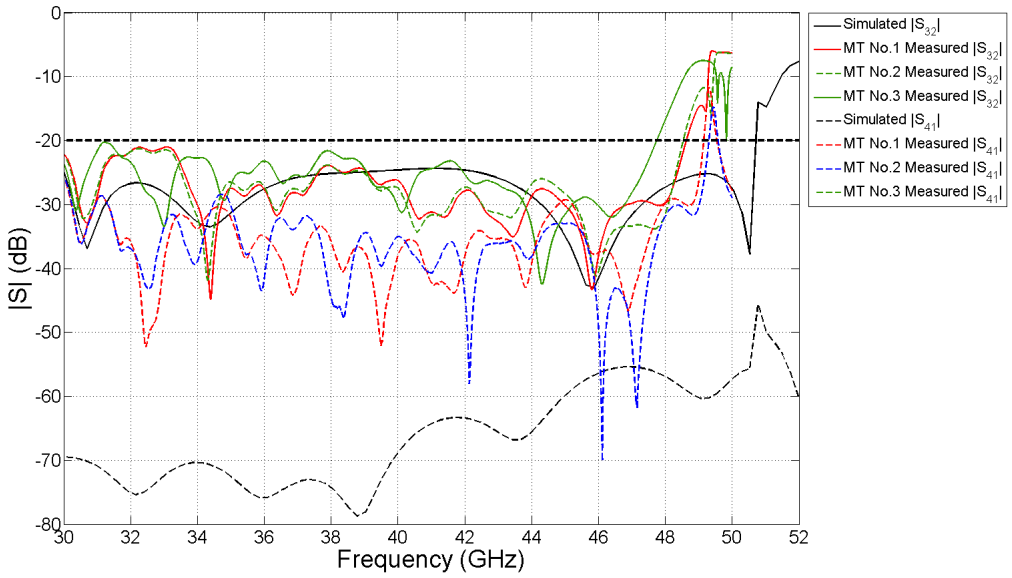


**Fig. 6.24** Comparison between simulated and measured isolation of 3D printed samples.

## 6.8 Discussion

### 6.8.1 Comparison with Other Waveguide Based Magic Tees

The Magic Tee demonstrated here shows return loss higher than 22 dB for ports 1 to 3. Port 4 shows a minimum return loss of 18.5 dB at 49.4 GHz, which is worse than the requirement of 20 dB. The port isolation is higher than 20 dB. The comparison with previously reported high-performance waveguide based wideband Magic Tees is show in Table. 6.1. Of theses works, Magic Tees that features an E-plane power divider were Chu et al. (2014) and Ma et al. (2023). Under the requirement of an waveguide based E-plane power divider with low reflection loss and high isolation, this work presents the widest fractional bandwidth of 47.9% compared to the alternative designs.

**Table 6.1** Comparison of waveguide based Magic Tees with reported return loss and isolation higher than 20 dB.

| | Frequency (FBW %) | RL (dB) | Isolation (dB) |
|---|---|---|---|
| Hwang (2009) | 8.51 - 10.41 GHz (20.1%) | $\geq$ 20 dB | $\geq$ 22 dB |
| Chu et al. (2014) | 27.5 - 34 GHz (21%) | $\geq$ 20 dB | $\geq$ 20 dB |
| Nagaraju and Verma (2021) | 14.2 - 16.2 GHz (15%) | $\geq$ 20 dB | $\geq$ 20 dB |
| Ameri et al. (2023) | 8.15 - 11.7 GHz (36%) | $\geq$ 20 dB | $\geq$ 20 dB |
| Ma et al. (2023) | 205 - 230 GHz (13%) | $\geq$ 20 dB | $\geq$ 20 dB |
| **This work**[3] | **30.0 - 48.9 GHz (47.9%)** | $\geq$ **20 dB** | $\geq$ **22 dB** |

[3]The results presented here may improve with updated measurements using a matched load

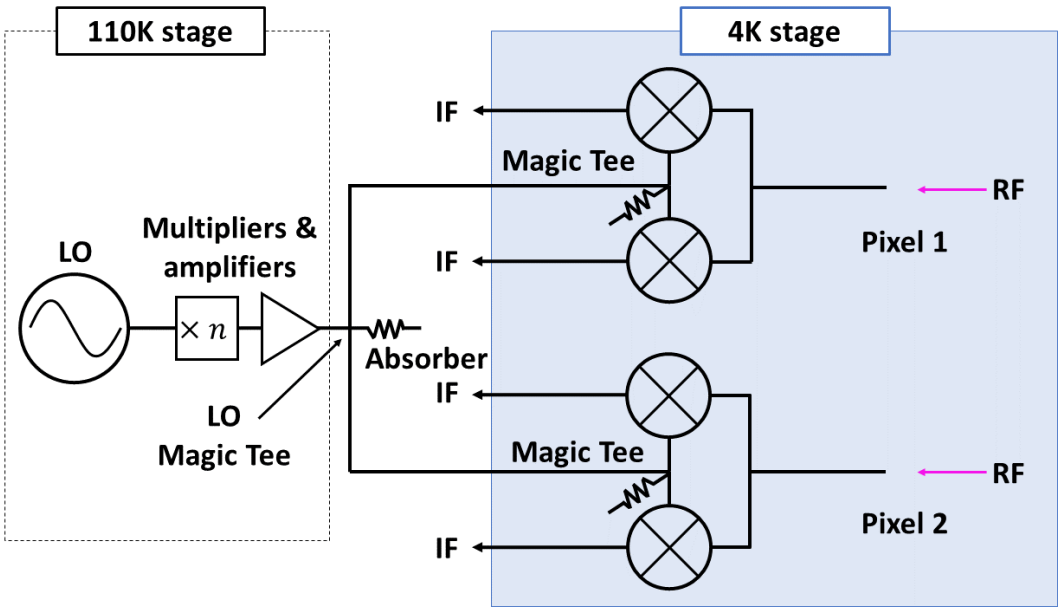


**Fig. 6.25** A possible LO distribution network utilizing Magic Tees for a (sub)mm multibeam receiver.

### 6.8.2 Implications

As stated in Section. 6.1.3, T/Y-junctions have no output isolation which will cause issues with LO distribution in a multibeam heterodyne receiver and have caused issues in key components such as OMTs. The Magic Tee developed here may directly address these core issues.

**LO distribution for a (sub)mm multibeam receiver** : The Magic Tee presented here may serve the role of a E-plane power divider if port 4 is terminated with a matched load. LO power may be input into port 1 to be split towards a mixer or to mixers if it is 2SB.

A Magic Tee may be placed in the first stages of the power distribution network for a (sub)mm multibeam receiver as depicted in Fig. 6.25. A common LO signal may be produced in the first stages of a cryostat (such as in the 110K stage of the ALMA cryostat) by utilizing frequency multipliers and, if necessary and enough thermal headroom is available, amplifiers may be used to increase the available power. The common LO can then be divided using a Magic Tee or other types of power dividers depending on the number of pixels and sent towards each pixel in the mutlibeam receiver. The LO Magic Tee will add isolation between the neighboring pixels. The LO may be sent to each pixel by using low-loss waveguides or by quasioptical propagation using an LO horn. The same sideband separating mixer blocks can be utilized if sufficient power can be supplied to each mixer. In-phase power dividers used in current sideband separating mixer blocks may be replaced with a Magic Tee to add isolation between mixers. The isolation between neighboring pixels and mixers should increase from 3 dB to 22 dB by using the Magic Tee developed here, drastically reducing the potential effect of standing waves caused by the reflections at the SIS mixers.

Here, the simplest case of LO distribution has been introduced. However, the imple-

mentation will depend on the telescope, LO source, and available power, and the number of pixels in the array. The Magic Tee presented here may serve as one element that can be used and applied when considering the design for high-isolation.

The Magic Tee presented here was designed for the 30-50 GHz frequency band for practical reasons, but it can be extended to higher frequencies since these fabrication techniques have been demonstrated up to 500 GHz (Gonzalez and Kaneko, 2021).

**Orthomode Transducers with integrated Magic Tees** : As mentioned in Section. 6.1.3, Bifot junction OMTs utilize 3-port junctions to recombine the same polarization signals. Fabrication errors may cause ripples or worse, excite resonant frequencies. Having a component with high resistance to fabrication errors with a robust design is crucial towards reliable mass production. The Magic Tee proposed here can replace the Y-junction in the current Boifot junction based OMTs. The redundant port may be terminated with an appropriately matched load to absorb the unwanted signals propagating back into the component. However, this is under the assumption that the proposed Magic Tee also has the resistance to the fabrication errors. Robust design considerations and yield analysis must be conducted on the proposed Magic Tee design.

Considering the physical integration and fabrication, current Boifot junction based OMTs have orthogonally placed ports for the V-Pol depending on the design. As a result, the Magic Tee presented here works under the manufacturing constraints and should not impose too many complications except for added complexity in the final OMT. However, if the integration proves too complex for machining, fabrication via 3D printing may be a possible option. This requires modifying the current Magic Tee design for 3D printing in this case.

### 6.8.3 Possible Improvements

#### 6.8.3.1 Considerations for Robust Design

The proposed design demonstrates that a high-performance wideband waveguide-based E-plane split Magic Tee can be fabricated with direct machining. However, A component will be of little use if it cannot be fabricated reliably. Measures to reduce the sensitivity to fabrication errors with a robust design should be considered for the next step. The component demonstrated here showed a trapped mode just outside of the frequency band at 51 GHz in the simulations. The direct machined component did now show the trapped mode as the tight fabrication tolerances did not allow the trapped mode to move into the frequency band. A VNA extender to measure the component beyond 50 GHz may be used to check the final location of the trapped mode if necessary.

The tolerance for the trapped mode can be analyzed further to understand sensitivities to fabrication errors. For relatively complex structures as shown in this design, analytical methods may prove to complicated. Tolerance studies can be done statistically with methods such as Monte-Carlo analyses giving random errors to key structures in the design such as the junction dimensions or the matching element.

A discussion with Douglas Henke at Herzberg Astronomy and Astrophysics Research Centre at the National Research Council of Canada (NRC-HAA) lead to the discovery of the connecting waveguides in the colinear arms as the main cause of the trapped mode. The slight height difference between the junction and the connecting waveguide creates a resonant frequency which prevents the propagation through the colinear ports. Changing the height seems to shift the resonant frequency. The step in the connecting waveguide does not serve a critical role and can be set to align with the junction floor and ceiling. However, this will require some minor re-optimization of the component.

#### 6.8.3.2 Possibility of a Q-Band 3D Printed Magic Tee

The 3D printed versions showed the trapped mode shift inside the target frequency band, which was mostly expected. The first tests conducted here have shown:

- The structures and designs intended for direct machining can be fabricated via metal 3D printing with relatively good quality depending on the structure.
- The designs intended for direct machining are not necessarily the best choice for 3D printing fabrication.
- A 3D printed wideband Magic Tee up to around 50 GHz may be potentially developed given the appropriate design and fine-tuning of fabrication.

The tolerance of metal 3D printing will depend on the component and the fine-tuning and adjustment of the fabrication parameters.

The prototypes presented here may be improved by the adjustment of the printing settings and will also benefit from a design tailored for 3D printing. A distinct advantage of 3D printing is the possibility to fabricate complex structures unrealizable with direct machining methods. However, complex and fine structures may not necessarily be the best option for 3D printing, and will also depend case-by-case on the machine.

Having simpler waveguide arms in general may be beneficial for 3D printing fabrication. The matching element presented here showed poor print qualities in the prototypes. This may be attributed to the fabrication settings, but having simpler designs is still an attractive trait. CNC machining limits gaps between structures to the end mill diameter. We may remove this constraint and explore simpler shapes (such as pyramidal shapes). There will also be no maximum height limit since there is no splitting plane. As a result, we may also consider taller structures past the junction half height.

Port 4 was fabricated with wire-cut EDM which cannot fabricate a stepped waveguide or a rectangular waveguide transitioning into a tapered waveguide. It can fabricate a tapered waveguide and transition. 3D printing can essentially fabricate any stepped, tappered, smooth transition wavegudies for the perpendicular port. We may thus remove the design constraints from machining and wire-cut EDM for port 4 and explore matching structures specifically for 3D printing. One example is an iris placed at the connection between port 4 and the junction top. Another possibility is using a tapered waveguide from WR-22 to a smaller dimension.

The final Magic Tee for 3D printing will require reoptimization of the junction shape and the matching element.

## 6.9 Summary for this Chapter

In this Chapter, the design, fabrication, and characterization of a novel wideband Magic Tee waveguide junction was discussed. Radio telescope receivers utilize waveguides for their low loss. A multibeam receiver will face a couple of issues when considering local oscillator (LO) signal distribution and high-yield of components. The common issue between the two is the use of 3-port junctions that have no isolation.

Waveguide blocks used in receiver front-ends often utilize split-block construction of waveguide components where a waveguide is split crosswise along the broadside wall. Because of this, a Magic Tee must be designed as an E-plane power divider to work with the construction of the waveguide block, while still having the state-of-the-art performance. Previous Magic Tees used in telecommunications and radar applications required different design and performance targets from radio astronomy radio receivers. Thus, the diverse catalog of Magic Tee designs were not fit for split-block waveguide blocks. As a result, a novel design that can be implemented in split-block was required.

A novel design of a high-performance waveguide based E-plane power divider Magic Tee was designed for extended Q-band frequencies of 30 to 50 GHz. The design implemented a E-plane power divider towards replacing T/Y-junctions and is compatible with split-block fabrication. The designed Magic Tee showed state-of-the-art performance of simulated return loss and isolation higher than -2 dB for all ports across the whole bandwidth of 50 %.

A prototype component was fabricated onto a split-block. The VNA measurement results showed a good match with the simulated performance despite some ripples introduced by the use of an unmatched termination. The direct machined prototype was able to achieve higher than 20 dB return loss for all ports except port 4, which showed some ripples and had a minimum of 18.5 dB return loss. The measured isolation was higher than 20 dB. The fabricated prototype demonstrated a fractional bandwidth of 47.9% and is the widest compared to other high-performance waveguide based Magic Tee junctions.

The same Magic Tee design was also 3D printed as an initial test to check the feasibility of a 3D printed Q-band Magic Tee. The 3D printed version showed overall worse performance compared to the direct machined prototype, which was expected. Here, the some limitations and next steps were identified towards a possible high-performance wideband 3D printed Q-band Magic Tee.

This Magic Tee has potential applications in LO distribution for multibeam heterodyne receivers and increasing the yield of crucial waveguide components such as orthomode transducers.

# CHAPTER 7

# Conclusion

## 7.1 What this Thesis Aimed to Address

The goal of this thesis was to discuss core issues for the receiver front-end development of high-performance multibeam heterodyne receivers. This thesis tackled several topics for the receiver front-end under the setting of replacing a single-beam receiver in an existing radio telescope with a small format array multibeam receiver, which is a uniquely challenging setting. The three main questions asked at the beginning of the thesis were:

**Question 1:** How can high-efficiency optics be designed for individual pixels in a multibeam receiver?

**Question 2:** Can high-efficiency multibeam receiver optics be designed and implemented in an antenna originally designed for single-beam receivers?

**Question 3:** How can LO power be efficiently distributed to each pixel with high-isolation?

## 7.2 What this Thesis Contributed

### 7.2.1 Addressing Question 1

In Chapter. 3, a novel software code to calculate aperture efficiency of an antenna with the effect of aberrations was developed. This software code was based on the most recent theoretical research on the effect of aberrations. The code was successfully able to calculate the aperture efficiency of the ALMA 12-m antenna which showed consistent results with the previous literature. This verification analysis also acted as a initial estimation of performance to explore the design optics for a multibeam receiver which satisfies the imaging condition for frequency independent design. This optical architecture has not been explored in depth for multibeam receiver. It was found that at submillimeter wave frequencies, the effect of aberrations are not a limiting factor if the feed horn can be aligned with a pupil.

### 7.2.2 Addressing Question 2

In Chapter. 4, the basic theory and conditions to achieve a constant illumination at the subreflector through frequency independent design was introduced. Chapter. 3 showed that frequency independent illumination will return high-aperture efficiency even when feed horns are

offset by a large amount. This analysis served as the first step for considering frequency independent array optics.

A method to design the individual receiver tertiary optics for feed horns in a multibeam receiver based on the frequency independent illumination at the sub-reflector was developed. The tertiary optics position and focal length were solved to create an image of the sub-reflector at the horn aperture. A two-beam multibeam receiver was designed, optimized, and analyzed using a combination of ray tracing software and physical optics software. The optics consisted of a pair of two-mirror units that were stacked laterally to achieve a compact design. Each pixel returned very high simulated aperture efficiencies of $\eta_{\mathrm{A}} \geq 0.80$ on the sky which is comparable to current single-beam receivers.

This design showed that high-aperture efficiency optics can be designed individually for each pixel. However, this presented issues with the design concerning the small cryostats window. The beams from the multibeam receiver could not all pass through the small window and simultaneously point towards the sub-reflector from their large offset position from the window. This design also showed a large separation of beams of roughly 10 beam sizes on the sky.

In Chapter. 5, re-imaging optics were utilized to allow receiver beams to pass through a small aperture of a cryostat from relatively large offset positions away from the window. The re-imaging allowed both receiver beams from a similar two-beam multibeam receiver demonstrated in Chapter. 4 to pass through a window originally meant for a single-beam receiver passively. The design principle of the re-imaging optics takes advantage of the fact that the sub-reflector acts as an aperture stop which directly creates its image as a pupil at an intermediate position through the re-imaging optics. The tertiary optics were then set to achieve the frequency independent design for at the re-imaged sub-reflector.

The re-imaging optics combined with the receiver optics were able to overcome the constraints introduced by an existing antenna system. However, the design returned lower aperture efficiency of roughly $\eta = 0.63$ due to two factors. 1) there was considerable amount of beam truncation at the window due to the beams passing through it at an offset position. 2) The beams had a large spill-over at one of the re-imaging optics mirrors because it acted as a decentered lens. Fortunately, the actual coupling between the target illumination and the receiver beam was as high as a single-beam receiver with an approximated beam coupling efficiency of $0.85$. Further improvements to minimize the beam truncation at the window and spill-over at the re-imaging optics should still be able to achieve high-aperture efficiency. This has shown, high-efficiency multibeam receiver optics can be designed to work for an antenna originally designed for single-beam receivers.

### 7.2.3 Addressing Question 3

Chapter. 6 focuses on the issues expected for LO distribution. Here, the first step was taken with the development of a novel wideband Magic Tee waveguide junction. A Magic Tee is a 4-port junction which is capable of achieving high port-to-port isolation. A strategically placed Magic Tee may resolve the issues that will be expected with LO power distribution and component yield for multibeam receivers. A design for a Magic Tee to work as an E-plane power

divider was designed and simulated. The simulated Magic Tee was able to achieve a fractional bandwidth of 50% for port reflection and isolation when acting as an E-plane power divider, which is the highest so far compared to the previous literature. The Magic Tee was designed at extended Q-band frequencies of 30 to 50 GHz and was designed to work with current receiver waveguide block fabrication methods utilizing split-block. A prototype was fabricated and VNA measurements were conducted. The VNA measurements agreed well with the simulations despite some minor differences which may be due in part to the measurement setup, since two loads were not available to terminate the two ports not connected to the VNA. The prototype showed state-of-the-art performance of measured return loss higher than 20 dB and isolation higher than 22 dB in a 47.9% fractional bandwidth, which is the widest so far.

The same Magic Tee was fabricated using metal 3D printing as 3D printing may serve useful for certain cases. The fabricated prototypes showed worse performance compared to the direct machined component which was expected. However, the 3D printed versions still showed very promising results which can be improved with tweaks in the design and fine tuning of the fabrication process.

## 7.3 Conclusion of Thesis

The methods developed in this thesis may serve as design tools for future consideration of a multibeam heterodyne receiver in a radio telescope looking to replace its current single-beam receiver as shown in Fig. 7.1. Future development of a submillimeter multibeam heterodyne receiver for ALMA will require well defined science targets and goals and conducting detailed trade-off studies of various multibeam receiver schemes. This thesis has provided analysis methods and initial results towards implementing a few pixel multibeam receiver with high-efficiency front-end components.

The extensive analyses conducted here have shown individual design of tertiary optics for each pixel can return aperture efficiency comparable to a single-beam receiver when considering only a few pixels. They have also provided additional useful information for further analysis about critical limitations and trade-offs for the optical design of a frequency independent array.

The Magic Tee developed here may applied and used as a fundamental component for wideband waveguide circuits. The component may be directly used or slightly modified to work with an existing component or waveguide circuit. The use of this Magic Tee will be particularly useful in the LO distribution of multibeam receivers, or to increase the yield of more complex waveguide components by providing isolation between branches and thus reducing standing waves.

In conclusion, the work presented here has provided many design and analysis methods which can be built upon further towards the development of high-performance submillimeter wave multibeam heterodyne receivers.

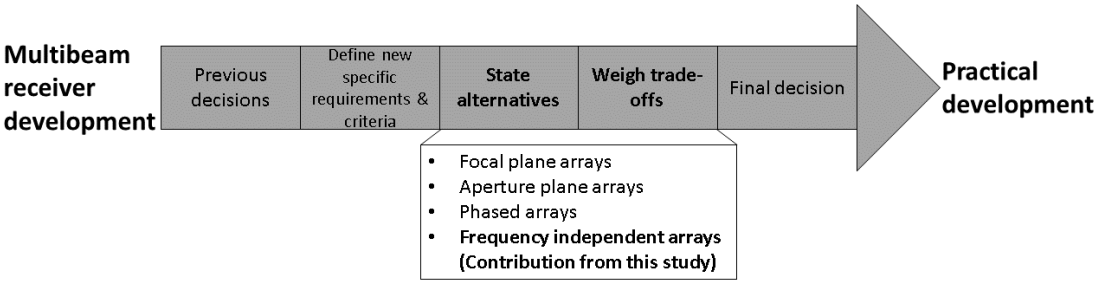


**Fig. 7.1** Placement and contributions from this thesis.

## 7.4 Future Prospects

The methods from Chapter. 4 and Chapter. 5 have laid out the framework to explore many different combinations of lenses, mirrors, and feed horns. Although many technical challenges were identified through the analyses conducted here, this thesis was able to explore only a few inchoate designs for a multibeam receiver with frequency independent optics. There is much work to be done before actual implementation in a real telescope, but this initial research shows promising results which can pave the way in the direction of future implementation

As discussed in Chapter. 4, The feed horn parameters may be varied independently to find better solutions for the mirrors. The current band 8 horn was assumed in most of the analyses conducted here as the design of the horn is already available. However, using a different horn will provide different solutions to the mirror focal lengths and positions. Different horn sizes can be assumed for each pixel to provide an optimal design. However, practical dimensions for the horn must be considered.

Possible improvements for the re-imaging optics from Chapter. 5 were also discussed. The re-imaging optics required considerable thickness to achieve the small focal lengths due to their relatively low refractive index. We may explore other materials such as quartz which still have low loss at submillimeter wavelengths and has a higher refractive index. If the original HDPE is still to be considered, zoned lenses may possibly reduce the thickness.

The intermediate pupil may also be set as a design constraint. The method here did not attempt to fix the intermediate pupil location. A convenient place to place the intermediate pupil is at the last window in the cryostat, which would be the 15 K window in the ALMA cryostat. Then, the receiver beams can be designed to point towards the 15 K window. Depending on the final configuration, this alone may remedy some of the truncation and spill-over issues discussed in Section. 5.6.2.

As stated in Section. 5.6.2, a slightly larger window will alleviate the beam truncation greatly increasing the aperture efficiency. We may use this opportunity to design a possible 2D array of unit-cells to design a 2D array. A 4-pixel multibeam receiver can be relatively easily designed by incorporating an X-incident angle for the chief ray. A four-beam multibeam receiver should still have a small physical footprint and may be able to fit onto a receiver cartridge. A four-beam

multibeam receiver will require fine tuning of the design and optimization methods to achieve an overall compact design.

Another possibility is utilizing wideband horns. The current band 8 horn is limited to 26 % fractional bandwidth. If a wideband horn can be designed at these frequencies, we may fully utilize the wideband performance thanks to the frequency independent design presented here. The combination of wideband and larger field-of-view achieved from a multibeam receiver will significantly improve a radio telescopes mapping efficiency opening up a whole new world of opportunities for observations.

A Boifot junction type ortho-mode transducer as the one in Gonzalez and Kaneko (2021) with an integrated Magic Tee may be an interesting design with many practical applications even besides for multibeam. The Magic Tee demonstrated in Chapter. 6, with minor modifications may replace the Y-junction power combiner in the OMT. Particularly, port 4 was designed so it can still be fabricated with direct machining instead of wire-cut EDM. If an absorber is placed inside port 4 during the fabrication, we may not require cutting through the waveguide block leading to a compact design because a load termination will not be physically connected.

LO distribution circuits without LO couplers will need major design considerations. The Magic Tee demonstrated here may serve as one ingredient for considering possible designs.

# REFERENCES


Ameri, E., Khalaj-Amirhosseini, M., Sedighy, S. and Azizi, Y. (2023), 'Design of new wideband waveguide magic-t for x-band applications', *Microwave and Optical Technology Letters* **65**.

Asayama, S., Takahashi, T., Kubo, K., Ito, T., Inata, M., Suzuki, T., Wada, T., Soga, T., Kamada, C., Karatsu, M., Fujii, Y., Obuchi, Y., Kawashima, S., Iwashita, H. and Uzawa, Y. (2014), 'Development of ALMA Band 4 (125–163 GHz) receiver', *Publications of the Astronomical Society of Japan* **66**(3), 57.

Balanis, C. (2016), *Antenna Theory Analysis and Design (Fourth Edition)*, Wiley.

Bawart, M., Bregenzer, N., Bernet, S. and Ritsch-Marte, M. (2020), 'Dynamic beam-steering by a pair of rotating diffractive elements', *Optics Communications* **460**, 125071.

Bird, T. S. (2016), *Reflector Antennas*, Springer Singapore.

Born, M., Wolf, E., Bhatia, A. B., Clemmow, P. C., Gabor, D., Stokes, A. R., Taylor, A. M., Wayman, P. A. and Wilcock, W. L. (1999), *Principles of Optics: Electromagnetic Theory of Propagation, Interference and Diffraction of Light*, 7 edn, Cambridge University Press.

Carpenter, J., Brogan, C., Iono, D. and Mroczkowski, T. (2023), The ALMA Wideband Sensitivity Upgrade, *in* 'Physics and Chemistry of Star Formation: The Dynamical ISM Across Time and Spatial Scales', p. 304.

Carpenter, J., Iono, D., Testi, L., Whyborn, N., Wootten, A. and Evans, N. (2018), 'The alma development roadmap', *ALMA Memo Series* (612).

Chao, H.-W., Chen, H.-H. and Chang, T.-H. (2021), 'Measuring the complex permittivities of plastics in irregular shapes', *Polymers* **13**(16).

Chatterjee, S., Maity, P., Chatterjee, S. and Majumder, A. (2015), Optimization of stepped cone matching element for improvement of isolation in magic tee, *in* '2015 IEEE Applied Electromagnetics Conference (AEMC)', pp. 1–2.

Chattopadhyay, G. (2011), 'Technology, capabilities, and performance of low power terahertz sources', *IEEE Transactions on Terahertz Science and Technology* **1**(1), 33–53.

Chu, Q.-X., Wu, Q.-S. and Mo, D.-Y. (2014), 'A $ka$ -band $e$ -plane waveguide magic-t with coplanar arms', *IEEE Transactions on Microwave Theory and Techniques* **62**(11), 2673–2679.

Chu, T.-S. (1983), 'An imaging beam waveguide feed', *IEEE Transactions on Antennas and Propagation* **31**(4), 614–619.

Clarricoats, P. J. B. and Olver, A. D. (1984), *Corrugated horns for microwave antennas*, peter peregrinus Ltd.

*CODE V Documentation Library* (2023).

Dragone, C. (1982), 'A first-order treatment of aberrations in cassegrainian and gregorian antennas', *IEEE Transactions on Antennas and Propagation* **30**(3), 331–339.

Duda, T. and Raghavan, L. V. (2016), '3d metal printing technology', *IFAC-PapersOnLine* **49**(29), 103–110. 17th IFAC Conference on International Stability, Technology and Culture TECIS 2016.

D'Addario, L., Bradley, R., Bryerton, E., Sramek, R., Shillue, W. and Thacker, S. (2001), 'ALMA Project Book, Chapter 7: LOCAL OSCILLATORS'.
**URL:** *https://www.cv.nrao.edu/ demerson/almapbk/construc/chap7/chap7.pdf*

Ekin, J. W. (2006), *Experimental Techniques for Low-Temperature Measurements*, Oxford University Press.

Farahbakhsh, A. (2020), 'Ka-band coplanar magic-t based on gap waveguide technology', *IEEE Microwave and Wireless Components Letters* **30**(9), 853–856.

Goldsmith, P. (1991), 'Zone plate lens antennas for millimeter and submillimeter wavelengths'.

Goldsmith, P. (1998), *Quasioptical Systems: Gaussian Beam Quasioptical Propagation and Applications*, Wiley-IEEE Press.

Gonzalez, A. (2016), 'Frequency independent design of quasi-optical systems', *Journal of Infrared, Millimeter, and Terahertz Waves* **37**(2), 147–159.

Gonzalez, A., Fujii, Y., Kojima, T. and Asayama, S. (2016), 'Reconfigurable near-field beam pattern measurement system from 0.03 to 1.6 thz', *IEEE Transactions on Terahertz Science and Technology* **6**(2), 300–305.

Gonzalez, A. and Kaneko, K. (2021), 'High-performance wideband double-ridged waveguide omt for the 275-500 ghz band', *IEEE Transactions on Terahertz Science and Technology* **PP**, 1–1.

Gonzalez, A., Kaneko, K., Huang, C.-D. and Huang, Y.-D. (2021), 'Metal 3d-printed 35–50-ghz corrugated horn for cryogenic operation', *Journal of Infrared, Millimeter, and Terahertz Waves* **42**(9), 960–973.

Graf, U. U., Honingh, C. E., Jacobs, K. and Stutzki, J. (2015), 'Terahertz Heterodyne Array Receivers for Astronomy', *Journal of Infrared, Millimeter, and Terahertz Waves* **36**(10), 896–921.

Guo, C., Li, J., Yu, Y., Zhang, F., Zhu, Y., Yang, Q., Zhu, W., Zhu, S., Shang, X., Gao, Y., Wang, Y., Huang, G.-L., Cheng, Q. S. and Zhang, A. (2019), 'A 3-d printed $e$ -plane waveguide magic-t using air-filled coax-to-waveguide transitions', *IEEE Transactions on Microwave Theory and Techniques* **67**(12), 4984–4994.

Hashimoto, T., Laporte, N., Mawatari, K., Ellis, R. S., Inoue, A. K., Zackrisson, E., Roberts-Borsani, G., Zheng, W., Tamura, Y., Bauer, F. E., Fletcher, T., Harikane, Y., Hatsukade, B., Hayatsu, N. H., Matsuda, Y., Matsuo, H., Okamoto, T., Ouchi, M., Pelló, R., Rydberg, C.-E., Shimizu, I., Taniguchi, Y., Umehata, H. and Yoshida, N. (2018), 'The onset of star formation 250 million years after the big bang', *Nature* **557**(7705), 392–395.

He, Y.-J., Mo, D.-Y., Wu, Q.-S. and Chu, Q.-X. (2017), 'A Ka-Band Waveguide Magic-T With Coplanar Arms Using Ridge-Waveguide Transition', *IEEE Microwave and Wireless Components Letters* **27**(11), 965–967.

Huang, G.-L., Zhou, S.-G. and Yuan, T. (2018), 'Design of a compact wideband feed cluster with dual-polarized sum- and difference-patterns implemented via 3-d metal printing', *IEEE Transactions on Industrial Electronics* **65**(9), 7353–7362.

Hwang, K. C. (2009), 'Design and optimization of a broadband waveguide magic-t using a stepped conducting cone', *IEEE Microwave and Wireless Components Letters* **19**, 539–541.

*IEEE Standard for Definitions of Terms for Antennas* (2014), *IEEE Std 145-2013 (Revision of IEEE Std 145-1993)* pp. 1–50.

Imada, H. and Nagai, M. (2020), 'Analytical expression of aperture efficiency affected by seidel aberrations', *Opt. Express* **28**(16), 23075–23090.

Imada, H., Nagai, M., Kino, M., Seta, M., Ishii, S. and Nakai, N. (2015), 'Condition of optical systems independent of frequency for wide field-of-view radio telescopes', *IEEE Transactions on Terahertz Science and Technology* **5**(1), 57–63.

Jacob, M., Mazierska, J., Leong, K. and Krupka, J. (2002), 'Microwave properties of low-loss polymers at cryogenic temperatures', *IEEE Transactions on Microwave Theory and Techniques* **50**(2), 474–480.

Jansky, K. G. (1982), *A Note on the Source of Interstellar Interference*, Springer Netherlands, pp. 36–41.

Kerr, A. R. and Horner, N. (2000), 'A broadband in-phase waveguide power divider/combiner', *ALMA Memo Series* (325).

Khorsandy, M., Salari, A., Pilevar, A. and Erricolo, D. (2019), An Optimized Broadband Waveguide Magic-T for X-band Applications, *in* '2019 PhotonIcs and Electromagnetics Research Symposium - Spring (PIERS-Spring)', pp. 207–211.

Kloosterman, J., Swift, B., Peters, W., Lesser, D., Kulesa, C., Honniball, C., Villegas, C., Schickling, P., Walker, C., Groppi, C., Mani, H., Davis, K., Wheeler, C., Veach, T., Weinreb, S., Kooi, J., Lichtenberger, A., Puetz, P. and Narayanan, G. (2014), Engineering and science data from SuperCam: A 64-pixel heterodyne receiver for CO J=3-2 at 345 GHz, *in* '2014 39th International Conference on Infrared, Millimeter, and Terahertz waves (IRMMW-THz)', pp. 1–2.

Kojima, T., Kiuchi, H., Uemizu, K., Uzawa, Y., Kroug, M., Gonzalez, A., Dippon, T. and Kageura, T. (2020), 'Demonstration of a wideband submillimeter-wave low-noise receiver with 4–21 ghz if output digitized by a high-speed 32 gsps adc', *AandA* **640**, L9.

Kojima, T., Masui, S., Shan, W. and Uzawa, Y. (2023), 'Characterization of a low-noise superconductor–insulator–superconductor-based microwave amplifier with local oscillator phase-adjusting architecture', *Applied Physics Letters* **122**(7), 072601.

Lamb, J. (2003), 'Low-noise, high-efficiency optics design for alma receivers', *IEEE Transactions on Antennas and Propagation* **51**(8), 2035–2047.

Lamb, J. W. (1993), 'Infrared filters for cryogenic millimeterwave receivers', *International Journal of Infrared and Millimeter Waves* **14**(5), 959–967.

Lamb, J. W. (1999), 'Optimized optical layout for MMA 12-m antennas', *ALMA Memo Series* (246).

Lamb, J. W., Baryshev, A., Carter, M. C., D'Addario, L. R., Ellison, B. N., Grammer, W., Lazareff, B., Sekimoto, Y. and Tham, C. Y. (2001), 'ALMA Receiver Optics Design', *ALMA Memo Series* (362).

Li, Y., Zhang, Y., Zhu, G., Sun, Z. and Fan, Y. (2016), A w-band miniature power divider based on e-faced-folded magic-t junction, *in* '2016 IEEE MTT-S International Microwave Workshop Series on Advanced Materials and Processes for RF and THz Applications (IMWS-AMP)', pp. 1–3.

Ma, Y., Cao, J. and Zhan, M. (2023), 'A 220-ghz 110-mw solid-state power combining amplifier based on novel e-plane waveguide magic-t', *Journal of Infrared, Millimeter, and Terahertz Waves* **44**(7), 491–502.

Mahajan, V. N. (1981), 'Zernike annular polynomials for imaging systems with annular pupils', *J. Opt. Soc. Am.* **71**(1), 75–85.

Mahajan, V. N. (1983), 'Strehl ratio for primary aberrations in terms of their aberration variance', *J. Opt. Soc. Am.* **73**(6), 860–861.

Milewski, J. O. (2017), *Origins of 3D Metal Printing*, Springer International Publishing.

Mimura, T. (2005), 'Development of high electron mobility transistor', *Japanese Journal of Applied Physics* **44**(12R), 8263.

Murphy, J. A. (1987), 'Distortion of a simple gaussian beam on reflection from off-axis ellipsoidal mirrors', *International Journal of Infrared and Millimeter Waves* **8**(9), 1165–1187.

Nagai, M., Imada, H. and Okumura, T. (2021), 'Factorization of antenna efficiency of aperture-type antenna: Beam coupling and two spillovers', *IEEE Transactions on Antennas and Propagation* **69**(7), 3750–3757.

Nagaraju, D. and Verma, Y. K. (2021), 'A Compact Wideband Planar Magic Tee for Monopulse Antenna Array Applications', *IEEE Microwave and Wireless Components Letters* **31**(5), 429–432.

Naruse, M., Ito, T., Sekimoto, Y., Toba, H., Satou, N., Sugimoto, M., Wenlei, S., Iizuka, Y., Kamba, T., Kamikura, M. and Serizawa, Y. (2009), 'Near-field beam pattern measurement of qualification model of ALMA band 8 (385–500 GHz) cartridge receiver', *Experimental Astronomy* **24**, 89–107.

Orlowska, A. (2005), 'Cryostat design report, fend-40.03.00.00-007-a-rep'.

Padman, R. (1995), Optical Fundamentals for Array Feeds, *in* D. T. Emerson and J. M. Payne, eds, 'Multi-Feed Systems for Radio Telescopes', Vol. 75 of *Astronomical Society of the Pacific Conference Series*, pp. 3–26.

Padman, R., Murphy, J. and Hills, R. (1987), 'Gaussian mode analysis of cassegrain antenna efficiency', *IEEE Transactions on Antennas and Propagation* **35**(10), 1093–1103.

Parshley, S. C., Kronshage, J., Blair, J., Herter, T., Nolta, M., Stacey, G. J., Bazarko, A., Bertoldi, F., Bustos, R., Campbell, D. B., Chapman, S., Cothard, N., Devlin, M., Erler, J., Fich, M., Gallardo, P. A., Giovanelli, R., Graf, U., Gramke, S., Haynes, M. P., Hills, R., Limon, M., Mangum, J. G., McMahon, J., Niemack, M. D., Nikola, T., Omlor, M., Riechers, D. A., Steeger, K., Stutzki, J. and Vavagiakis, E. M. (2018), CCAT-prime: a novel telescope for sub-millimeter astronomy, *in* 'Ground-based and Airborne Telescopes VII', Vol. 10700, International Society for Optics and Photonics, SPIE.

Peng, S., Pu, Y., Wu, Z. and Luo, Y. (2022), 'Assembly convenient w-band waveguide magic-t', *IEEE Microwave and Wireless Components Letters* **32**(1), 13–16.

Phillips, T. and Dolan, G. (1982), 'Sis mixers', *Physica B+C* **109-110**, 2010–2019. 16th International Conference on Low Temperature Physics, Part 3.

Pozar, D. M. (2011), *Microwave Engineering. 4th ed*, Wiley.

Quertier, B., Gauffre, S., Randriamanantena, A. and Studniarek, M. (2021), 'Upgrading the alma digital system, from digitization to correlation final report', *ALMA Development Studies 2019* .

Riddle, B., Baker-Jarvis, J. and Krupka, J. (2003), 'Complex permittivity measurements of common plastics over variable temperatures', *IEEE Transactions on Microwave Theory and Techniques* **51**(3), 727–733.

Rohlfs, K. and Wilson, T. L. (2000), *Tools of Radio Astronomy*, Springer.

Ross, T. S. (2009), 'Limitations and applicability of the maréchal approximation', *Appl. Opt.* **48**(10), 1812–1818.

Ruze, J. (1966), 'Antenna tolerance theory—a review', *Proceedings of the IEEE* **54**(4), 633–640.

Saito, T., Takano, S., Harada, N., Nakajima, T., Schinnerer, E., Liu, D., Taniguchi, A., Izumi, T., Watanabe, Y., Bamba, K., Herbst, E., Kohno, K., Nishimura, Y., Stuber, S., Tamura, Y. and Tosaki, T. (2022), 'The Kiloparsec-scale Neutral Atomic Carbon Outflow in the Nearby Type 2 Seyfert Galaxy NGC 1068: Evidence for Negative AGN Feedback', *ApJ L* **927**(2), L32.

Schuster, K.-F., Boucher, C., Brunswig, W., Carter, M., Chenu, J.-Y., Foullieux, B., Greve, A., John, D., Lazareff, B., Navarro, S., Perrigouard, A., Pollet, J.-L., Sievers, A., Thum, C. and Wiesemeyer, H. (2004), 'A 230 ghz heterodyne receiver array for the iram 30 m telescope', *AandA* **423**(3), 1171–1177.

Sekimoto, Y., Iizuka, Y., Satou, N., Ito, T., Kumagai, K., Kamikura, M., Naruse, M. and Wenlei, S. (2008), 'Development of alma band 8 (385-500 ghz) cartridge'.

Shan, W., Ezaki, S., Liu, J., Asayama, S., Noguchi, T. and Iguchi, S. (2018), Planar superconductor-insulator-superconductor mixer array receivers for wide field of view astronomical observation, *in* J. Zmuidzinas and J.-R. Gao, eds, 'Millimeter, Submillimeter, and Far-Infrared Detectors and Instrumentation for Astronomy IX', Vol. 10708, International Society for Optics and Photonics, SPIE, p. 1070814.

Shurakov, A., Lobanov, Y. and Goltsman, G. (2016), 'Superconducting hot-electron bolometer: from the discovery of hot-electron phenomena to practical applications', *Supercond. Sci. Technol* **29**(2).

Smith, H., Hills, R. E., Withington, S., Richer, J., Leech, J., Williamson, R., Gibson, H., Dace, R., Ananthasubramanian, P. G., Barker, R. W., Baldwin, R., Stevenson, H., Doherty, P., Molloy, D., Quy, V., Lush, C., Hales, S., Dent, W. R. F., Pain, I., Wall, R., Hastings, P. R., Graham, B., Baillie, T. E. C., Laidlaw, K., Bennett, R. J., Laidlaw, I., Duncan, W., Ellis, M. A., Redman, R. O., Wooff, R., Yeung, K. K., Fitzsimmons, J. T., Avery, L., Derdall, D., Josephson, D., Anthony, A., Atwal, R., Chylek, T., Shutt, D. J., Friberg, P., Rees, N. P., Philips, R., Kroug, M., Klapwijk, T. M. and Zijlstra, T. (2003), HARP-B: a 350-GHz 16-element focal plane array for the James Clerk Maxwell Telescope, *in* T. G. Phillips and J. Zmuidzinas, eds, 'Millimeter and Submillimeter Detectors for Astronomy', Vol. 4855, International Society for Optics and Photonics, SPIE, pp. 338 – 348.

Thompson, A. R., Moran, J. M. and Jr., G. W. S. (2018), *Interferometry and Synthesis in Radio Astronomy*, Springer Cham.

Wang, J. and Ling, T. (2019), 'A novel ultra-wideband design of ridged siw magic-t', *Progress In Electromagnetics Research Letters* **82**, 113–120.

Wang, Y., Hua, G. and Du, J. (2015), Design of ultra-wideband magic-t using microstrip/slot coupler and phase shifter, *in* '2015 Asia-Pacific Microwave Conference (APMC)', Vol. 1, pp. 1–3.

White, D., McGenn, W., George, D., Fuller, G. A., Cleary, K., Readhead, A., Lai, R. and Mei, G. (2019), '125 - 211 ghz low noise mmic amplifier design for radio astronomy', *Experimental Astronomy* **48**(2), 137–143.

Winkler, D. and Claeson, T. (1987), 'High-frequency limits of superconducting tunnel junction mixers', *Journal of Applied Physics* **62**(11), 4482–4498.

Wylde, R. J. (1984), 'Millimetre-wave Gaussian beam-mode optics and corrugated feed horns', *IEE Proceedings H: Microwaves Optics and Antennas* **131**(4).

Yang, C., Navarro, M., Zhao, B., Leng, G., Xu, G., Wang, L., Jin, Y. and Ding, Y. (2016), 'Thermal conductivity enhancement of recycled high density polyethylene as a storage media for latent heat thermal energy storage', *Solar Energy Materials and Solar Cells* **152**, 103–110.

Yokogawa, S., Sekimoto, Y., Sugimoto, M., Okuda, T., Sekiguchi, T., Kamba, T., Tatematsu, K., Nishino, T., Ogawa, H., Kimura, K., Noda, K. and Narasaki, K. (2003), 'Plug-in cryogenic system for cartridge-type sis receivers', *Publications of The Astronomical Society of Japan - PUBL ASTRON SOC JPN* **55**.

Zavala, J. A., Casey, C. M., Manning, S. M., Aravena, M., Bethermin, M., Caputi, K. I., Clements, D. L., da Cunha, E., Drew, P., Finkelstein, S. L., Fujimoto, S., Hayward, C., Hodge, J., Kartaltepe, J. S., Knudsen, K., Koekemoer, A. M., Long, A. S., Magdis, G. E., Man, A. W. S., Popping, G., Sanders, D., Scoville, N., Sheth, K., Staguhn, J., Toft, S., Treister, E., Vieira, J. D. and Yun, M. S. (2021), 'The evolution of the ir luminosity function and dust-obscured star formation over the past 13 billion years', *The Astrophysical Journal* **909**(2), 165.

Zhang, W., Miao, W., Ren, Y., Zhou, K.-M. and Shi, S.-C. (2022), 'Superconducting hot-electron bolometer mixers and their applications', *Superconductivity* **2**, 100009.

Zhu, Z.-B., Dong, S.-W., Wang, Y. and Dong, Y.-Z. (2011), A design of k band e-plane folded magic tee matched in two ways for spatial power combining, *in* '2011 International Conference on Electronics, Communications and Control (ICECC)', pp. 4078–4081.

# Appendices

**Appendix A**

## End-to-End Analysis of ALMA Band 8 Receiver Optics

An analysis of the current ALMA band 8 optics was conducted to directly compare the calculated aperture efficiencies with the analyses presented in this thesis.

## A.1 Overview of ALMA Band 8 Receiver Optics

The ALMA band 8 receiver cartridge is shown in Fig. A.1. ALMA band 8 optics consists of a corrugated horn for the feed with a single ellipsoidal mirror. The band 8 horn has a diameter of 7.99 mm and axial slant length of 24.43 mm.

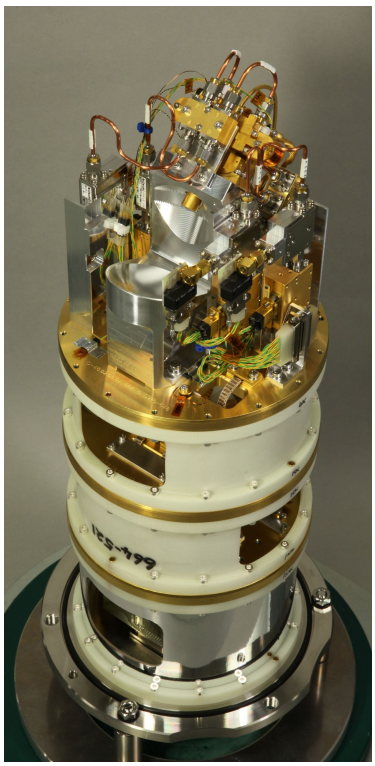

**Fig. A.1** The ALMA band 8 receiver cartridge. Credit: ALMA (ESO/NAOJ/NRAO)

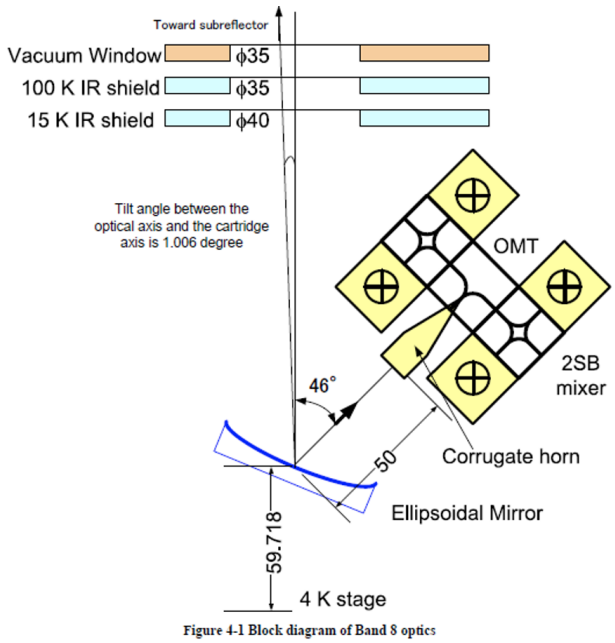


**Fig. A.2** Band 8 optics schematic from Front-end report. Courtesy of ALMA receiver development team at ATC.

### A.1.1 Reported Design

#### A.1.1.1 Values Reported from Front-End Design Report

The Band 8 front-end report shows the schematic (Fig. A.2) and lists the optical parameters from the band 8 receiver optics (Fig. A.3). The front-end report indicates the radius of curvature target beam as 6000 mm to match the antenna and the edge taper of 12.21 dB for the beam at the sub-reflector. This corresponds to a Gaussian beam with a beam radius of 316.266 mm. The ALMA band 8 receiver uses a corrugated horn with a diameter of 7.99 mm and an axial length of 24.10 mm. The fields at the horn aperture can be approximated with a Gaussian beam with a beam radius of 2.57 mm and a radius of curvature of 24.43 mm as indicated in Fig. A.3.

The receiver optics consists of a single ellipsoidal mirror to reflect and refocus the beam from the sub-reflector to match the horn. The ellipsoidal mirror has an effective focal length of 49.59 mm and the distance between the ellipsoidal mirror and the horn aperture is 50 mm.

#### A.1.1.2 Mirror Position

The distance from between the sub-reflector center to the ellipsoidal mirror (denoted as d(mirror-subref) in Fig. A.3) is reported as 6148.6 mm. However, for the frequency independent condition to be satisfied, the geometrical relation between the input-output (horn - sub-reflector) beam radii and distances must satisfy,

$$
\begin{aligned}
w_{\text{sub}} &= \frac{d_{\text{mirror-subref}}}{d_{\text{horn-mirror}}} w_{\text{horn}} \\
316.266 &= \frac{d_{\text{mirror-subref}}}{50} 2.5708 \\
\therefore d_{\text{mirror-subref}} &= 6151.112, \qquad \text{(A.1.1)}
\end{aligned}
$$

Table 4-1 Optical parameters of ALMA band 8.

| | Symbol | Unit | | Frequency [GHz] | | |
|---|---|---|---|---|---|---|
| Frequency | | GHz | | 385 | 442 | 500 |
| horn diameter | dh | mm | 7.99 | | | |
| horn axial length | Lh | mm | 24.1012 | | | |
| horn slant length | Rh | mm | 24.4300 | | | |
| horn waist | w0 | mm | | 1.7367 | 1.6036 | 1.4820 |
| horn waist offset | dz(w0) | mm | | -13.2810 | -14.9244 | -16.3114 |
| waist at horn aperture | wha | mm | | 2.5708 | 2.5708 | 2.5708 |
| distance between horn and mirro | d1 | mm | 50.0 | | | |
| curvature of mirror | Rs1 | mm | 67.529 | 65.6209 | 67.1095 | 68.3085 |
| focal length | f1 | mm | 49.5895 | | | |
| curvature of mirror | Ril | mm | 186.668 | 202.9834 | 189.9501 | 180.9597 |
| waist at mirror 1 | | mm | | 9.1970 | 8.8869 | 8.6674 |
| theta_1 (+offset) | | degree | 46.006 | | | |
| | zw | mm | 150 | 149.390 | 149.614 | 149.390 |
| | wcass | mm | | 4.7018 | 4.0955 | 3.6205 |
| d(mirror-subref) | | mm | | 6148.613 | 6148.607 | 6148.604 |
| | w(subreff) | mm | | 316.266 | 316.266 | 316.266 |
| | R(subrefl) | mm | 6000 | | | |
| Edge taper | | dB | 12 | 12.21 | 12.21 | 12.21 |
| Multimode truncation | | dB | | 9.75 | 9.75 | 9.75 |
| | | | | | | |
| waveguide width | a | micro m | 508 | | | |
| waveguide height | b | micro m | 274 | | | |
| waveguide radius | r | micro m | 289 | | | |

**Fig. A.3** Table 4-1 of optical parameters from front-end report. Courtesy of ALMA receiver development team at ATC.

which is roughly 3 mm longer than the reported value in Table. A.3.

The diagram in Fig. A.2 clearly shows the mirror center to be 59.718 mm away from the 4K stage. This value is consistent with the mechanical drawings for the ALMA 12-m antenna and Band 8 receiver and should represent the real position of the mirror in the antenna. The distance from the dewar top (located on the plane containing the Cassegrain focus) to the 4K stage is 293mm. The angle between the sub-reflector vertex and the ellipsoidal mirror center is 1.006 degrees (shown in Fig. A.2). We can calculate the position of the mirror center from theses values as,

$$\begin{aligned} d_{\text{mirror-subref}} &= (5882.8125 + 293 - 59.718)/\cos(1.006^\circ). \\ \therefore d_{\text{mirror-subref}} &= 6117.0379 \text{ mm}. \end{aligned} \tag{A.1.2}$$

This value is significantly different to the reported value in Fig. A.3. If we assume the ellipsoidal mirror has an effective focal length of $f_e = 49.5969$ mm as reported in Fig. A.3, the distance from the mirror to the horn aperture (denoted as d1 in Fig. A.3) must satisfy the lens equation for the frequency independent condition and $d_{\text{horn-mirror}}$ will need to be,

$$\begin{aligned} d_{\text{horn-mirror}} &= \frac{d_{\text{mirror-subref}} f_e}{d_{\text{mirror-subref}} - f_e} \\ \therefore d_{\text{horn-mirror}} &= 50.0023 \text{ mm}. \end{aligned} \tag{A.1.3}$$

This is consistent with the Front-End Design Report (within the reported decimal points). The resulting beam radius on the sub-reflector will however be,

$$\begin{aligned} w_{\text{sub}} &= \frac{d_{\text{mirror-subref}}}{d_{\text{horn-mirror}}} w_{\text{horn}} \\ \therefore w_{\text{sub}} &= 314.514 \text{ mm}. \end{aligned} \tag{A.1.4}$$

This results in an illumination edge taper level of 12.35 dB, which is slightly different to the target beam radius.

### A.1.1.3 Mirror Effective Focal Length

For the illumination on the sub-reflector to have a beam radius of 316.266 mm, using the distance from the sub-reflector to the mirror from Eq. (A.1.1), the required effective focal length of the mirror will need to be,

$$\begin{aligned} f_e &= \frac{d_{\text{mirror-subref}} d_{\text{horn-mirror}}}{d_{\text{mirror-subref}} + d_{\text{horn-mirror}}} \\ \therefore f_e &= 49.5969 \text{ mm}. \end{aligned} \tag{A.1.5}$$

This value does not match the reported effective focal length of the mirror in Fig. A.3. The focal radii for the ellipsoidal mirror are listed as $R_1 = 67.529$ mm and $186.668$ mm respectively. Using these values, the effective focal length of the mirror will be,

$$\begin{aligned} f_e &= \frac{R_1 R_2}{R_1 + R_2} \\ \therefore f_e &= 49.5895 \text{ mm}. \end{aligned} \tag{A.1.6}$$

This value exactly matches the value reported in Fig. A.3. If we assume the ellipsoidal mirror has the reported effective focal length of $f_e = 49.5895$ mm, then the band 8 horn positioned 50 mm away from the mirror will produce a frequency independent beam at a position,

$$\begin{aligned} d &= \frac{50.0000 * 49.5895}{50.000 - 49.5895} \\ \therefore d &= 6040.2064 \text{ mm}, \end{aligned} \tag{A.1.7}$$

away from the mirror. This is drastically different from the required distance between the mirror and sub-reflector of 6151.112 mm, and the reported value of 6148.6 mm. Thus, the band 8 horn positioned 50 mm away from the mirror with effective focal length 49.5895 mm will not produce a frequency independent illumination at the sub-reflector.

The various cases from the Front-End Design Report and the calculated values are summarized in Table. A.1. Here, the required values are the necessary values to obtain the target illumination edge taper of 12.21 dB.

**Table A.1** Summary of the various differences from the FEND report and calculated values.

| Parameter | Reported (mm) | Required (mm) | **Currently implemented** (mm) |
|---|---|---|---|
| $d_{\text{mirror-subref}}$ | 6148.6 | 6151.112 | **6117.038** |
| $d_{\text{horn-mirror}}$ | 50 | 50.002 | **50** |
| $f_e$ | 49.5895 | 49.5969 | **49.5895** |

### A.1.1.4 Reported Optics Performance

The reference Naruse et al. (2009) shows the aperture efficiency at the sub-reflector using the near-field measurement results. However, these values do not explicitly reflect the aperture efficiency of the antenna on the sky.

## A.2 Ray Tracing Analysis

A simplified diagram of the ALMA 12-m antenna and the band 8 optics are shown in Fig. A.4. Here, the mechanical drawings were used as the reference, thus the mirror is positioned 6117.0379 mm away from the sub-reflector with an effective focal length of 49.5895 mm. Figure A.5 shows the ALMA 12-m antenna with the ALMA band 8 receiver optics modeled in CODE V.

The CODE V model clearly shows an image of the sub-reflector 50 mm away from the mirror. The image of the sub-reflector has a large tilt with respect to the chief ray. However, this is to be expected since the band 8 receiver position is offset from the antenna axis thus making the sub-reflector slightly tilted with respect to the chief ray. The rays do not converge towards the phase center of the horn 24.43 mm away from the horn aperture plane.

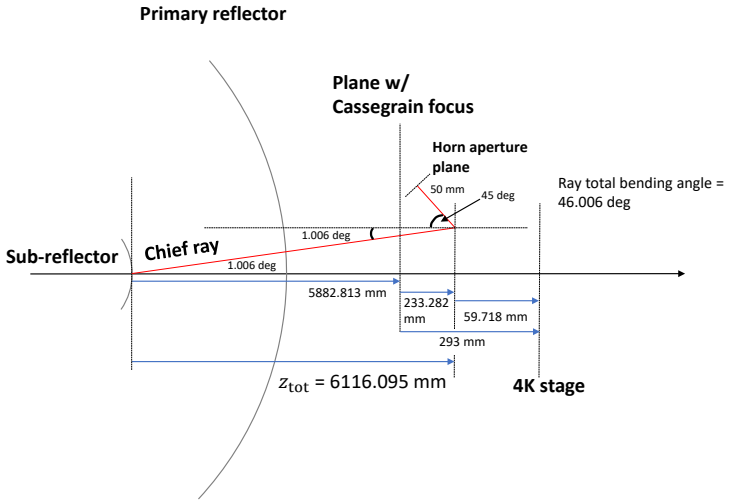


**Fig. A.4** Simplified schematic of ALMA 12-m antenna and band 8 optics.

## A.3 Physical Optics Analysis

The ALMA band 8 receiver optics were modeled in the physical optics software GRASP to obtain the far-fields on the sky and the fields at the sub-reflector. An ideal balanced hybrid condition feed horn with the same dimensions as the band 8 horn was used for all analyses.

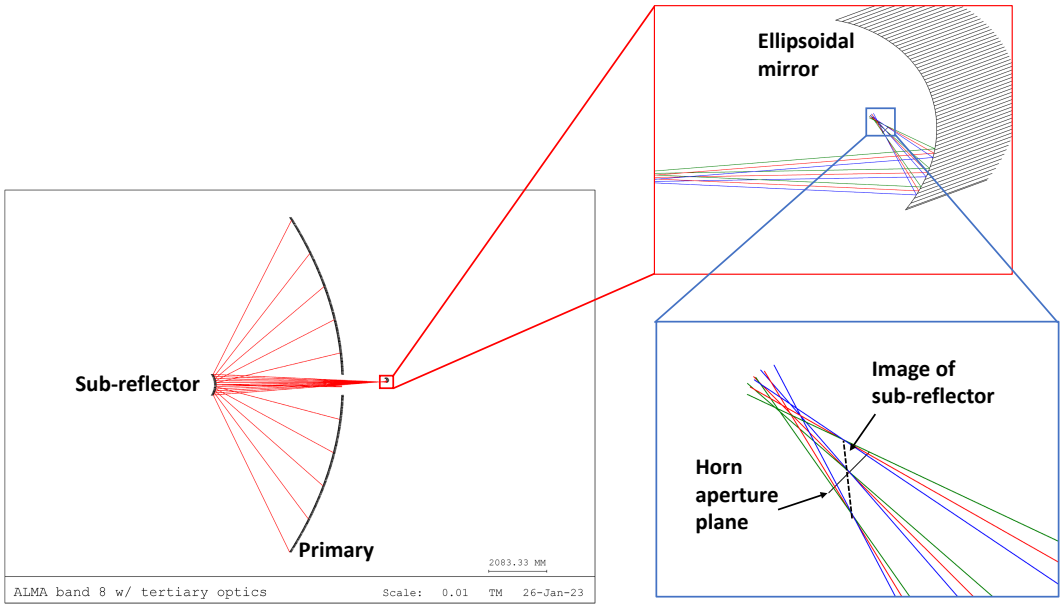


**Fig. A.5** ALMA 12-m antenna modeled with band 8 receiver optics

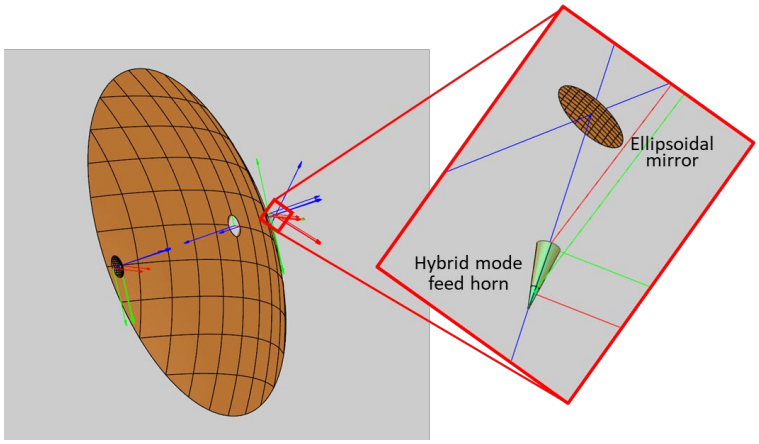


**Fig. A.6** Single mirror tertiary optics modeled in GRASP

#### A.3.0.1 Fields on Sub-Reflector

The fields on the sub-reflector from the feed were calculated at 385, 442, and 500 GHz. The fields were calculated on a spherical surface centered at the off-axis Cassegrain focus with $\theta = 1.006$ degrees and $R = 5886.097$ mm away from the sub-reflector vertex. The co-polarization is denoted as CoP and the cross-polarization as XsP. The field amplitude is shown in Fig. A.7 and the phase in Fig. A.8.

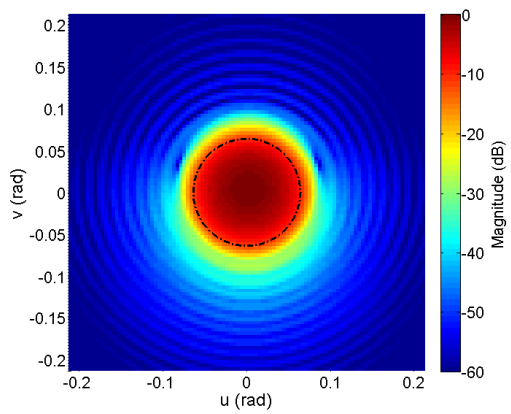


**(a)** 385 GHz

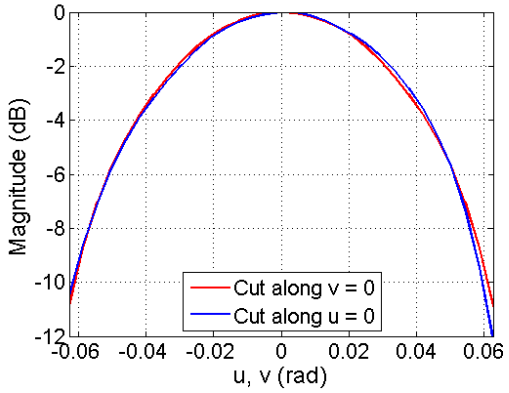


**(b)** 385 GHz

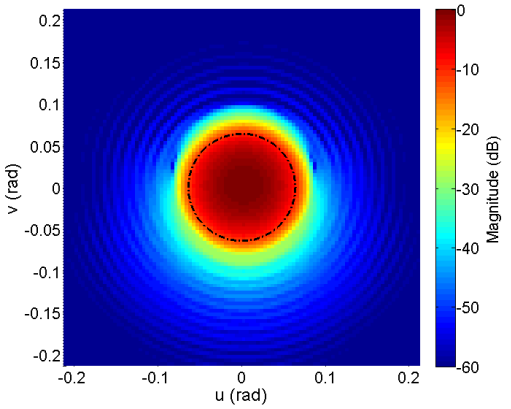


**(c)** 442 GHz

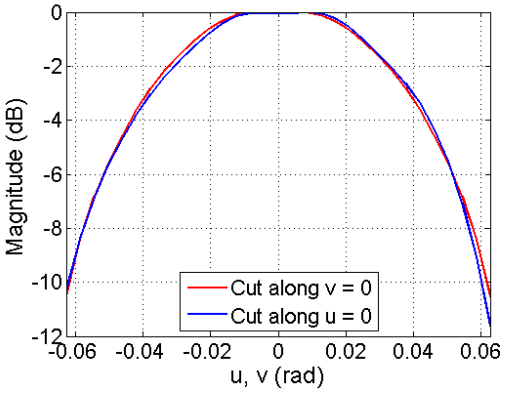


**(d)** 442 GHz

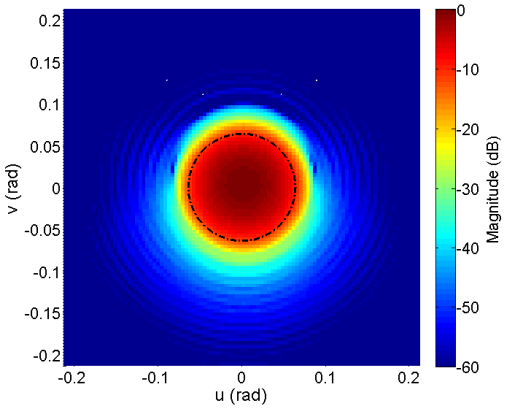


**(e)** 500GHz

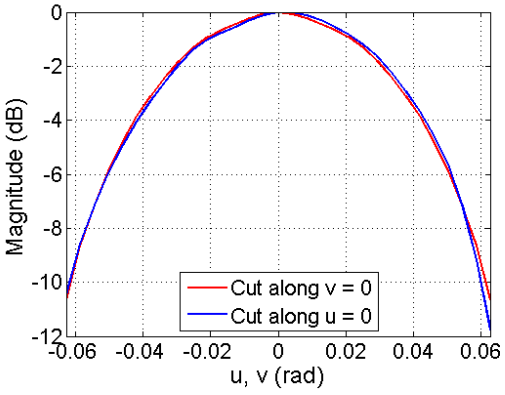


**(f)** 500 GHz

**Fig. A.7** The field magnitude on the sub-reflector at 385, 442, and 500 GHz. The dashed dotted circle shows the angular range of the sub-reflector. The left columns shows the full profile and the right column shows the cuts along $u = 0$ and $v = 0$ in the range of the sub-reflector (dotted dashed circle in left column).

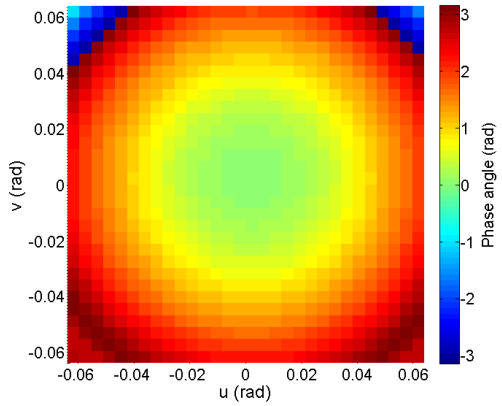


**(a)** 385 GHz

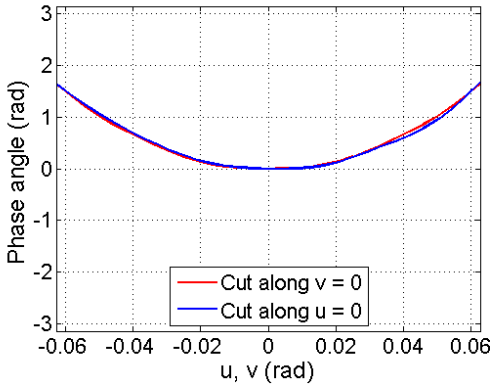


**(b)** 385 GHz

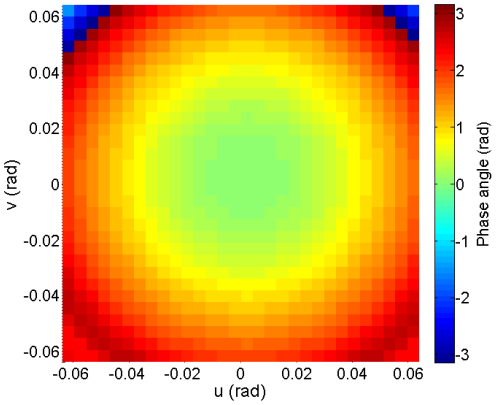


**(c)** 442 GHz

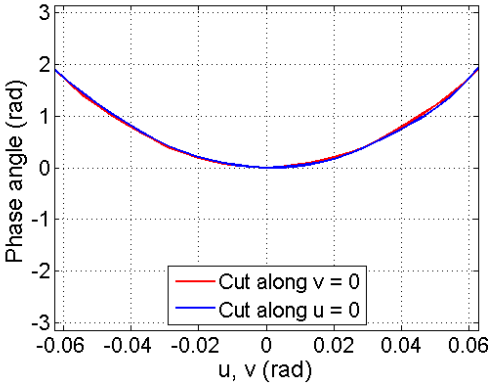


**(d)** 442 GHz

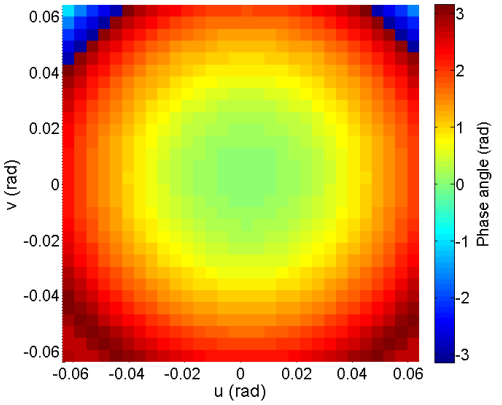


**(e)** 500GHz

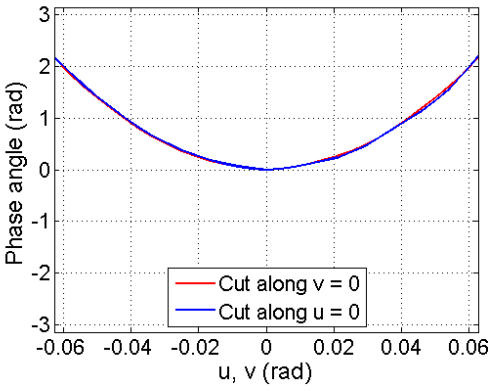


**(f)** 500 GHz

**Fig. A.8** The phase at the sub-reflector at 385, 442, and 500 GHz. The left columns shows the full profile in the range of the sub-reflector and the right column shows the cuts along $u = 0$ and $v = 0$.

### A.3.0.2 Beams on Sky

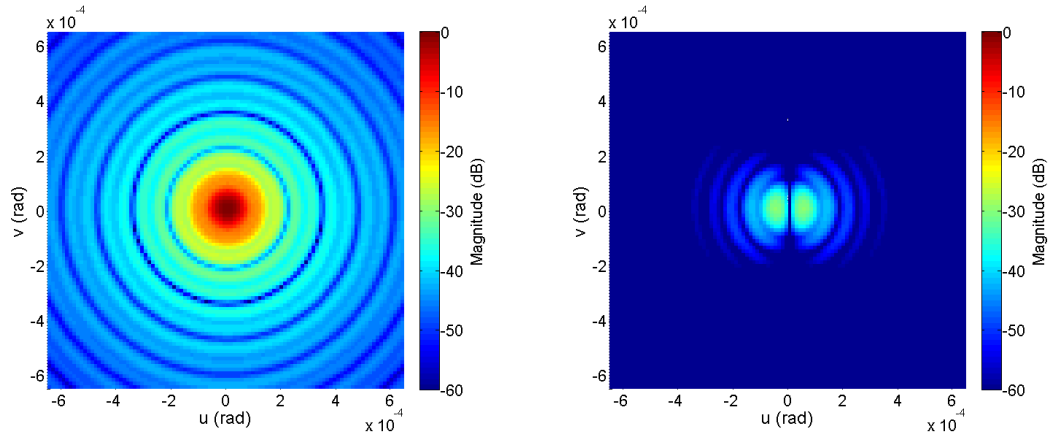


**(a)** Co-Pol: 85 GHz




**(b)** Xs-Pol: 385 GHz

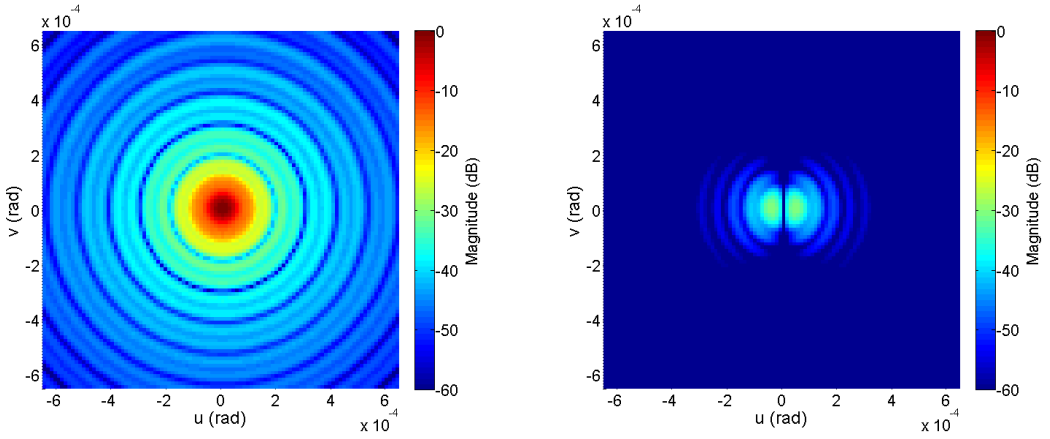


**(c)** Co-Pol: 442 GHz




**(d)** Xs-Pol: 442 GHz

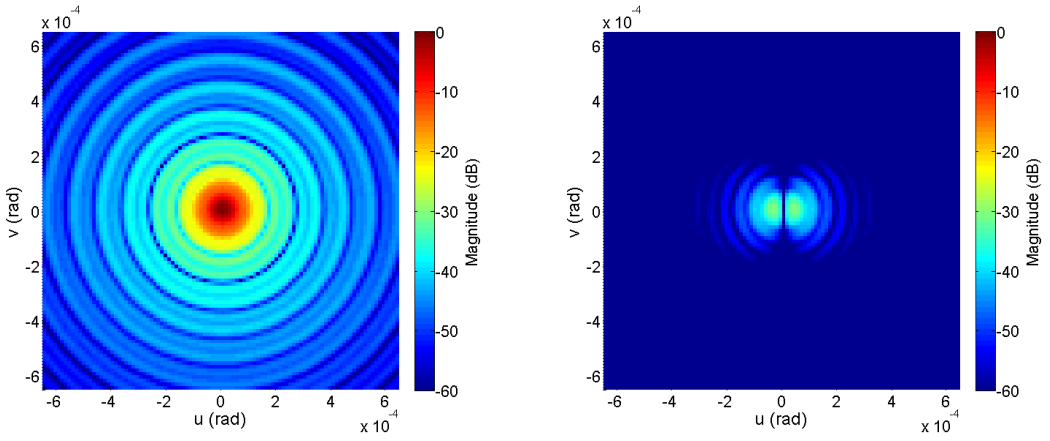


**(e)** Co-Pol: 500 GHz




**(f)** Xs-Pol: 500 GHz

**Fig. A.9** The far-fields on the sky. The left column shows the Co-Pol, the right column shows the Xs-Pol.

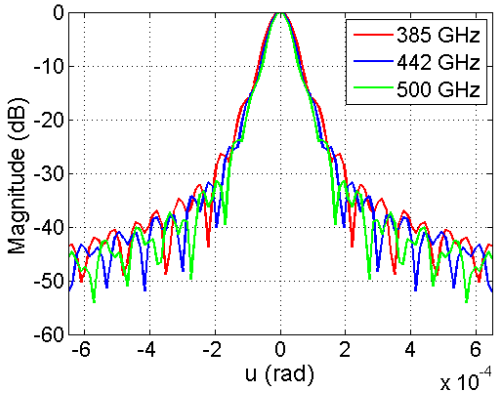


**(a)** Co-Pol: Cut along v = 0

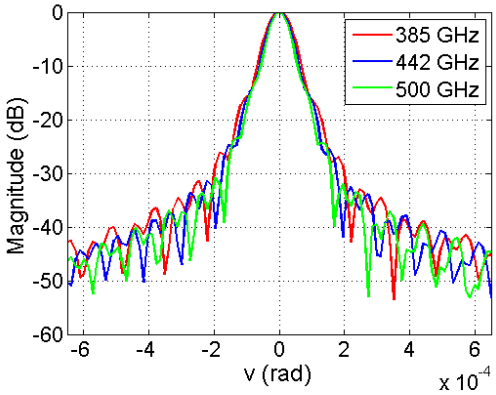


**(b)** Co-Pol: Cut along u = 0

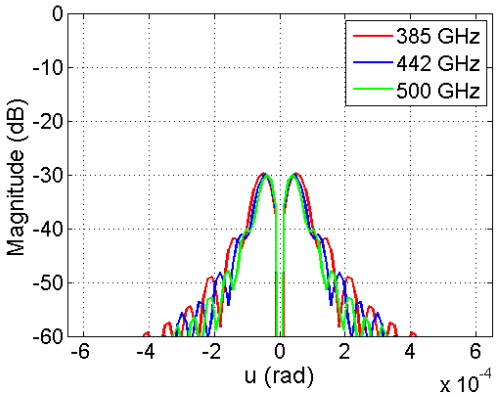


**(c)** Xs-Pol: Cut along v = 0

**Fig. A.10** The symmetrical and asymmetrical cuts of the far-fields on the sky.

#### A.3.0.3 Aperture Efficiency

The aperture efficiency is shown in Table. A.2.

**Table A.2** Aperture efficiency of the current ALMA band 8 optics

| | 385 GHz | 442 GHz | 500 GHz |
|---|---|---|---|
| $\eta_{\mathrm{A}}$ | 0.7021 | 0.6615 | 0.6153 |
| $\eta_{\mathrm{sub,\ feed}}$ | 0.7036 | 0.6581 | 0.6068 |
| $\eta_{\mathrm{sub,\ beam}}$ | 0.7061 | 0.6602 | 0.6085 |

## A.4 Sub-Reflector Movement

The ALMA antenna utilizes a movable sub-reflector to adjust the final focus of the telescope to compensate for any defocusing. A common defocusing phenomenon is the gravitational deformation of the primary reflector changing its focal length. Gravitational sag of the primary will alter its parabolic shape into a different paraboloid with a different focal length. The sub-reflector back focal point can be repositioned to the altered focus of the primary to compensate

for the shift and recreate a Cassegrain reflector but with a different effective focal length. This is an effective way to maintain good optical performance actively during observations when the antenna is required to continuously track targets on the sky with shifting elevation angles.

Adjusting the sub-reflector position will change the final focus of the antenna. The change in focus position will be affected by the squared optical magnification of the antenna. Thus, a small change in sub-reflector position will result in large changes in the final focus position (Fig. A.11). For the ALMA 12-m antenna, the focus position will shift by a factor of 400 given the magnification of 20 of the antenna. A Gaussian beam from a feed will however, not be affected much by the change in sub-reflector position. The Gaussian beam will only change from the target illumination by the propagation difference given by the sub-reflector movement, which for small movements, does not change the beam radius or radius of curvature by much (Fig. A.12).

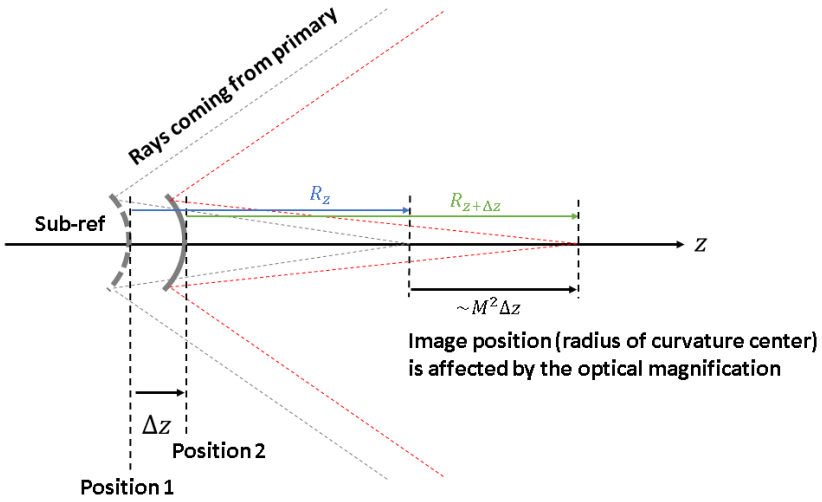


**Fig. A.11** Diagram showing the change in focus position when the sub-reflector is repositioned.

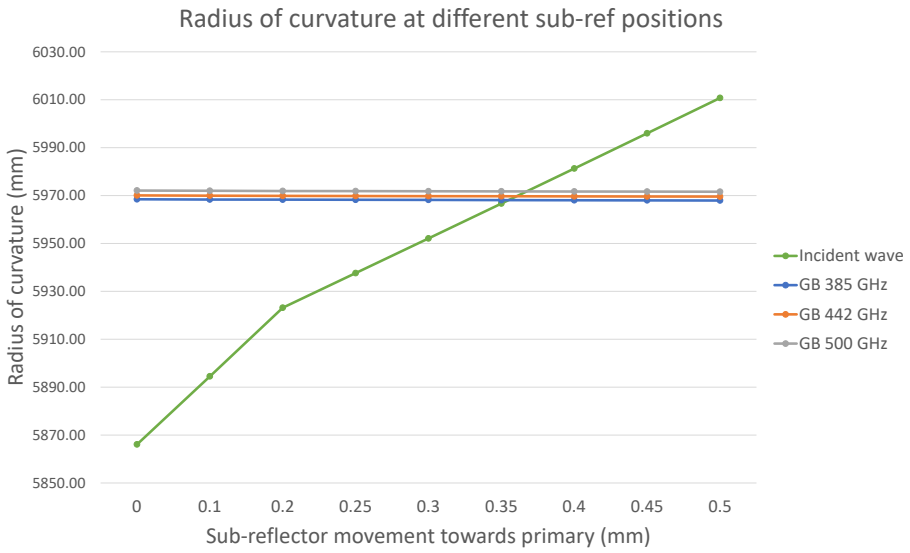


**Fig. A.12** The change in radius of curvature for the incident wave and a Gaussian beam.

## A.5 Simulations with Sub-Reflector Movement

### A.5.1 Fields at Sub-Reflector

The field amplitude and phase at the sub-reflector when repositioned 0.35 mm towards the primary are shown in Fig. A.13 and Fig.A.14. The phase shows a flat distribution at each frequency indicating minimal defocus.

### A.5.2 Beam on Sky

The highest aperture efficiency from this analysis was when the sub-reflector was moved 0.35 mm towards the primary reflector. The far-fields when the sub-reflector is repositioned 0.35 mm towards the primary and the comparison along $v = 0$ rad are shown in Fig. A.15 and the comparison between symmetrical and asymmetrical cuts are shown in Fig. A.16. The far-fields when the sub-reflector is moved 0.35 mm shows a distinct mainlobe and concentric sidelobes compared to the far-fields when the sub-reflector is at the nominal position.

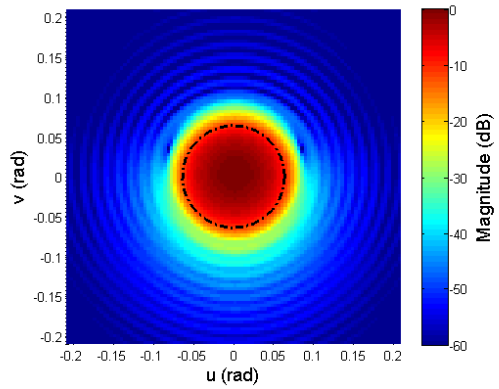


**(a)** 385 GHz

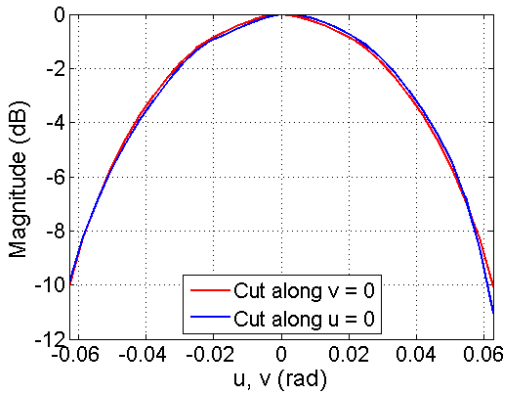


**(b)** 385 GHz

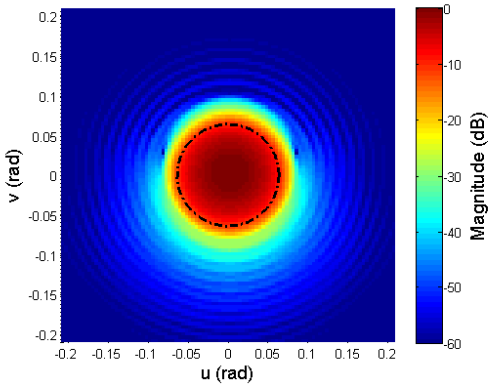


**(c)** 442 GHz

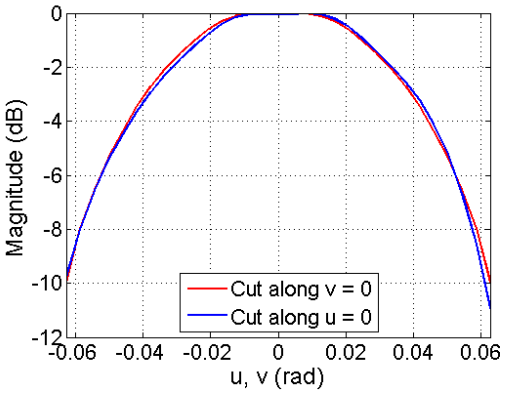


**(d)** 442 GHz

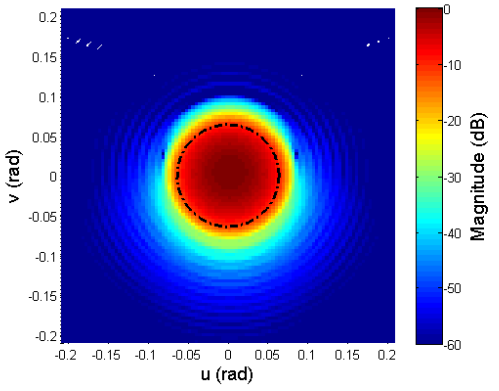


**(e)** 500GHz

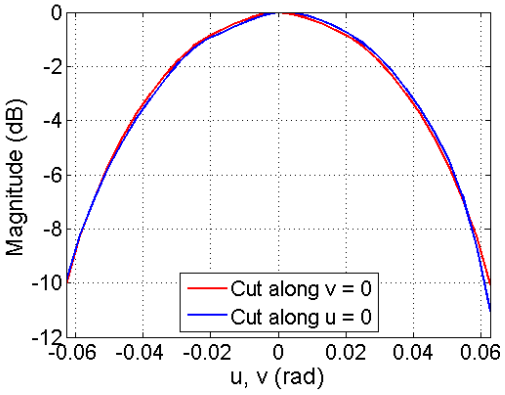


**(f)** 500 GHz

**Fig. A.13** The field magnitude on the sub-reflector when repositioned 0.35 mm towards the primary reflector at 385, 442, and 500 GHz. The dashed dotted circle shows the angular range of the sub-reflector. The left columns shows the full profile and the right column shows the cuts along $u = 0$ and $v = 0$ in the range of the sub-reflector (dotted dashed circle in left column).

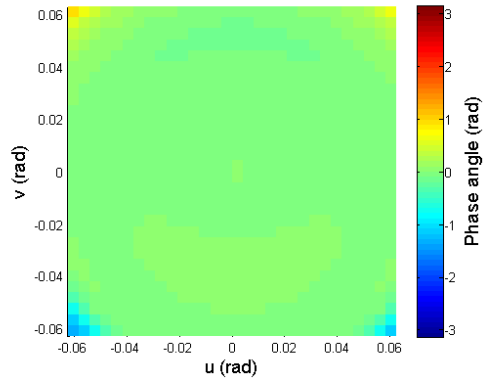


**(a)** 385 GHz

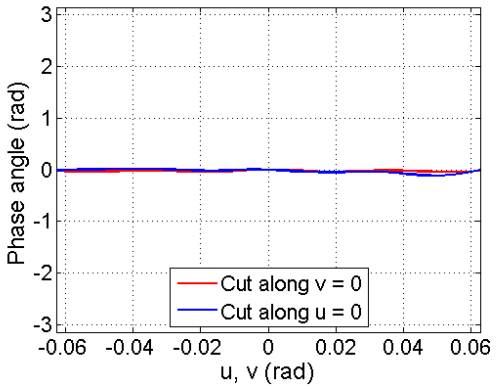


**(b)** 385 GHz

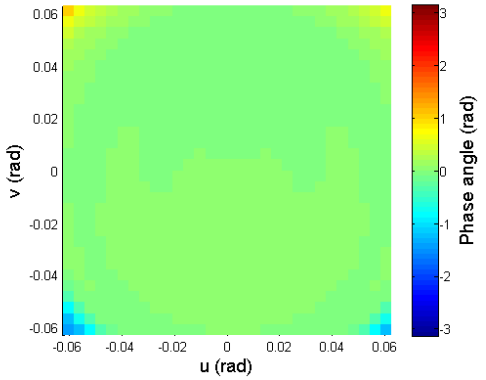


**(c)** 442 GHz

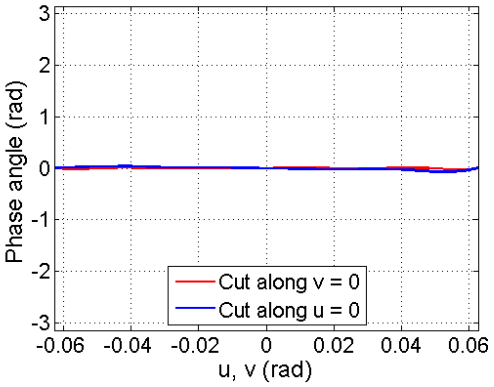


**(d)** 442 GHz

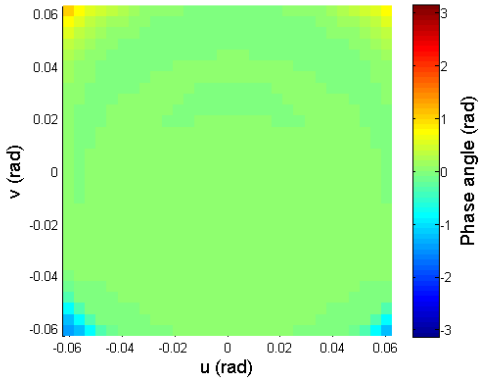


**(e)** 500GHz

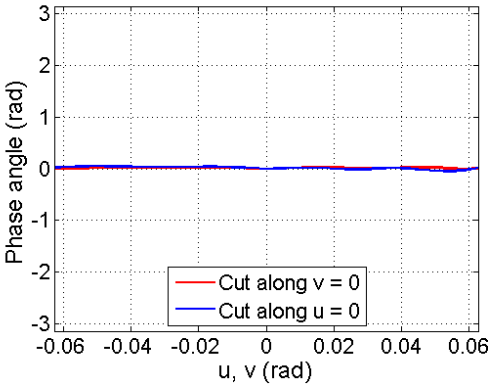


**(f)** 500 GHz

**Fig. A.14** The phase at the sub-reflector when repositioned 0.35 mm towards the primary at 385, 442, and 500 GHz. The left columns shows the full profile in the range of the sub-reflector and the right column shows the cuts along $u = 0$ and $v = 0$.

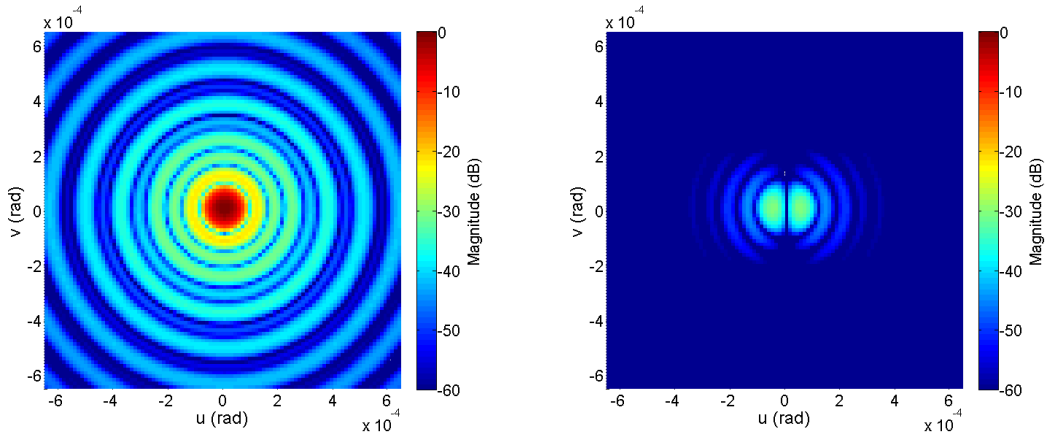


**(a)** Co-Pol: 385 GHz




**(b)** Xs-Pol: 385 GHz

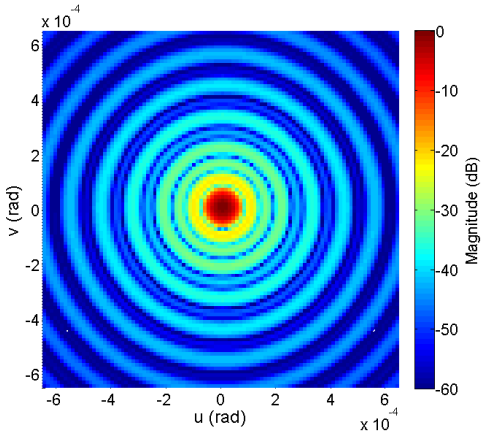


**(c)** Co-Pol: 442 GHz

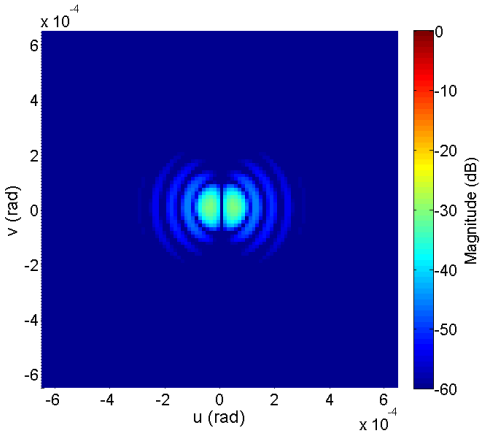


**(d)** Xs-Pol: 442 GHz

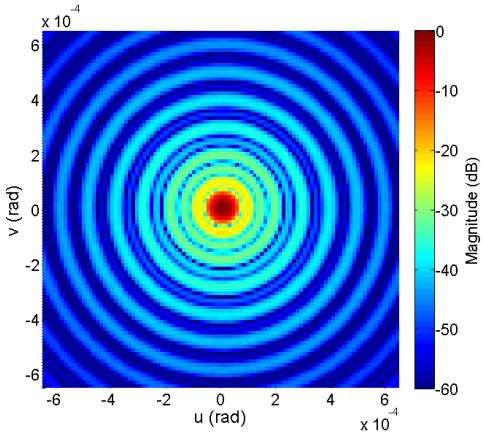


**(e)** Co-Pol: 500 GHz

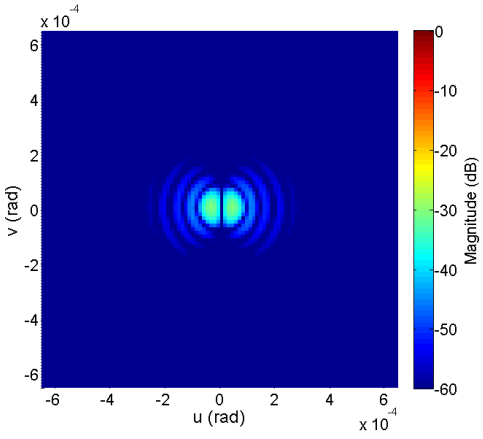


**(f)** Xs-Pol: 500 GHz

**Fig. A.15** The far-fields on the sky when the sub-reflector is moved 0.35mm closer to the primary.

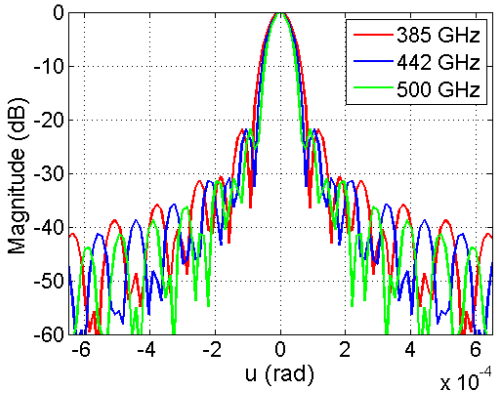


**(a)** Co-Pol: Cut along $v = 0$

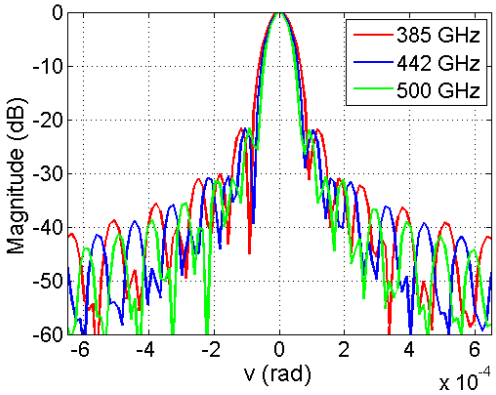


**(b)** Co-Pol: Cut along $u = 0$

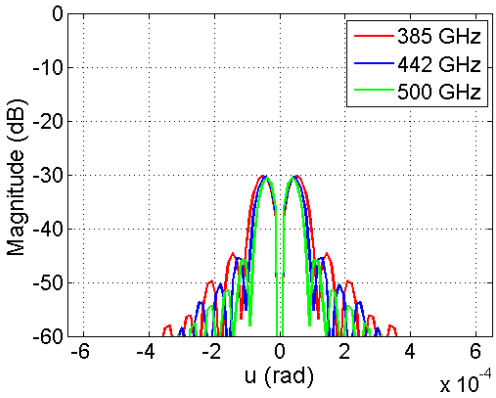


**(c)** Xs-Pol: Cut along $v = 0$

**Fig. A.16** The far-fields on the sky when the sub-reflector is moved 0.35mm closer to the primary.

### A.5.3 Aperture Efficiency

The focus position from the sub-reflector center was tracked using CODE V when the sub-reflector in the ALMA antenna was moved axially 0.30 mm to 0.50 mm with 0.05 mm intervals from the nominal position along the antenna axis. The aperture efficiency was calculated for each sub-reflector position and is shown in Fig. A.19. The maximum aperture efficiencies are summarized in table. A.3.

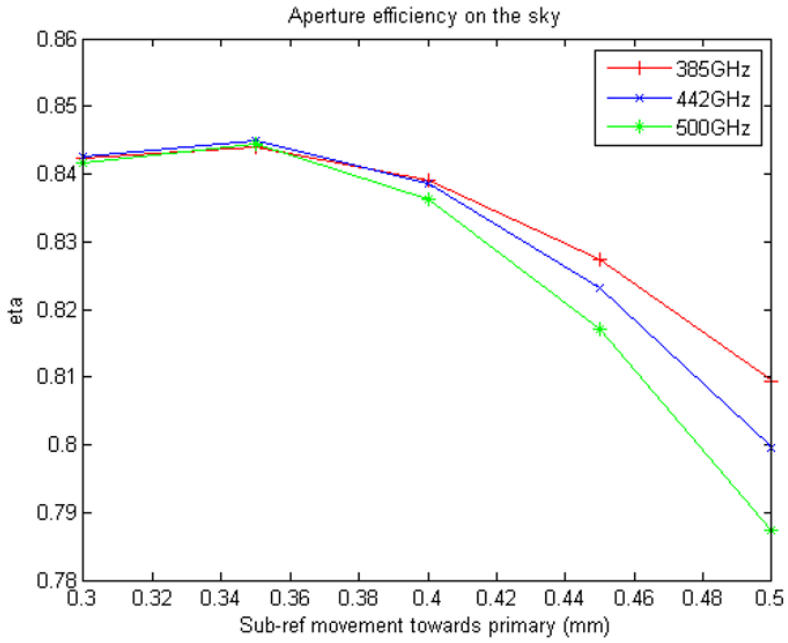


**Fig. A.17** The aperture efficiency of the antenna with different sub-reflector positions.

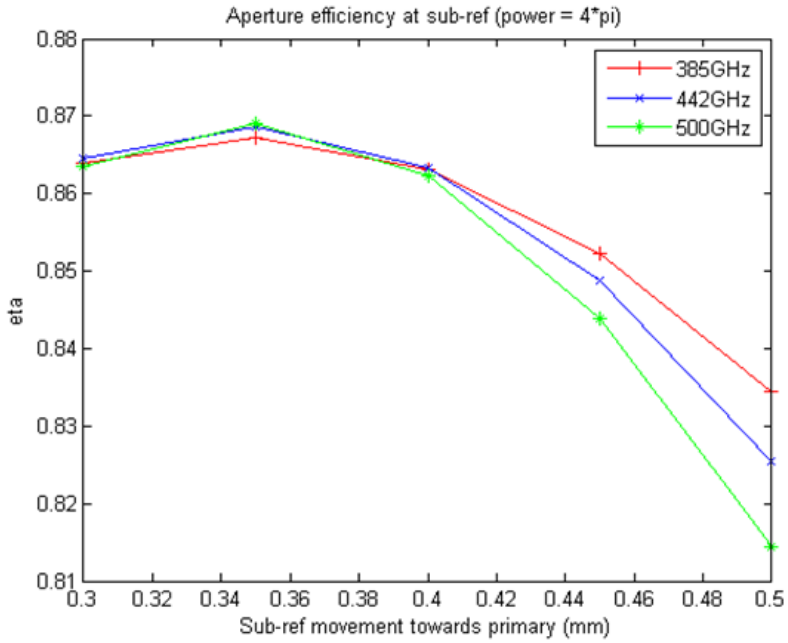


**Fig. A.18** The aperture efficiency of the antenna with different sub-reflector positions.

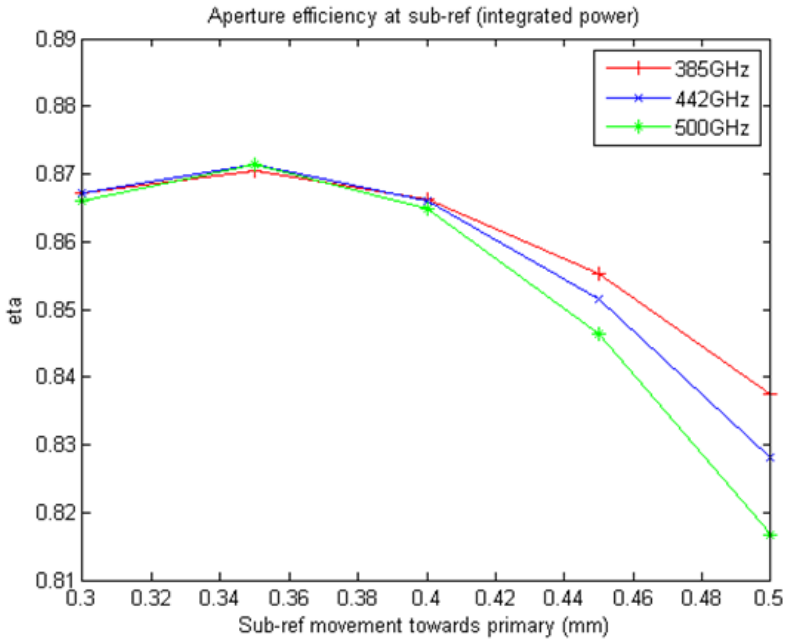


**Fig. A.19** The aperture efficiency of the antenna with different sub-reflector positions.

**Table A.3** Aperture efficiency of the current ALMA band 8 optics when sub-reflector is moved 0.35 mm towards the primary reflector

| | 385 GHz | 442 GHz | 500 GHz |
|---|---|---|---|
| $\eta_{\mathrm{A}}$ | 0.8441 | 0.8450 | 0.8445 |
| $\eta_{\mathrm{sub,\ feed}}$ | 0.8672 | 0.8687 | 0.8691 |
| $\eta_{\mathrm{sub,\ beam}}$ | 0.8704 | 0.8715 | 0.8715 |

**Appendix B**

**Single-Mirror Tertiary Optics for ALMA Band 8**

## B.1 Single-Mirror Design

The solution to the position and focal length for a single mirror system can be solved if the horn parameters are fixed. Considering the setting in Fig. B.1, for an object with distance $d_1$ away from a lens with focal length $f$, the distance to the image $d_2$ will be given by,

$$\frac{1}{f} = \frac{1}{d_1} + \frac{1}{d_2}. \tag{B.1.1}$$

A point $R_1$ away from the object will have an image $d_2 + R_2$ away from the lens and will again satisfy,

$$\frac{1}{f} = \frac{1}{d_1 - R_1} + \frac{1}{d_2 + R_2}. \tag{B.1.2}$$

The image height will be given by the magnification,

$$h_2 = -\frac{d_2}{d_1} h_1. \tag{B.1.3}$$

Here, a negative image height represents a inverted image of the object, and a negative image distance indicates a virtual image.

By setting the beam radius at the sub-reflector $w_{\text{sub}}$, beam radius at the horn aperture $w_{\text{horn}}$, radius of curvature of the beam at the sub-reflector $R_{\text{sub}}$, and the radius of curvature of the beam at the horn aperture $R_{\text{horn}}$ as $h_1$, $h_2$, $R_1$, and $R_2$ respectively, the equations (B.1.1), (B.1.2), and (B.1.3) can be solved to obtain the distance from the sub-reflector $d_1$, the distance from the mirror to the horn aperture $d_2$, and the effective focal length of the mirror $f$ with,

$$\begin{cases} d_2 &= -R_{\text{sub}} R_{\text{horn}} \frac{1 + \frac{w_{\text{sub}}}{w_{\text{horn}}}}{R_{\text{sub}} - R_{\text{horn}} \left(\frac{w_{\text{sub}}}{w_{\text{horn}}}\right)^2} \\ d_1 &= \frac{w_{\text{sub}}}{w_{\text{horn}}} d_2 \\ f &= \frac{d_1 d_2}{d_1 + d_2}. \end{cases} \tag{B.1.4}$$

Using the horn parameters for the band 8 horn, we set $R_{\text{horn}} = 24.43$ mm, $w_{\text{horn}} = 2.5708$ mm. We set the target illumination to be 12.21 dB to match the current target for ALMA band 8 which results in a beam radius at the sub-reflector $w_{\text{sub}} = 316.266$ mm. The curvature center is set to match the off-axis Cassegrain focus $R_{\text{sub}} = 5866.097$ mm. Using these values, $d_1$, $d_2$,

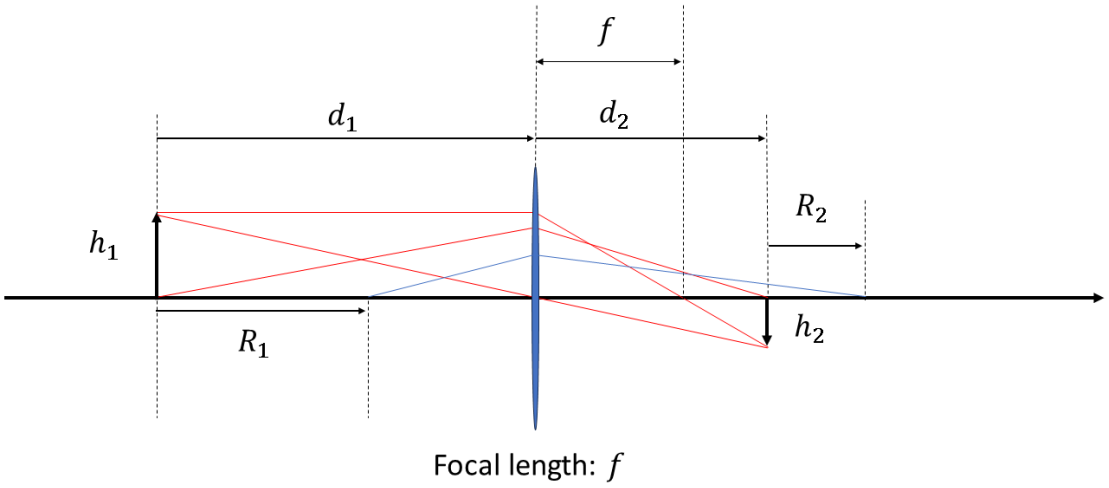


**Fig. B.1** System setting for single-mirror tertiary optics

and $f$ will return,

$$\begin{cases} d_1 &= 6009.06 \text{ mm}, \\ d_2 &= 48.85 \text{ mm}, \\ f &= 48.45 \text{ mm}. \end{cases} \tag{B.1.5}$$

### B.1.1 Modeling and Analysis with Ray Tracing

The solution to the single-mirror from Eq. (B.1.5) was modeled in CODE V and is shown in Fig. B.2. The mirror surface is an ellipsoid with an effective focal length equal to the solution in eq. (B.1.5). The reflection angle at the mirror is set to 46.01 degrees, the same as the current ALMA band 8 receiver optics. The aperture plane is set 48.85 mm away from the mirror and is rotated 45 degrees to so the chief ray axis (beam axis) intersects the antenna center axis at a 45 degree angle.

The image of the sub-reflector is clearly formed and can be seen at the horn aperture plane 48.85 mm away from the mirror. The rays converge towards the phase center of the horn 24.43 mm away from the horn aperture.

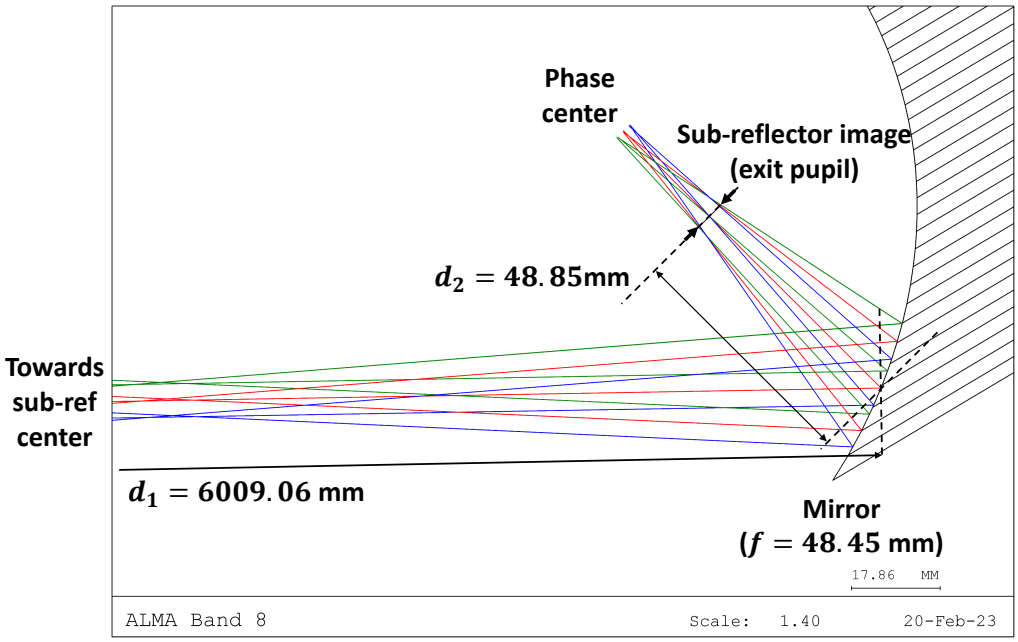


**Fig. B.2** Single mirror tertiary optics modeled in CODE V.

### B.1.2 PO Analysis

The same parameters were used to model the single mirror optics in GRASP and is shown in Fig. B.3. Physical optics simulations were conducted at 385 GHz, 442 GHz, and 500 GHz to obtain the illumination on the sub-reflector, the far-fields on the sky, and to calculate the aperture efficiency. An ideal hybrid-mode feed horn with a diameter 7.99 mm and slant length 24.43 mm was used as the feed. A power of $4\pi$ (W) is fed to the horn and the fields from the feed are propagated to each element in the order of, the feed to the tertiary optics, the tertiary optics to the sub-reflector, the sub-reflector to the primary reflector, and the primary reflector to the sky. The cryostat window can be seen in the lower left in Fig. B.3. However, the window was not included in the calculations since the beam will pass through its center and we expect little effects from the beam truncation.

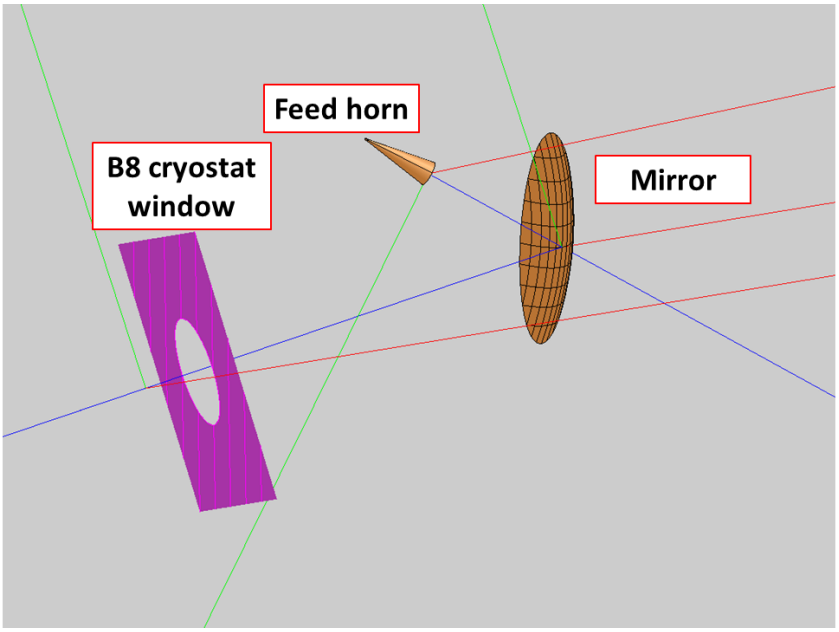


**Fig. B.3** Single mirror tertiary optics modeled in GRASP

#### B.1.2.1 Fields at Sub-Reflector

The fields on the sub-reflector were calculated on a reference spherical surface with radius $R = 5866.097$ mm centered at the off-axis Cassegrain focus. The field magnitude is shown in Fig. B.4 and the phase in Fig. B.5. The left columns show the two-dimensional distribution along the surface. The dotted lines in Fig. B.4 shows the angular extent of the sub-reflector from the off-axis Cassegrain focus. The right columns show the symmetrical cuts along $v = 0$ (red curves) and the asymmetrical cuts along $u = 0$ (blue curves), respectively. The phase distribution in Fig. B.5 is showing the difference between the feed phase and the spherical surface reference.

The amplitude distribution shows little deviation between frequencies successfully producing a constant illumination on the sub-reflector. The phase is also well matched showing a flat phase difference within the bounds of the sub-reflector. The minor asymmetry in the field magnitude arises from the off-axis reflection in the ellipsoidal mirrors.

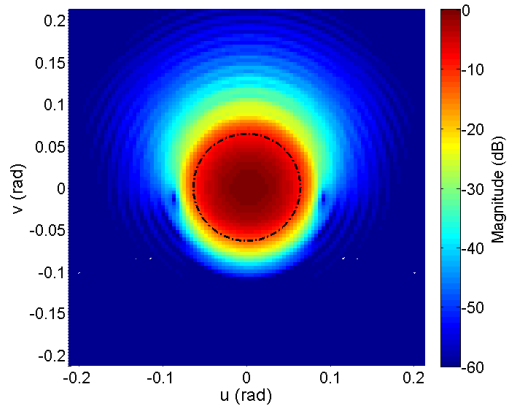


**(a)** 385 GHz

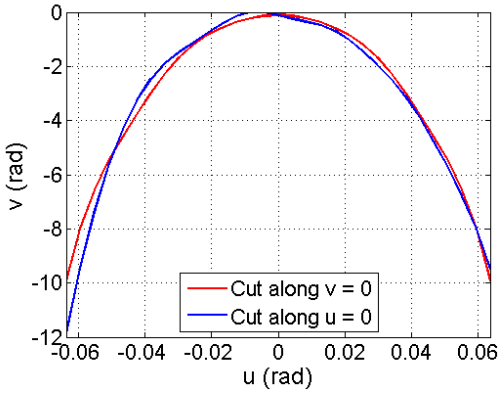


**(b)** 385 GHz

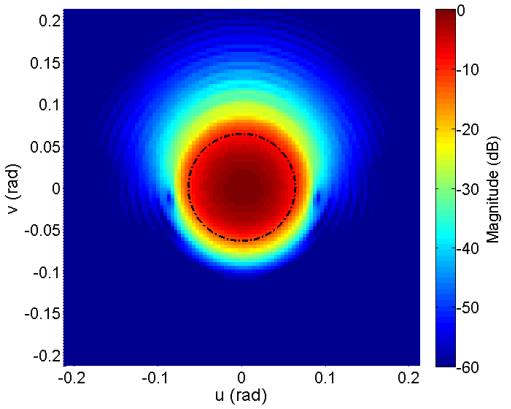


**(c)** 442 GHz

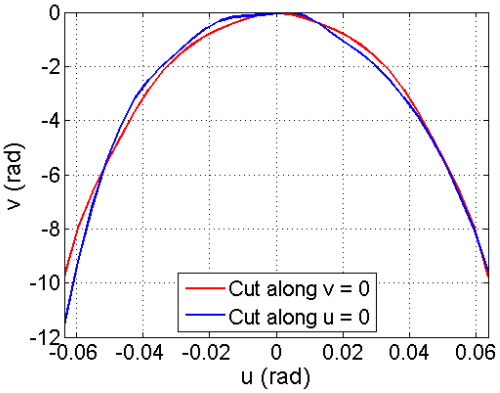


**(d)** 442 GHz

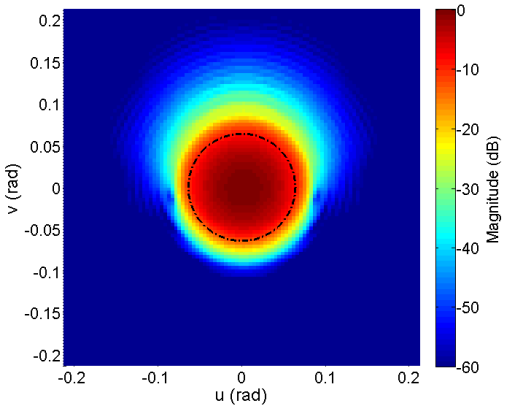


**(e)** 500GHz

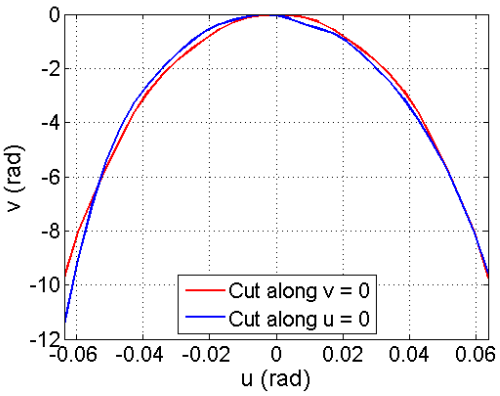


**(f)** 500 GHz

**Fig. B.4** The field magnitude on the sub-reflector with the single-mirror tertiary optics.

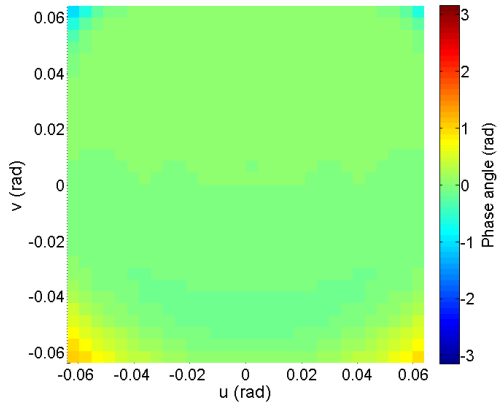


**(a)** 385 GHz

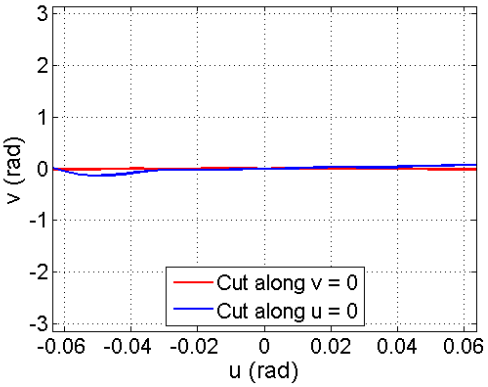


**(b)** 385 GHz

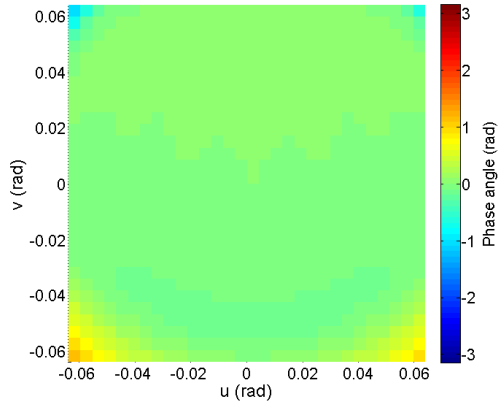


**(c)** 442 GHz

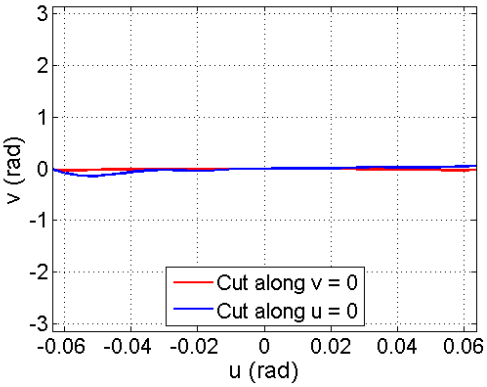


**(d)** 442 GHz

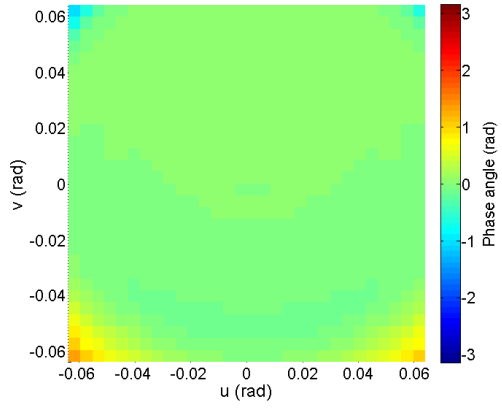


**(e)** 500GHz

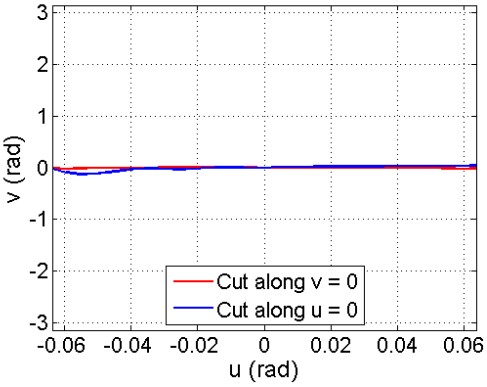


**(f)** 500 GHz

**Fig. B.5** The phase difference between the reference sphere and the receiver beam at the sub-reflector with the single-mirror tertiary optics.

#### B.1.2.2 Beam on Sky

The far-fields on the sky were calculated with the $u - v$ plane origin was offset by 0.0617 degrees ($1.076 \times 10^{-3}$ radians) from the antenna bore-sight direction to align the origin with the calculated peak position of the beams. The far-fields for the Co-polarization (Co-Pol) and cross-polarization (Xs-Pol) patterns are shown in Fig. B.6 and their symmetrical and asymmetrical cuts shown in Fig. B.7.

The beams on the sky show high symmetry with the first sidelobe lower than -21 dB. The maximum Xs-pol was lower than -30 dB. There was negligible beam squint due to the off-axis feed and mirror and the peak position was at $v = 0.0617$ degrees.

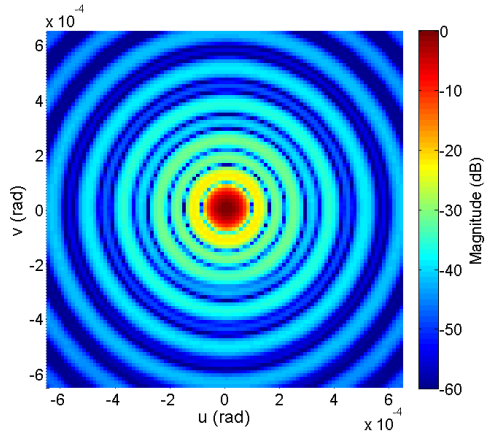


**(a)** Co-Pol: 385 GHz

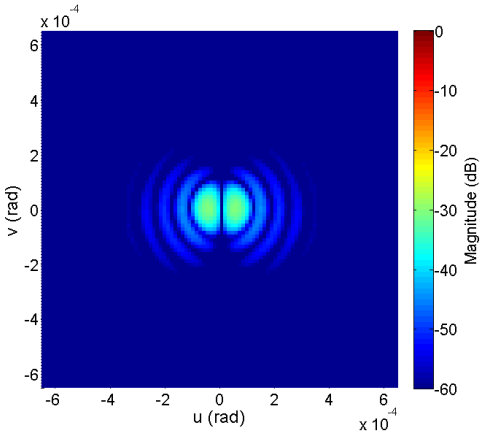


**(b)** Xs-Pol: 385 GHz

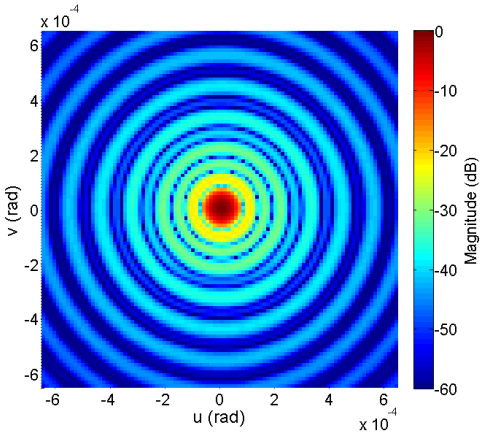


**(c)** Co-Pol: 442 GHz

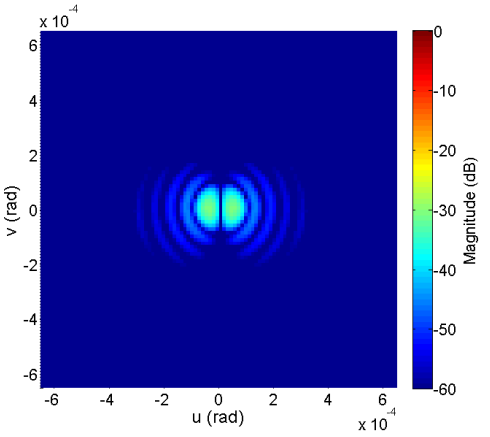


**(d)** Xs-Pol: 442 GHz

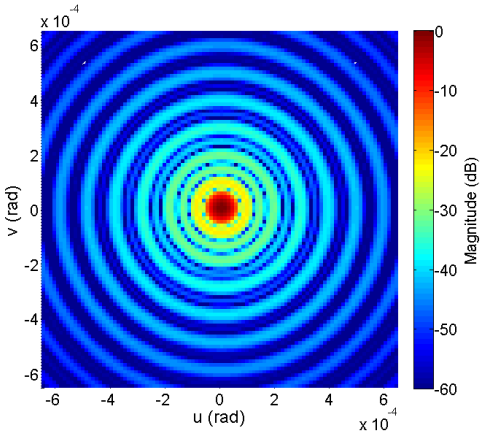


**(e)** Co-Pol: 500 GHz

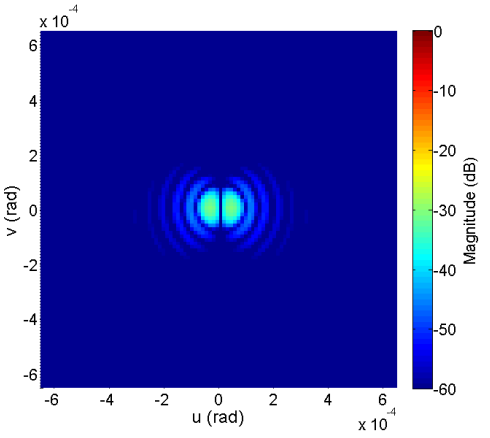


**(f)** Xs-Pol: 500 GHz

**Fig. B.6** The far-fields on the sky using single-mirror optics.

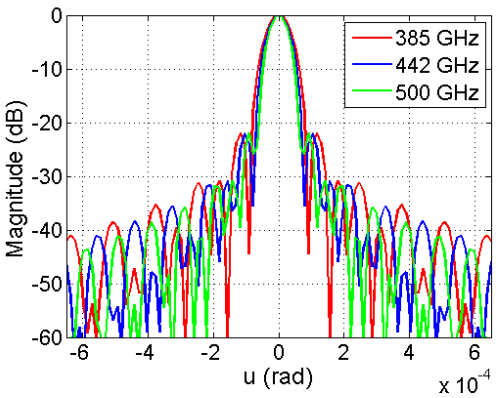


**(a)** Co-Pol: Cut along $v = 0$

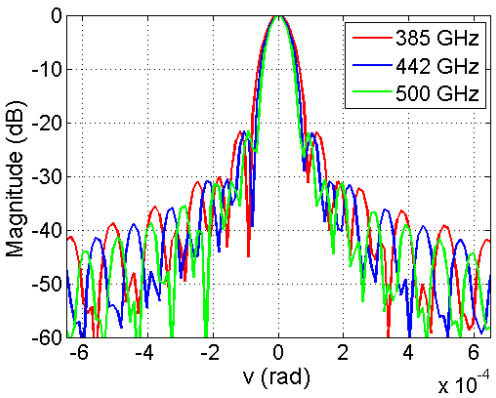


**(b)** Col-Pol: Cut along $u = 0$

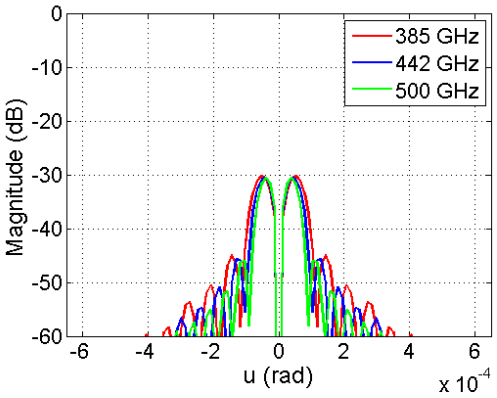


**(c)** Xs-Pol: Cut along $u = 0$

**Fig. B.7** The cuts of the far-fields on the sky using single-mirror optics.

### B.1.2.3 Aperture Efficiency

The aperture efficiency of the antenna using Eq (2.4.5) was calculated using the peak gain value from the far-fields, and the aperture efficiencies evaluated at the sub-reflector from Section. 4.2.3 were calculated using the fields at the sub-reflector. The total power from the feed is $4\pi$ as indicated in Section. B.1.2.

The aperture efficiency values are listed in Table. B.1. The single-mirror optics returns the expected high-aperture efficiency of greater than 0.80 on the sky and at the sub-reflector and is consistent with the expected aperture efficiency of the current ALMA band 8 receiver shown in Appendix A. The aperture efficiency also shows very little variation of less than 0.3 % at the frequency band edges. The minute frequency dependence seen in all aperture efficiencies is caused by the spill-over at the ellipsoidal mirror since the beam size is not constant with frequency there.

**Table B.1** Aperture efficiency of antenna with single-mirror tertiary optics

| | 385 (GHz) | 442 (GHz) | 500 (GHz) | $1 - \frac{\eta_{385}}{\eta_{500}}$ (%) |
|---|---|---|---|---|
| $\eta_{\mathrm{A}}$ | 0.8408 | 0.8421 | 0.8435 | 0.32 |
| $\eta_{\mathrm{sub,\ feed}}$ | 0.8603 | 0.8620 | 0.8632 | 0.34 |
| $\eta_{\mathrm{sub,\ beam}}$ | 0.8630 | 0.8644 | 0.8655 | 0.29 |

### B.1.3 Limitations of Single-Mirror Design

The attractiveness of a single-mirror design is the simplicity of the design. However, we are left with very little degrees of freedom since the distance from the horn aperture to the sub-reflector will be determined by the horn. For the case of the band 8 horn, the distance from the sub-reflector to the mirror is 6009.06mm which is only roughly 10mm away from the 110K window in the ALMA cryostat. If the reflection angle of 46.006 degrees from the current band 8 optics is to be maintained, the feed horn will not be able to fit within the 4K stage of the ALMA cryostat. Larger reflection angles may resolve this issue, however it will introduce more beam distortion due to using a more off-axis section in the ellipsoidal mirrors Murphy (1987). We may explore more solutions for the mirror position if we remove the constraints of using the current band 8 horn. We may also add more freedom in design by introducing another focusing element.